



Preface

This Activity Report covers scientific and technological activities carried out at the UVSOR-III Synchrotron Facility in FY2015 (April 2015-March 2016). This is the third volume in the blue series for the fourth decade of UVSOR Synchrotron, corresponding to the third year after the success of the second major upgrade project UVSOR-III in 2012. The UVSOR-III Synchrotron is a diffraction limit light source in the VUV region and is one of the most advanced low energy synchrotron radiation (SR) facilities in the world.

The UVSOR-III Synchrotron has a small electron storage ring of approximately 50 m-circumference with only 6 undulator beamlines (3 VUV and 3 in-vacuum soft X-ray undulators) and 8 dipole beamlines. The UVSOR Synchrotron belongs to the Institute for Molecular Science (IMS), one of the inter-university research institutes supported by MEXT (the Ministry of Education, Culture, Sports, Science and Technology in Japan), and has been leading chemical applications of SR-based VUV and soft X-rays since 1983, the beginning of UVSOR-I. Molecular science is growing up as an interdisciplinary science covering not only chemical and physical



sciences but also biosciences, and is now one of the most important targets of the low energy SR.

The total number of users is about 1,200 people · week; this means ca. 100 people/beamline/year and ca. 30 people/week. Most users stay for one or two weeks for the experiment. To support them at the high level of science and technology, staff members are always essential. Fortunately, in Accelerator Physics Division, two new staff scientists joined: Assistant Professor Dr. Masaki Fujimoto from Osaka University in April 2016 and Dr. Najmeh Sadat Mirian from the Institute for Research in Fundamental Sciences, Tehran, in July 2015. In addition, two new staff engineers joined in April 2016: Mr. Takayuki Yano from the Equipment Development Center of IMS and Mr. Yuichi Inagaki. They will work for the development of precise handling devices of various types of samples and the operation and upgrade of soft X-ray microscopies.

I hope many users will perform excellent work by fully utilizing UVSOR-III Synchrotron as a unique international hub for the SR research in advanced molecular science.

April 2016

Nobuhiro Kosugi

Director of UVSOR-III Synchrotron

The 68th Chemical Society of Japan (CSJ) Award

Prof. Nobuhiro Kosugi

Advanced Experimental and Theoretical Studies on Molecular Inner-shell Excitation

Dr. N. Kosugi has accomplished leading research projects based on soft X-ray absorption spectroscopy as follows:

1. Methodological developments in experiment and theory for the chemical application of molecular inner-shell excitations,
2. Local intermolecular interactions revealed by the chemical shift in inner-shell excitations,
3. Multi-electron and multi-state interactions revealed by the polarization dependence in inner-shell excitations.

He succeeded in finding various new aspects in molecular systems by his original chemical applications of soft X-ray absorption spectroscopy. His pioneering studies on the molecular inner-shell excitation as a unique probe are well known internationally and are affecting soft X-ray photoelectron spectroscopy and soft X-ray emission spectroscopy resonating with precisely selected inner-shell excited states. Furthermore, he led the upgrade projects UVSOR-II and UVSOR-III of the UVSOR Synchrotron and expanded chemical studies using soft X-rays in complementary collaboration with foreign synchrotron radiation facilities. His achievements in advanced experimental and theoretical studies on molecular inner-shell excitation have been recognized with the 68th Chemical Society of Japan (CSJ) Award. The CSJ Award started in 1948 and is historically most important in the CSJ. It is the first time this award has been given for the synchrotron radiation based research.

For more detail, see <http://www.chemistry.or.jp/en/awards/2015/>



IMS celebrated Prof. Kosugi's achievements awarded by the Chemical Society of Japan.

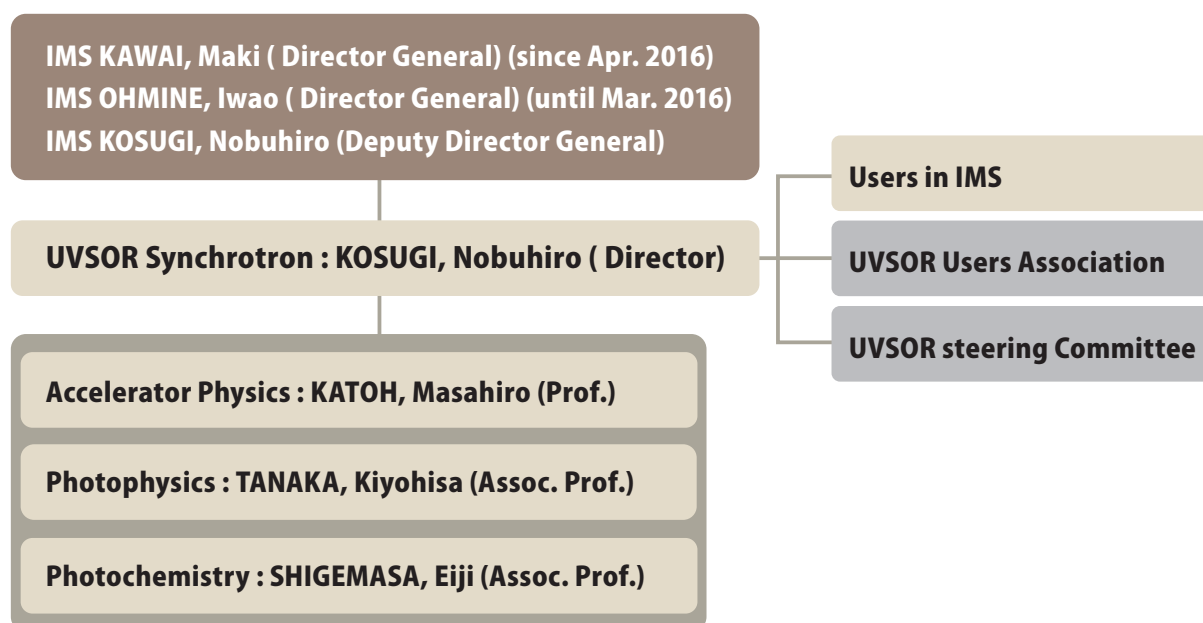
I

Organization and Staff List



UVSOR Organization

May 2016



Staff List

UVSOR Staff

Director

KOSUGI, Nobuhiro	Professor	kosugi@ims.ac.jp
------------------	-----------	------------------

Light Source Division (Accelerator Physics)

KATOH, Masahiro	Professor	mkatoh@ims.ac.jp	
FUJIMOTO, Masaki	Assistant Professor	mfmoto@ims.ac.jp	(since Apr. 2016)
MIRIAN, Najmeh Sadat	Research Fellow	mirian@ims.ac.jp	(since May 2015)
YAMAZAKI, Jun-ichiro	Unit Chief Engineer	yamazaki@ims.ac.jp	
HAYASHI, Kenji	Unit Chief Engineer	h-kenji@ims.ac.jp	
TESHIMA, Fumitsuna	Assistant Unit Chief Engineer	tetsu@ims.ac.jp	
MINAKUCHI, Aki	Supporting Engineer	minakuchi@ims.ac.jp	

Light Source Division (X-ray Imaging Optics)

OHIGASHI, Takuji	Assistant Professor	ohigashi@ims.ac.jp
INAGAKI, Yuichi	Engineer	yinagaki@ims.ac.jp

Beamline Division (Photophysics)

TANAKA, Kiyohisa	Associate Professor	k-tanaka@ims.ac.jp	
HIRAHARA, Toru	Visiting Associate Professor		
MATSUNAMI, Masaharu	Assistant Professor	matunami@ims.ac.jp	(until May 2015)
IDETA, Shin-ichiro	Assistant Professor	idetas@ims.ac.jp	
HASUMOTO, Masami	Unit Chief Engineer	hasumoto@ims.ac.jp	
SAKAI, Masahiro	Assistant Unit Chief Engineer	sakai@ims.ac.jp	
TOKUSHI, Tetsuzyo	Supporting Engineer	tetsuzyo@ims.ac.jp	
KOSWATTAGE, Kaveenga Rasika	Visiting Researcher	rasika@ims.ac.jp	(until Mar. 2016)

Beamline Division (Photochemistry)

SHIGEMASA, Eiji	Associate Professor	sigemasa@ims.ac.jp
IWAYAMA, Hiroshi	Assistant Professor	iwayama@ims.ac.jp
NAKAMURA, Eiken	Facility Chief Engineer	eiken@ims.ac.jp
KONDO, Naonori	Assistant Unit Chief Engineer	nkondo@ims.ac.jp
YANO, Takayuki	Assistant Unit Chief Engineer	yano@ims.ac.jp
HORIGOME, Toshio	Senior Engineer	horigome@ims.ac.jp
HAYASHI, Kenichi	Supporting Engineer	khayasi@ims.ac.jp

Secretary

HAGIWARA, Hisayo	hagiwara@ims.ac.jp
MASUDA, Michiko	masuda@ims.ac.jp

UVSOR Steering Committee

KOSUGI, Nobuhiro	UVSOR, IMS	Chair
KATOH, Masahiro	UVSOR, IMS	
SHIGEMASA, Eiji	UVSOR, IMS	
TANAKA, Kiyohisa	UVSOR, IMS	
HIRAHARA, Toru	UVSOR, IMS	
YOKOYAMA, Toshihiko	IMS	
KERA, Satoshi	IMS	
AKIYAMA, Shuji	IMS	
FUJI, Takao	IMS	
HARADA, Yoshihisa	Univ. of Tokyo	(until Mar. 2016)
NAKAGAWA, Kazumichi	Kobe Univ.	(until Mar. 2016)
SODA, Kazuo	Nagoya Univ.	(until Mar. 2016)
ADACHI, Shin-ichi	KEK-PF	
DAIMON, Hiroshi	NAIST	
OHASHI, Haruhiko	JASRI	

SASAKI, Shigemi	Hiroshima Univ.	
KITAUAR, Mamoru	Yamagata Univ.	(since Apr. 2016)
KOMORI, Fumio	Univ. of Tokyo	(since Apr. 2016)
OKABAYASHI, Jun	Univ. of Tokyo	(since Apr. 2016)

UVSOR Users Association

HIKOSAKA, Yasumasa	Toyama Univ.	(until Mar. 2016)
KIMURA, Shin-ichi	Osaka Univ.	(until Mar. 2016)
FUKUI, Kazutoshi	Fukui Univ.	(since Apr. 2016)
HIRAHARA, Toru	Tokyo Institute of Technology	(since Apr. 2016)
ITO, Takahiro	Nagoya Univ.	(since Apr. 2016)
KITAUURA, Mamoru	Yamagata Univ.	(since Apr. 2016)
YOSHIDA, Tomoko	Osaka City Univ.	(since Apr. 2016)

Graduate Students

FUJITA, Taishi	Nagoya Univ.	(since Oct. 2015)
FUKUE, Syuhei	Nagoya Univ.	(since Oct. 2015)
MIYAUCHI, Tomohiro	Nagoya Univ.	(since Oct. 2015)
NAGASAKI, Kazuya	Nagoya Univ.	(since Oct. 2015)
YAMAGUCHI, Kenta	Nagoya Univ.	(since Oct. 2015)
YAMAMOTO, Kouki	Nagoya Univ.	(since Oct. 2015)
YAMAMURA, Kouhei	Nagoya Univ.	(since Oct. 2015)
FUJISE, Hikaru	SOKENDAI	(since Apr. 2016)
ITO, Keiya	Nagoya Univ.	(until Sep. 2015)
KOUCHI, Shogo	Nagoya Univ.	(until Sep. 2015)
OODAKE, Daichi	Nagoya Univ.	(until Sep. 2015)
SUGIHARA, Shintarou	Nagoya Univ.	(until Sep. 2015)

Visiting Scientists

CHIU, Chao-Wen	National Univ. of Kaohsiung	Jun. 2015
WANG, Yu-Fu	Tamkang Univ.	Jun. 2015, Nov. 2015
KWON, Ki-Won	Pohang Univ. of Science and Technolog	Jul. 2015
SOHN, Yeong-Sup	Pohang Univ. of Science and Technolog	Jul. 2015, Jan. 2016
KIM, Keun-Su	Pohang Univ. of Science and Technolog	Jul. 2015
JUNG, Sung-Won	Pohang Univ. of Science and Technolog	Jul. 2015, Jan. 2016
FRITZ, Torsten	Friedrich Schiller Univ. Jena	Aug. 2015
Rühl, Eckart	Freie Univ. Berlin	Aug. 2015
KLOSSEK, Andre	Freie Univ. Berlin	Aug. 2015, Feb. 2016

FLESCH, Roman	Freie Univ. Berlin	Aug. 2015, Feb. 2016
SCHULZ, Robert	Freie Univ. Berlin	Aug. 2015
YAMAMOTO, Kenji	Freie Univ. Berlin	Aug. 2015, Feb. 2016
BRANDENBURG, Tim	Helmholtz Zentrum Berlin	Nov. 2015
WANG, Yu-Fu	Tamkang Univ.	Nov. 2015
PETIT, Tristan	Helmholtz Zentrum Berlin	Dec. 2015
LIN, Ming-Wei	NSRRC	Dec. 2015
LAI, Yu-Ling	NSRRC	Dec. 2015
CHEN, Chi-Liang	NSRRC	Dec. 2015
DONG, Chung-Li	Tamkang Univ.	Dec. 2015
CHIOU, Jau-Wern	National Univ. of Kaohsiung	Dec. 2015
MEIJERINK, Andries	Utrecht Univ.	Dec. 2015
PETTERSSOM, Lars	Stockholm Univ.	Jan. 2016
PARK, Seung Ryong	Incheon National Univ.	Feb. 2016
CHO, Soo Hyun	Yonsei Univ.	Feb. 2016
OH, Dong Jin	Incheon National Univ.	Feb. 2016
HUH, Min Jae	Pohang Univ. of Science and Technolog	Jan. 2016
HUTTULA, Marko	Univ. of Oulu	Feb. 2016
PATANEN, Minna	Univ. of Oulu	Feb. 2016
PISCHORN, Hannah	Freie Univ. Berlin	Feb. 2016
RANCAN, Fiorenza	Charite Berlin	Feb. 2016
REINERT, Friedrich	Univ. of Wuerzburg	Mar. 2016
MYRGORODSKA, Iuliia	Univ. Nice Sophia Antipolis	Mar. 2016

A large, white, stylized Roman numeral 'II' is centered in the upper half of the page. The background is a vibrant teal color with abstract, futuristic patterns. A prominent feature is a large, circular, multi-layered structure resembling a particle accelerator or a light source, with concentric rings and a dashed outer boundary. The bottom half of the page features a grid of small, light-colored dots.

Current Status of
Light Sources and
Beamlines

Light Source in 2015

1. Status of UVSOR Accelerators

In the fiscal year 2015, we operated UVSOR-III from May to March, for 38 weeks for users as usual. We had a shutdown period in April and May for about 6 weeks. This was scheduled for maintenance works, to replace the RF power amplifier of the booster synchrotron, and the ceramic vacuum duct of an injection kicker magnet in the storage ring.

We operated the machine for 34 weeks in the multi-bunch top-up mode, in which the beam current was kept at 300 mA, and 2 weeks in the single-bunch mode, in which the machine is operated in single-bunch top-up mode with the beam current at 50 mA. The monthly statistics of the operation time and the integrated beam current are shown in Fig. 1.

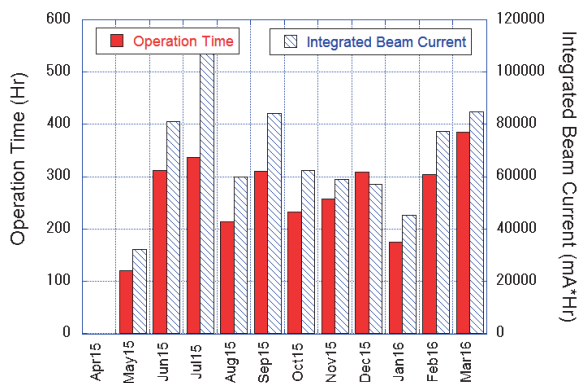


Fig. 1. Monthly statistics in FY2015.

The weekly operation schedule is as follows. On Monday, from 9 am to 9 pm, the machine is operated for machine studies. On Tuesday and Wednesday, from 9 am to 9 pm, the machine is operated for users. From Thursday 9 am to Friday 9 pm, the machine is operated for 36 hours continuously for users. Therefore, the beam time for users in a week is 60 hours. We had 3 weeks dedicated for machine studies, in November, just after the New Year vacation, and the last week in March. The machine study week in November is mainly dedicated for the accelerator conditioning after the annual planned power outage.

We had a few machine troubles on the power supplies of the steering magnet in the storage ring and pulse magnets both in the booster synchrotron and the storage ring. However, fortunately, in all cases the beam time for users could be secured by extending the operation time during the same week. A more Serious occurrence was the water leakages from magnets both in the storage ring and the booster synchrotron. Fortunately, both of these troubles did not affect the users' beam time by quick restoration. The leakage from a quadrupole magnet in the storage

ring is considered due to a problem in piping of only this magnet. However, that in the booster-synchrotron magnet is considered due to aging. Therefore, it is probable to happen to other magnets sooner or later.

Concerning the vacuum trouble of the 3rd harmonic cavity described in the previous report, we have decided to design and construct a new cavity instead of repairing the present cavity. This is to avoid unexpected troubles during the on-site repair work.

2. Improvements and Developments

For the past few years, we had been observing strong leakage of the RF signal induced by the electron beam from one of three ceramic vacuum ducts for injection kicker magnets in the storage ring. It was worried that the duct might have a problem inside and could affect the stability of the electron beam. Therefore we removed the duct during the spring shut down and checked inside. It was found that a part of the Au coating on the inner wall was lost and consequently the electric conductivity between the flanges was lost. We replaced the duct with an older one that had been used many years ago, but the Au coating had no problem. After the replacement, the RF noise leakage was reduced to a normal level. However, the electron stability seemed not to be affect by this.



Fig. 2 The inside view of ceramic duct. A part of the Au coating was lost. The lost part can be seen as a black belt.

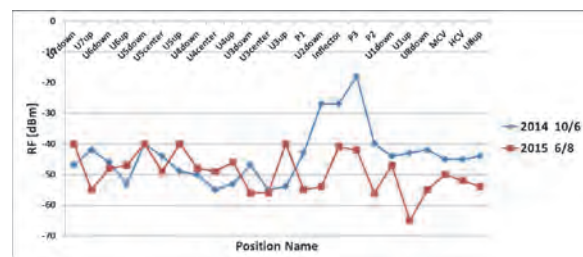


Fig. 3 RF noise distribution in the storage ring before (blue line) and after (red line).

The solid state RF power amplifiers of the booster synchrotron and of the storage ring had been used for about 20 years. They had been working well, however it has become difficult to maintain them because of the outage of electronic parts. We decided to replace the amplifiers, with basically same performances but with some improvements such as compactness and water cooling. We expect that the latter would be effective to stabilize the accelerator room temperature and also to reduce the noise in the experimental hall. In the spring shut down 2015, we have replaced the amplifier for the booster synchrotron and in the following year, we will replace that of the storage ring. The former was successfully commissioned and stably used in the users runs.

Light Source Developments and Beam Physics Studies

We continue the efforts to develop light source technologies and their applications such as free electron lasers, coherent harmonic generation, coherent synchrotron radiation, laser Compton scattering gamma-rays, intense polarized UV light and vortex UV radiation at the new source development station BL1U, which was constructed under the support of Quantum Beam Technology Program by MEXT/JST.

This year, we intensively studied the optical vortex beam from a helical undulator in collaboration with Hiroshima U., Nagoya U. and other institutes. Since the UVSOR electron beam is diffraction-limited in the UV range, we could clearly observe the vortex nature of the helical undulator harmonics in various

methods, such as diffraction or interference. Also, we started an experimental study on the interaction between optical vortex radiation and matters in collaboration with Saga LS and Niigata U.

We are continuing the effort to reconstruct the optical cavity for the resonator free electron laser at BL1U, which has been investigated for many years at UVSOR. This time, the main objective is the intra-cavity gamma-ray production for the nuclear resonance fluorescence imaging in cooperation with Kyoto University. Currently gamma-rays are produced by using a conventional fiber laser for the proof-of-principle study. The gamma-rays are also used for investigating the origin of the homo-chirality of biomolecules in nature in collaboration with Hiroshima U., Yokohama N. U. and others.

An irradiation experiment using polarized ultraviolet light is being carried out in corporation with Tokyo U. Sci. They are also used for the study on the origin of homo-chirality with Yokohama N. U. and other institutes.

A spin polarized electron gun is being developed in collaboration with Nagoya U. and KEK. This is being developed towards inverse photo-electron spectroscopy. We are also preparing for utilizing this polarized beam for the study on the origin of the homo-chirality.

We have started designing harmonic cavity in collaboration with Nagoya U., to replace the present cavity which has a vacuum trouble. The new cavity will be introduced in the ring hopefully within two years.

Masahiro KATOH (UVSOR Facility)

UVSOR Accelerator Complex

Injection Linear Accelerator

Energy	15 MeV
Length	2.5 m
Frequency	2856 MHz
Accelerating RF Field	2 π /3 Traveling Wave
Klystron Power	1.8 MW
Energy Spread	~1.6 MeV
Repetition Rate	2.6 Hz

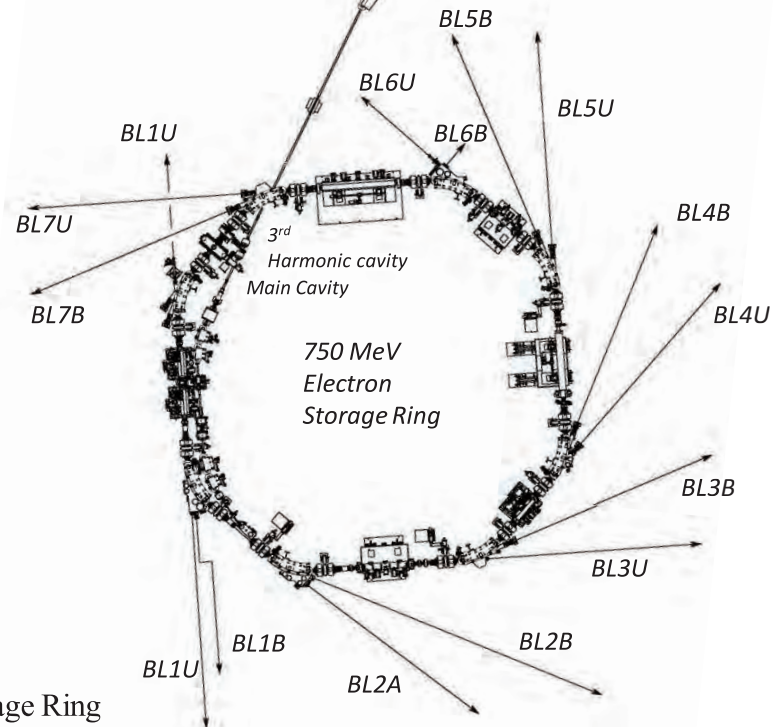
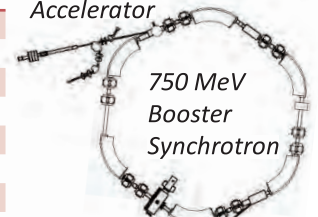
UVSOR-III Storage-Ring

Energy	750 MeV
Injection Energy	750 MeV
Maximum Storage Current	500 mA (multi bunch) 100 mA (single bunch)
Normal operation current (Top-up mode)	300 mA (multi bunch) 50 mA (single bunch)
Natural Emittance	17.5 nm-rad
Circumference	53.2 m
RF Frequency	90.1 MHz
Harmonic Number	16
Bending Radius	2.2 m
Lattice	Extended DBA \times 4
Straight Section	(4 m \times 4)+(1.5 m \times 4)
RF Voltage	120 kV
Betatron Tune	
Horizontal	3.75
Vertical	3.20
Momentum Compaction	0.030
Natural Chromaticity	
Horizontal	-8.1
Vertical	-7.3
Energy Spread	5.26 \times 10 ⁻⁴
Coupling Ratio	1%
Natural Bunch Length	128 ps

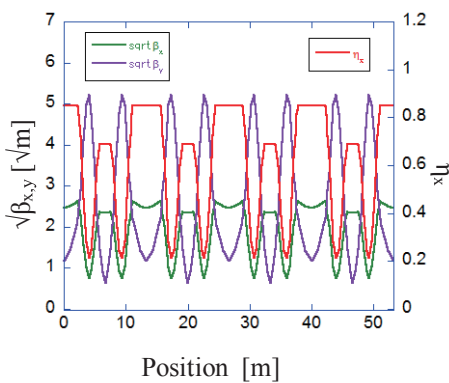
Booster Synchrotron

Energy	750 MeV
Injection	15 MeV
Frequency	32 mA (uniform filling)
Circumference	26.6 m
RF Frequency	90.1 MHz
Harmonic Number	8
Bending Radius	1.8m
Lattice	FODO \times 8
Betatron Tune	
Horizontal	2.25
Vertical	1.25
Momentum Compaction	0.138
Repetition Rate	1 Hz (750 MeV)

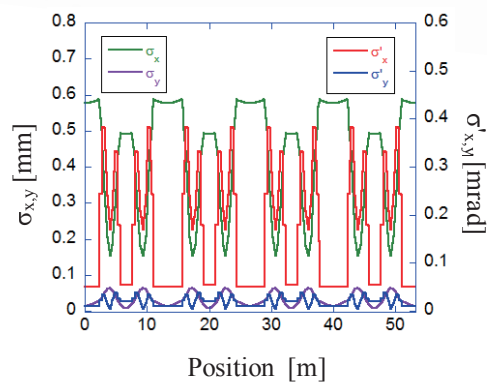
15 MeV
Linear
Accelerator



Electron Beam Optics of UVSOR-III Storage Ring

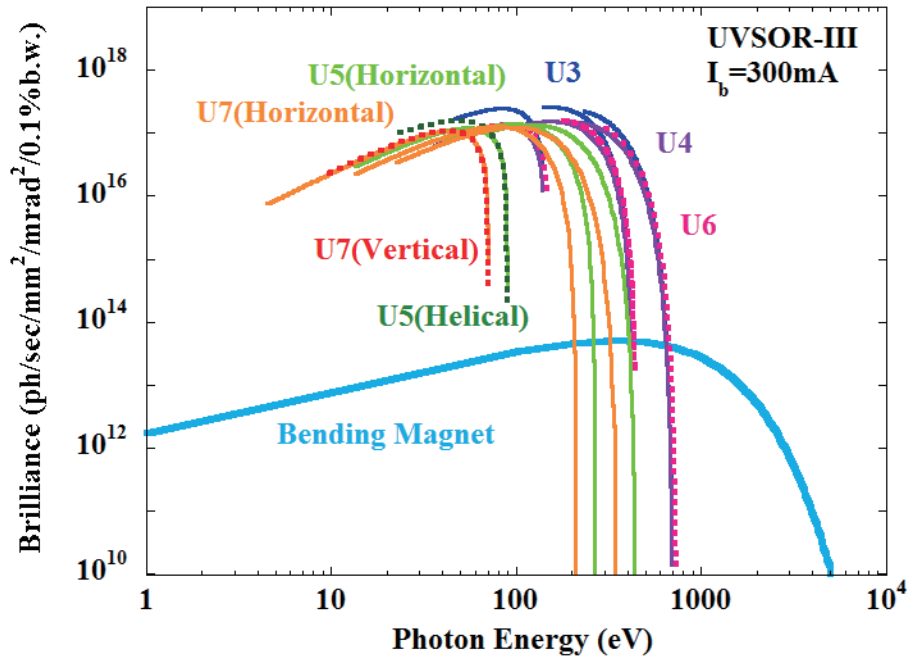


Horizontal/vertical betatron functions and dispersion function



Horizontal/vertical electron beam size and beam divergence

Insertion Device



Brilliance of radiation from the insertion devices (U3, U4, U5, U6 and U7) and a bending magnet of UVSOR-III

U1 Apple-II Undulator /

Optical Klystron

Number of Periods	10+10
Period length	88 mm
Pole Length	0.968 m + 0.968 m
Pole Gap	24-200 mm
Deflection Parameter	7.36 (Max. Horizontal) 4.93 (Max. Vertical) 4.06 (Max. Helical)

U3 In-vacuum Undulator

Number of Periods	50
Period length	38 mm
Pole Length	1.9 m
Pole Gap	15-40 mm
Deflection Parameter	2.0-0.24

U4 In-vacuum Undulator

Number of Periods	26
Period length	38 mm
Pole Length	0.99 m
Pole Gap	13-40 mm
Deflection Parameter	2.4-0.19

U5 Apple-II

Variable Polarization Undulator

Number of Periods	38
Period length	60 mm
Pole Length	2.28 m
Pole Gap	24-190 mm
Deflection Parameter	3.4 (Max. Horizontal) 2.1 (Max. Vertical) 1.8 (Max. Helical)

U6 In-vacuum Undulator

Number of Periods	26
Period length	36 mm
Pole Length	0.94 m
Pole Gap	13-40 mm
Deflection Parameter	1.78 - 0.19

U7 Apple-II

Variable Polarization Undulator

Number of Periods	40
Period length	76 mm
Pole Length	3.04 m
Pole Gap	24-200 mm
Deflection Parameter	5.4 (Max. Horizontal) 3.6 (Max. Vertical) 3.0 (Max. Helical)

Bending Magnets

Bending Radius	2.2 m
Critical Energy	425 eV

Beamlines in 2015

Kiyohisa TANAKA

UVSOR Facility, Institute for Molecular Science

UVSOR is one of the highest-brilliance light sources in the extreme-ultraviolet region among synchrotron radiation facilities with electron energies of less than 1 GeV. The natural emittance of the UVSOR-III storage ring is as low as 17.5 nm-rad after the successful completion of the storage ring upgrade project (the UVSOR-III project) in 2012.

Eight bending magnets and five insertion devices are available as synchrotron light sources at UVSOR. As of 2015, there are a total of fourteen operational beamlines, which are classified into two categories. Eleven of them are the so-called “Open beamlines”, which are open to scientists from universities and research institutes belonging to the government, public organizations, private enterprises and also those from foreign countries. The remaining three beamlines are the “In-house beamlines”, and are dedicated to the use of research groups within IMS.

At UVSOR, there is one soft X-ray station equipped with a double-crystal monochromator, seven extreme ultraviolet and soft X-ray stations with grazing incidence monochromators, three vacuum ultraviolet (VUV) stations with normal incidence monochromators, two infrared (IR) stations equipped with Fourier-Transform interferometers, and one free electron laser beamline with no monochromator, as shown in the appended table (next page) for all available beamlines in 2015.

BL8B has been officially closed and BL2B, which is another angle-resolved photoelectron spectroscopy (ARPES) beamline for inorganic thin films, has been open for users in 2015. The preparation chamber and some vacuum products at BL8B were moved and reused at BL2B so that BL8B users can perform same measurements at BL2B.

BL3B has been conducted as one of the long-term project proposals. In the last three years, the endstation has been developed and the number of users increased including users from foreign countries. A newly designed chamber for VUV emission spectroscopy will be available soon.

BL4U, equipped with a scanning transmission soft X-ray microscope (STXM), has been open to users since June 2013. The performance of BL4U is close to theoretical predictions, except in the photon energy region near the C K-shell ionization threshold (~300 eV) due to the so-called “carbon contamination” of the optical elements, which makes the imaging of C distribution difficult. To

remove the carbon contamination, several methods have been examined such as recoating of mirrors with gold, washing the vacuum chamber as well as all parts of the mirror holder with hot water, and so on. Although the photon intensity around 300 eV has tentatively been improved, it has gradually decreased with time. In 2015, we have repeated *in situ* cleaning of mirrors by exposure to oxygen at a pressure of 1×10^{-2} Pa under irradiation of non-monochromated synchrotron radiation (SR). As a result, the photon intensity around 300 eV has greatly been improved, and STXM analyses near the C-K edge have become useful.

BL7U, a high energy resolution ARPES beamline, is one of the most popular beamlines in UVSOR and has been difficult to get beamtime these days. For users who need sample surface preparation such as annealing, Ar-sputtering, deposition and so on, one or two week beamtime is not enough to prepare samples. To make the beamtime efficiently, “Offline-ARPES system” with helium discharge lamp at IMS (Nanotechnology Platform Japan program) has been open for users who requested. Three user groups used the offline-ARPES system before their beamtime to prepare sample in 2015.

The construction of a new soft X-ray beamline BL5U began in January 2014. The beamline performance had been once tested and it had been confirmed that the resolving power and photon intensity were very close to the expected values. However, in December 2014, it was found that the photons below 30 eV hit the grating mount and could not reach the endstation. The grating mount has been taken out, modified and attached again in March 2015. During the second beamline performance test, we found that the first mirror and probably the grating surfaces were covered by carbon contamination, which made the photon intensity one order of magnitude smaller than the first test. The *in situ* cleaning method, which was used at BL4U, has been applied and photon flux has recovered to a half of the first test level. BL5U will be officially open for users from 2016.

All users are required to refer to the beamline manuals and the UVSOR guidebook (the latest revision in PDF format uploaded on the UVSOR web site in June 2010), on the occasion of conducting actual experimental procedures. Those wishing to use the open and in-house beamlines are recommended to contact the appropriate beamline master (see next page). For updated information on UVSOR, please see <http://www.uvsor.ims.ac.jp>.

Beamlines at UVSOR

Beamline	Monochromator / Spectrometer	Energy Range	Targets	Techniques	Contact
BL1U	Free electron laser	1.6 - 13.9 eV			M. Katoh mkatoh@ims.ac.jp
BL1B	Martin-Puplett FT-FIR	0.5 - 30 meV	Solid	Reflection Absorption	F. Teshima tetsu@ims.ac.jp
BL2A	Double crystal	585 eV - 4 keV	Solid	Reflection Absorption	N. Kondo nkondo@ims.ac.jp
BL2B	18-m spherical grating (Dragon)	23 - 205 eV	Solid	Photoemission	S. Kera kera@ims.ac.jp
BL3U*	Varied-line-spacing plane grating (Monk-Gillieson)	60 - 800 eV	Gas Liquid Solid	Absorption Photoemission Photon-emission	N. Kosugi kosugi@ims.ac.jp
BL3B	2.5-m off-plane Eagle	1.7 - 31 eV	Solid	Reflection Absorption Photon-emission	M. Hasumoto hasumoto@ims.ac.jp
BL4U	Varied-line-spacing plane grating (Monk-Gillieson)	130 - 700 eV	Gas Liquid Solid	Absorption (Microscopy)	T. Ohgashi ohgashi@ims.ac.jp
BL4B	Varied-line-spacing plane grating (Monk-Gillieson)	25 eV - 1 keV	Gas Solid	Photoionization Photodissociation Photoemission	E. Shigemasa sigemasa@ims.ac.jp
BL5U	Varied-line-spacing plane grating (Monk-Gillieson)	20 - 200 eV	Solid	Photoemission	M. Sakai sakai@ims.ac.jp
BL5B	Plane grating	6 - 600 eV	Solid	Calibration Absorption	M. Hasumoto hasumoto@ims.ac.jp
BL6U*	Variable-included-angle varied-line-spacing plane grating	40 - 800 eV	Gas Solid	Photoionization Photodissociation Photoemission	E. Shigemasa sigemasa@ims.ac.jp
BL6B	Michelson FT-IR	4 meV - 2.5 eV	Solid	Reflection Absorption IR microscope	F. Teshima tetsu@ims.ac.jp
BL7U	10-m normal incidence (modified Wadsworth)	6 - 40 eV	Solid	Photoemission	S. Ideta idetas@ims.ac.jp
BL7B	3-m normal incidence	1.2 - 25 eV	Solid	Reflection Absorption Photon-emission	M. Hasumoto hasumoto@ims.ac.jp

Yellow columns represent undulator beamlines.

* In-house beamline.

BL1U

Light Source Development Station

▼ Description

BL1U has been constructed for developments and applications of various photon sources including free electron laser in the range from visible to deep UV, coherent harmonic generation in the deep UV and VUV, laser Compton scattering gamma-rays and undulator radiation with various polarization properties including optical vortices.

The beam-line is equipped with a dedicated twin polarization variable undulator system with a buncher section, which can be used for a FEL oscillator and a VUV CHG. It is also equipped with a femto-second laser system synchronized with the accelerator, which is used for CHG, slicing, LCS and coherent THz radiation generation.

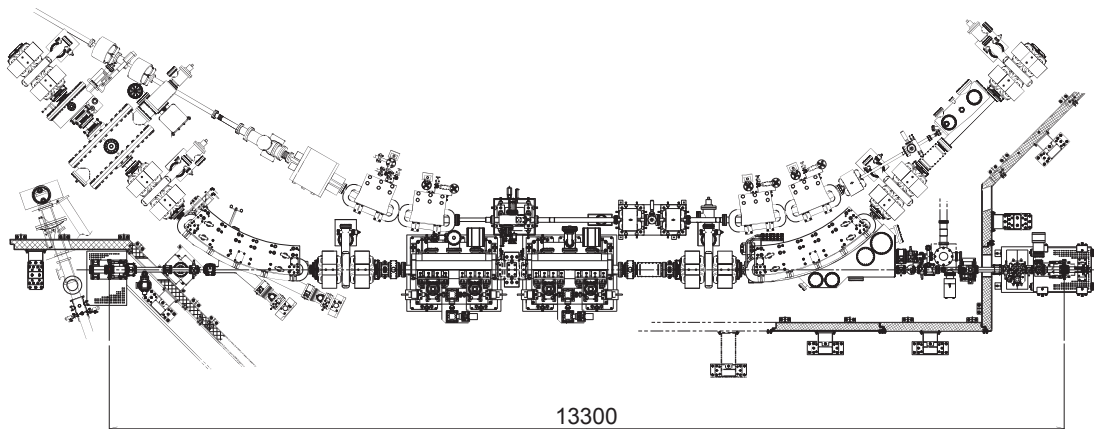


Fig. 1. Configuration of the free electron laser (under reconstruction).



Fig. 2. Twin Apple-II Undulator.

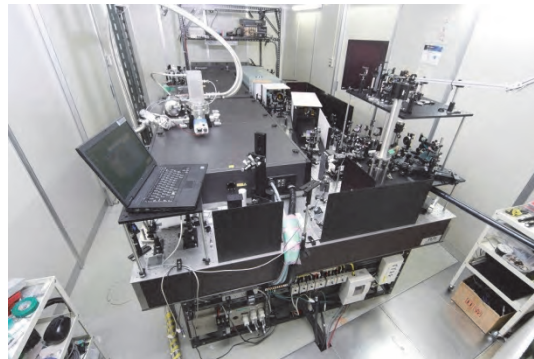


Fig. 3. Accelerator synchronized Laser System.

▼ Technical Data of FEL

Wave Length	199-800 nm
Spectral Band Width	$\sim 10^{-4}$
Polarization	Circular/Linear
Pulse Rate	11.26 MHz
Max. Ave. Power	~ 1 W

Technical Data of Ti:Sa Laser

Wave Length	800 nm
Pulse Length	130 fsec
Oscillator	90.1 MHz
Pulse Energy	2.5mJ 10mJ 50mJ
Repetition Rate	1kHz 1kHz 10Hz

BL1B

Terahertz Spectroscopy Using Coherent Synchrotron Radiation

II

▼ Description

Coherent synchrotron radiation (CSR) is a powerful light source in the terahertz (THz) region. This beamline has been constructed for basic studies on the properties of THz-CSR. However, it can be also used for measurements of reflectivity and transmission spectra of solids using conventional synchrotron radiation.

The emitted THz light is collected by a three-dimensional magic mirror (3D-MM, M0) of the same type as those already successfully installed at BL431R in SPring-8 and BL6B in UVSOR-II. The 3D-MM was installed in bending-magnet chamber #1 and is controlled by a 5-axis pulse motor stage (x , z translation; θ_x , θ_y , θ_z rotation). The acceptance angle was set at 17.5-34 degrees (total 288 mrad) in the horizontal direction. The vertical angle was set at ± 40 mrad to collect the widely expanded THz-CSR.

The beamline is equipped with a Martin-Puplett type interferometer (JASCO FARIS-1) to cover the THz spectral region from 4 to 240 cm^{-1} ($h\nu = 500 \mu\text{eV}$ -30 meV). There is a reflection/absorption spectroscopy (RAS) end-station for large samples (\sim several mm). At the RAS end-station, a liquid-helium-flow type cryostat with a minimum temperature of 4 K is installed.

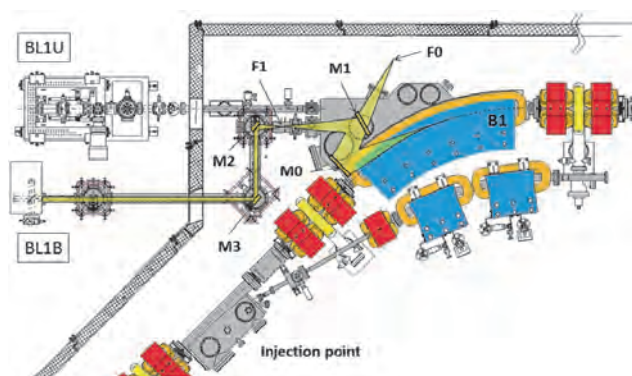


Fig. 1. Schematic top view of the beam extraction part of the THz-CSR beamline, BL1B. The three-dimensional magic mirror (3D-MM, M0) and a plane mirror (M1) are located in the bending-magnet chamber. A parabolic mirror (M2) is installed to form a parallel beam. The straight section (BL1U) is used for coherent harmonic generation (CHG) in the VUV region.

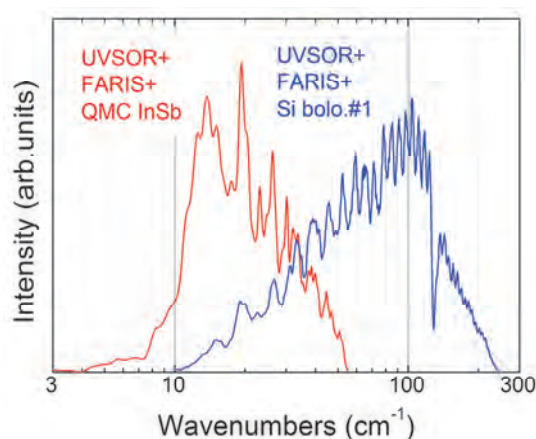


Fig. 2. Obtained intensity spectra with the combination of a light source (UVSOR), interferometer (FARIS-1), and detectors (Si bolometer and InSb hot-electron bolometer).

▼ Technical Data

Interferometer	Martin-Puplett (JASCO FARIS-1)
Wavenumber range	4-240 cm^{-1}
(Energy range)	(500 μeV -30 meV)
Resolution in cm^{-1}	0.25 cm^{-1}
Experiments	Reflection/transmission spectroscopy
Miscellaneous	Users can use their experimental system in this beamline.

BL2A

Soft X-Ray Beamline for Photoabsorption Spectroscopy

▼ Description

BL2A, which was moved its previous location as BL1A in 2011, is a soft X-ray beamline for photoabsorption spectroscopy. The beamline is equipped with a focusing premirror and a double-crystal monochromator [1]. The monochromator serves soft X-rays in the energy region from 585 to 4000 eV using several types of single crystals, such as β - Al_2O_3 , beryl, KTP (KTiOPO_4), quartz, InSb, and Ge. The throughput spectra measured using a Si photodiode (AXUV-100, IRD Inc.) are shown in Fig. 1. The typical energy resolution ($E / \Delta E$) of the monochromator is approximately 1500 for beryl and InSb.

A small vacuum chamber equipped with an electron multiplier (EM) detector is available. Photoabsorption spectra for powdery samples are usually measured in total electron yield mode, with the use of the EM detector. A silicon drift detector is also available for measuring partial fluorescence yields from solid samples.

[1] Hiraya *et al.*, Rev. Sci. Instrum. **63** (1992) 1264.

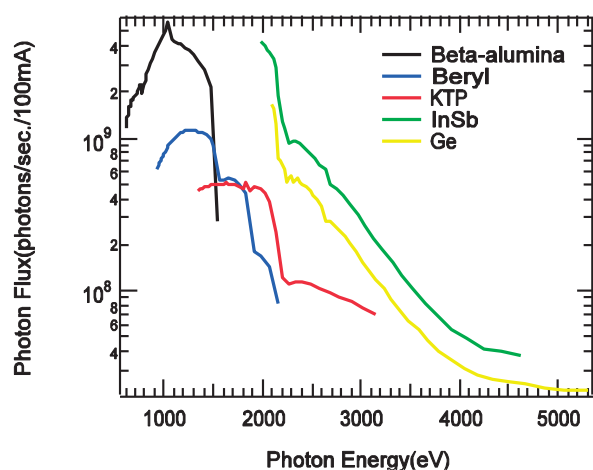


Fig. 1. Throughput spectra of the double-crystal monochromator at BL2A.



Fig. 2. Side view of BL2A.

▼ Technical Data

Monochromator	Double crystal monochromator
Monochromator crystals: (2 θ value, energy range)	β - Al_2O_3 (22.53 \AA , 585–1609 eV), beryl (15.965 \AA , 826–2271 eV), KTP (10.95 \AA , 1205–3310 eV), quartz (8.512 \AA , 1550–4000 eV), InSb (7.481 \AA , 1764–4000 eV), Ge (6.532 \AA , 2094–4000 eV)
Resolution	$E / \Delta E = 1500$ for beryl and InSb
Experiments	Photoabsorption spectroscopy (total electron yield using EM and partial fluorescence yield using SDD)

BL2B

Photoelectron Spectroscopy of Molecular Solids

II

▼ Description

This beamline previously dedicated for experiments in the field of gas phase photoionization and reaction dynamics. Then, the beamline has been reconstructed for photoelectron spectroscopy of molecular solids with a new end station, and experiments can be performed from May 2014. The monochromator is a spherical grating Dragon type with 18-m focal length. High throughput (1×10^{10} photons s^{-1}) and high resolution ($E / \Delta E = 2000 - 8000$) are achieved simultaneously under the condition of the ring current of 100 mA [1]. The optical system consists of two pre-focusing mirrors, an entrance slit, three spherical gratings (G1 - G3), two folding mirrors, a movable exit slit, and a refocusing mirror [2]. The monochromator is designed to cover the energy range of 23–205 eV with the three gratings: G1 (2400 lines mm^{-1} , $R = 18$ m) at 80–205 eV; G2 (1200 lines mm^{-1} , $R = 18$ m) at 40–100 eV; G3 (2400 lines mm^{-1} , $R = 9.25$ m) at 23–50 eV. The percentage of the second-order light contamination at $h\nu = 45.6$ eV is 23% for G2 or 7% for G3.

A UHV chamber is placed downstream of the refocusing mirror chamber and equipped silicon photodiode, sapphire plate Au mesh and filters for absolute photon flux measurement, monitor the photon-beam position, relative photon flux measurements and attenuate higher order light, respectively.

The new end station consists of a main chamber with a hemispherical analyzer (SCIENTA R3000) and a liquid-He-cooled cryostat (temperature range of 15-400 K) with 5-axis stage, a sample preparation chamber with a fast-entry load-lock chamber and a cleaning chamber with LEED, ion gun for sputtering and IR heating unit.

[1] M. Ono, H. Yoshida, H. Hattori and K. Mitsuke, Nucl. Instrum. Meth. Phys. Res. A **467-468** (2001) 577.

[2] H. Yoshida and K. Mitsuke, J. Synchrotron Radiation **5** (1998) 774.



Fig. 1. 18 m spherical grating monochromator at BL2B.

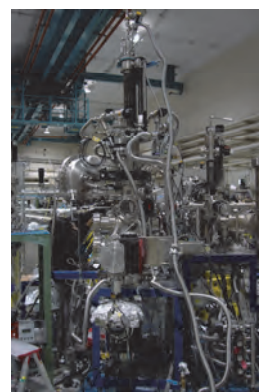


Fig. 2. End station of BL2B for photoelectron spectroscopy of molecular solids.

▼ Technical Data

Monochromator	18 m spherical grating Dragon-type
Wavelength Range	23-205 eV
Resolution	2000–8000 depending on the gratings
Experiments	Angle-resolved ultraviolet photoemission spectroscopy

BL3U

Varied-Line-Spacing Plane Grating Monochromator for Molecular Soft X-Ray Spectroscopy

▼ Description

The beamline BL3U is equipped with an in-vacuum undulator composed of 50 periods of 3.8 cm period length. The emitted photons are monochromatized by the varied-line-spacing plane grating monochromator (VLS-PGM) designed for various spectroscopic investigations in the soft X-ray range including soft X-ray emission studies. Three holographically ruled laminar profile plane gratings are designed to cover the photon energy range from 60 to 800 eV. The beamline has two endstations, namely, XES setup and multi-purpose setup. The XES setup is used for soft X-ray emission spectroscopy. The beam is horizontally focused onto the sample position by a plane-elliptical mirror, M2X. In the multi-purpose setup, the beam is focused by the toroidal mirror M2. Between the sample position and M2, the differential pumping is placed. XAS of liquid samples and the application of in operando observations are performed at the experimental stage of the multi-purpose setup.

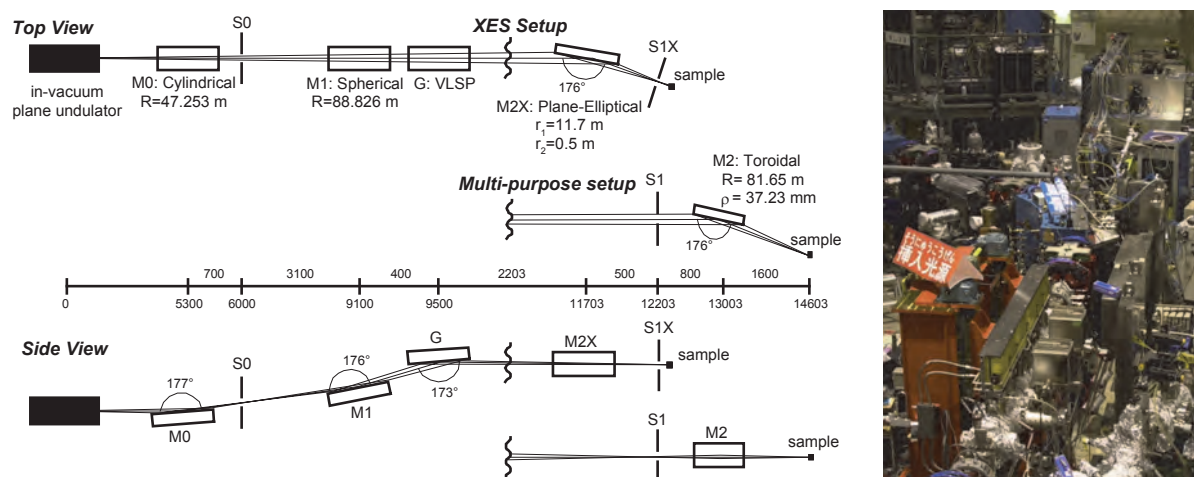


Fig. 1. Schematic layout (left) and the photography (right) of the BL3U. The distances along the beam from the center of the in-vacuum plane undulator are shown in millimeters. S1X and M2X can be replaced with the other exit slit S1 so that experiments can be carried out at either the XES or the multipurpose endstation. In the XES setup, the sample is placed 5–10 mm downstream of S1X.

▼ Technical Data

Monochromator	Varied-line-spacing plane grating monochromator
Energy Range	60-800 eV
Resolution	$E / \Delta E > 10\,000$
Experiments	Soft X-ray spectroscopy (XPS, XES, XAS)
Beam Size	Gaussian shape
(XES Endstation)	Vertical 5-20 μm ; Horizontal 41 μm (FWHM)

BL3B (HOTRLU)

VIS-VUV Photoluminescence and Reflection/Absorption Spectroscopy

▼ Description

BL3B has been constructed to study photoluminescence (PL) in the visible (VIS) to vacuum ultraviolet (VUV) region [1]. This beamline consists of a 2.5 m off-plane Eagle type normal-incidence monochromator, which covers the VUV, UV, and VIS regions, i.e., the energy (wavelength) region of 1.7-31 eV (40-730 nm), with three spherical gratings having constant grooving densities of 1200, 600, and 300 l/mm optimized at the photon energies of ~ 20 , ~ 16 , and ~ 6 eV, respectively. The schematic side view and top view layouts are shown in Figs. 1(a) and 1(b), respectively. The FWHM of the beam spot at the sample position is 0.25 mm (V) \times 0.75 mm (H). Low energy pass filters (LiF, quartz, WG32, OG53) can be inserted automatically to maintain the optical purity in the G3 (300 l/mm) grating region (1.7–11.8 eV). Figure 2 shows the throughput spectra (photon numbers at a beam current of 300 mA) for each grating with entrance and exit slit openings of 0.1 mm (resolving power $E / \Delta E$ of ~ 2000 (G3, ~ 6.8 eV)). Since both slits can be opened up to 0.5 mm, a monochromatized photon flux of 10^{10} photons/s or higher is available for PL measurements in the whole energy region.

The end station is equipped with a liquid-helium-flow type cryostat for sample cooling and two detectors; one of which is a photomultiplier with sodium salicylate and the other a Si photodiode for reflection/absorption measurement. For the PL measurements in the wide energy region from VIS to VUV, two PL monochromators, comprising not only a conventional VIS monochromator but also a VUV monochromator with a CCD detector, are installed at the end station.

[1] K. Fukui *et al.*, J. Sync. Rad. **21** (2014) 452.

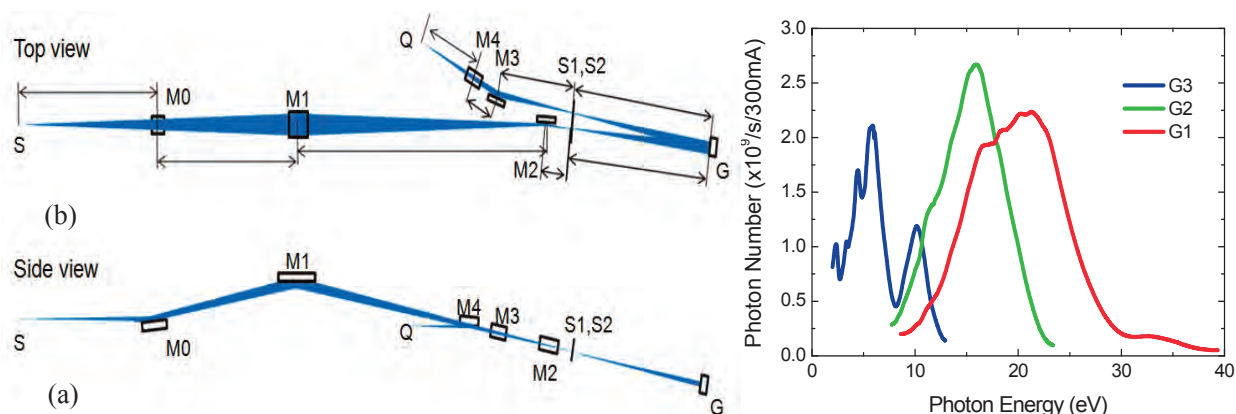


Fig. 1. Schematic layout of the BL3B (a) side view and (b) top view.

▼ Technical Data

Monochromator	-2.5 m normal-incidence monochromator
Energy range	1.7-31 eV (40~730 nm)
Resolution ($\Delta h\nu / h\nu$)	≥ 12000 (at ~ 6.9 eV, 0.02 mm slits, G1 (1200 l/mm))
Experiments	Photoluminescence, reflection, and absorption spectroscopy, mainly for solids

BL4U

Scanning Transmission X-Ray Microscopy in the Soft X-Ray Region

▼ Description

In the soft x-ray region, there are several absorption edges of light elements and transition metals. The near edge X-ray absorption fine structure (NEXAFS) brings detailed information about the chemical state of target elements. A scanning transmission X-ray microscope (STXM) in the soft X-ray region is a kind of extended technique of the NEXAFS with high spatial resolution. The STXM has a capability of several additional options, for example, in-situ observations, 3-dimensional observation by computed tomography and ptychography, by utilizing the characteristics of the X-rays. The STXM can be applied to several sciences, such as polymer science, material science, cell biology, environmental science, and so on.

This beamline equips an in-vacuum undulator, a varied-line-spacing plane grating monochromator and a fixed exit slit. The soft X-ray energy range from 130 to 770 eV with the resolving power ($E / \Delta E$) of 6,000 is available. The aperture size of the fixed exit slit determines not only the resolving power but also the size of a microprobe. A Fresnel zone plate is used as a focusing optical device through an order select aperture and its focal spot size of ~ 30 nm is available at minimum. An image is acquired by detecting intensities of the transmitted X-rays by a photomultiplier tube with scintillator with scanning a sample 2-dimensionally. By changing the energy of the incident beam, each 2-dimensional NEXAFS image is stacked. A main chamber of STXM is separated from the beamline optics by a silicon nitride membrane of 100-nm thickness; therefore, sample folders can be handled in vacuum or in helium.

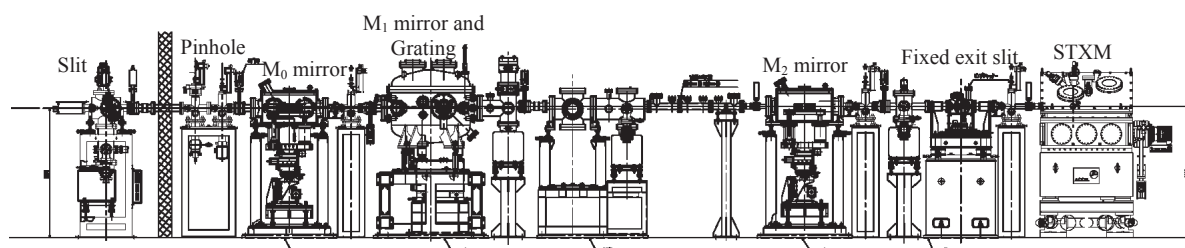


Fig. 1. Schematic image of BL4U.

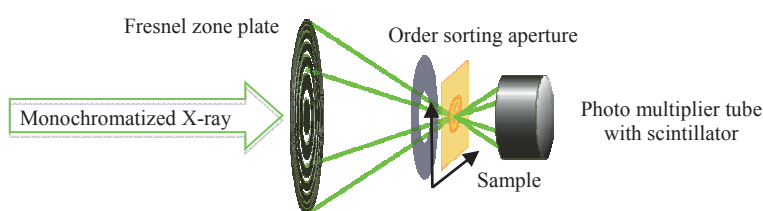


Fig. 2. Schematic image of the STXM.

▼ Technical Data

Energy range (E)	130 -770 eV
Resolving power ($E / \Delta E$)	~ 6000
Focusing optical element	Fresnel zone plate
Spatial resolution	~ 30 nm
Experiments	2-dimensinal absorption spectroscopy
Measurement environment	standard sample folder in vacuum or in helium, specially designed sample cell in ambient condition

BL4B

Varied-Line-Spacing Plane Grating Monochromator for Molecular Soft X-Ray Spectroscopy

II

▼ Description

The beamline BL4B equipped with a varied-line-spacing plane grating monochromator (VLS-PGM) was constructed for various spectroscopic investigations in a gas phase and/or on solids in the soft X-ray range. Three holographically ruled laminar profile plane gratings with SiO₂ substrates are designed to cover the photon energy range from 25 to 800 eV. The gratings with groove densities of 100, 267, and 800 l/mm cover the spectral ranges of 25–100, 60–300, and 200–1000 eV, respectively, and are interchangeable without breaking the vacuum. Figure 1 shows the absolute photon flux for each grating measured using a Si photodiode (IRD Inc.), with the entrance- and exit-slit openings set at 50 and 50 μm, respectively. The maximum resolving power ($E / \Delta E$) achieved for each grating exceeds 5000.

There is no fixed endstation on this beamline. A small vacuum chamber equipped with an electron multiplier (EM) detector is available. Soft X-ray absorption spectra of solid samples are usually measured by means of the total electron yield method using EM, and the partial fluorescence yield method using a silicon drift detector (SDD).

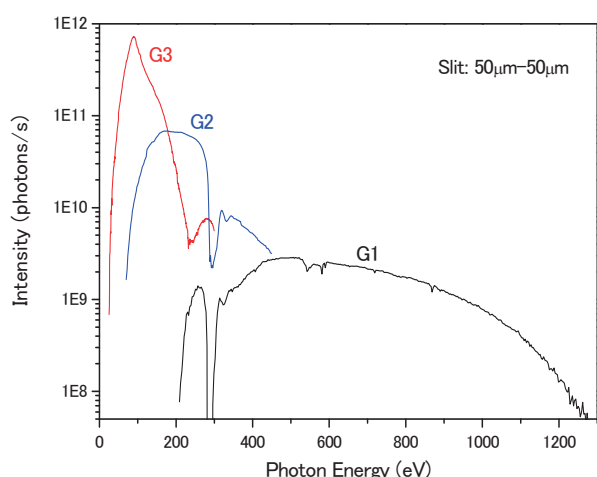


Fig. 1. Throughput from the VLS-PGM monochromator on BL4B.



Fig. 2. Photo of BL4B.

▼ Technical Data

Monochromator	Varied-line-spacing Plane Grating Monochromator
Energy range	25-1000 eV
Resolution	$E / \Delta E > 5000$ (at maximum)
Experiments	Soft X-ray spectroscopy (mainly, photoabsorption spectroscopy for solid targets by means of total electron yield method using EM and partial fluorescence yield method using SDD)

BL5U

Photoemission Spectroscopy of Solids and Surfaces

▼ Description

This beamline was originally used for angle-resolved photoemission spectroscopy (ARPES) study of solids and surfaces. After Jan 2014, the beamline has been shutdown for upgrade. The whole beamline, including the undulator and the endstation, will be renewed to perform higher energy resolution ARPES experiments. This beamline will also have new capability to obtain spin- and spatial-dependence of the electronic structure of solids using new spin detector and micro-focused beam. This beamline will be open for users from FY2016.



Fig. 1. Pictures of BL5U on May 2014.

▼ Technical Data (Expected Performance)

Monochromator	Monk-Gillieson VLS-PGM
Energy Range	20-200 eV
Resolution	$h\nu/\Delta E > 10,000$ for $< 10 \mu\text{m}$ slits
Experiment	ARPES, Spin-resolved ARPES, Space-resolved ARPES
Flux	$< 10^{12}$ photons/s for $< 10 \mu\text{m}$ slits (at the sample position)
Beam spot size	400 (H) x 5-20 (V) μm , 10 (H) x 4-6 (V) μm (microscope)
Main Instruments	Hemispherical photoelectron analyzer (MBS A-1), Liq-He flow cryostat with 5-axis manipulator (5-400 K)

BL5B

Calibration Apparatus for Optical Elements and Detectors

II

▼ Description

BL5B has been constructed to perform calibration measurements for optical elements and detectors. This beamline is composed of a plane grating monochromator (PGM) and three endstations in tandem. The most upstream station is used for the calibration measurements of optical elements, the middle one for optical measurements for solids, and the last for photo-stimulated desorption experiments. The experimental chamber at the most downstream station is sometimes changed to a chamber for photoemission spectroscopy. The calibration chamber shown in Fig. 2 is equipped with a goniometer for the characterization of optical elements, which has six degrees of freedom, X-Y translation of a sample, and interchanging of samples and filters. These are driven by pulse motors in vacuum. Because the polarization of synchrotron radiation is essential for such measurements, the rotation axis can be made in either the horizontal or vertical direction (s- or p-polarization).

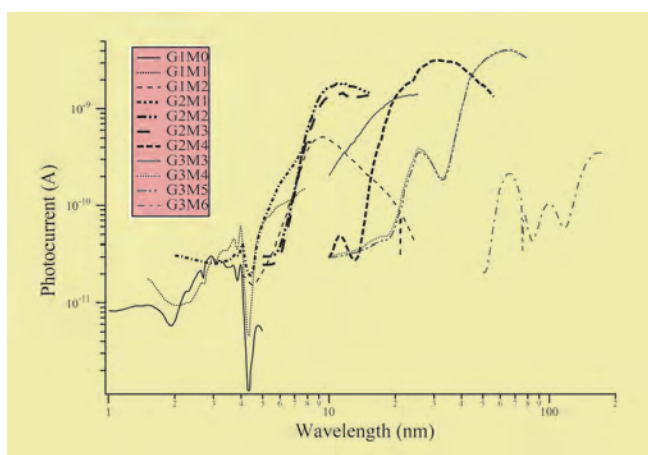


Fig. 1. Throughput spectra for possible combinations of gratings and mirrors at BL5B measured by a gold mesh.

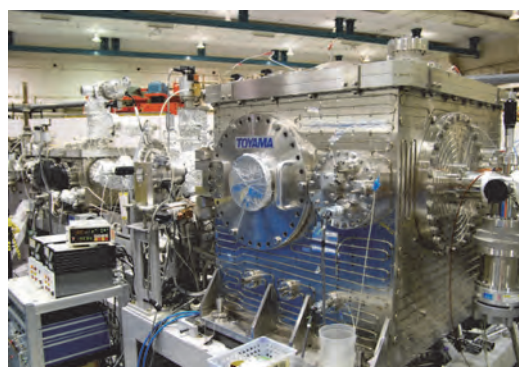


Fig. 2. A side view of the experimental chamber for calibration measurements.

▼ Technical Data

Monochromator	Plane Grating Monochromator
Energy range	6-600 eV (2-200 nm)
Resolution	$E / \Delta E \sim 500$
Experiments	Calibration of optical elements, reflection and absorption spectroscopy mainly for solids

BL6U

Variable-Included-Angle VLS-PGM for Molecular Soft X-Ray Spectroscopy

▼ Description

The beamline BL6U equipped with a variable-included-angle Monk-Gillieson mounting monochromator with a varied-line-spacing plane grating was constructed for various spectroscopic investigations requiring high-brilliance soft X-rays in a gas phase and/or on solids. Through a combination of undulator radiation and sophisticated monochromator design (entrance slit-less configuration and variable-included-angle mechanism), using a single grating, the monochromator can cover the photon energy ranging from 40 to 800 eV, with resolving power of greater than 10000 and photon flux of more than 10^{10} photons/s. Figure 1 shows an example of the monochromator throughput spectra measured using a Si photodiode, with the exit-slit opening set at 30 μm , which corresponds to the theoretical resolving power of 10000 at 80 eV.

There is no fixed endstation on this beamline.

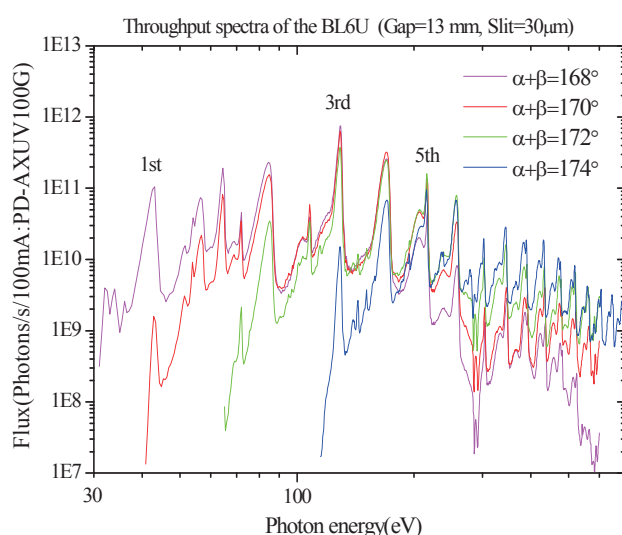


Fig. 1. Throughput spectra of the BL6U monochromator at various included angles.



Fig. 2. Photo of BL6U.

▼ Technical Data

Monochromator	Variable-included-angle Varied-line-spacing Plane Grating Monochromator
Energy range	40-800 eV
Resolution	$E / \Delta E > 10000$ (at maximum)
Experiments	High-resolution soft X-ray spectroscopy (mainly photoelectron spectroscopy for gaseous and solid targets)

BL6B

Infrared and Terahertz Spectroscopy/Microscopy of Solids

II

▼ Description

Synchrotron radiation (SR) has good performance (high brilliance and high flux) not only in the VUV and soft X-ray (SX) regions but also in the infrared (IR) and THz regions. BL6B covers the IR and THz regions. The previous beamline, BL6A1, which was constructed in 1985, was the pioneer in IRSR research. The beamline was deactivated at the end of FY2003 and a new IR/THz beamline, BL6B (IR), was constructed in FY2004. The front-end part including bending duct #6 was replaced with a new part having a higher acceptance angle ($215 \text{ (H)} \times 80 \text{ (V)} \text{ mrad}^2$) using a magic mirror, as shown in Fig. 1.

There are two Michelson type interferometers in this endstation; with first one (Bruker Vertex70v), which covers a wide spectral region from 30 to $20,000 \text{ cm}^{-1}$ ($h\nu = 4 \text{ meV}-2.5 \text{ eV}$), reflection/absorption spectroscopy measurements of large samples (up to several mm) and IR/THz microscopy measurements of tiny samples (up to several tens of μm) can be performed. For reflection/absorption spectroscopy measurements, a liquid-helium-flow type cryostat with a minimum temperature of 4 K is installed. The other interferometer (Jasco FT/IR-6100), which covers 350 to $15,000 \text{ cm}^{-1}$ ($h\nu = 45 \text{ meV}-1.8 \text{ eV}$), has been available for IR microscopy imaging measurements from FY2014. One can also perform ATR measurements using diamond ATR prism.

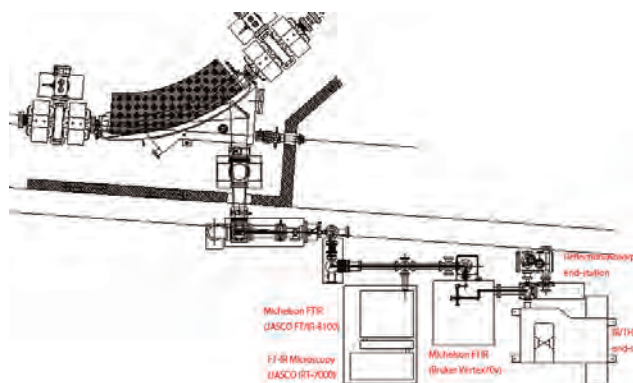
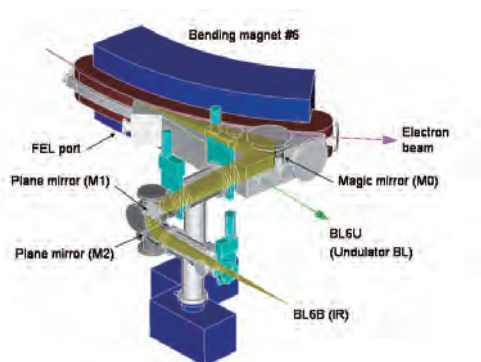


Fig. 1. Design of the optics and front end of BL6B. Fig. 2. Schematic top view of BL6B.

▼ Technical Data

Interferometer	Michelson (Bruker Vertex70v)	Michelson (Jasco FT/IR-6100)
Wavenumber Range (Energy range)	$30-20,000 \text{ cm}^{-1}$ ($4 \text{ meV}-2.5 \text{ eV}$)	$350-15,000 \text{ cm}^{-1}$ ($45 \text{ meV}-1.8 \text{ eV}$)
Resolution in cm^{-1}	0.1 cm^{-1}	0.5 cm^{-1}
Experiments	Reflectivity and transmission spectroscopy THz Microspectroscopy	IR microscopy imaging (JASCO IRT-7000) ATR spectroscopy

BL7U (SAMRAI)

Angle-Resolved Photoemission of Solids in the VUV Region

▼ Description

Beamline 7U, named the Symmetry- And Momentum-Resolved electronic structure Analysis Instrument (SAMRAI) for functional materials, was constructed to provide a photon flux with high energy resolution and high flux mainly for high-resolution angle-resolved photoemission spectroscopy of solids [1]. An APPLE-II-type variable-polarization undulator is installed as the light source. The undulator can produce intense VUV light with horizontal/vertical linear and right/left circular polarization. The undulator light is monochromatized by a modified Wadsworth type monochromator with three gratings (10 m radius; 1200, 2400, and 3600 lines/mm optimized at $h\nu = 10, 20, \text{ and } 33 \text{ eV}$). The energy resolution of the light ($h\nu / \Delta h\nu$) is more than 10^4 with a photon flux of 10^{11} - 10^{12} ph/s or higher on samples in the entire energy region.

The beamline has a photoemission end-station equipped with a 200 mm-radius hemispherical photoelectron analyzer (MB Scientific AB, A-1 analyzer) with a wide-angle electron lens and a liquid-helium-cooled cryostat with 6-axis pulse motor control (AVC Co., Ltd., i-GONIO). The main function of the beamline is to determine the three-dimensional Fermi surface and electronic structure of solids at low temperatures and their temperature dependence in order to reveal the origin of their physical properties.

[1] S. Kimura, T. Ito, M. Sakai, E. Nakamura, N. Kondo, K. Hayashi, T. Horigome, M. Hosaka, M. Katoh, T. Goto, T. Ejima and K. Soda, "SAMRAI: A variably polarized angle-resolved photoemission beamline in the VUV region at UVSOR-II," Rev. Sci. Instrum. **81** (2010) 053104.

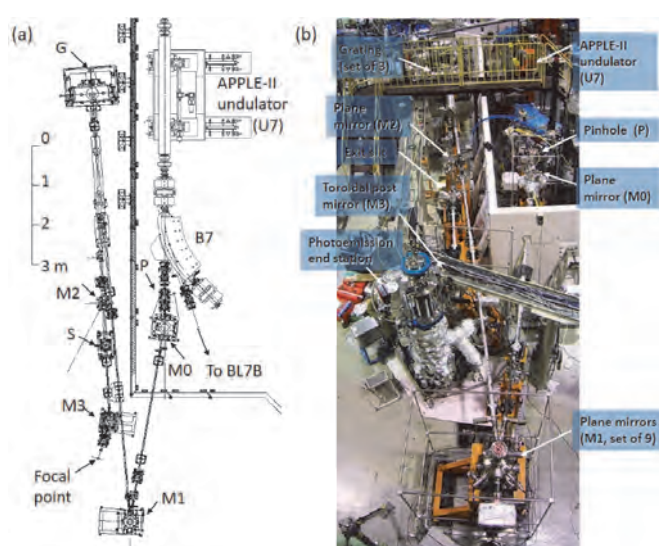


Fig. 1. Layout (a) and photograph (b) of the SAMRAI beamline consisting of an APPLE-II type undulator (U7), a modified Wadsworth type monochromator (M0-S), and a high-resolution photoemission analyzer at the focal point. The monochromator has five major optical components: two plane mirrors (M0 and M1) with water cooling, one set of three spherical gratings (G), an exit slit (S), and one toroidal refocusing mirror (M3). The spherical gratings have a radius of 10 m and are located 22 m from the center of the undulator. There is no entrance slit. S is located 6.47 m from G. A second branch for a VUV microscope end-station is planned to be constructed after the plane mirror (M2) located between G and S.

▼ Technical Data

Light source	APPLE-II type undulator ($\lambda_u = 76 \text{ mm}$, $N = 36$) vertical/horizontal linear, right/left circular
Monochromator	10 m normal-incidence monochromator (modified Wadsworth type)
Photon energy range	6-40 eV ($\lambda = 30\sim 200 \text{ nm}$)
Resolution ($h\nu / \Delta h\nu$)	1×10^4 - 5×10^4
Photon flux on sample	$\geq 10^{12}$ - 10^{11} ph/s (depending on $h\nu$)
Beam size on sample	$200 \text{ (H)} \times 50 \text{ (V)} \mu\text{m}^2$
Experiments	Angle-resolved photoemission of solids (MB Scientific A-1 analyzer, acceptance angle: $\pm 18 \text{ deg}$)

BL7B

3 m Normal-Incidence Monochromator for Solid-State Spectroscopy

II

▼ Description

BL7B has been constructed to provide sufficiently high resolution for conventional solid-state spectroscopy, sufficient intensity for luminescence measurements, wide wavelength coverage for Kramers–Kronig analyses, and minimum deformation to the polarization characteristic of incident synchrotron radiation. This beamline consists of a 3-m normal incidence monochromator, which covers the vacuum ultraviolet, ultraviolet, visible, and infrared, i.e., the wavelength region of 50–1000 nm, with three gratings (1200, 600, and 300 l/mm). Two interchangeable refocusing mirrors provide two different focusing positions. For the mirror with the longer focal length, an LiF or a MgF₂ window valve can be installed between the end valve of the beamline and the focusing position. Figure 1 shows the absolute photon intensity for each grating with the entrance and exit slit openings of 0.5 mm. A silicon photodiode (AXUV-100, IRD Inc.) was utilized to measure the photon intensity and the absolute photon flux was estimated, taking the quantum efficiency of the photodiode into account.

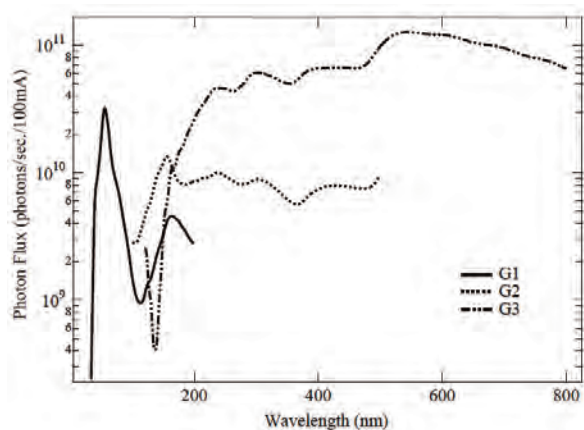


Fig. 1. Throughput spectra of BL7B measured using a silicon photodiode.

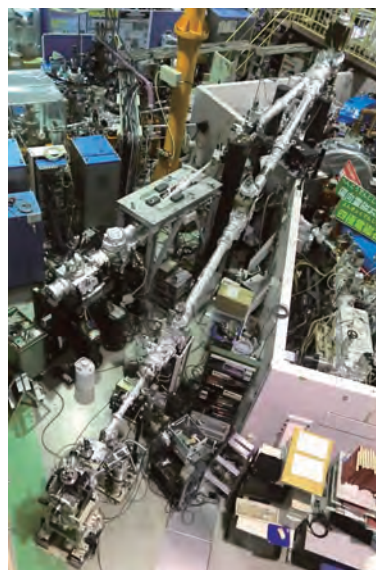


Fig. 2. Photo of BL7B.

▼ Technical Data

Monochromator	3 m Normal-Incidence Monochromator
Wavelength Range	1.5-25 eV (50-1000 nm)
Resolution	$E / \Delta E = 4000-8000$ for 0.01 mm slits
Experiments	Absorption, reflection, and fluorescence spectroscopy, mainly for solids

III-1

Accelerators and
Instruments

BL7B

Seven Years' Developments and Evaluations of Optical Components for CLASP Sounding Rocket Project at UVSOR BL7B

N. Narukage¹, M. Kubo¹, R. Ishikawa¹, Y. Katsukawa¹, S. Ishikawa¹, T. Kobiki¹, G. Giono¹,
R. Kano¹, T. Bando¹ and S. Tsuneta²

¹National Astronomical Observatory of Japan, Mitaka 181-8588, Japan

²Institute of Space and Astronautical Science, Japan Aerospace Exploration Agency, Sagamihara 252-5210, JAPAN

Our team consisting of Japan, US, Spain, France, and Norway developed a Chromospheric Lyman-Alpha SpectroPolarimeter (CLASP). CLASP is aimed at exploring the magnetic fields in the solar atmosphere (the upper chromosphere and transition region) via the Hanle effect in the Lyman-alpha ($\text{Ly}\alpha$) line (121.6 nm) for the first time [1, 2]. This experiment requires precise spectropolarimetric observations with a polarimetric sensitivity of $3\sigma \sim 0.1\%$ and a wavelength resolution of 0.01 nm.

In order to achieve the polarimetric sensitivity of $3\sigma \sim 0.1\%$, we designed a new type VUV spectropolarimeter [3] and developed its optical components (e.g., waveplate [4], polarizer, etc.) and some types of high reflectivity coatings using UVSOR BL7B. These developments and evaluations spent seven years [5].

On September 3rd 2015, CLASP was launched with a NASA sounding rocket at the White Sands Missile Range in New Mexico, United States. During five minutes observation, CLASP successfully observed linear polarizations (Stokes I, Q, U) in the solar $\text{Ly}\alpha$ line with a polarization accuracy of 0.1% for the first time [6, 7]. We also took 2D $\text{Ly}\alpha$ images with 0.6 sec cadence.

This data is very beautiful and its quality is perfect. Now, we are analyzing the data in detail [6, 7]. This full success of the CALSP project is significantly due to the $\text{Ly}\alpha$ beam of UVSOR BL7B, since its beam (that is very intense, strongly linearly polarized, very pure in wavelength, and very stable) is ideal for the evaluation of the CLASP optical components. We really acknowledge the staff of UVSOR, especially, M. Hasumoto and K. Tanaka, S. Kimura at Osaka University, and K. Fukui at Fukui University for their support of our experiment at UVSOR.

[1] R. Kano *et al.*, SPIE **8443** (2012) 84434F.

[2] K. Kobayashi *et al.*, Proc. Fifth Hinode Science Meeting, Astronomical Society of the Pacific Conference Series **456** (2012) 233.

[3] N. Narukage *et al.*, Applied Optics **54** (2015) 2080.

[4] R. Ishikawa *et al.*, Applied Optics **52** (2013) 8205.

[5] UVSOR Activity Reports from 2009 to 2014

[6] NAOJ news, **270** (2016), Issue in January 2016
http://www.nao.ac.jp/contents/naoj-news/data/nao_news_0270.pdf

[7] CLASP web pages:

http://hinode.nao.ac.jp/news/CLASP_Launch/
<http://hinode.nao.ac.jp/KakenS/CLASP.shtml>



Fig. 1. Photo of CLASP and Japanese members of the CLASP project.



Fig. 2. Photo of the CLASP launch.

Others

Development of Large Grain Size Nuclear Emulsion

A. Nishio¹, M. Moto¹, Y. Manabe¹, K. Kuwabara¹, K. Morishima^{1,2} and M. Nakamura^{1,3}

¹Graduate School of Science, Nagoya University, Nagoya 464-8602, Japan

²Institute for Advanced Research, Nagoya University, Nagoya 464-8601, Japan

³Ecotopia Science Institute, Nagoya University, Nagoya 464-8601, Japan

Nuclear emulsion is a kind of photographic film and has sensitivity for ionizing radiation. The film record tracks of charged particle with angular accuracy under several mrad.

Nuclear emulsion is made by coating emulsion gel on plastic base. In Nagoya University, started a emulsion gel production machine in 2010. It was enable us to develop new-type emulsion gel by ourself. Emulsion gel is mainly consisted by silver bromide crystal and gelatin. We report about properties of large grain size nuclear emulsion developed in Nagoya University.

We made emulsion gels which have silver bromide crystal with diameter about 200, 300, 600 nm. The traditional crystal size (incl. OPERA FILM [1]) is 200 nm. Figure 1 shows electron microscopic view of silver bromide crystals (left below : OPERA FILM ~200 nm, center : Large grain size nuclear emulsion ~600 nm). Emulsion gel of each crystal size were chemically sensitized in an optimal way [2]. Nuclear emulsion films were prepared using these gel. Emulsion films were exposed electron beam at UVSOR which has equivalent energy with minimum ionizing particle. We did chemical development in Nagoya University after exposure.

After development, electron tracks were visible with a light microscope (Fig. 2). We measured Grain Density, counts of silver grains per 100 μm. And we defined Crystal Sensitivity as ratio of Grain Density divided by Number of penetrated crystals. We show a table of them in each crystal size (Fig. 3).

Figure 2 shows the larger the diameter of the silver bromide crystal, it also increases the size of the developed silver grains. And Fig. 3 shows the larger the diameter of the silver bromide crystal, the crystal sensitivity was high. Crystal sensitivity was 44% at ~600 nm crystal nuclear emulsion.

Large grain size nuclear emulsion opens up a new vision of wide-field automatic nuclear emulsion scanning by low magnification optical systems. And it has possibilities to improve latent image fading. Also this result of latent image formation in large crystals is efficient performance suggest its potential.

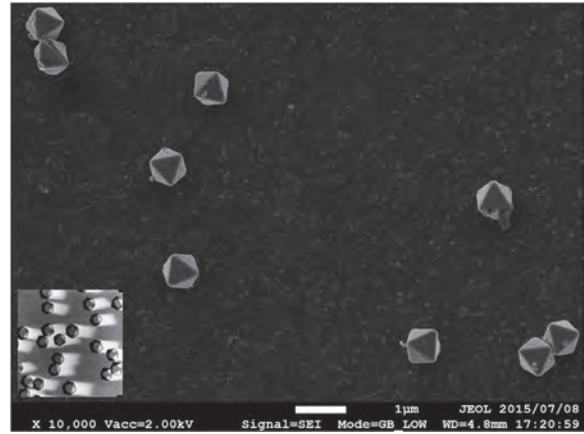


Fig. 1. Electron microscopic view of silver bromide crystal (left below : OPERA FILM ~200nm, center : Large grain size nuclear emulsion ~600nm).

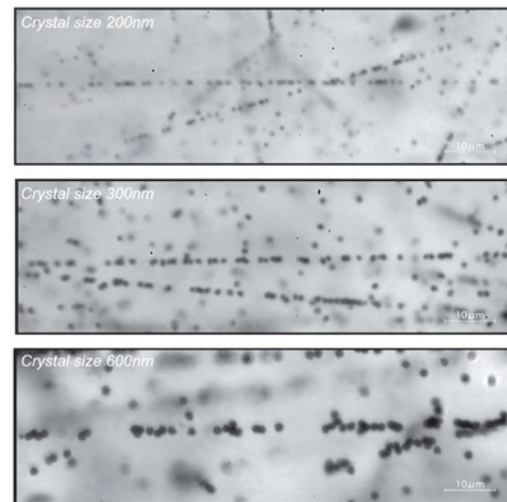


Fig. 2. Light microscopic view of electron tracks.

Crystal size (nm)	200	300	600
Grain Density (/100μm)	34	45	33
Number of crystals (/100μm)	225	150	75
Crystal Sensitivity (%)	15.1	30.0	44.0

Fig. 3. Basic properties of nuclear emulsion in each crystal size.

[1] T. Nakamura *et al.*, Nucl. Instrum. Meth. A556 (2006) 80.

[2] M. Moto *et al.*, 2nd Fall meeting of Federation of Imaging Societies. (2015) 29.

Accelerators, BL1U

Transmission Nuclear Resonance Fluorescence Measurement of ^{208}Pb in Natural Lead Target with Laser-Compton-Scattering Gamma-Ray at BL1U

H. Zen¹, Y. Taira², J. Yamazaki³, T. Hayakawa⁴, T. Shizuma⁴, T. Kii¹,
H. Toyokawa², M. Katoh^{3,5} and H. Ohgaki¹

¹Institute of Advanced Energy, Kyoto University, Uji 611-0011, Japan

²National Institute of Advanced Industrial Science and Technology (AIST), Tsukuba 305-8568, Japan

³UVSOR Facility, Institute for Molecular Science, Okazaki 444-8585, Japan

⁴Japan Atomic Energy Agency, Tokai-mura 319-1184, Japan

⁵School of Physical Sciences, The Graduate University for Advanced Studies (SOKENDAI), Okazaki 444-8585, Japan

High intensity and quasi-monochromatic gamma-rays has been generated by laser Compton scattering between the high energy electron beams and intense laser beams at BL1U in UVSOR-III. Gamma-ray beam with the maximum energy of 5.4 MeV and the total flux of 1×10^7 photons/sec can be generated by use of 1.94- μm 5-W fiber laser and 300-mA 746-MeV electron beams. In this fiscal year, we tested the transmission Nuclear Resonance Fluorescence (NRF) measurement [1] of ^{208}Pb in a natural lead target.

The schematic diagram of the transmission NRF measurement and the energy spectra of incident gamma-ray beams, transmitted gamma-ray beams, and NRF from the witness foil (a natural lead) are shown in Fig. 1. The gamma-ray with energy of a NRF level of 5.291 MeV resonantly absorbed by ^{208}Pb in the first target (a natural lead) and transmitted gamma-ray spectrum will be the notch spectrum as shown Fig. 1. The transmitted gamma-rays will hit the second target, called as the witness foil, which emits NRF gamma-rays. Therefore we can measure the nuclear resonance absorption in the first target as the reduction rate of the NRF peak by using a High Purity Germanium (HPGe) detector.

In this experiment we measured the NRF yield from the witness foil as the function of thickness of the first target. Since the NRF gamma-ray yield from witness foil depends both on the amount of the resonant (nuclear) absorption and on the atomic absorption of the first target, we need to measure the atomic absorption of the first target and corrected the NRF yield. Figure 2 shows the measured result. The NRF yield clearly shows linearity to the thickness of the first target as we have expected for thin target measurements. The required integration time of NRF events in case of a 6-mm target was around 2 hours in this experiment.

[1] B. J. Quiter, B. A. Ludewigt, V. V. Mozin and S. J. Tobin, 50th Annual Meeting of the Institute of Nuclear Materials Management 1 (2009) 786.

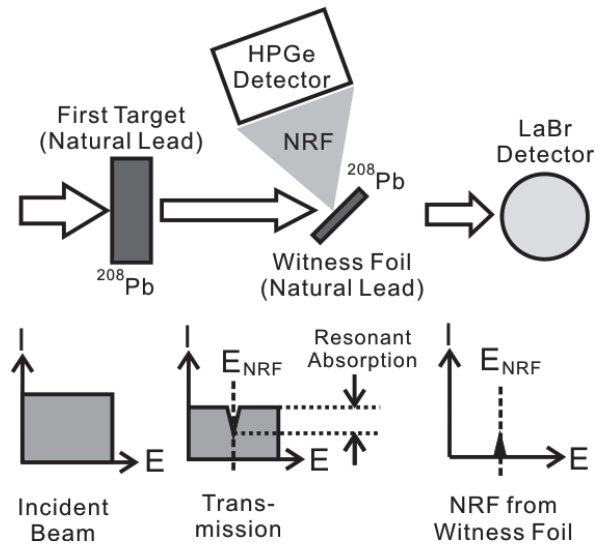


Fig. 1. Schematic diagram of NRF transmission measurement and energy spectrums of incident gamma-ray beam, transmitted gamma-ray beam through the target and NRF from the witness foil.

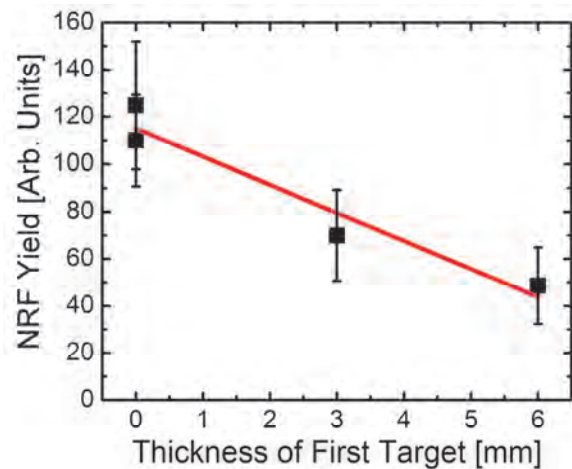


Fig. 2. Measured dependence of the NRF yield from the witness foil on the thickness of the first target.

BL1B

Improvement of Accuracy of Reflectivity Spectrum in the THz Region

S. Kimura

Graduate School of Frontier Biosciences, Osaka University, Suita 657-0871, Japan

Strongly correlated electron systems have a characteristic electronic structure near the Fermi level (E_F) owing to the strong electron correlation, and the electronic structure is the origins of unusual physical properties such as unconventional superconductors, heavy fermions and so on. To observe the electronic structure is important to clarify the effect of the electron correlation.

One of the methods to detect the electronic structure very near E_F is reflectivity (optical conductivity) measurement in the terahertz (THz) region [1]. The method is bulk sensitive compared with photoemission spectroscopies that are widely used recently. Since results of a THz spectroscopy can be regarded as from bulk properties, they can be directly compared with thermodynamic physical properties. However, since reflectivity of such metallic materials in the THz region is almost unity, so a tiny change, typically less than 1%, and the absolute value of the reflectivity must be measured [2]. To perform such accurate measurement of reflectivity spectra, we need intense and stable THz light such as synchrotron radiation. Then we are developing high accurate THz reflectivity measurement system at BL1B of UVSOR-III. The block diagram of the measurement is shown in Fig. 1.

At UVSOR-III, a top-up operation at one-minute intervals is now adopted, but the beam current is reduced slightly during the interval. To eliminate the effect of the beam current reduction, we introduced a digital divider (made by Equipment Development Center of IMS) in which the output signal from a detector (a Si bolometer) is instantly normalized by the beam current of SR. In addition, to eliminate the signal during the top-up injection, we get the top-up signal from the accelerator by a personal computer (PC) and put a TTL signal to the data accumulator. During the top-up injection (the TTL signal is on), the data accumulator rejects the signal from the detector. Finally, the data accumulator gives an interferogram (detector intensity vs mirror position of the moving mirror in the FTIR) to the PC.

The effect of the top-up rejection as a 100% line, which is the first spectrum divided by the second one with a same condition, is shown in Fig. 2. Both lines are used the digital divider. Without the top-up rejection, the 100% line is 0.995 ± 0.003 , but it becomes 1.000 ± 0.002 with the top-up rejection in the wavenumber region of 20–100 cm^{-1} . Therefore, the top-up rejection is effective to determine the accuracy of reflectivity spectra in the THz region.

The PC also operates a temperature controller of

samples. For the measurement of temperature-dependent reflectivity spectra, we introduced a specially designed feedback positioning system [3] to maintain the overall uncertainty level less than $\pm 0.5\%$ at sample temperatures in the range of 4–300 K at BL1B. By the preparation, highly accurate reflectivity measurements in the THz region can be performed.

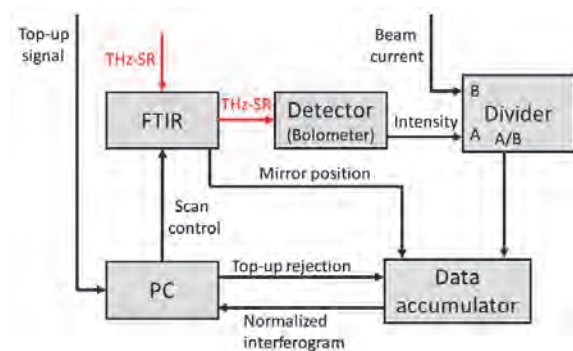


Fig. 1. Block diagram of the measurement system with the rejection during top-up injections and the normalization by the beam current.

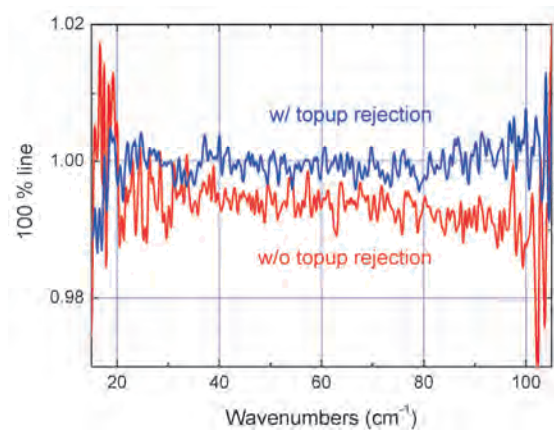


Fig. 2. 100% lines with and without top-up rejection.

[1] S. Kimura and H. Okamura, *J. Phys. Soc. Jpn.* **82** (2013) 021004.

[2] S. Kimura, J. Sichelschmidt, J. Ferstl, C. Krellner, C. Geibel and F. Steglich, *Phys. Rev. B* **74** (2006) 132408.

[3] S. Kimura, *JASCO Report* **50** (2008) 6. [in Japanese]

BL2B

Reconstruction of the Beamline BL2B for Photoelectron Spectroscopy of Organic Materials

K. R. Koswattage¹, T. Ueba², Y. Nakayama³, K. K. Okudaira⁴, H. Ishii^{1,4} and S. Kera^{2,4}

¹ Center for Frontier Science, Chiba University, Chiba 263–8522, Japan

² Institute for Molecular Science, Okazaki 444–8585, Japan

³ Department of Pure and Applied Chemistry, Faculty of Science and Technology, Tokyo University of Science, Noda 278–8510, Japan

⁴ Graduate School of Advanced Integration Science, Chiba University, Chiba 263–8522, Japan

The reconstructed beamline 2B is dedicated to photoelectron emission experiments to investigate electronic structures of surfaces and interfaces of wide range of molecular materials. Here we summarize the three-year program of the beamline reconstruction.

The beamline is equipped with a spherical grating dragon type monochromator. The monochromator covers the photon energy range from 23 to 205 eV with resolving power of 2000 – 8000 range [1-2].

In the reconstruction process, we have solved a malfunction in the monochromator, introduced a UHV chamber (monitoring and filtering the photons) downstream of the M4 mirror chamber, built a new interlock system, and placed a new end-station where a load-lock and two sample preparation chambers are connected. At the deposition chamber, samples can be heated by a radiation heating. By the load-lock and sample transfer systems, samples can be introduced to the preparation chamber without breaking UHV. Three evaporators can be equipped from the downstream. Another chamber so called cleaning chamber is equipped with surface preparation apparatus such as IR heater, sputter gun, and LEED system. At the measurement chamber, VG-Scienta R3000 angle-resolved photoemission spectrometer is installed. The sample is mounted in the sample holder on cryogenic manipulator with manually operated 5-axis motion in this chamber and the sample can be cooled down to around 15 K. The sample temperature is controlled by a combination of liquid He cooling and a resistive heater.

After the alignment, beam spot size is roughly estimated to be about 1.5 mm × 0.8 mm (vertical × horizontal) after the final refocusing mirror for exist slit of 300 μm. Also, the photon flux for an exit slit width of 300 μm are estimated to be $1 \times 10^{10} - 3 \times 10^{10}$, $4 \times 10^{10} - 2 \times 10^{11}$, and $1 \times 10^{10} - 2 \times 10^{10}$ photons/s for G1 (80 – 150 eV), G2 (50– 120 eV) and G3 (25 – 55 eV) gratings, respectively using a silicon photodiode and Au mesh in the monitoring chamber.

A filter (Al20nm/Mg300nm/Al20nm-Ni70nm mesh, LUXEL) in the monitoring chamber is equipped in order to reduce second order light. It is estimated that the second order light contribution can be reduced to 2.4% from 10% at photon energy 28 eV by inserting the filter. Also, the photon energy accuracy can be checked by using the first and second

order light and it is estimated to be a difference of -0.04 eV at photon energy 28 eV.

The beam line resolution is determined by measuring a clean Au(111) at 15 K as shown in the figure together with ARPES of surface state region. The energy resolution ΔE_R of analyzer was set to be 20 meV, giving the photon energy width of $\Delta E_\omega = 30$ meV at $h\nu = 28$ eV, which is much greater than that of the beamline specification and the previously estimated value ($\Delta E_\omega = 14$ meV) in the last year. The momentum resolution will be saturated by a large spot size of the beam. Unfortunately, the stabilities of photon flux and beam position are not sufficient for a long experimental acquisition due to the cooling problem of M0 system. It may also affect to the resolution problem above mentioned.

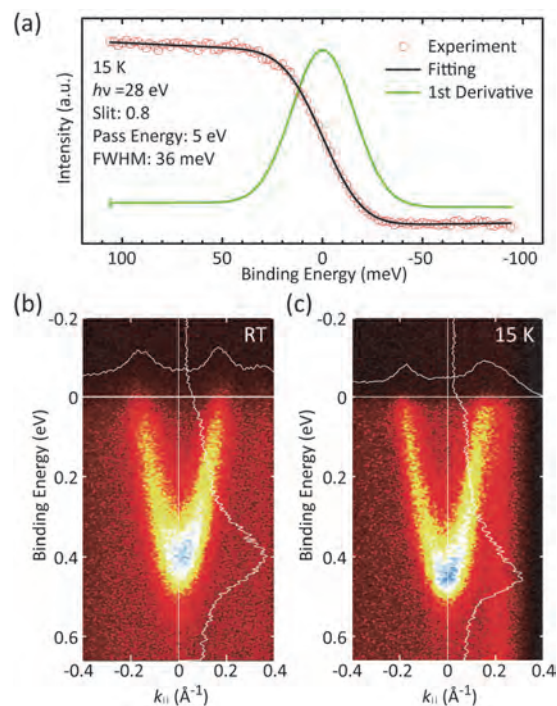


Fig. 1. (a) Low-temperature PES spectra of Fermi edge of Au (111). (b) Surface state region of Au(111) at room temperature (RT) and 15 K at $h\nu = 28$ eV.

[1] H. Yoshida *et al.*, J. Synch. Rad. **5** (1998) 774.

[2] M. Ono *et al.*, Nucl. Instrum. Meth. Phys. Res. A **467-468** (2001) 577.

BL5B

EUV Multilayer Mirrors for Focusing Isolated Attosecond Pulse in 40 nm Wavelength Region

M. Toyoda¹, Y. Tamaru^{2,3}, S. Mori¹, K. Sawada^{2,4}, Y. Fu², E. J. Takahashi², A. Suda³,
F. Kannari⁴, K. Midorikawa² and M. Yanagihara¹

¹Center for Advanced Microscopy and Spectroscopy, IMRAM, Tohoku Univ., Sendai 980-8577, Japan

²RIKEN Center for Advanced Photonics, 2-1 Hirosawa, Wako 351-0198, Japan

³Tokyo University of Science, Noda 278-8510, Japan

⁴Keio University, Yokohama 233-8522, Japan.

In the past decade, coherent light sources based on higher-order harmonics generation in extreme ultraviolet (EUV) region have been investigated. Recently, Takahashi *et al.* has reported isolated attosecond pulse (IAP) generation in a 40 nm wavelength region, where an isolated intense pulse with pulse energy of a few μJ was demonstrated by applying the novel two-color excitation technique [1]. When such the intense EUV pulse is focused with diffraction limited objective so as to produce a small focal spot with size of a few hundred nanometers, we can generate extremely intense light fields with the maximum intensity of over 10^{16} W/cm², which enables us to access the new frontier of nonlinear optics in EUV region.

For the diffraction-limited focusing of the IAP, we are developing the Schwarzschild objective made of two-curved multilayer mirrors [2]. The objective has two practical advantages, i.e., high spatial resolution resulting from large-numerical aperture optical design, and spectral selectivity based on the Bragg reflection on multilayer mirrors. To realize the intense light fields with the objective, firstly, we need multilayer mirrors with practical high reflectivity. In this report, we describe design, fabrication, and test of multilayer mirrors that is suitable for the focusing application in the 40 nm wavelength region.

Design of the multilayer mirrors are summarized in Table 1. After applying the selection rule for high reflectivity, which has been given by Yamamoto, [3] three material pairs, i.e., SiC/Mg, Cr/Mg, and Sc/Si, were chosen. The multilayer coating was consisted of 20 bi-layers. The period, d_{design} , and thickness ratio, Γ , were numerically optimized with the multilayer modeling software, IMD, [4] to give the maximum reflectivity at a wavelength of 40 nm. Then, the three multilayer coatings were deposited on a Si wafer by using the magnetron sputtering apparatus (SPL-500, Canon Anelva Corp.). We also experimentally confirmed a period of the multilayer coating with small-angle X-ray diffraction (RGXR, Rigaku Corp.). As shown in Table 1, the actual period of the sample, d_{actual} , was precisely controlled within 1% of the design value.

At-wavelength reflectivity was examined with the EUV reflectometer equipped on beamline BL5B of UVSOR. A 300-nm thick Mg filter placed upstream

of the reflectometer removes higher-order lights from the monochromator. Figure 1 shows the measured reflectivity, as a function of a wavelength. The peak reflectivity, R_{peak} , and band width, $\Delta\lambda_{\text{HWHM}}$, are also tabulated on Tab. 1. We observed relatively high reflectivity between 30 to 40% on the Mg-based multilayer mirrors. Especially in SiC/Mg multilayer mirror, practical high reflectivity and wide band width were confirmed simultaneously, where we can expect the maximum intensity of over 10^{16} W/cm² with pulse duration below 800 attosecond on the focus of the two-mirror objective.

Table 1. Design parameters for the multilayer mirrors.

	SiC/Mg	Cr/Mg	Sc/Si
d_{design} (nm)	21.2	21.2	21.0
Γ	0.25	0.23	0.33
d_{actual} (nm)	21.0	21.4	20.9
R_{peak} (%)	38.3	28.7	23.3
$\Delta\lambda_{\text{HWHM}}$ (nm)	2.8	3.0	4.9

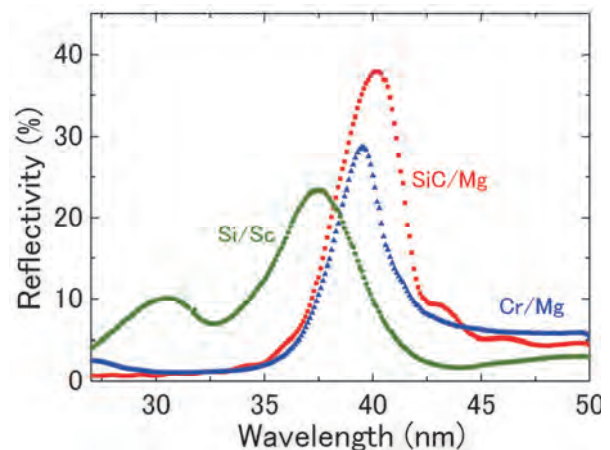


Fig. 1. EUV reflectivity spectra of the mirrors. Data were measured with an incident angle of 11 deg.

[1] E. J. Takahashi *et al.*, Nat. Commun. **4** (2013) 2691.

[2] M. Toyoda *et al.*, Appl. Phys. Exp. **5** (2012) 112501.

[3] M. Yamamoto and T. Namioka, Appl. Opt. **31** (1992) 1622.

[4] D. L. Windt, Computers in Physics, **12** (1998) 360.

BL5B

Reflectance Measurement of Mo/Si Multilayer Coated Mirror by Using Pure-Calibrated EUV Beam

M. Kuwabara¹, F. Suzuki², R. Hikida² and I. Yoshikawa¹

¹*Department of Complexity Science and Engineering, Graduate School of Frontier Sciences, The University of Tokyo, Chiba 277-8561, Japan*

²*Department of Earth and Planetary Science, Graduate School of Science, The University of Tokyo, Tokyo 113-0033, Japan*

We are developing space-based imagers for plasma emissions from the plasmasphere. The main target of our instruments is He ion in the plasmasphere. He ion resonantly scatters solar He II (30.4 nm) radiation. He column densities along the field of view of instruments can be obtained because intensities of emissions are proportional to them under the assumption that observational regions are optically thin. Therefore, the accuracies of the efficiencies of the optics systems of instruments are critical for estimation of the densities and to achieve the scientific goals of our missions.

In space and planetary science, a number of imaging and spectroscopic observations in the spectral range of extreme ultraviolet have been and will be performed. High-reflectivity multilayer coatings for the He II radiation have been required and developed for some of these applications. A multilayer coated mirror of Mo/Si has been usually and conventionally used in the He II emission line, because it is highly stable [1].

In this experiment, we measure the reflectance of Mo/Si multilayer mirror at the wavelength of 30.4 nm. We install an Al/Mg/Al filter and an Sn filter at the entrance of the SOR beam in order to achieve the pure 30.4 nm light [2-4].

With the pure 30.4 nm line, we measure the reflectance of the multilayer coated mirror at various incident angles by using the photo diode.

The result is shown in Fig. 1 and the reflectances of Mo/Si multilayer mirror are 13, 9, 6, 4, and 3% at incident angles of 10, 15, 20, 25, and 30 degrees, respectively. Note that the statistical error bars of reflectivity measurement are over-plotted, but they are so small (approximately 1%) that you might not identify them.

For the next step, in addition to the 30.4 nm line, we plan to measure the reflectance at 83.4 nm line. O ions have emission line at 83.4 nm and are known as one of the main components in the plasmasphere.

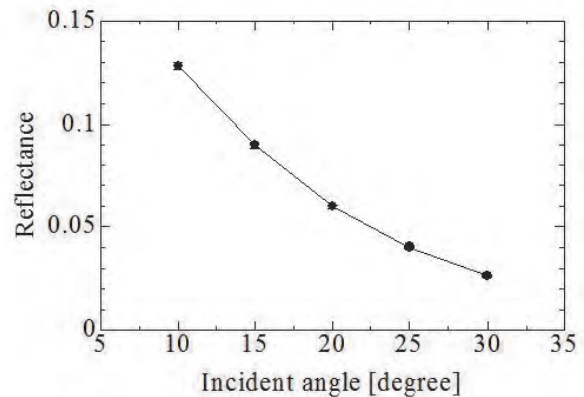


Fig. 1. Reflectance of the Mo/Si multilayer coated mirror at the wavelength of 30.4 nm.

- [1] Yoshikawa *et al.*, *Earth Planets Space* **60** (2008) 407.
- [2] Ogawa *et al.*, *UVSOR Activity Report* **36** (2008) 127.
- [3] Murakami *et al.*, *UVSOR Activity Report* **37** (2009) 47.
- [4] Sakai *et al.*, *UVSOR Activity Report* **38** (2010) 45.

BL6B

An Investigation into the Cause of Instability at BL6B

T. Iizuka¹, F. Teshima², E. Nakamura², H. Zen³ and K. Tanaka^{2,4}

¹Toyota Technological Institute, Nagoya 468-8511, Japan

²UVSOR Facility, Institute for Molecular Science, Okazaki 444-8585, Japan

³Institute of Advanced Energy, Kyoto University, Uji 611-0011, Japan

⁴School of Physical Sciences, The Graduate University for Advanced Studies (SOKENDAI), Okazaki 444-8585, Japan

Beamline 6B (BL6B) is an Infrared-THz beamline which has confocal type micro-spectroscopy station, reflection/transmission station and IR microscope imaging station. This beamline can provide measurement-techniques which are not available in conventional IR sources, utilizing the characteristics of synchrotron radiation (SR) such as high brilliance, polarization, or broad spectrum.

Spectroscopy in THz-IR region is performed with FT/IR: Michelson-type Interferometer which requires stable light source. However, the top-up operation of UVSOR induces two types of instability: short term blinking coincides with electron beam injection on every minutes, and long term attenuation of power.

The former causes spike noise on interferogram, and it can be solved by excluding those scan data during the beam injection, by synchronizing data collection of FT/IR. The latter one might originate from the drifting of the focal point of M0 mirror, first mirror of BL6B. And a qualitative observation was required to eradicate the drifting instability which influence on S/N ratio.

Because the drift continues for about 10 hours after the first injection, the most suspected origin is temperature change caused by heat from synchrotron radiation. Addition to this, M0 mirror of BL6B and vacuum chamber has no cooling system to avoid vibration comes from coolant flow. Therefore, thermal expansion of M0 mirror holder or vacuum chamber might cause the drift of the focal point. It can be simply estimated by observing a He-Ne visible laser spot reflected from M0 mirror. In this study, we monitored the position of the laser spot to clarify the origin of the instability at BL6B.

The change of spot position was observed by interval photographing by a web camera. Each laser spot positions were then estimated by handmade LabVIEW program by following procedure. First, color pictures were converted to grayscale, and region of interests (ROI) was segmented around the laser spot, to get two-dimensional distribution. After substituting the background data, i.e. picture without laser spot, one-dimensional profile were obtained to estimate the center of laser spot in X and Y directions. After that, base line was subtracted and peak position were estimated with following formula,

$$Center = \frac{\sum x \cdot f(x)}{\sum f(x)},$$

where $f(x)$ is the light intensity at pixel position of x .

It is applicable not only to laser spot but also the focal point of M0 mirror which is not circular shape.

Figure 1 shows the change of laser spot position from M0 mirror during a week. It can be seen the oscillation of mirror angle which moves one direction during top-up operation and saturate, then moves to the other direction during shutdown. The displacement of laser light saturated about 9 hours later after the start of top-up operation, and it is consistent with previously observed long term drift of SR power at the end station. The comparison of the changes of mirror direction (laser spot) and SR focal spot is shown in Fig. 2. Two results show pretty close correlation, and one can thus conclude that the spot drift originates from mirror direction. From another point of view, it is available to stabilize the SR focal spot position by a feedback control with M0 mirror direction which can be obtained from laser spot position, and is able to perform simultaneously with user experiments at the end station.

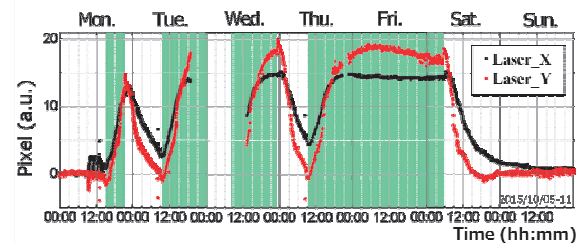


Fig 1. One week observation result of laser spot position reflected from M0 mirror. X, Y is horizontal, perpendicular change to the ground, respectively. Green areas indicate the operation time of UVSOR.

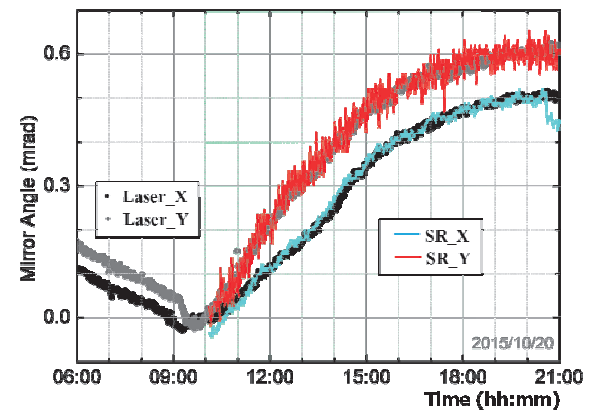


Fig. 2. Comparison of reflected laser spot (gray) and focal point of SR light (color).

BL7B

Performance Evaluation of Spectrometer for High-Resolution Vacuum Ultraviolet Inverse Photoemission Spectroscopy

Y. Ohta¹, A. Yoshizumi¹, Y. Ohtsubo^{1,2} and S. Kimura^{1,2}

¹ Graduate School of Science, Osaka University, Suita 565-0043, Japan

² Graduate School of Frontier Biosciences, Osaka University, Toyonaka 565-0871, Japan

Photoemission spectroscopy (PES), which is a photon-in/electron-out process, is one of experimental tools to detect electronic structure of materials. Since the energy resolution of PES has become better than several meV nominally, the method is usually used for the determination of precise electronic structure as well as orbital-selective interactions. Even though PES is widely used at present, it has a serious shortcoming to be unable to detect unoccupied electronic structure. In contrast to PES, inverse photoemission spectroscopy (IPES), which is an electron-in/photon-out process, is a method to determine unoccupied electronic structure [1]. Accordingly, although the method has been used for a long time, the energy resolution is not good compared to that of PES. The best energy resolution of IPES as far as we know is 190 meV [2]. The combination of IPES to PES provides the perfect information of electronic structure of materials. However, spectra of IPES cannot be directly compared with those of PES because of poor energy resolution of IPES.

To perform IPES experiment with good energy resolution, for instance better than 100 meV, both the electron source and the photon detector should be improved. Since the quantum efficiency of the IPES process is about five orders of magnitude smaller than that of the PES process [3], the throughput of the IPES system should be improved. Then, we are now developing a new IPES system using a high brilliant photo-cathode electron source based on a strained GaAs-GaAsP superlattice [4] and a VUV spectrometer using a Seya-Namioka-type monochromator (focal length: 20 cm, grating: laminar-type, 2400 L/mm) combined with an X-ray CCD detector (1024x256 pixels). Here, we report the energy resolution and throughput of the VUV spectrometer.

To check the performance of the VUV spectrometer, we set the spectrometer at the end of the sample chamber of BL7B. The entrance slit of the monochromator is located at the off-focus position of the beamline to reduce the intensity of SR. The center wavelength of spectrometer was set at eleven wavelengths of 40 – 120 nm and monochromarized lights from the beamline with the wavelengths of 30 – 120 nm were introduced to the spectrometer. The intensity images on the CCD detector were accumulated. The CCD images content the correspondence between wavelengths and CCD pixel numbers and the efficiency, which is the intensity normalized by incident photons, and wavelength

resolutions at a center wavelength of the spectrometer.

As a result, we obtained a linear relation between wavelength and pixel number of the CCD detector at all center wavelengths. The obtained wavelength resolutions and efficiency (intensity normalized by incident photon flux) as functions of incident wavelength and center wavelength of the spectrometer are shown in Fig. 1. From this data, we could know that the area of the incident wavelength of 40 – 70 nm and the center wavelength of 50 – 60 nm has both good efficiency and good resolution.

From the data and considered the monochromator and spectrometer slit size, the best resolution of the spectrometer can be evaluated as 0.1 nm at 50 nm wavelength ($h\nu \sim 25$ eV). This wavelength resolution corresponds to the energy resolution of about 50 meV. Since our electron source is expected to have the energy resolution of about 50 meV [5], the total energy resolution of the IPES system is expected as 71 meV ideally. This value is better than our target energy resolution of the IPES system.

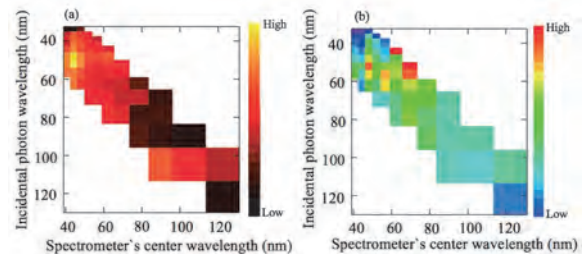


Fig. 1. Obtained wavelength resolution (a) and efficiency (b) as functions of incident and spectrometer wavelengths of the newly developed VUV spectrometer for the IPES system.

- [1] P. D. Johnson and S. L. Hulbert, *Rev. Sci. Instrum.* **61** (1990) 2277.
- [2] M. Budke and V. Renken, *Rev. Sci. Instrum.* **78** (2007) 083903.
- [3] J. B. Pendry, *Phys. Rev. Lett.* **45** (1980) 1356.
- [4] N. Yamamoto *et al.*, *J. Appl. Phys.* **102** (2007) 024904.
- [5] S. Pastuszka, M. Hoppe, D. Kratzmann, D. Schwalm and A. Wolf., *J. Appl. Phys.* **11** (2000) 88.

BL7B

Development of Reflective and Transmissive Polarizers in 280 nm

R. Ishikawa¹, N. Narukage¹, N. Yoshida², S. Ishikawa³ and M. Kubo¹

¹National Astronomical Observatory of Japan, Mitaka 181-8588, Japan

²School of Physical Sciences, The Graduate University for Advanced Studies (SOKENDAI), Mitaka 181-8588, Japan

³Institute of Space and Astronautical Science, Japan Aerospace Exploration Agency, Sagamihara 252-5210, Japan

Spectro-polarimetry in the ultra violet (UV) range is a new astrophysical diagnostic tool to explore the magnetic field of the hot plasma of $>10^4$ K. Following the success of CLASP [1], a team of researchers from Japan, the USA, and Europa plans to propose the second flight of CLASP (CLASP2: Chromospheric LAYER Spectro-Polarimeter 2) to perform the spectro-polarimetry in the MgII lines around 280 nm at the high polarization sensitivity of $<0.1\%$. In order to meet this stringent requirement on the polarization sensitivity, the high throughput of $>50\%$ and the high extinction ratio of >100 around 280 nm are required for new polarization analyzers.

For this purpose, we have fabricated and tested the two different types of polarizers. The first one is the reflective type; applied multi-layer coating of MgF_2 and Al_2O_3 over BK7 substrates. This is the high-efficiency reflective polarizer based on the same design concept as what was used for the CLASP1 instrument although the materials are different [2]. Another one is the transmissive type; wire-grid type linear polarizers that were printed using atomic layer deposition technology on 1 mm thick fused silica (SiO_2) substrates [3]. In order to evaluate the performance of the polarizers, 100% linearly polarized beam is required. Thus, we placed the beam cleaner, which is the SiO_2 substrate mounted at the Brewster's angle to eliminate the p-polarized beam, at the upstream of our measurement system.

Two panels in Fig. 1 are the measured reflectivity of 2 samples of the reflective polarizer for s- and p-polarized beams (R_s & R_p) as a function of angle of incidence (AOI) at 280 nm. It is found that the reflective type has the performance of $R_s=65\%$ and $R_p=0.27\%$ at the Brewster's angle of 68 degree, resulting in the extinction ratio of $R_s/R_p=240$. The extinction ratio T_1/T_2 of the transmissive polarizer was measured to be >300 around 280 nm, where T_1 is the transmissivity parallel to the grid and T_2 is the one perpendicular to the grid. Note that the fluctuation over the wavelength is caused by the dark current fluctuations indicating the detection limit. The transmissivity T_1 was measured to be $\sim 70\%$.

Based on these measurements, we conclude that we have successfully developed the high performance reflective and transmissive polarizers. According to the final decision on the optical design of CLASP2 instrument, one of these polarizers will be applied as

the flight polarization analyzer.

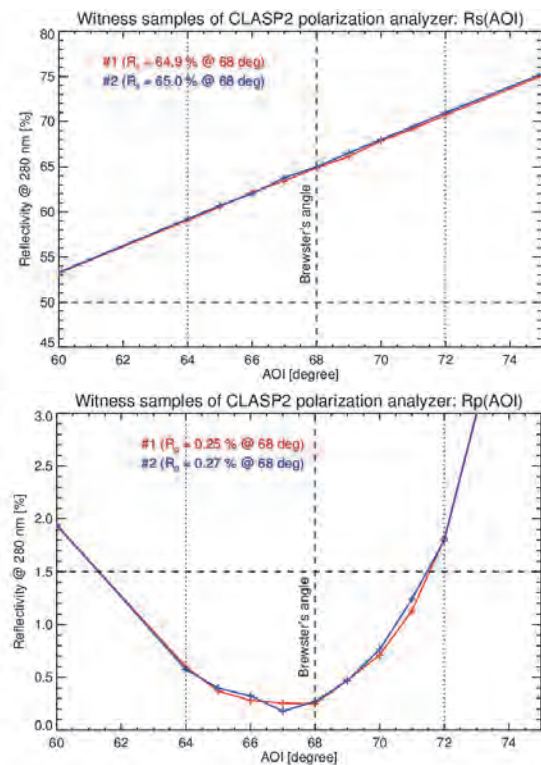


Fig. 1. Measured reflectivity of two reflective polarizer samples for s- and p-polarization.

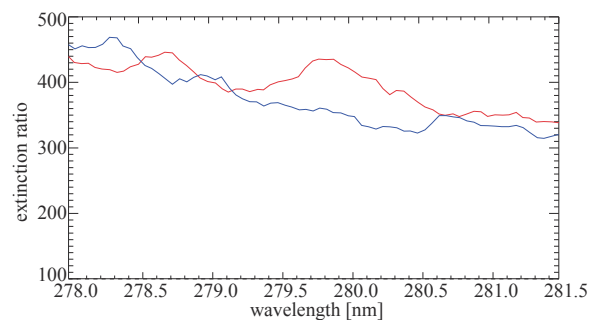


Fig. 2. Measured extinction ratio of two transmissive polarizer samples (red and blue).

[1] R. Kano *et al.*, in preparation.

[2] N. Narukage *et al.*, UVSOR Activity Report **40** (2012) 47.

[3] T. Berger *et al.*, Proc. of SPIE, **8486** (2012) 8486G-1.

BL7B

Stokes Parameters Measurements for BL7B Beamline

M. Miyashita¹, Y. Kubo¹, Y. Nasu¹, Y. Fujii¹, K. Fukui¹,
K. Yamamoto², T. Saito³ and T. Horigome⁴

¹Department of Electrical and Electronics Engineering, University of Fukui, Fukui 910-8507, Japan

²Far-infrared region Development Research Center, University of Fukui, Fukui 910-8507, Japan

³Department of Environment and Energy, Tohoku Institute of Technology, Sendai 982-8577, Japan

⁴UVSOR Facility, Institute for Molecular Science, Okazaki 444-8585, Japan

Ellipsometers are known as powerful tools to determine optical constants of materials. However, due to the fact that all the solid materials cannot have transparency in the vacuum ultraviolet (VUV) region, an ellipsometer in VUV region must consist of both reflection type polarizer and analyzer in vacuum. Since these requirements make it difficult to construct the VUV ellipsometer, there is only one beamline (at BESSY) equipped with VUV spectroscopic ellipsometer (SE) [1] in the world to our knowledge. The other idea for VUV SE was proposed by Saito *et al.* which used both Synchrotron radiation (SR) and oblique incidence detector [2]. Compared with standard ellipsometers, this type SE has an advantage of obtaining not only optical constants of the sample, but also Stokes parameters (S_1/S_0 , S_2/S_0 , S_3/S_0) of the incident beam. In this report, we show Stokes parameters of the monochromatized output radiation of BL7B beamline (3 m McPherson type normal incidence monochromator beamline).

Our VUV SE is an improved SE which was designed and constructed by an AIST group [2], and is optimized for the use at BL7B. Figure 1 shows schematic drawing of VUV SE. A sample chamber and an oblique incident photodiode are rotated independently along the incident light axis (α and β rotations) instead of the rotation of a polarizer and an analyzer, respectively. This system is mounted on the

computer controlled parallel link mechanism base [3]. Measurements are carried out by rotating α with fixed β at characteristic angles (0° , 45° and 90°). Since the α dependence of the photodiode intensity S_0' at each three β angles is simply expressed by using $\mathbf{M}(\Psi, \Delta)$, $\mathbf{M}_a(\Psi_a, \Delta_a)$ and $\mathbf{S}(S_0, S_1, S_2, S_3)$ where \mathbf{M} and \mathbf{M}_a are Mueller matrixes of a sample and a photodiode, and \mathbf{S} is a Stokes vector of the incident light, seven parameters Ψ , Δ , Ψ_a , S_1/S_0 , S_2/S_0 , S_3/S_0 are obtained analytically. An Au mirror is used as the sample.

Figure 2 shows Stokes parameters of BL7B monochromatized output radiation as a function of photon energy. BL7B has three gratings G1, G2 (Au coatings) and G3 (Al coating), and lower energy pass filters (quartz and Pyrex glass) are used in the G3 region. As expected, while both S_2/S_0 and S_3/S_0 maintain small values S_1/S_0 have large values over almost the entire energy region surveyed. The S_1/S_0 values around the G3 region are in good agreement with the results using a polarization plate (purple line).

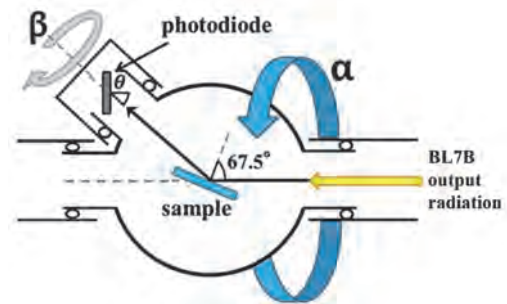


Fig. 1. Schematic drawing of VUV ellipsometer.

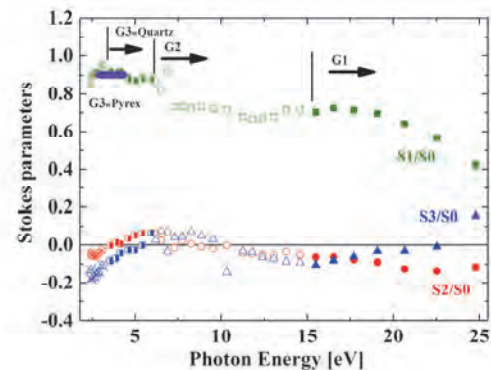


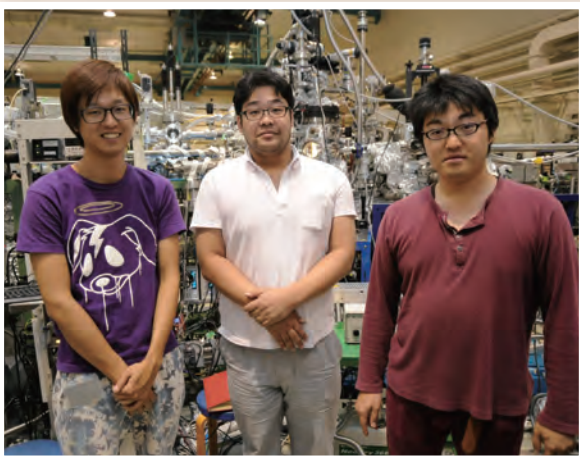
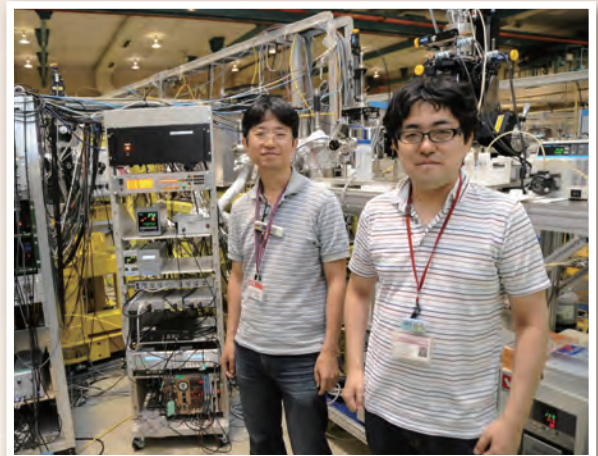
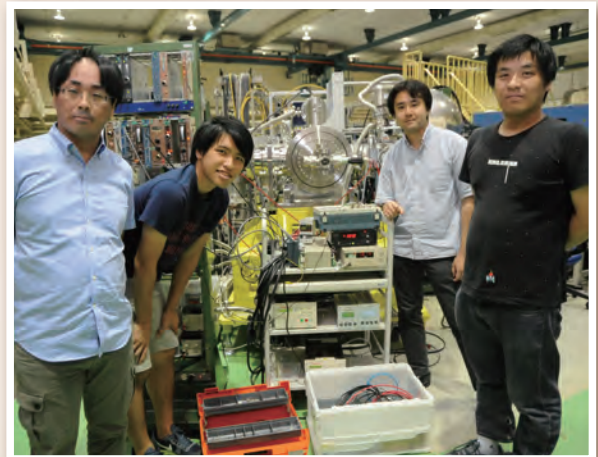
Fig. 2. Stokes parameters of the BL7B

[1] T. Saito, M. Yuri and H. Onuki, Rev. Sci. Instrum. **66** (1995) 1570.

[2] W. Budde and R. Dittmann, PTB-Mitt. **83** (1973) 1.

[3] Y. Kubo, K. Fukui, K. Yamamoto, T. Saito and T. Horigome, UVSOR Activity Reports **41** (2014) 43.

UVSOR User 2



The background is a vibrant blue. In the upper right, there is a large, semi-transparent circular graphic composed of several concentric rings. The outermost ring features a series of small, light-blue circles. Below this graphic, the text 'III-2' is prominently displayed in a large, white, serif font. Underneath the main title, the words 'Materials Sciences' are written in a smaller, white, sans-serif font. The bottom half of the page is filled with a fine, light-blue dot pattern that creates a textured effect.

III-2

Materials Sciences

BL7U

Electronic Structure of Triple-Layer Cuprate Superconductor $\text{Bi}_2\text{Sr}_2\text{Ca}_2\text{Cu}_3\text{O}_{10+\delta}$ Observed by ARPES

S. Ideta¹, T. Yoshida², S. Ishida³, K. Takashima⁴, S. Uchida³, A. Fujimori⁴ and K. Tanaka¹¹National Institutes of Natural Science, Institute for Molecular Science, Okazaki, 444-8585, Japan²Graduate School of Human and Environmental Studies, Kyoto University, Kyoto 606-8501, Japan³National Institute of Advanced Industrial Science and Technology (AIST), Tsukuba 305-8568, Japan⁴Department of Physics, University of Tokyo, Tokyo 113-0033, Japan

Effects of intra-multilayer interaction between the CuO_2 planes, which may contribute to the enhancement of the critical temperature (T_c) in the multi-layer high- T_c cuprate superconductors (HTSCs) [1], have been investigated to elucidate the mechanism of superconductivity. The Bi-based HTSC is classified by the number of the neighboring CuO_2 layers (n): single-layer ($n = 1$) $\text{Bi}_2\text{Sr}_2\text{CuO}_{6+\delta}$ (Bi2201), double-layer ($n = 2$) $\text{Bi}_2\text{Sr}_2\text{CaCu}_2\text{O}_{8+\delta}$ (Bi2212), and triple-layer ($n = 3$) $\text{Bi}_2\text{Cr}_2\text{Ca}_2\text{Cu}_3\text{O}_{10+\delta}$ (Bi2223). The T_c of optimally doped Bi2223, 110 K, is the highest among the Bi-family cuprates. In spite of both extensive experimental and theoretical studies [2-6], the microscopic origin of the T_c enhancement in the triple-layer HTSCs still remains unclear.

In recent ARPES studies of Bi2223, we have reported two bands originating from the outer and inner CuO_2 planes [7-9]. Here, we report an ARPES study of Bi2223 using low-energy photons with linear polarization along the Cu-O bond direction. We observed three bands and three Fermi surfaces (FSs) resulting from interaction between the three CuO_2 planes.

High-quality single crystals of optimally doped Bi2223 ($T_c = 110$ K) were grown by the travelling solvent floating zone method. ARPES experiments were carried out at BL 7U of UVSOR using linearly polarized light of $h\nu = 7$ eV - 8.5 eV. The total energy resolution and angular resolution were set at 7 - 8 meV and 0.05 deg, respectively. Temperature was set at $T = 12$ K and clean sample surfaces were obtained by cleaving the single crystals *in-situ* in an ultrahigh vacuum better than 7×10^{-9} Pa.

A schematic picture of FSs is shown in Fig. 1(a). The FS from the outer plane (previously denoted as OP) is split into two FSs due to the bonding and antibonding combinations of the two OPs, as denoted by OP-B and OP-A, respectively. Their superstructures due to the structural modulation of the BiO layer are also shown. Energy-momentum (E - k) intensity taken in the SC state along the momentum cuts indicated by black curves in panel (a) are shown in Figs. 1(b)-1(e). While the OP band is not clearly split near the nodal region [Fig.1(b)], away from the nodal region, this seemingly single feature splits into two dispersions as indicated by arrows for OP-B and OP-A bands.

In conclusion, we have observed the splitting of the triple-layer bands by ARPES. This result may give a

key to elucidate the mechanism of the triple-layer cuprate superconductivity with the highest T_c of 110 K.

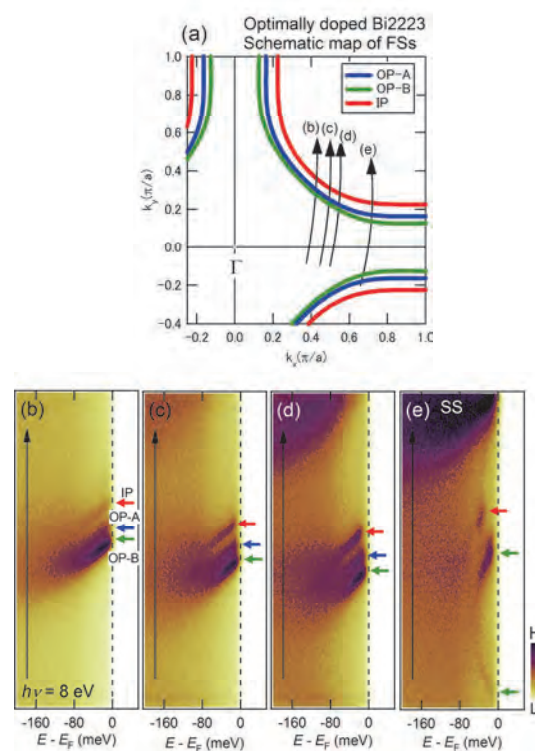


Fig. 1. Energy-momentum intensity plots in the Cu-O bond direction taken with $h\nu = 8$ eV at $T = 12$ K. ARPES intensity plots [(b)-(e)] correspond to cuts in panel (a). IP, OP-B, and OP-A denote the inner-plane, bonding outer-plane, and antibonding outer-plane bands, and SS is the superstructures.

- [1] J. M. Wheatley *et al.*, Nature **333** (1988) 121.
- [2] E. Pavarini *et al.*, Phys. Rev. Lett. **87** (2001) 047003.
- [3] S. Chakraverty *et al.*, Nature **428** (2004) 53.
- [4] S. Okamoto *et al.*, Phys. Rev. Lett. **101** (2008) 156401.
- [5] D. L. Feng *et al.*, Phys. Rev. Lett. **88** (2002) 107001.
- [6] T. Sato *et al.*, Phys. Rev. Lett. **91** (2003) 157003.
- [7] S. Ideta *et al.*, Phys. Rev. Lett. **104** (2010) 227001.
- [8] S. Ideta *et al.*, Phys. Rev. B **85** (2012) 104515.
- [9] S. Ideta *et al.*, Physica C **470** (2010) S14-S16.

BL1B

Terahertz Spectroscopy of Solid Acid Proton Conductor CsHSO₄ - CsH₂PO₄ Single Crystals

T. Awano

Faculty of Engineering, Tohoku Gakuin University, Tagajo 985-8537, Japan

Proton conductors are interested because of the use in fuel cells. Those in medium temperature are important for eco-system in house with high efficiency. Inorganic solid acids such as Cs₂(HSO₄)(H₂PO₄) crystal are newly discovered proton conductors in such medium temperature. Especially, this crystal keeps high ionic conductivity once after heating above 380 K. It is interesting to make clear the mechanism of such conductivity dependence on thermal history.

Meanwhile, terahertz spectral region is located between vibration and translation motion of the mobile ion. The “attempt mode” of conduction ion is also observed in superionic conducting crystals of silver, cuprous and alkali ions at the frequency as their atomic mass. This vibrational mode is directly connected with translational movement of conduction ion. Namely, the conduction ions surrounded by tetrahedral cage try to move out at this frequency.

Three methods have been reported for crystal growth of Cs₂(HSO₄)(H₂PO₄). Haile who discovered this compound obtained it from stoichiometric aqueous solutions of cesium carbonate, sulfuric acid and phosphate acid [1]. By this method, both of Cs₂(HSO₄)(H₂PO₄) and Cs₃(HSO₄)₂(H₂PO₄) are grown. Other two methods were used by some groups. The one is growth from stoichiometric aqueous solutions of CsHSO₄ and CsH₂PO₄ [2]. The other is growth from stoichiometric sulfuric acid solution of CsH₂PO₄ [3]. Cs₃(HSO₄)₂(H₂PO₄) also has superionic conducting phase at high temperatures [4]. The grown Cs₂(HSO₄)(H₂PO₄) and Cs₃(HSO₄)₂(H₂PO₄) single crystals were 0.2 mm × 2 mm × 6 mm and 5 mm × 8 mm × 15 mm in maximum size after one week growth, respectively.

Figure 1 shows reflectivity spectra of Cs₃(HSO₄)₂(H₂PO₄). Anisotropic peaks were observed as shown in the figure. The proton conduction assisted by hydrogen bond with rotating of SO₄ or PO₄ tetrahedron occur along *b*-axis of the crystal. Reflectivity increase at low wave number region at the *E*//*b* spectrum at 300 K seems to be due to the proton conduction.

Figure 2 shows reflectivity spectra of Cs₂(HSO₄)(H₂PO₄). Anisotropic peaks were observed also in these spectra, however, the difference was not so clear. Crystal structures of Cs₃(HSO₄)₂(H₂PO₄) and Cs₂(HSO₄)(H₂PO₄) are similar and corresponding peaks were observed. The high temperature phase is cubic and there was no difference with direction of electric field. Increase at low wave number was also observed at the 300 K spectrum.

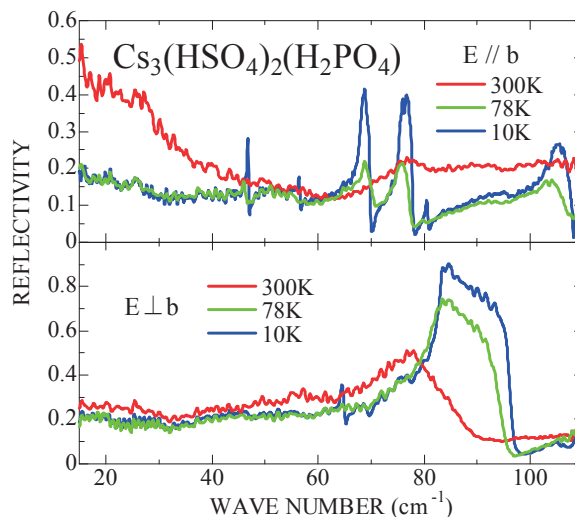


Fig. 1. Reflectivity spectra of Cs₃(HSO₄)₂(H₂PO₄) crystal from CsCO₃, H₂SO₄ and H₃PO₄.

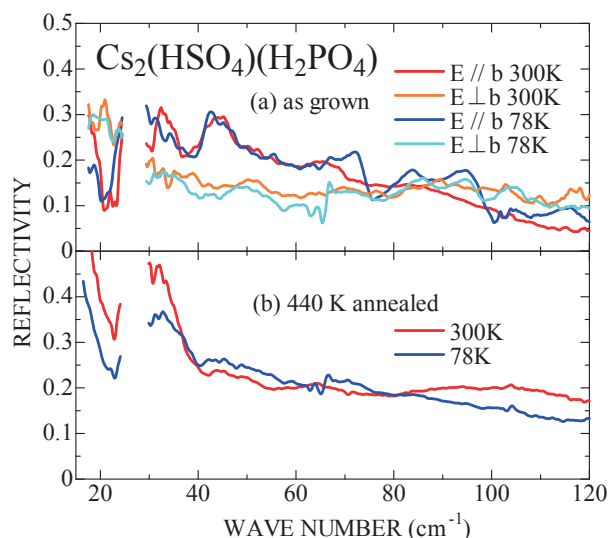


Fig. 2. Reflectivity spectra of Cs₂(HSO₄)(H₂PO₄) crystal from CsHSO₄ and CsH₂PO₄; (a) as grown (b) after heating at 440 K.

[1] C. R. I. Chisholm and S. M. Haile, *Acta Cryst. B* **55** (1999) 937.

[2] A. Matsuda, T. Kikuchi, K. Katagiri, H. Muto and M. Sakai, *Solid State Ionics* **177** (2006) 2421.

[3] Y. Yamane, K. Yamada and K. Inoue, *Solid State Ionics* **179** (2008) 483.

[4] S. M. Haile, G. Lentz, K.-D. Kreuer and M. Maier, *Solid State Ionics* **77** (1995) 128.

BL2B

Degradation of $\text{CH}_3\text{NH}_3\text{PbI}_3$ to PbI_2 Driven by Annealing in Vacuum

S. Tanaka¹, T. Kajikawa¹ and K. R. Koswattage²¹Graduate School of Science and Engineering, Kindai University, Osaka 577-0818, Japan²Center for Frontier Science, Chiba University, Chiba 263-8522, Japan

Organolead halide perovskites have recently emerged as a photovoltaic material for high-efficiency organic photovoltaic [1-3]. The organolead halide perovskites have the advantageous characteristics for the photovoltaics such as the direct bandgap near the visible region, the small electron/hole effective masses, the large absorption coefficients, and long diffusion length of excited carriers, etc. The power conversion efficiency (PCE) of the organic photovoltaic used perovskites is approaching the PCE of silicon solar cells. However, there are several problems for practical use of the perovskite solar cells. One of the problems is its stability. A prototype organolead halide $\text{CH}_3\text{NH}_3\text{PbI}_3$ (MAPbI₃) shows degradation to PbI_2 , a material has different electronic properties from those of the starting perovskite. As the degradation mechanisms of MAPbI₃, the chemical degradation through the interaction with water and the thermodynamic degradation through the creation of volatile molecular defects has been proposed [4]. In this report, we studied effect of the thermal annealing of MAPbI₃ on the electronic structure by using photoelectron spectroscopy to understand an impact of the decomposition of the perovskite structure.

Thin films of organolead halide perovskite MAPbI₃ were fabricated by the 2-step vapor deposition method at the Kindai University. As the first step, lead chloride (PbCl_2) was deposited on a pre-cleaned indium-tin-oxide substrate. Methylammonium iodide ($\text{CH}_3\text{NH}_3\text{I}$) was subsequently deposited on the PbCl_2 film as the second step. Upon $\text{CH}_3\text{NH}_3\text{I}$ deposition, PbCl_2 reacted with $\text{CH}_3\text{NH}_3\text{I}$ *in situ* and formed MAPbI₃ films. The fabricated samples were stored in dark, and transferred to the UVSOR BL2B. The samples were exposed in air before the photoelectron measurements. Hence the surface of samples would be partially degraded.

Figure 1 shows the photograph of the MAPbI₃ sample before and after annealing. The annealing treatment was performed in vacuum with a base pressure of 3×10^{-7} Pa. The annealing temperature and time were 140 °C and 10 min, respectively. During the annealing, the pressure was increased to 3×10^{-5} Pa. The red-brownish color of MAPbI₃ film was turned yellowish after the annealing treatment. This indicated the annealing treatment induced the degradation of MAPbI₃ to PbI_2 . The photoelectron spectra of before and after the annealing treatment were measured with the photon energy of 100 eV. The results are shown in Fig. 2. The secondary cutoff of the sample was shifted toward higher kinetic energies after annealing. On the other hand, the Pb 5*d* core-levels were shifted toward lower kinetic energies after annealing. The

photoelectron signal from I 4*d* core-levels were also shifted toward lower kinetic energies with same values by annealing. (not shown here) The valence band region showed slight changes of shape but no significant shift of the valence band edge position. However, the signal-to-noise ratio of the spectrum was not adequate to detailed discussions about the valence band region.

The coordination number of Pb ions in the MAPbI₃ lattice is 6 and is also maintained in the PbI_2 lattice. Therefore, it is expected that the chemical environment for Pb ions in MAPbI₃ are similar that in PbI_2 . Hence, the variation of kinetic energy of Pb 5*d* photoelectrons implies differences of the interaction from the surrounding molecules during the escape process. The shift toward the same direction of I 4*d* core-levels may also support this assumption. Further analysis of photoelectron spectra to understanding the effects of MAPbI₃ degradation is in progress.

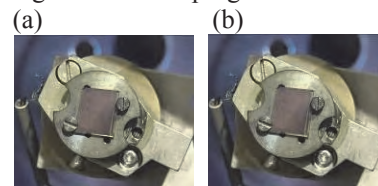


Fig. 1. Photograph of the $\text{CH}_3\text{NH}_3\text{PbI}_3$ thin film (a) before and (b) after annealing.

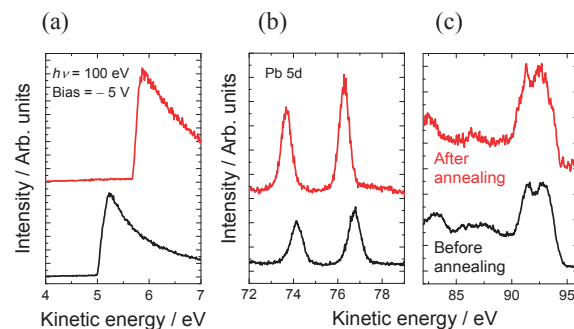


Fig. 2. Photoelectron spectra of (a) secondary electron cutoff, (b) Pb 5*d* and (c) valence band regions. Bias voltage of -5 V was applied for the secondary electron measurements. Black and red line are the photoelectron spectrum of before and after annealing treatment, respectively.

[1] A. Kojima *et al.*, *J. Am. Chem. Soc.* **131** (2009) 6050.

[2] M. M. Lee *et al.*, *Science* **338** (2012) 643.

[3] P. P. Boix *et al.*, *J. Phys. Chem. Lett.* **6** (2015) 898.

[4] I. Deretzi *et al.*, *Appl. Phys. Lett.* **106** (2015) 131904.

BL2A

Trial of Line Analysis for Si-Doped Porous Hydroxyapatite Prepared on Mg-Based Alloy

M. Sato¹, M. Togo² and A. Nakahira^{2,3}

¹Institute for Materials Research, Tohoku University, Sendai 980-8577, Japan

²Graduate school of Engineering, Osaka Prefecture University, Sakai 599-8531, Japan

³Kansai Center for Industrial Materials Research, Tohoku University, Sakai 599-8531, Japan

Hydroxyapatite (HAp) has been widely used as alternate materials our hard tissue due to its excellent biocompatibility and osteo-conductivity. In addition, HAp also has protein absorption ability and ion-exchange ability. On the basis of these properties, we have prepared the functional element-doped HAp such as Mg, Si, Fe, Cu, and Ag by conventional wet process so far and investigated the effect of addition of those elements on generation phase, microstructure, and other properties. Since HAp powders are usually coating on the surface of implant in a practical use, structural investigation of these interface is important in order to perform of its full potential as artificial hard tissue. Hydrothermal Hot Press (HHP) is unique technique to obtain HAp bulk sample having a porous structure [1]. This porous structure has many advantages for bone formation. In this study, Si-doped HAp was grafted with AZ-31 (Mg-3Al-1Zn) alloy by HHP method, and elution behavior of Mg ion from AZ-31 substrate toward a HAp phase was investigated by XAFS measurement.

First of all, Si-doped amorphous calcium phosphate (ACP) powder was prepared by sol-gel method using calcium metal, tetraethyl orthosilicate (TEOS), phosphoric acid and ethanol at 273 K. Since the Ca/P ratio of obtained ACP powder is usually around 1.5, the obtained Si-doped ACP and Ca(OH)₂ powders were mixed so that their (Ca+Si)/P ratio is 1.67. And then, Si-doped HAp bulk sample was prepared on AZ-31 alloy by hydrothermal hot press method at 423 K for 2h. In order to obtain the interface information, obtained bulk sample was cut and polished, and synchrotron beam was irradiated respectively at the substrate, the interface and the HAp phase by changing a measurement position of sample. The Si K-edge and Mg K-edge XANES spectra for obtained bulk sample were corrected by fluorescence method using InSb and Beryl double crystal monochrometer and silicon drift detector (SDD) at BL2A in UVSOR, respectively. Figure 1 shows Si K-edge XANES spectra of Si-HAp prepared by HHP process obtained from interface and HAp phase. The obtained XANES spectra did not change by the obtaining position and resembled to that of calculated spectrum. This result indicate that the added Si ion exist into HAp structure and Si doped HAp bulk sample had been obtained by HHP technique. Moreover the shape of spectrum did not change by correcting position.

Figure 2 shows Mg K-edge XANES spectra of sample obtained at different position. Obtained

XANES spectra changed by changing the position, and that obtained from HAp phase showed similar spectrum to calculated spectra. This result indicates that the Mg ion eluted from substrate during HHP process forms a solid solution with HAp structure. In addition, spectrum obtained from near-interface has similar trend to that of Mg(OH)₂. From this result, it is suggested that the local structure around Mg atom changes gradually toward the HAp phase from substrate.

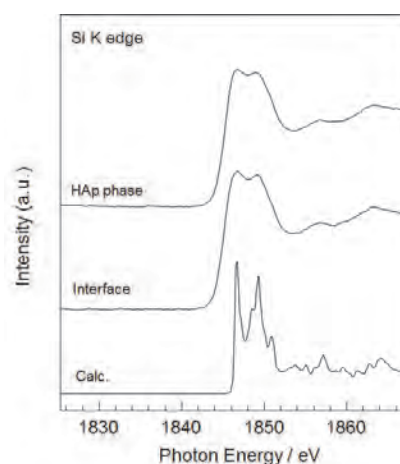


Fig. 1. Si K-edge XANES spectra of samples.

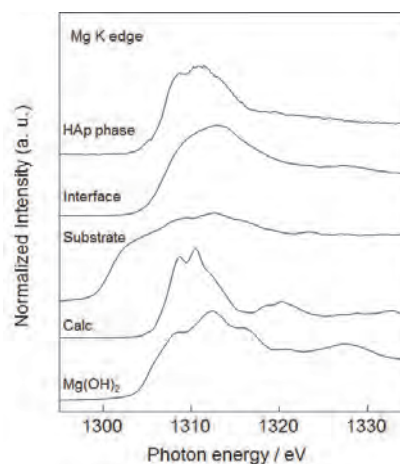


Fig. 2. Mg K-edge XANES spectra of samples.

[1] T. Onoki, S. Yamamoto, H. Onodera and A. Nakahira: Mater. Sci. Eng. C **31** (2011) 499.

BL2A

Mo L-Edge XANES Study on the Formation of Catalytically Active Mo Carbide Species on H-MFI for MTB Catalysts

H. Aritani¹, S. Mogi¹, N. Naijo¹, T. Sugawara¹, M. Akutsu¹, K. Kawashima¹ and A. Nakahira³

¹Graduate School of Engineering, Saitama Institute of Technology, Fukaya 369-0293 Japan

²Advanced Science Research Laboratory, Saitama Institute of Technology, Fukaya 369-0293 Japan

³Graduate School of Engineering, Osaka Prefecture University, Sakai 599-8531 Japan

MTB (Methane To Benzene) reaction is one of a revolutionary process for direct conversion of natural gas to petroleum compounds, *i.e.*, from methane to benzene. Mo-modified H-MFI is a typical catalyst with high activity for MTB. During the methane dehydroaromatization, Mo₂C-like active carbide species are formed on H-MFI catalysts. However, deactivation of MTB reactivity can not be avoided because of carbon contamination due to excess dehydrogenation of methane. In this case, structural change of active Mo species should occur during the deactivation [1]. For highly active and durable reactivity for MTB reaction, detail of local structure of active Mo species and their structural changes needs to be characterized. In the present study, Mo L_{III}-edge XANES study has been applied to characterize the active Mo species on H-MFI during the MTB reaction.

Catalyst samples were prepared by impregnation of each H-GaAlMFI (Si/Al₂=40) support with MoO₂(acac)₂-VO(C₃H₇O₂)₃-CHCl₃ solution (5wt% as MoO₃), and followed by dried and calcined at 773 K. The H-GaAlMFI (Al/Ga=100) supports were synthesized hydrothermally at 413 K for a week, and followed by ion-exchanging with NH₄Cl and calcined at 873 K. The catalytic MTB reactivity was evaluated by means of fixed-bed flow reaction at 1023 K, as described in a separate paper [1]. Mo L_{III}-edge XANES spectra were measured in BL2A of UVSOR-IMS in a total-electron yield mode using InSb double-crystal monochromator. Photon energy was calibrated by using Mo metal-foil. REX-2000 (Rigaku Co.) software was used for normalization of each XANES spectrum.

In our previous study, Mo-V (Mo/V=40) co-modified H-GaAlMFI (Al/Ga=100) catalyst shows higher activity and lower deactivation rate than Mo/H-MFI. In the case of Mo/H-MFI, partially carbonized Mo (Mo²⁺ and Mo⁴⁺) species can be seen after CO pretreatment. Figure 1 shows the L_{III}-XANES spectra of reduced MoO₂ by CH₄(10-20%)-H₂ treatment at 973 K. Metallic Mo are formed, as well as the reduction with H₂. In this case, formation of Mo-carbide species such as Mo₂C can not be seen. In contrast, Mo₂C-like carbide species seems to be formed on the Mo-V/H-GaAlMFI catalyst by CO(2%)-H₂ treatment at 1023 K, as shown in Fig. 2. It suggests that Mo₂C-like carbide species are formed before the MTB reaction by CO pretreatment. After the MTB reaction, metallic Mo species are also seen during the reaction for 10-200 minutes. For Mo/H-MFI, formation of α-Mo₂C species

is remarkable during the MTB reaction after 60 minutes. These results indicate that formation of α-Mo₂C species relates to the deactivation, and inhibition of the carbonization is effective for high and durable MTB reactivity.

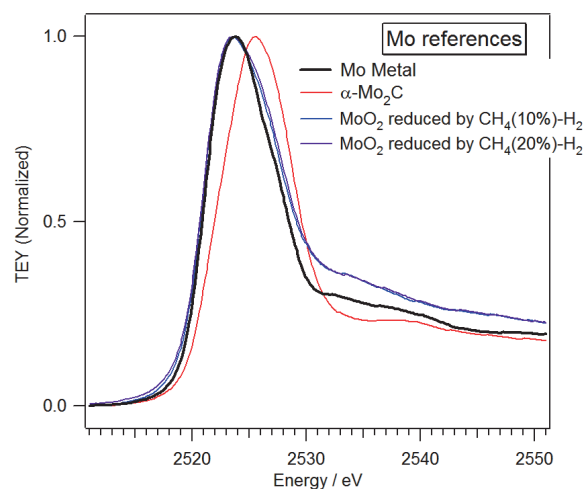


Fig. 1. Mo L_{III}-edge XANES of reference Mo compounds (Mo metal and α-Mo₂C) and reduced MoO₂ with CH₄-H₂ atmosphere at 973 K.

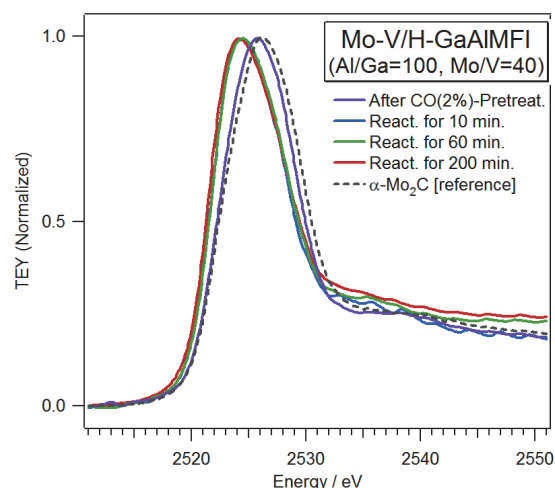


Fig. 2. Mo L_{III}-edge XANES of Mo-V/H-GaAlMFI catalysts after MTB reaction for 0-200 minutes at 1023 K.

[1] H. Aritani, H. Shibasaki, H. Orihara and A. Nakahira, *J. Environm. Sci.* **21** (2009) 736.

BL2A

X-Ray Absorption Near-Edge Structure Analysis of Yb Ions in Er-Doped CaZrO_3

A. Kanemoto¹ and T. Yamamoto^{1,2}¹Faculty of Science and Engineering, Waseda University, Tokyo 169-8555, Japan²Institute of Condensed-Matter Science, Waseda University, Tokyo 169-8555, Japan

Phosphor materials have been extensively studied because of their importance in industrial applications. Among them, rare-earth doped oxides with perovskite structures are very attractive inorganic phosphors, because of their luminescence efficiency and stability. In addition to such conventional phosphors, upconversion type phosphors, which can emit photons with higher energy (shorter wavelength) by irradiation of lower energy (longer wavelength) photons, have been also actively investigated. It was reported that Er doped CaZrO_3 shows such upconversion luminescence by irradiation of approx. 1000 nm photons to produce green emissions and additional Yb doping enhances luminescence intensity of Er-doped CaZrO_3 [1]. In order to understand the upconversion mechanism and the reason why Yb doping could enhance emission intensity, it is essential to know local environment of Yb ions in Er-doped CaZrO_3 . In the current study, we tried to analyze electronic structure of dilute Yb ions in Er-doped CaZrO_3 by Yb-M X-ray absorption near-edge structure (XANES) measurements.

Samples were synthesized by the solid state reaction method. Reagent grade high purity powders of CaCO_3 , ZrO_2 , Er_2O_3 and Yb_2O_3 were weighed changing the concentration of Yb ions. These powders were mixed and ground in an agate mortar for 30 min, which were pressed into pellet form. Resultant pellets were sintered in air at 1673 K for 6 hrs.

Crystal structure of the synthesized specimens was examined by powder X-ray diffraction. Although tiny amount of secondary phases appears, majority of the sample specimens could be determined to be crystallized in orthorhombic perovskite structured CaZrO_3 .

Yb-M XANES measurements were performed at BL2A of UVSOR. Incident beams were monochromatized with InSb double-crystal monochrometer. Sample powders were placed upon the carbon adhesive tape, which are attached on first Cu-Be dinode of the electron multiplier.

Observed Yb-M₅ XANES spectra of Yb codoped Er- CaZrO_3 were compared with that of Yb_2O_3 , which are shown in Fig. 1. As shown in this figure, fine structures of Yb-M₅ XANES spectra of the samples here synthesized, i.e., Yb doped CaZrO_3 :Er, are almost identical without any dependencies upon concentration of Yb ions in Er-doped CaZrO_3 . In addition, those show similar profiles as that of Yb_2O_3 . Hence it can be concluded that the doped Yb ions are trivalent state from the current XANES analysis.

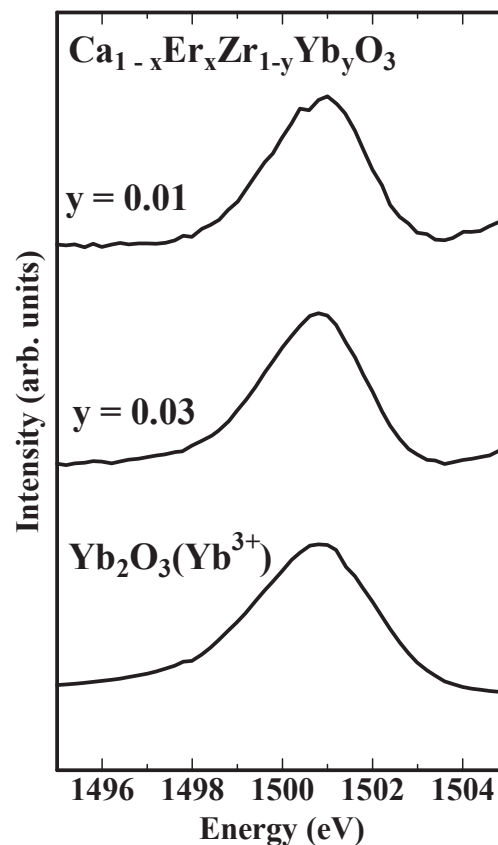


Fig. 1. Observed Yb-M₅ XANES spectra of Yb-doped CaZrO_3 :Er and that of Yb_2O_3 .

[1] V. Singh *et al.*, J. Appl. Phys. **112** (2012) 063105.

BL2A

Structural Evaluation of AlPO-5 Synthesized by Hydrothermal Process with XAFS

A. Nakahira^{1,2}, M. Togo¹, H. Takahashi¹, K. Yoshikawa¹, M. Sato³ and H. Aritani⁴

¹Faculty of Engineering, Osaka Prefecture University, Sakai 599-8531, Japan

²Kansai Center, IMR, Tohoku University, Sakai 599-8531, Japan

³Institute of Materials Research, Tohoku University, Sendai 980-8577, Japan

⁴Saitama Institute of Technology, Fukaya 369-0293, Japan

ALPO-5 is one of the most popular aluminum phosphates (AlPO_4), although there are many of aluminum phosphate, generically known as "AlPO-n". These aluminum phosphates, AlPO-n, have the unique framework structures similar to zeolites. Also, they have unique microporous structures and are expected to be used as a catalyst and a molecular sieve [1-2]. Recently these microporous aluminum phosphates have attracted much attention, because AlPO-n framework can be incorporated with cationic species from monovalent to pentavalent. Also, the syntheses of heteroatom-doped AlPO-n were attempted to modify the microporous structures and enhance their properties through a variety of processing. For example, molecular-sieve catalysts of AlPO are significantly useful for the selective oxidation of linear alkanes, such as the catalytic oxidation in air of cyclohexane [3]. In this study, AlPO-5 were focused on among AlPO-n families. In special, the synthesis for AlPO-5 was attempted by hydrothermal process and the structural evaluations were carried out for samples by hydrothermal process.

AlPO-5 were synthesized by the hydrothermal method. $\text{Al}(\text{OH})_3$ and aluminum alkoxide as an aluminum source and phosphoric acid as a phosphorus source were used. Furthermore, TEAOH (tetraethylammonium hydroxide) were used as an organic template. The molar composition of the hydrothermal synthesis materials was $\text{Al}:\text{P}:\text{TEAOH}:\text{H}_2\text{O} = 2:2:\text{X}:250$ ($\text{X}=3\sim 6$).

These starting reagents were mixed under magnetic stirring and pH was maintained to be pH3 with H_2SO_4 solution. After aging for 1h, starting materials solutions were transferred into teflon-lined stainless steel autoclave and carried out by the hydrothermal treatment at 423 K to 463 K for 0 h to 48 h. After the hydrothermal treatments, obtained samples were collected with Buchner filter and washed with sufficient deionized water. And after drying at 323 K overnight, samples were crushed with agate mortar. The dried samples were characterized by X-ray diffraction analysis (XRD) and FT-IR and TG-DTA. Microstructures were observed with FE-SEM. The local structures around Al-K for the obtained products were characterized by measuring X-ray adsorption near edge structure (XANES) at BL2A in UVSOR.

Various aluminum phosphates were synthesized though hydrothermal treatment under a variety of

hydrothermal conditions (hydrothermal temperatures, synthetic time, various pressures, and various starting materials).

The evaluation of X-ray diffraction analysis revealed that products obtained by the hydrothermal process at 443 K for 12 h to 48 h were identified to be crystalline AlPO-5 without another phase. SEM observation showed that products were rectangular with approximately 5 μm in length and 500 nm in diameter. Figure 1 shows the results of Al-K XANES spectra of AlPO-5 samples synthesized by the hydrothermal treatment for 0 h to 12 h. From these results, the local structure of Al-K XANES for AlPO-5 synthesized by the hydrothermal treatment for 12 h was different from ones for AlPO-5 samples synthesized by the hydrothermal treatment for 0 h to 8 h, suggesting that AlPO-5 local-structure was successfully synthesized by the hydrothermal treatment for 12 h.

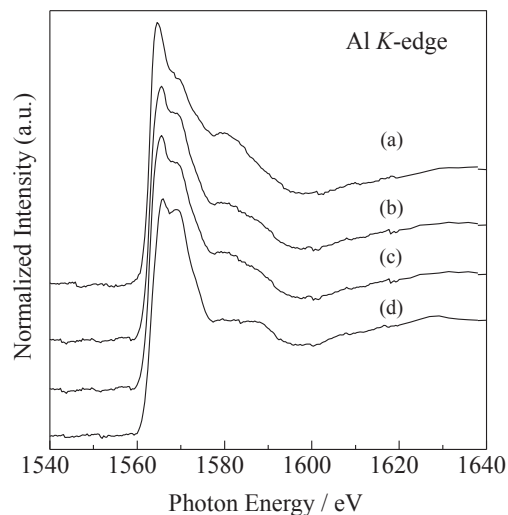


Fig. 1. Al-K XANES spectra of AlPO-5 synthesized by the hydrothermal treatment for 0 h to 48 h. (a) 0h, (b) 4h, (c) 8h, and (d) 12h.

[1] D. R. Pyke, P. Whitney, and H. Houghton, *Applied Catalysis*, **18** (1985) 173.

[2] D. Li, J. Yao and H. Wang, *Progress in Natural Science: Materials International* **22** (2012) 684.

[3] J. M. Thomas, R. Raja, G. Sankar and R. G. Bell, *Nature* **398** (1999) 27.

BL2A

In Situ Observation of the Dielectric Breakdown of Insulating Material Using Soft X-Ray Absorption Spectroscopy

E. Kobayashi¹, K. K. Bando², K. K. Okudaira³ and T. Okajima¹

¹Kyushu Synchrotron Light Research Center, Tosu, 841-0005, Japan

²National Institute of Advanced Industrial Science and Technology, Tsukuba, 305-8565, Japan

³Chiba University, Chiba, 263-8522, Japan

Insulating materials are used in various parts of electric device. In recent years, it has become necessary to develop excellent insulating material with improvement in performance. In this study, the electronic state on aluminum oxide thin film under voltage applied conditions was studied by using near-edge X-ray absorption fine structure (NEXAFS). Aluminum oxide is recognized as an important material because it is the prototype of wide-gap insulator. The elementary processes of dielectric breakdown of insulating materials are not understood very well from a microscopic point of view.

An alumina film was made on a polished stainless steel plate by dip-coating with a diluted alumina sol (Kawaken Fine Chemicals, F1000). The coated plate was dried at 333 K, 6 hours and calcined at 573 K, 3 hours in an oven.

Al *K*-edge NEXAFS spectra of aluminum oxide thin film were measured at the beamline 2A of the UVSOR. The experimental setup for NEXAFS measurement is shown in Fig. 1. The soft x-ray was passed through a metal mesh and was irradiated to the sample. The fluorescence from sample was detected by silicon drift detectors. Potential of the sample was applied between the metal mesh and metal plate. All experiments were performed at room temperature.

Figure 2 shows the Al *K*-edge NEXAFS spectra of aluminum oxide obtained from PFY mode at various applied voltage. The spectra were measured while applying a voltage. This sample was breakdown at ~ 14 V. After breakdown, the potential to the sample could not be applied. These spectral features are almost same. And the spectra show two strong peaks at around 1569 eV and 1572 eV, respectively. These spectral features are also different from those of Al₂O₃ powder [1]. This indicates the local structure of Al in aluminum oxide thin film using in this study is different from those in Al₂O₃ crystal.

Inset of the Fig. 2 shows the expanded spectra at rising part of the spectra. The spectra with under applied voltages of 8 V show little energy shift. But the spectra at over 9.9 V are shifted slightly to the low energy side. Then, the spectrum after the breakdown was shifted significantly to the low energy side. This trend was also observed for an aluminum oxide thin film calcined at 473 K.

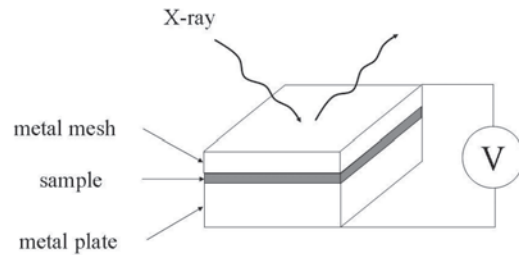


Fig. 1. Experimental setup.

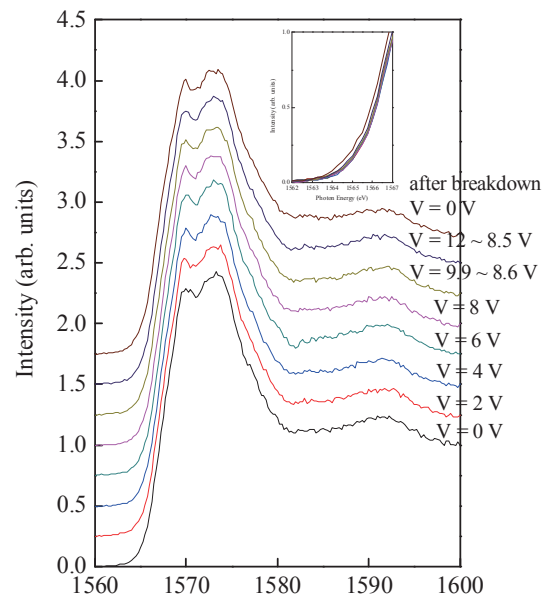


Fig. 2. Al *K*-edge NEXAFS spectra of aluminum oxide thin film obtained from PFY mode at various applied voltage.

[1] M. Mogi *et al.*, Mat. Trans. **45** (2004) 2031.

BL3B

Material Dependence of Multiple Luminescence from Self-Trapped Excitons in Orthoborates with Complex Oxoanions upon Vacuum UV Excitation

N. Kodama, K. Yanagidaira, M. Kudo and T. Takahashi

Graduate School of Engineering and Resource Science, Akita University, Akita 010-8502, Japan

We report the temperature and material dependence of multiple intrinsic luminescence spectra from self-trapped excitons (STEs) in the three low-symmetry orthoborates with complex oxoanions: $\text{LaSc}_3(\text{BO}_3)_4$ (LSB), $\text{Ca}_4\text{LaO}(\text{BO}_3)_3$ (CLOB), and $\text{YSc}(\text{BO}_3)_2$ (YSB). Furthermore, we examine the possibility of generating “multiple self-trapped excitons” (MSTE) in LSB, CLOB, and YSB crystals upon excitation by photons with more than twice the band gap energy, on the basis of STE excitation spectra in the VUV region.

Absorption spectrum of an LSB single crystal is shown in Figure 1. The absorption increased rapidly below about 200 nm. This result indicates that the band edge of LSB is around 200 nm. Moreover, the rise wavelength (rising) of absorption was in agreement with that of excitation. On the basis of this result, the rises around 200 nm were assigned to the band edges of LCOB and YSB, similar to that of LSB.

Figures 2(a), 2(b), and 2(c) show the temperature dependence of the intrinsic luminescence spectra for LSB, LCOB, and YSB, respectively, at 11 or 8 K. The luminescence spectra exhibited multiple bands of STE(I) and (II) (and/or (III)) for LSB, LCOB, and YSB, respectively, located at energies corresponding to the STE bands. The luminescence spectra for LSB under VUV excitation contained three distinct broad bands associated with STE(I), (II), and (III), with peaks at 245–272 nm, 311–320 nm, and 386–389 nm, respectively, in the range of 11–293 K, as shown in Fig. 1(a). For CLOB and LSB, three distinct broad bands (two weak bands and one intense band) appeared. These bands are associated with STE(I), (II), and (III), with peaks at 245–273 nm, 326–328 nm, and 410–413 nm, respectively, in the range of 8–293 K, as shown in Fig. 2(b). YSB exhibited one intense broad emission band, with the shortest wavelength of the three samples, associated with STE(I) with a peak at 247–254 nm, and another broad band associated with STE(II) with a peak at 290–296 nm in the range of 8–293 K.

As the STE(I) emission intensity decreased in LSB and YSB, the STE(II) and STE(III) emission intensities increased. This suggests that there are multiple (three in LSB, two in YSB) local minima on the adiabatic potential energy surfaces, i.e., barriers for exciton self-trapping in LSB and YSB.

The decay times for the luminescence in LSB at 78 K were 20 ns for STE(I), 230 ns and 4.5 μs for STE(II), and 7.4 μs for STE(III). The decay times for the luminescence in CLOB at 78 K were 24 ns for STE(I), 540 ns and 2.0 μs for STE(II), and 6.0 μs for STE(III). For YSB, the decay times for STE(I) and (II) luminescence at 293 K were 23 and 643 ns, respectively. Taking into account the above results, the site symmetry of the BO_3^{3-} oxoanion group, and the B-O bond length, we considered the structures and spin states of the STEs in LSB, CLOB, and YSB crystals. The existence of multiple stable structures and spin states for STEs in these crystals can be inferred from the temperature dependence of the intensities and

decay times of the STE luminescence, as follows. The fast decay components of STE(I) and STE(II) in LSB and CLOB and the fast component of STE(I) in YSB originate from singlet STE states in the BO_3^{3-} group with C_1 or C_s symmetry, respectively. In contrast, the slow components of STE(II) and STE(III) in LSB have been ascribed to a triplet STE with C_1 symmetry and those of CLOB have been ascribed to a triplet STE with C_s symmetry. Furthermore, the slow component of STE(II) in YSB is thought to originate from a triplet STE with C_1 symmetry.

The excitation spectra of LSB, CLOB, and YSB shown in Figs. 3(a), (b), and (c), measured at 293 K, 8 K, and 293 K, respectively, were detected at various fixed wavelengths. The excitation spectra of LSB increased stepwise in intensity with increasing excitation energy; that is, with decreasing excitation wavelength. The features of the excitation spectra below the band edge are very similar to those of CLOB and YSB. The excitation intensities at 90 nm for LSB, LCOB, and YSB were two to five times greater than at 180 nm, near the band edge. These results suggest that two or more electron-hole pairs are produced from one absorbed photon when excited by photons with

energies greater than or equal to twice the band gap energy; that is, it may be possible to generate double- or multiple-self-trapped excitons (double- or multiple-STEs) in LSB, CLOB, and YSB.

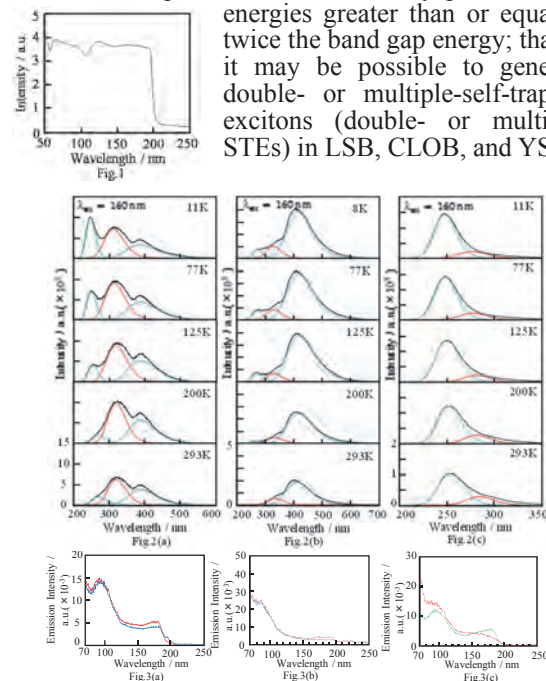


Fig. 1. The absorption spectrum of an LSB single crystal at 293 K.

Fig. 2. Temperature dependence of intrinsic luminescence spectra in (a) LSB, (b) CLOB, and (c) YSB in the range of 11(8)–293 K.

Fig. 3. Excitation spectra obtained by monitoring the intensity of the intrinsic luminescence at different fixed wavelengths in (a) LSB at 293 K, (b) CLOB at 8 K, and (c) YSB at 293 K.

BL3B

Transmittance Spectra and Other Properties of Metal Elements Doped LiCaAlF₆ Single Crystals

C. Tanaka¹, S. Kurosawa², Y. Yokota², A. Yamaji¹, R. Murakami¹, T. Horiai¹, H. Chiba¹, Y. Ohashi¹, K. Kamada^{2,3} and A. Yoshikawa^{1,2,3}

¹Institute for Materials Research, Tohoku University, Sendai 980-8577, Japan

²New Industry Creation Hatchery Center (NICHe), Tohoku University, Sendai 980-0845, Japan

³C&A corporation, Sendai 980-8579, Japan

Neutron detectors using neutron scintillators have been investigated to find their application in the homeland security scanning. A ³He-gas proportional counter has been used widely as a conventional sensor for the thermal neutron detection due to the high capture cross-section for the thermal neutrons and the low sensitivity to γ -rays. However, the importance of alternative neutron detectors such as scintillators has increased due to the supply crisis of ³He gas by the excessive demand. Therefore, the neutron scintillators have become gradually of interest as an alternative for the ³He gas.

In the search for novel neutron scintillators, we have developed a LiCaAlF₆ (LiCAF) scintillator crystal containing ⁶Li with the high capture cross-section for the thermal neutrons. In addition, the effective atomic number and density of the LiCAF are relatively low which results in the desired small detection efficiency for γ -ray.

The ns²-type cations such as In⁺ and Pb²⁺ are expected to show luminescence. In this study, we grew LiCAF crystals doped by the ns²-type elements and investigated their properties to obtain a new candidate for the doping ion in the LiCAF crystal.

Non-doped and In, Pb-doped LiCAF crystals with the diameter of 2 mm were grown by a micro-pulling-down (μ -PD) method. We measured transmittance spectra of the polished specimens of non-doped and In, Pb doped LiCAF by the SI-Photodetector (AXUV 100 (IRD)) in the wavelength range from 80 to 300 nm at liquid helium temperature at BL3 of UVSOR.

Transmittance spectra of the Non-doped and In, Pb doped LiCAF are shown in Fig. 1. The spectrum of In-doped LiCAF has no remarkable difference from non-doped one except for the onset of the transmittance drop near the band-edge which is shifted towards longer wavelengths. This may be caused by some defects created by the doping. In the transmittance spectra of Pb doped LiCAF specimen an intense absorption peak was observed at 196 nm followed by other absorption peaks at shorter wavelengths and the band edge of LiCAF host at about 115 nm. Absorption peaks at 196 and 135 nm could be ascribed to the so called A and C absorption bands of the Pb²⁺ center [1].

Radioluminescence spectra of non-doped and Pb doped LiCAF crystals under X-ray irradiation were measured at RT. The emission peaks around 290, 380 and 510 nm were observed for non-doped LiCAF

crystal, and were ascribed to self-trapped and trapped exciton [2]. In this wavelength region, an emission peak around 205-210 nm was observed and ascribed to Pb²⁺ center consistently with the previous report about the Pb doped LiCAF crystal [3]. In addition, we revealed that there was another emission peak around 830 nm in the long wavelength region. This emission peak can originate from defect in the structure due to nonstoichiometry of LiCAF lattice caused by Pb evaporation, or Pb⁺ center like in the LiBaF₃ lattice which has the emission around 880 nm in [4].

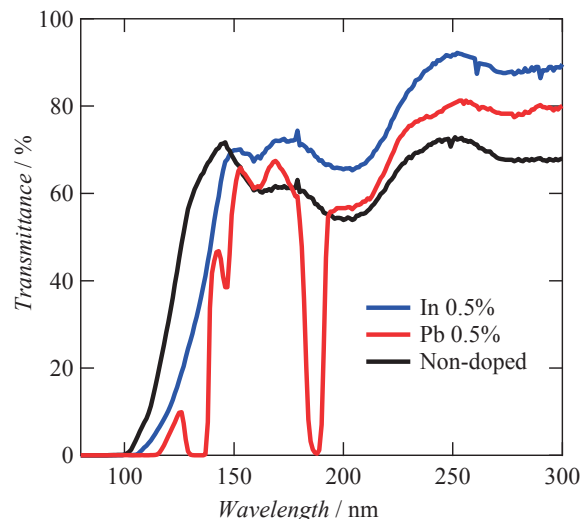


Fig. 1. Transmittance spectra of non-doped and In, Pb doped LiCAF in 80 – 300 nm at liquid helium temperature.

- [1] P. W. M. Jacobs, J. Phys. Chem. Solids **52** (1991) 35.
- [2] M. True, Y. Chen, M. Kirm, S. Vielhauer and G. Zimmerer, J. Lumin. **124** (2007) 279.
- [3] A. Novoselov, J. Pejchal, M. Nikl and A. Yoshikawa, Nucl. Sci. Symp. Conf. Rec. **N45-7** (2007) 2184.
- [4] L. Prado, N. D. Vieira Jr, S. L. Baldochi, S. P. Morato, J. P. Denis, N. Tercier and B. Blanzat, J. Phys. Chem Solids **57** (1996) 413

BL3B

Charge Transfer Luminescence of Ce-Doped and Undoped Ytterbium Pyrosilicate

T. Horiai¹, S. Kurosawa², R. Murakami¹, A. Yamaji¹, Y. Shoji^{1,3}, J. Pejchal⁴, Y. Ohashi^{1,3}, K. Kamada^{2,3}, Y. Yokota² and A. Yoshikawa^{1,2,3}

¹Institute for Materials Research, Tohoku University, Sendai 980-8577, Japan

²New Industry Creation Hatchery Center (NICHe), Tohoku University, Sendai 980-8579, Japan

³C&A Corporation, Sendai 980-8579, Japan

⁴Institute of Physics CAS, Cukrovamicka 10, Prague, 162 00, Czech Republic

Charge transfer (CT) luminescence of Yb^{3+} can have fast scintillation decay time, and such scintillation materials are expected to be applied to medical imaging. In previous study, the charge transfer luminescence of Ce-doped Yb_2SiO_5 was evaluated, and the intensity became highest at near 40 K [1,2]. In this study, we search the CT luminescence for pyrosilicate group as the first step.

We prepared Ce-doped and undoped $\text{Yb}_2\text{Si}_2\text{O}_7$ single crystals grown by the micro-pulling-down method, and photoluminescence spectra for these samples were evaluated within 7.5-300 K at BL3 of UVSOR. The emission spectra were examined with a spectrometer (spectropro-300i, Acton research).

Figures 1 and 2 shown the temperature dependences of the PL emission spectra for the undoped and Ce-doped $\text{Yb}_2\text{Si}_2\text{O}_7$ single crystals under 210 nm excitation in the temperature range of 7.5-300K, respectively. Since absorption edge was around 230 nm, the 210 nm photons were selected as an excitation source. Moreover, variations of the excitation wavelengths demonstrated that the strongest emission was observed at 210 nm excitation.

The undoped $\text{Yb}_2\text{Si}_2\text{O}_7$ had emission peaks at around 420 and 580 nm. The intensity of the 420 nm emission band was degraded when temperature of the specimen exceeded 100K, while that of the 580 nm band remained almost constant and independent on temperature. Thus, 420 nm band would be originated by CT system to ${}^2\text{F}_{5/2}$ of Yb^{3+} , and thermal quenching was observed. On the other hand, the emission at 580 nm may originate from defects.

Oppositely, the intensity of the 420 nm emission band of the Ce-doped $\text{Yb}_2\text{Si}_2\text{O}_7$ increased when temperature of the specimen became higher. Mainly this peak was assigned to Ce^{3+} 5d-4f emission, and CTS to ${}^2\text{F}_{5/2}$ of Yb^{3+} components can be included. 580 nm emission peak was also observed in the PL spectra of Ce-doped $\text{Yb}_2\text{Si}_2\text{O}_7$, while this emission was suppressed at RT. Moreover, from 200 to 300 K, Ce^{3+} emission intensity increased. Thus, the electron can be re-trapped into Ce^{3+} absorption band, and this result suggested energy transfer from this defect site to Ce^{3+} .

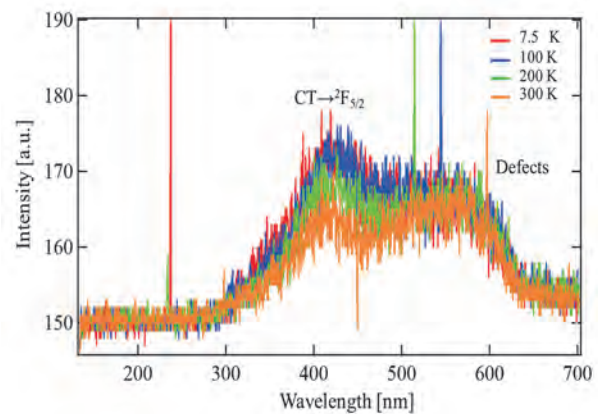


Fig. 1. The photoluminescence of undoped YbPS excited by 210 nm within 7.5-300 K.

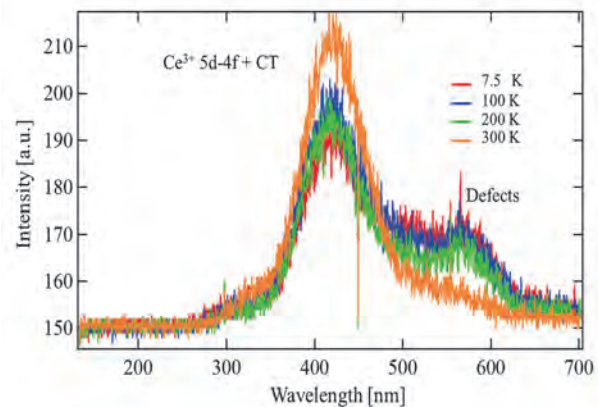


Fig. 2. The photoluminescence of Ce-doped YbPS excited by 210 nm within 7.5-300 K.

[1] L. V. Pieterse *et al.*, *J. Luminescence* **91** (2000) 177.

[2] D. W. Cook *et al.*, *J. Luminescence* **79** (1998) 185.

BL3B

Evaluation of the Bandgap Energies for Garnet-Type Infra-Red Scintillators

A. Yamaji¹, S. Kurosawa^{1,2}, R. Murakami¹, T. Horiai¹, M. Kitaura³, Y. Ohashi¹, K. Kamada², Y. Yokota², A. Ohnishi³ and A. Yoshikawa^{1,2}

¹ Institute for Materials Research, Tohoku University, Sendai 980-8577, Japan

² New Industry Creation Hatchery Center, Tohoku University, Sendai 980-8579, Japan

³ Yamagata University, Yamagata 990-8560, Japan

Inorganic scintillator crystals have been widely used for radiation detection such as high energy physics, security applications and medical imaging. Recently, we have studied the real-time dose monitor system during the radiation therapy using scintillator with infrared emission. Radiation therapy is one of the primary treatments of tumor; however, radiation overdoses which cause medical accidents or underdoses which cause incomplete treatments have often been reported. Thus, real-time dose monitoring systems are required.

One of the concepts for the monitoring is the use of a 2-3 mm size scintillator material in the irradiated area (tumor) in the patient's body [1]. When the scintillator is irradiated with the incident X-rays, the intensity of the scintillation light give us information related to the dose in real time. Since human body had a low absorption region from approximately 700-1400 nm [2], scintillator with near infrared emission could be applied in the real time dose monitor system. Thus, we have investigated the optical and scintillation properties of some materials in the near infra-red region.

In this work, we grew garnet-type oxide crystals for scintillators with near infrared emission and evaluated their optical properties. Since the light yield depends on the band gap energy of a host crystal, we estimated the band-gap energies of the studied crystals. Band gap measurement is useful for the material design of scintillator.

The crystal growth of garnet-type oxide crystals were performed from the melt by the micro pulling down method using an Ir crucible with a radio frequency heating system. Nominal compositions of grown crystals were $Gd_3Ga_5O_{12}$ (GGG), $Lu_3Ga_5O_{12}$ (LGG), $Y_3Ga_5O_{12}$ (YGG) and $(Gd_{0.9}M_{0.1})_3Ga_{4.7}M'_{0.3}O_{12}$ ($M = Mg, Ca, Sr$ and Ba , $M' = Zr, Hf$), respectively. The crystals were mechanically polished to the 1 mm thickness.

Transmittance spectra were measured at the beam line BL3B at the UVSOR facility; The specimens were glued on holes (1.5 mm diameter) of a copper plate with a silver paste (Fujikura Kasei, DOTITE D-550), and their temperature was kept at 8 K with liquid helium in order to suppress lattice vibrations. Transmitted light was detected with a silicon photodetector (IRD, AXUV 100).

The transmittance spectra were obtained as shown

in Fig.1. Band gap energies were estimated from the absorption edges of these transmittance spectra. The calculated bandgaps are listed in table 1. These results contribute to the material design of scintillator with near infrared emission

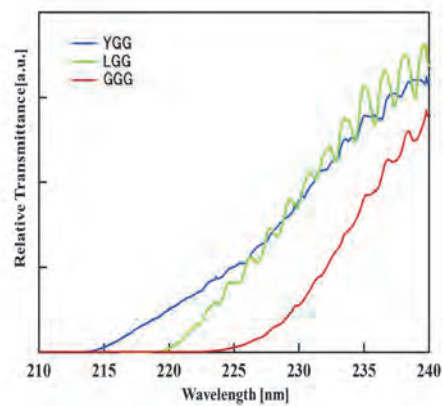


Fig. 1. Transmittance spectra of YGG, LGG and GGG crystals at 8 K.

Table 1. Bandgaps of garnet-type oxide crystals.

	Absorption band [nm]	Band gap [eV]
$Gd_3Ga_5O_{12}$	223	5.4
$Lu_3Ga_5O_{12}$	219	5.8
$Y_3Ga_5O_{12}$	214	5.7
$(Gd_{0.9}Mg_{0.1})_3Ga_{4.7}Zr_{0.3}O_{12}$	235	5.2
$(Gd_{0.9}Ca_{0.1})_3Ga_{4.7}Zr_{0.3}O_{12}$	236	4.9
$(Gd_{0.9}Sr_{0.1})_3Ga_{4.7}Zr_{0.3}O_{12}$	248	4.7
$(Gd_{0.9}Ba_{0.1})_3Ga_{4.7}Zr_{0.3}O_{12}$	254	4.6
$(Gd_{0.9}Mg_{0.1})_3Ga_{4.7}Hf_{0.3}O_{12}$	235	5.2
$(Gd_{0.9}Ca_{0.1})_3Ga_{4.7}Hf_{0.3}O_{12}$	238	4.9
$(Gd_{0.9}Sr_{0.1})_3Ga_{4.7}Hf_{0.3}O_{12}$	248	4.7
$(Gd_{0.9}Ba_{0.1})_3Ga_{4.7}Hf_{0.3}O_{12}$	255	4.6

[1] E. Nakata *et al.*, Presentation at Radiological Society of North America (2008).

[2] Y. Y. Huang *et al.*, Dose-Response (Prepress) Formerly Nonlinearity in Biology, Toxicology, and Medicine (2009).

BL3B

Determination of the Band-Gap Energy of (Gd, La)₂Si₂O₇ Scintillator Crystals Using the UVSOR Facility

R. Murakami¹, S. Kurosawa², A. Yamaji¹, M. Kitaura⁴, T. Horiai¹, Y. Shoji^{1,3},
Y. Ohashi¹, Y. Yokota², K. Kamada^{2,3}, A. Ohnishi⁴ and A. Yoshikawa^{1,2,3}

¹Institute for Materials Research, Tohoku University, Sendai, Japan

²New Industry Creation Hatchery Center, Tohoku University, Sendai, Japan

³C&A Corp., Sendai, Japan

⁴Yamagata University, Yamagata, Japan

Inorganic scintillating materials are widely used for the medical imaging, oil well logging, astronomy, etc. Silicate scintillators such as Ce:Gd₂SiO₅ (Ce:GSO) and Ce:(Lu,Y)₂SiO₅ (Ce:LYSO) are applied in these fields, due to their high light outputs, short decay times, and so on. For example, Ce:GSO, has a good light output of ~12,500 photons/MeV and short scintillation decay time of ~56 ns [1]. Recent studies demonstrated that pyrosilicate-type crystals including Ce:Gd₂Si₂O₇ (Ce:GPS) and Ce:Lu₂Si₂O₇ (Ce:LPS) are also very promising scintillating materials [2,3]. Their light output exceeds that of Ce:GSO over two times [4]. Heavily Ce-doped (~10%) GPS crystals can be successfully grown from melt, and have the diameter over 1 inch. On the other hand, undoped GPS crystals cannot be grown from melt, because this material melts incongruently. However, heavily Ce-doped GPS crystals are not favorable, because high Ce concentration would lead to the degradation of light yield due to concentration quenching and self-absorption. In contrast, Ce:(Gd,La)₂Si₂O₇ (Ce:La-GPS) does not demonstrate the quenching problems. In Ce:La-GPS, part of Ce³⁺ is easily substituted with inactive La³⁺, because both Ce³⁺ and La³⁺ have similar ionic radius [5].

Scintillation properties of Ce:La-GPS have been investigated using the crystals grown by the floating zone (FZ) method [5,6]. La 9% substituted crystal showed high light output (~36,000 photons/MeV) and high energy-resolution (~5.0%, 662 keV, FWHM) [5]. The FZ-grown crystals were a few mm in dimensions. Alternatively, the Ce:La-GPS crystals grown by the Czochralski (Cz) process were over 1 inch in diameter. It was also demonstrated that 25 - 50% La-substituted GPS crystals can be repeatedly grown by the Cz method [7].

Such pyrosilicate-type scintillators show high light output at high temperature. The light output of Tl:NaI, which have been used for oil well logging degrade to roughly 80% at 150°C [8], while the light output of the Ce:La-GPS does not almost degrade at temperature over 150°C [9]. One of the important keys is the tolerance for the photoionization, and it depends on the energy difference between the top of 5*d* level and conduction band. However, band-gap energy of La-GPS has not been reported; therefore, there are few guides for the material design.

We have succeeded the growth of undoped La-GPS with the chemical composition of (Gd,La)₂Si₂O₇ single crystals by the micro-pulling-down (μ -PD) method. The crystals with 1 mm thickness were cut from the ingots and were polished. The band-gap energies were determined at the BL3B beamline in the UVSOR facility. The transmittance spectra were measured at low temperature (~5 K) with the liquid He under ultra-high vacuum (~10⁻⁷ Pa). The band-gap energies were estimated to be 7.1 -7.2 eV.

- [1] K. Takagi and T. Fukuzawa, *Appl. Phys. Lett.*, **42** (1983) 43.
- [2] C. L. Melcher *et al.*, Delft University Press (SCINT95), ISBN 90-407-1215-8, (1996) 309.
- [3] S. Kawamura *et al.*, *IEEE Nuclear Sci. Symp. Conf. Rec.* (2006) 1160.
- [4] S. Kawamura *et al.*, *IEEE TNS* **54** No.4 (2007) 1383.
- [5] A. Suzuki, A. Yoshikawa *et al.*, *Appl. Phys. Express* **5** (2012) 102601.
- [6] S. Kurosawa *et al.*, *NIMA* **744** (2014) 30.
- [7] A. Yoshikawa *et al.*, *Cryst. Growth Des.*, **15** (2015) 1642.
- [8] Saint Gobain, NaI(Tl) Data Sheet, [http://www.crystals.saint-gobain.com/uploadedFiles/SG-Crystals/Documents/NaI\(Tl\)%20Data%20Sheet.pdf](http://www.crystals.saint-gobain.com/uploadedFiles/SG-Crystals/Documents/NaI(Tl)%20Data%20Sheet.pdf)
- [9] S. Kurosawa *et al.*, *NIMA* **772** (2015) 72.

BL3B

Evaluation of Ce:(Gd, La)₂Si₂O₇ Scintillator Using an UVSOR Beam Line

S. Kurosawa¹, R. Murakami², Y. Shoji^{2,3}, A. Yamaji², T. Horiai², Y. Ohashi²,
Y. Yokota¹, K. Kamada^{1,3} and A. Yoshikawa^{1,2,3}

¹Institute for Materials Research, Tohoku University, Sendai, Japan

²New Industry Creation Hatchery Center, Tohoku University, Sendai, Japan

³C&A Corp., Sendai, Japan

Scintillators are used in various fields such as medical imaging, astronomy and so on. Evaluation of temperature dependences of some scintillation parameters such as light output and decay time is important to understand if the scintillation material is suitable for applications in low or high temperature conditions.

In oil well logging, scintillator is exposed to temperatures above 350 K measuring the subsurface geologic formation properties. Therefore, scintillator with a high light output even at high temperatures is required.

Recently, scintillation properties of (Ce_{0.01}, Gd_{0.90}, La_{0.09})₂Si₂O₇ (Ce:La-GPS) have been reported. The Ce:La-GPS crystal had a light output of approximately 35,000 photons/MeV, FWHM energy resolution of 5.0% at 662 keV [1,2]. Moreover, the light output over 35,000 photons/MeV was found constant in the temperature range from 0 to 423 K. In addition, FWHM energy resolution of Ce:La-GPS (roughly 7–8%) at 662 keV remained constant up to 373 K [3]. Thus, this crystal can be applied to oil well logging or other radiation detection application at high temperature conditions.

In this study, we evaluated luminescence properties of Ce:La-GPS in low temperature in BL3B of UVSOR. The luminescence was measured with a spectrometer (spectropro-300i, Acton research) consisting of a CCD camera from approximately 5 – 300 K.

Figure 1 shows the emission intensity around 390 nm originated from 5d-4f transition of Ce³⁺ as function of temperature, where excitation wavelength was approximately 240 nm originated from 4f-5d₄ transition of Ce³⁺. This result showed that the luminescence intensity remained constant, not only up to 400 K, also down to 5 K.

Compared with other scintillation materials, we found the invariable properties is rare case; in general, intensities of several scintillators doped with Ce³⁺ increase as temperature fall or disappear at low temperature (5-100 K). Thus, we found Ce:La-GPS has “strange” and “unique” temperature dependence.

We also measured thermo-luminescence for this material in UVSOR (BL3B), and we found that this material had small number of traps between valence and conduction band compared with conventional scintillators. Some traps would suppress the light output (luminance intensity), and the suppression from the traps are related to temperature. Thus, the small number of traps would be related to be “strange” and

“unique” temperature dependence.

Moreover, we also measured the bandgap energy of La-GPS in UVSOR, and this material had wider gap energy than conventional scintillators [4]. This wide bandgap can be related to the “strange” and “unique” temperature dependence in high temperature region (up to approximately 400 K), because, in this case, the energy difference between the bottom of the conduction band and excitation band of Ce³⁺ (5d₁ level) can be wider than conventional scintillators. Due to the wide energy, even in high temperature, electron located in excitation band of Ce³⁺ can de-excite to ground state of Ce³⁺ (4f), and a scintillation photon is generated. On the other hand, in the case of the low difference, electrons tend to move from the excitation band of Ce³⁺ to conduction band, and light output is quenched.

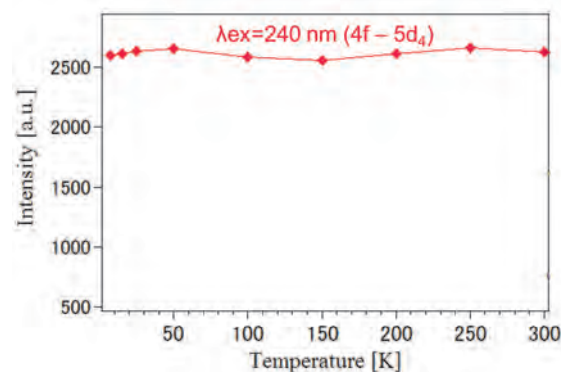


Fig. 1. Intensity of Ce³⁺ 5d-4f transition as a function of temperature.

- [1] A. Suzuki, S. Kurosawa, A. Yoshikawa *et al.*, *Applied Physics Express* **5** (2012) 102601.
- [2] S. Kurosawa, A. Yoshikawa *et al.*, *Nucl. Inst. and Meth. in Phys. Res. A* **774** (2014) 30.
- [3] S. Kurosawa, A. Yoshikawa *et al.*, *Nucl. Inst. and Meth. in Phys. Res. A* **772** (2015) 72.
- [4] R. Murakami and S. Kurosawa, UVSOR Activity Report, submitted.

BL3B

Thermoluminescence of SrHfO₃ Ceramics

H. Chiba¹, S. Kurosawa^{1,2}, R. Murakami¹, A. Yamaji¹, Y. Ohashi¹, J. Pejchal^{1,3}, K. Kamada^{2,4},
Y. Yokota^{1,2} and A. Yoshikawa^{1,2,4}

¹Institute for Materials Research, Tohoku University, Sendai 980-8577, Japan

²New Industry Creation Hatchery Center (NICHe), Sendai 980-8579, Japan

³Institute of Physics, AS CR, Cukrovarnická 10, 162 53 Prague, Czech Republic

⁴C&A Corporation, Sendai 980-8577, Japan

In Positron Emission Tomography (PET), Lutetium based scintillators are typically used because of their good performance and high density. However, Lu-containing scintillators have high-rate intrinsic background of roughly 300 counts/s/cm³ because natural abundance of ¹⁷⁶Lu radio isotope (beta emitter) is 2.59%. This is why Lu-containing scintillators can have worse sensitivity. Hafnium has a high atomic number of 72, and the abundance of its only radioisotope is less than 0.2% (¹⁷⁴Hf, half-life is more than 1015 year). Thus, a new scintillator containing Hafnium can have low intrinsic background and high detection efficiency.

Recently, SrHfO₃ doped with Ce (Ce:SHO) has attracted attention as a scintillating material due to a high density of 7.65 g/cm³, a high effective atomic number of 64 and negligible intrinsic-background [1]. Al/Ce:SrHfO₃ ceramics can be prepared by the Spark Plasma Sintering (SPS) method due to the high melting point of Hafnium [2]. It has improved optical properties and radiation response when compared to the Al-free material.

Considering the above, we fabricated Al/Ce:SrHfO₃ by the SPS method; For starting materials, HfO₂ (99.95% pure), SrCO₃ (99.99% pure), α -Al₂O₃ (99.99% pure), CeO₂ (99.99% pure) powders were used. Ce:SHO ceramic samples were pre-sintered in a chamber filled with air. SHO ceramic samples were prepared from the SHO powder using a 10-mm-diameter carbon punch and 30-mm-diameter carbon dies, SPS chamber (Fuji Denpa, DR.SINTER)

We used carbon punch and dies were used in the sintering process under vacuum, strongly reduction environment is established. This leads to creation of the oxygen vacancies in the material. These defects decrease the light output of the samples, they need to be investigated to optimize the material performance. Thus, thermoluminescence method was employed.

In BL3B of UVSOR, we used thermoluminescence measurement from 4 K to room temperature for SrHfO₃ samples; The samples were irradiated at 220 nm for 10 minutes at very low temperature 4-6 K. After the irradiation, we raised temperature slowly and measured the emission intensity with a CCD.

The thermoluminescence glow curve is shown in Fig. 1 howse can observe some peaks from 100 to 200K, and these peaks may originate from Oxygen defects.

As for future plans, we will investigate how the annealing can diminish Oxygen defects concentration

using the same method.

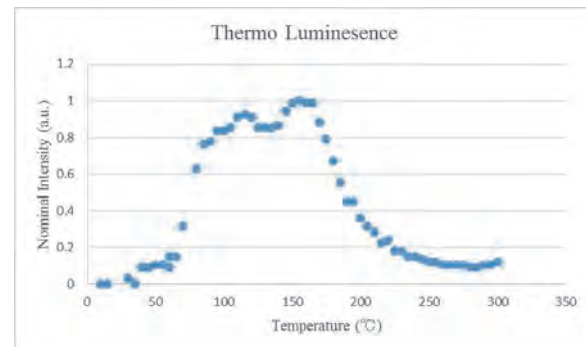


Fig. 1. Thermo Luminescence spectra of AlCeSrHfO₃.

[1] E. Mihóková, V. Jary', L. S. Schulman and M. Nikl, Chemical Physics Letters (in press).

[2] S. Kurosawa *et al.*, Radiat. Meas. **56** (2013) 155.

[3] S. Blahuta *et al.*, IEEE Transaction on Nuclear Science NS **60** (2013) 3134.

BL3B

Study of Emitting Mechanism on UV Emitting ZnAl₂O₄ Phosphor Using Vacuum Ultra Violet Photoluminescence System

H. Kominami¹, T. Ito¹ and S. Kubota²

¹Graduate School of Integrated Science and Technology, Shizuoka University, Hamamatsu 432-8651 Japan

²Faculty of Engineering, Shizuoka University, Hamamatsu 432-8651 Japan

In our previous work, it was found that ZnO-based oxide materials showed UV emission under excitation by electron beam. Especially, ZnAl₂O₄ showed strong UV emission peaked around 250 nm. However, the basic property and the emission mechanism of ZnAl₂O₄ were not cleared. For the evaluation of the physical properties, it is difficult to evaluate because it is the influence of surface scattering, such as the absorption coefficient and refractive index reflectance. By thinning the ZnAl₂O₄, we thought that it is possible to evaluate these fundamental properties and the mechanism of UV emission from ZnAl₂O₄. In this study, ZnAl₂O₄ thin film was prepared by sputtering and thermal diffusion to the sapphire substrate.

ZnAl₂O₄ thin films was prepared by thermal diffusion of ZnO film to sapphire substrate. After deposition, the films were annealed in air. From crystal analysis, ZnAl₂O₄ polycrystalline was obtained.

Figure 1 shows CL spectra of the ZnAl₂O₄ thin films before and after annealing for 2, 100 and 200 hours, respectively, excited at anode voltage of 10 and 4 kV and sample current density of 30 μA/cm². Both films showed UV emission from ZnAl₂O₄. From the spectrum of 2 hours annealing, in spite of ZnO thick film was still remained, the visible emission around 500 nm was not appeared. CL intensity of 100 hours annealed film showed 25 times stronger than that of 2 hours annealing. In other words, it suggested that the not only increasing of thickness but also improvement of crystallinity of ZnAl₂O₄ film by longer annealing time.

Figure 2 shows PL excitation spectra of ZnAl₂O₄ powders prepared by different ZnO/Al₂O₃ ratio. The excitation band was shifted to higher energy when Zn/Al ratio was decreased. It indicates that Zn/Al ratio was influenced the optical properties. The red line in the figure is the transmittance spectrum of ZnAl₂O₄ thin film. The absorption edge was closed to lower ZnO/Al₂O₃ ratio. It seems that the film was not stoichiometry. Moreover, the refraction index and dielectric constant were not obtained from the analysis of transmittance and reflection spectra. It was thought that the ZnAl₂O₄ film was not uniform and clear the boundary between ZnAl₂O₄ and substrate. To obtain the optical parameters such as refraction index and dielectric constant, it is necessary to prepare the film which is clear boundary at the each layer.

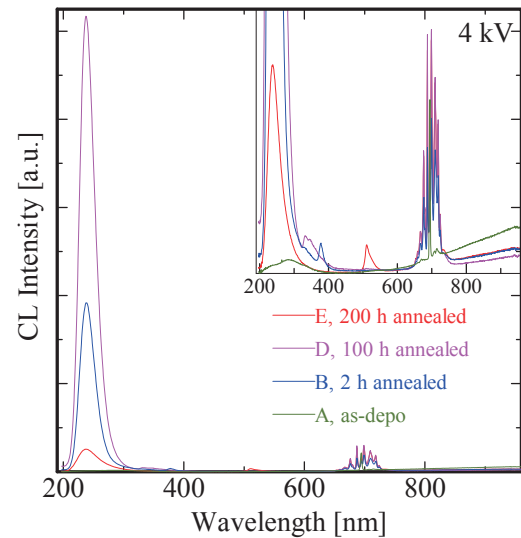


Fig. 1. Cathodoluminescence of ZnAl₂O₄ thin films prepared by thermal diffusion of ZnO and sapphire substrate, excited by anode voltages of 4 and 10 kV and sample current density of 30 μA/cm².

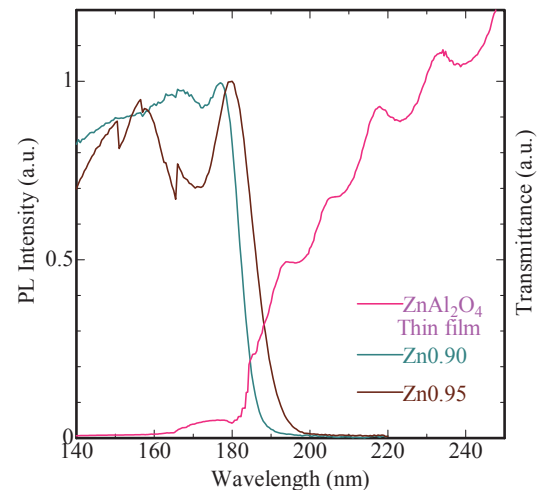


Fig. 2. Photoluminescent excitation spectra of ZnAl₂O₄ powders and transmittance spectrum of ZnAl₂O₄ thin film measured at BL3B.

BL3B, BL7B

PL Spectra of Laser Irradiated a -CN_x Thin Films

K. Nakamura¹, K. Ikeda¹, K. Fukui¹ and K. Yamamoto²

¹Department of Electrical and Electronics Engineering, University of Fukui, Fukui 910-8507, Japan

²Far-infrared region Development Research Center, University of Fukui, Fukui 910-8507, Japan

Amorphous carbon nitride (a -CN_x) is known to have an interesting mechanical, electrical and optical properties. Therefore, it has been actively carried out research on synthesis, structure and properties. The a -CN_x has also been expected as an inexpensive white light emitting diode material. However, since the optical properties of a -CN_x are sensitive to the preparation conditions, photoluminescence (PL) spectra of the samples evaporated under same conditions are, in some cases, different with each other. Recently, it is found that laser irradiated a -CN_x thin films after depositing show much higher PL intensity than those of as-deposited a -CN_x thin films, and their PL spectra have better reproducibility [1,2]. In this report, we show the RF power dependence of the combined excitation emission spectra (CEES) by using laser irradiated a -CN_x thin films.

All samples on Si substrates are deposited about 1 μ m by the RF-sputtering method at Ryukoku University [1]. The sputtering conditions with graphite target in the low pressure nitrogen gas environment of every samples are same without RF power of 40 W, 60 W and 100 W. Beam diameter of laser-irradiation is about 1.2 mm, and irradiation time is 240 minutes by using He-Cd laser (325 nm) with 20 mW. All CEES measurements have been performed at BL3B and BL7B at about 20 K.

Figure 1 shows CEES of RF power 60 W a -CN_x thin film. High intensity regions are represented by warm colors. It is found that the PL peak is located around 2.8 eV, and peak energy has no excitation energy dependence. It means that this emission process is unique process upon the band to band excitation of a -CN_x. Figure 1 also suggest that this PL is strongly excited around 4.5 eV and 5.5 eV. Both the excitation energy independence of the PL peak and the existence of two peaks (4.5 eV and 5.5 eV) in the excitation spectra are observed in both 40 W and 100 W a -CN_x.

Figure 2 shows the emission spectra at the excitation energy 4.6 eV for all samples. All spectra normalized by the maximum intensity. Although it is clear that the emission peak is shifted to lower photon energy side with an increase of the RF power, these three samples are emitted almost same photon energy region from 1.6 eV to 4.0 eV. In addition to the asymmetric spectral shape of these emission bands, it probably suggests that these PL bands consists of many emission bands which are continuously distributed from 1.6 eV to 4.0 eV, and RF power affects the distribution of the a -CN_x component which corresponds to each emission band.

In summary, we measured the combined excitation emission spectra of laser irradiated a -CN_x thin films.

Upon band to band excitation, a -CN_x thin film show a wide visible range emission band. This band consists of many emission bands which reflect the variation of the a -CN_x components and/or structures. However, all emission bands are commonly excited same two photon energy range around 4.5 eV and 5.5 eV.

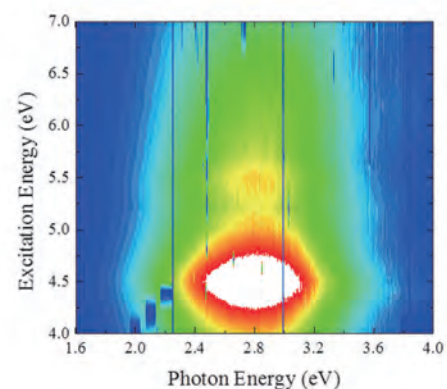


Fig. 1. CEES of a-CNRF-60W at 9K.

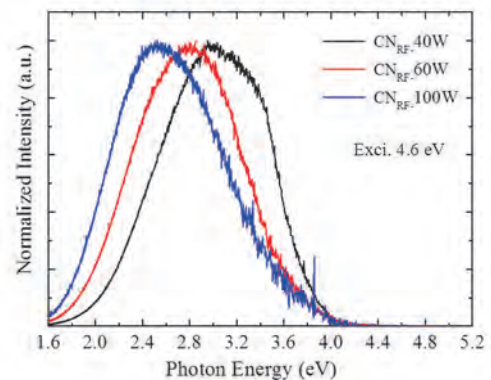


Fig. 2. Emission Spectrum at 9K.

[1] M. Satake *et al.*, 2013 JSAP Autumn Meeting 28p-PB3-11.

[2] D. Itoh *et al.*, UVSOR Activity Reports **41** (2014) 68.

BL3B

Energy Transfer from Γ^- Centers to In^+ Centers in Co-Doped $\text{NaCl}:\Gamma^-, \text{In}^+$ Crystals

A. Iguchi and T. Kawai

Graduate School of Science, Osaka Prefecture University, Sakai 599-8531, Japan

Alkali halide crystals have the wide band-gap up to the vacuum ultraviolet energy region and are a suitable candidate host for doping of impurity ions. Though optical studies for impurity centers doped in the alkali halide crystals have been extensively performed, energy transfer between two kinds of impurity centers in co-doped alkali halide crystals is comparatively less studied [1,2]. In this study, we have investigated the energy transfer from Γ^- centers to In^+ centers in NaCl crystals co-doped with the Γ^- and In^+ ions at the BL-3B line of UVSOR.

Figure 1 shows the absorption spectrum of $\text{NaCl}:\text{In}^+$ and the luminescence spectrum of $\text{NaCl}:\Gamma^-$ in the energy range from 4.4 to 6.0 eV. In $\text{NaCl}:\text{In}^+$, the absorption band observed around 5.2 eV is called the C absorption band and is attributed to the intra-ionic transition from the $^1A_{1g}$ to $^1T_{1u}$ states [3,4]. In $\text{NaCl}:\Gamma^-$, the luminescence band appearing around 5.3 eV is called the NE luminescence band and comes from the one-center type localized exciton, which is localized mainly on the central site of a substituted Γ^- impurity with small lattice relaxation [5]. The NE luminescence band in $\text{NaCl}:\Gamma^-$ has a large overlap with the C absorption band in $\text{NaCl}:\text{In}^+$. The fact indicates the potential of the energy transfer from the Γ^- centers to the In^+ centers in co-doped $\text{NaCl}:\Gamma^-, \text{In}^+$ crystals. According to the Förster model [6,7], the critical distance between both centers for resonant energy transfer is estimated to be about 3.0 nm from the overlap with the luminescence and absorption bands.

Figure 2 shows the excitation spectra in $\text{NaCl}:\Gamma^-$, $\text{NaCl}:\text{In}^+$, and co-doped $\text{NaCl}:\Gamma^-, \text{In}^+$ crystals at room temperature (RT). The NE luminescence band in $\text{NaCl}:\Gamma^-$ is efficiently excited in the energy region around 6.4 eV and 7.3 eV, where the absorption band due to the Γ^- centers is located. In $\text{NaCl}:\text{In}^+$, the luminescence band at 3.0 eV, which comes from the In^+ centers, is efficiently excited at the C absorption bands of the In^+ centers.

In the co-doped $\text{NaCl}:\Gamma^-, \text{In}^+$ crystal, the excitation spectrum for the 3.0 eV luminescence band of the In^+ centers has the broad band around 5.7 eV in addition to the C band of the In^+ centers. Since the 5.7 eV band corresponds to the excitation band for the NE luminescence band in $\text{NaCl}:\Gamma^-$, the fact implies the existence of the energy transfer from the Γ^- centers to the In^+ centers in the co-doped $\text{NaCl}:\Gamma^-, \text{In}^+$ crystal. In order to clarify the energy transfer mechanism from the Γ^- centers to the In^+ centers in the co-doped $\text{NaCl}:\Gamma^-, \text{In}^+$ crystals, the measurements of the decay kinetics of the luminescence are needed.

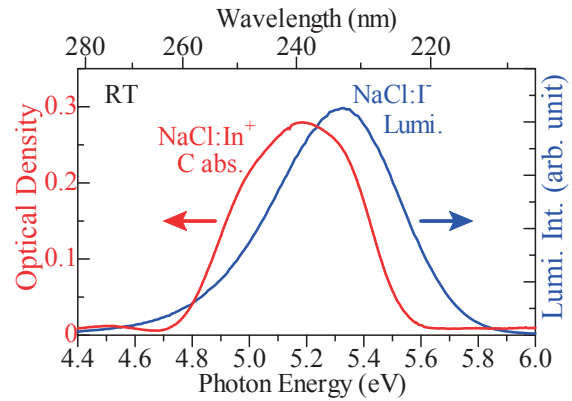


Fig. 1. Luminescence spectrum (blue) of $\text{NaCl}:\Gamma^-$ and absorption spectrum (red) of $\text{NaCl}:\text{In}^+$ at RT.

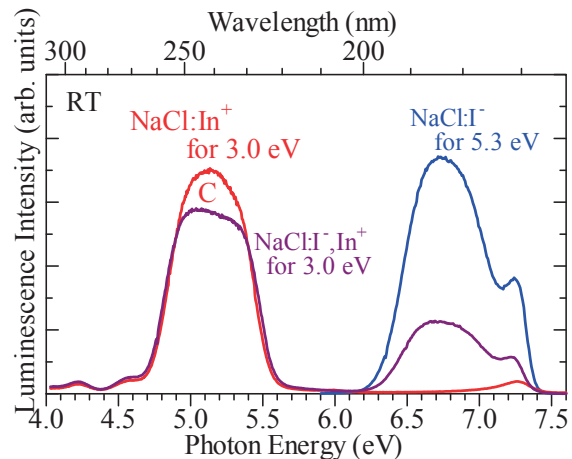


Fig. 2. Excitation spectra of $\text{NaCl}:\text{In}^+$ (red), $\text{NaCl}:\Gamma^-$ (blue), and co-doped $\text{NaCl}:\Gamma^-, \text{In}^+$ (purple).

- [1] A. F. Muñoz and J. O. Rubio, *Phys. Rev. B* **38** (1988) 9980.
- [2] A. Méndez *et al.*, *J. Lumin.* **79** (1998) 269.
- [3] A. Ranfagni *et al.*, *Advances in Physics* **32** (1983) 823.
- [4] P. W. M. Jacobs, *J. Phys. Chem. Solids* **52** (1991) 35.
- [5] I. Akimoto *et al.*, *Phys. Status Solidi C* **6** (2009) 342.
- [6] T. Förster, *Disc. Faraday Soc.* **27** (1959) 7.
- [7] D. L. Dexter, *J. Chem. Phys.* **21** (1953) 836.

BL3B

Luminescence of Copper-Heavily-Doped Cesium Iodide Crystals

T. Hirai¹ and T. Kawai²¹ College of Science and Engineering, Ritsumeikan University, Kusatsu 525-8577, Japan² Graduate School of Science, Osaka Prefecture University, Sakai 599-8531, Japan

Impurity ions doped into insulating materials, such as Tl: CsI and Tb: Gd₂O₂S, have been widely used as scintillators in γ - and X-ray detectors. In order to remarkably improve performance of those detectors, attempts have been recently made to develop a new type of scintillator utilizing semiconductor microcrystals instead of the impurity ions, since the radiative recombination rates of excitons in semiconductor microcrystals should be much higher than those in the impurity ions [1]. In the present study, we have focused on microcrystals of semiconducting Cu compounds that can be formed in a CsI crystal [2]. We have investigated photoluminescence (PL) and photoluminescence excitation (PLE) spectra of Cu heavily doped into CsI bulk crystals, which were prepared by the Bridgman method, by use of synchrotron radiation at the BL3B line in UVSOR.

Figure 1 shows a PL spectrum (black) of a Cu (10 mol%): CsI crystal at 5 K under excitation at 200 nm, which corresponds to the band-to-band excitation of CsI. A strong PL band is observed at 440 nm. A weak PL band can be also observed at around 405 nm as a shoulder of the PL band at 440 nm. In addition, there appear two PL bands at 290 and 340 nm, which originate from radiative recombination of self-trapped excitons (STEs) in CsI [3]. Three PLE spectra detected at 340 (violet), 440 (red) and 405 (blue) nm are also shown in Fig. 1. The PLE spectrum for the 340-nm PL band corresponds to that for the PL bands of STEs in CsI. In the PLE spectrum for the 405-nm PL band, two PLE bands are observed at 260 and 280 nm. For the 440-nm PL band, there appear three PLE bands at 245, 270 and 290 nm.

In Fig. 2, a PL spectrum (black) of a Cu (40 mol%): CsI crystal under excitation at 200 nm at 5 K is shown. According to the phase diagram of the CuI-CsI system [4], the mixed melts of 60 mol% CsI and 40 mol% CuI form Cs₃Cu₂I₅ crystals. In the PL spectrum, there appear two PL bands at 440 and 405 nm, which are quite similar to the 440- and 405-nm PL bands in Cu (10 mol%): CsI (Fig. 1). Furthermore, two PLE spectra detected at 440 (red) and 405 (blue) nm shown in Fig. 2 are likely to correspond to those for the 440- and 405-nm PL bands shown in Fig. 1. These PL and PLE spectra suggest that those PL bands in the two samples have the same origin. The 440-nm PL band is certainly identical to the 440-nm PL band arising from radiative recombination of excitons in Cs₃Cu₂I₅, which has been reported by Hirao *et al.* [5]. Although the origin of the 405-nm PL band is unclear, the PL band perhaps comes from Cu impurities in CsI crystals.

From the above results, we can conclude that the Cu

(10 mol%): CsI crystal contains Cs₃Cu₂I₅ microcrystals. Additionally, we notice that the excitation of CsI host crystals in the Cu (10 mol%): CsI crystal gives rise to the photoluminescence originating from the Cs₃Cu₂I₅ microcrystals.

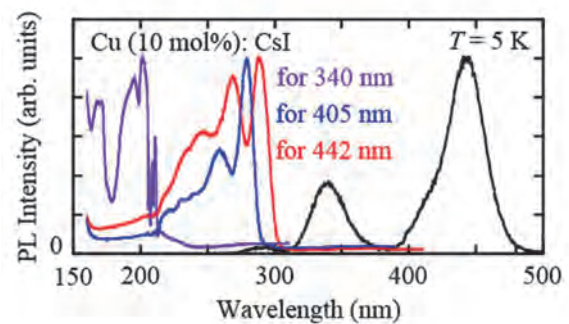


Fig. 1. PL spectrum of a Cu (10 mol%) : CsI crystal under excitation at 200 nm (black), and its PLE spectra detected at 340 (violet), 405 (blue) and 440 (red) nm.

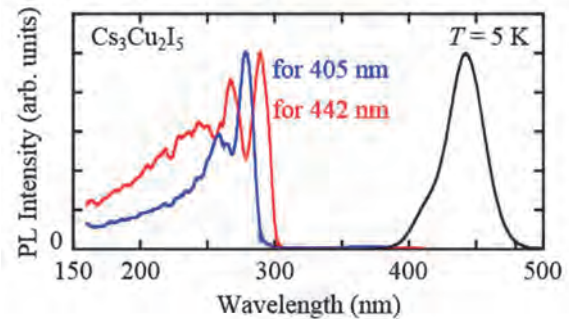


Fig. 2. PL spectrum of Cs₃Cu₂I₅ excited at 200 nm (black), and its PLE spectra detected at 405 (blue) and 440 (red) nm.

[1] K. Shibuya *et al.*, Rev. Sci. Instrum. **78** (2007) 083303.

[2] M. Nakayama *et al.*, Japanese Unexamined Patent Application No. 2003-147343.

[3] H. Nishimura *et al.*, Phys. Rev. B **51** (1995) 2167.

[4] A. Wojakowska *et al.*, J. Chem. Eng. Data **48** (2003) 468.

[5] N. Hirao *et al.*, Meet. Abs. Phys. Soc. Jpn. **58** (2003) 742.

BL3B

Excitation and Emission Spectra of Pr³⁺ in Ga- Doped SrY₂O₄

M. Yoshino, S. Nishiki and S. Watanabe

Graduate School of Engineering, Nagoya University, Nagoya 464-8603, Japan

The trivalent lanthanide ions (e.g., Ce³⁺, Nd³⁺, Er³⁺) in Oxide crystals have drawn attentions due to their application for luminescent materials in NIR to UV regions such as solid-state lasers or phosphors. The trivalent cerium ion, Pr³⁺, has also attracted attentions as luminescence centers. In this work, the excitation spectra and emission spectra for Pr³⁺ in Ga-doped SrY₂O₄ crystal have been measured. For the comparison, the spectra for host oxide, Ga-doped SrY₂O₄ have been also measured. The Ga-doped SrY₂O₄ sample and Pr,Ga-doped SrY₂O₄ sample are produced by solid state reactions. Pr-doped samples are annealed in N₂-H₂ atmosphere. The concentration of Ga and Pr in the samples are 3 mol% and 1 mol%, respectively. The emission spectrum of Ga-doped SrY₂O₄ at 200 nm excitation is shown in Fig. 1. The broad peaks from interband optical transition exist around 400 nm. The excitation spectrum monitored at 400 nm emission is shown in Fig. 2. The peak near 200 nm relates the absorption from the optical transition

around the band edge in Ga-doped SrY₂O₄. This corresponds with that in the spectrum monitored at 423 nm in SrY₂O₄ [1]. The emission spectrum for Pr³⁺ in Ga-doped SrY₂O₄ is shown in Fig. 3. The spectrum shows sharp peaks originated from Pr³⁺ 4f-4f transition and the broad peaks of interband optical transition from the host are weak while the excitation wavelength is 200 nm. It can be said that excitation energy could transferred from host to Pr³⁺ ion. Figure 4 shows the excitation spectrum monitored 520 nm for Pr³⁺ in Ga-doped SrY₂O₄. The peaks around 320 nm and 280nm originate in the absorption of the 4f-5d transitions of Pr³⁺. Then, in the excitation at around 320 nm and 280 nm, Pr³⁺ ions are excited directly, the emission spectrum mainly shows the sharp peaks originated from Pr³⁺ 4f-4f transition as shown in Fig. 3.

[1] M. Yoshino, S. Watanabe and Y. Ichikawa, UVSOR Activity Report **36** (2009) 122.

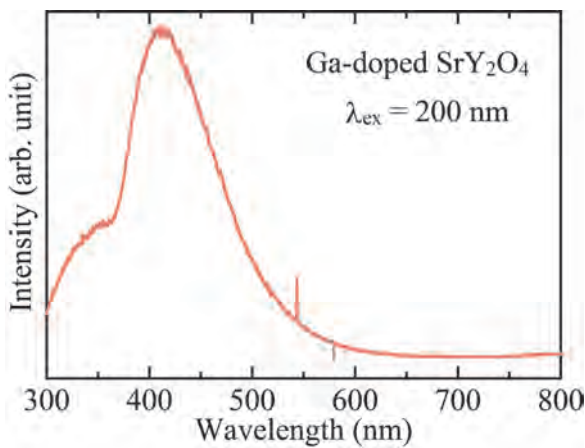


Fig. 1 Emission spectrum of Ga-doped SrY₂O₄.

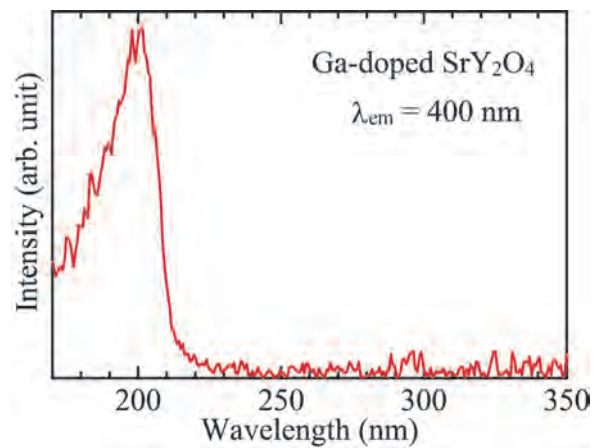


Fig. 2 Excitation spectrum of Ga-doped SrY₂O₄.

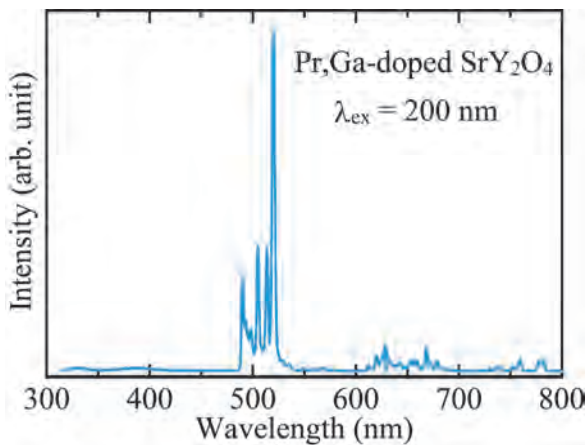


Fig. 3. Emission spectrum of Pr, Ga-doped SrY₂O₄.

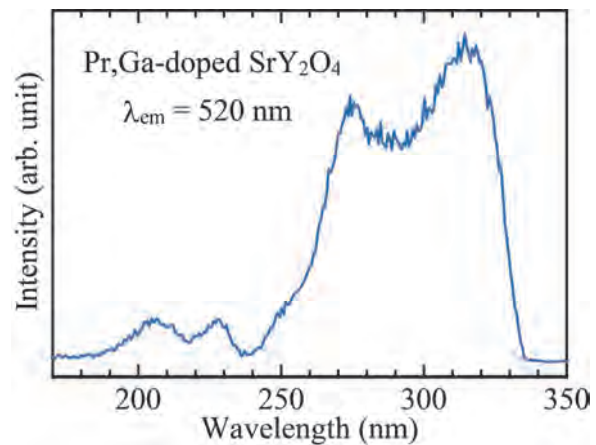


Fig. 4. Excitation spectrum of Pr, Ga-doped SrY₂O₄.

BL3B

Photoluminescence of TlBr-TlI Mixed Crystals

N. Ohno¹ and K. Matsui²

¹Fundamental Electronics Research Institute, Osaka Electro-Communication University,
Neyagawa 572-8530, Japan

²Graduate School of Engineering, Osaka Electro-Communication University,
Neyagawa 572-8530, Japan

Thallous halide crystals are compound semiconductors attractive for fabrication of γ ray detectors. They exhibit high stopping power originated from high atomic number and high density [1]. TlCl and TlBr crystalize in cubic CsCl-type structure, while the stable form of TlI is orthorhombic structure below 170°C [2] and is cubic CsCl-type one above it [3,4]. Therefore, it is difficult to grow a large-sized single crystal of TlI under atmospheric conditions. In the present study, mixed singles of TlBr-TlI in cubic CsCl-type structure have been grown and examined to reveal the optical properties such as the optical absorption, photoluminescence and luminescence excitation spectra.

The crystals $\text{TlBr}_x\text{I}_{1-x}$ were grown by the Bridgeman method after mixing appropriate amounts of purified TlBr and TlI. A plate of the sample cut from as-grown crystals was polished with alumina abrasive plastic film, then etched in hot distilled water. The optical measurements were made at 10 K and at temperatures up to 300 K at BL3B station.

Figure 1 shows emission and absorption spectra (black curves) of $\text{TlBr}_x\text{I}_{1-x}$ mixed crystals for different compositions measured at 10 K. In pure TlBr ($x=1.0$), the fundamental absorption edge is of the indirect-forbidden exciton transition [5]. As clearly seen in Fig.1, the indirect absorption edge moves to lower energy with increasing iodine concentration. At $x=0.4$, the absorption-edge energy is located at around 2.0 eV. Below $x \leq 0.3$, the absorption spectra showed no clear absorption edge which was ascribed to the phase transition in $\text{TlBr}_x\text{I}_{1-x}$ mixed crystals. In I-rich mixed crystal, the cubic phase becomes unstable below the room temperature.

On exciting $\text{TlBr}_x\text{I}_{1-x}$ mixed crystals with light at the energy above the indirect absorption edge, a Stokes-shifted broad luminescence band is observed as clearly seen in Fig. 1 (blue curves). In TlBr ($x=1.0$), the shape of the spectra is almost Gaussian as previously observed in lightly I-doped TlBr [6]. The broad band was identified to be originated from annihilation of excitons self-trapped at an iodine ion due to the impurity-induced self-trapping. It is worth noting in Fig. 1 that the amount of the Stokes shift and the full width at the half maximum of the observed luminescence band become continuously smaller as the iodine concentration is increased. Therefore, with increasing I-ion concentration in $\text{TlBr}_x\text{I}_{1-x}$ mixed crystals, the lattice relaxation of the

self-trapped excitons decreases due to the smaller exciton-phonon interaction, resulting in decreasing of Stokes shift of the luminescence band width.

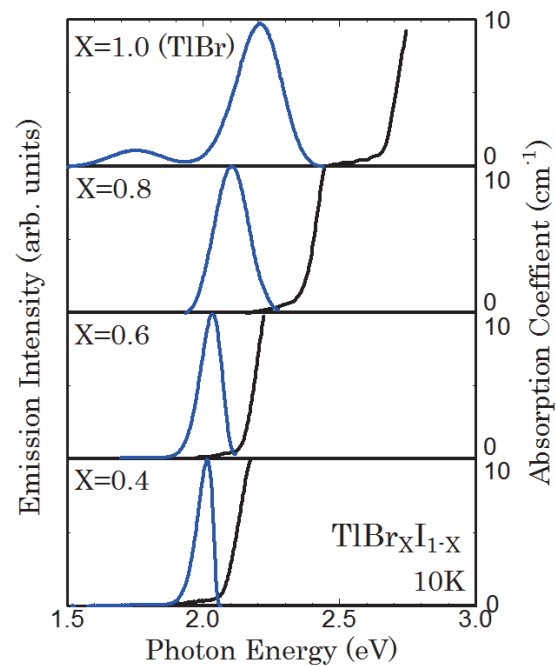


Fig. 1. Photoluminescence (blue) and absorption coefficient (black) spectra of $\text{TlBr}_x\text{I}_{1-x}$ at 10 K.

- [1] K. Hitomi, T. Shoji and K. Ishii, *J. Crystal Growth* **379** (2013) 93.
- [2] N. Ohno and M. Itoh, *J. Phys. Soc. Jpn.* **62** (1993) 2966.
- [3] K. Heidrich, W. Staude, J. Treusch and H. Overhof, *Solid State Commun.* **16** (1975) 1043.
- [4] A. Fujii and I. Ishikawa, *J. Phys. Soc. Jpn.* **56** (1987) 4581.
- [5] J. Nakahara, K. Kobayashi and A. Fujii, *J. Phys. Soc. Jpn.* **37** (1974) 1312.
- [6] J. Nakahara and K. Kobayashi, *J. Phys. Soc. Jpn.* **40** (1976) 180.

BL3B

VUV Absorption Spectra of Racemic Alanine Crystals

S. Tanaka, M. Kitaura and A. Ohnishi

Department of Physics, Faculty of Science, Yamagata University, Yamagata 990-8560, Japan

Amino acids are simple chiral molecules with L- and D-forms. Protein molecules are composed of only L-amino acids. This is called “homochirality”, which has attracted much attention in relation to the mystery of life. It has been generally accepted that the homochirality of proteins comes from the creation of L-amino acids by circularly polarized VUV light in outer space region. So far, VUV absorption spectra of amino acids have been studied using aqueous solutions [2] and thin films [3]. To our knowledge, there is no report on VUV absorption spectra of amino acid crystals. We have measured VUV reflectivity spectra of L-alanine single crystals to obtain the spectra of various optical constants. In the present study, we have measured reflectivity spectra of racemic alanine crystals, and investigated the change of VUV absorption spectra on crystal structure, which gives us information on intermolecular interaction among alanine molecules.

Racemic alanine single crystals were obtained from saturated aqueous solution of commercial alanine powder. The crystals are of needle shape. The crystal axes were distinguished by two polarizers arranged in a cross Nicole alignment. To obtain VUV absorption spectra, we performed the Kramers-Kronig (K-K) analysis of reflectivity spectra. In the K-K analysis, it is necessary to determine absolute reflectivity over the energy range as wide as possible. We obtained absolute reflectivity by the correction using refractive indexes in the transparent region below 2 eV.

Figure 1 shows VUV absorption spectra of a racemic alanine crystal for different configurations of linearly polarized light. A few peaks appear below 15 eV. No remarkable peak is found above 15 eV. This feature is similar to VUV absorption spectra of L-alanine crystals [4]. On the other hand, there is a linear dichroism between them. Figure 2 shows VUV absorption spectra extended in the 5-12 eV range. Absorption peaks for a racemic alanine crystal are apparently broader than those for L-alanine crystals [4]. The reason for such broadening of absorption peaks is not clear. To clarify it, theoretical approaches based on electronic state calculations are effective. Theoretical calculations were applied for alanine molecules [5,6]. However, there is no instance applied for alanine bulk crystals. Therefore, theoretical calculations for alanine bulk crystals are desired.

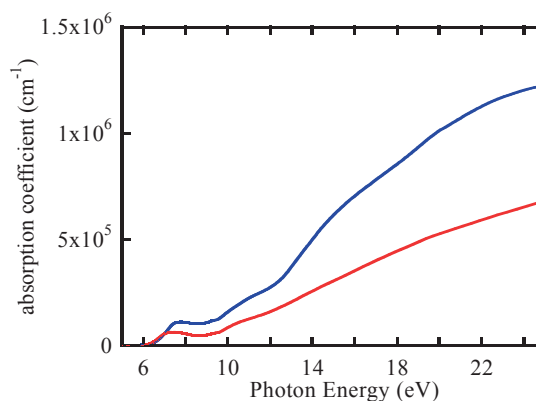


Fig. 1. VUV absorption spectra of a racemic alanine crystal, derived from the Kramers-Kronig analysis of reflectivity spectra in 5-25 eV range. The data were measured at room temperature.

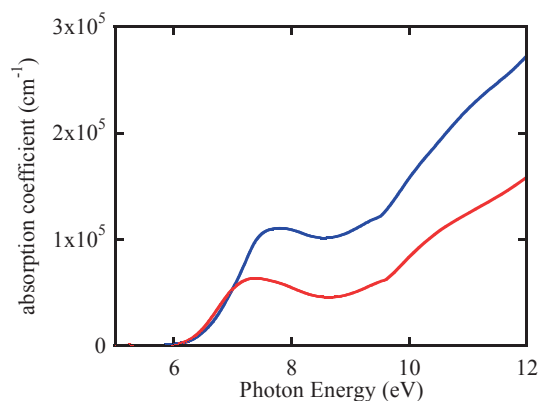


Fig. 2. VUV absorption spectra of a racemic alanine crystal, extended in the 5-12 eV range.

- [1] P. A. Snyder *et al.*, *Biopolymers* **12** (1973) 975.
- [2] T. Inagaki *et al.*, *Biopolymers* **12** (1973) 1353.
- [3] M. Tanaka *et al.*, *J. Electron Spectrosc. Relat. Phenom.* **181** (2001) 177.
- [4] S. Tanaka *et al.*, *UVSOR ACTIVITY REPORT* **42** (2015) 70.
- [5] F. Kaneko *et al.*, *J. Phys. Soc. Jpn.* **78** (2009) 013001.
- [6] T. Kaneko *et al.*, *CHIRALITY* **23** (2011) E52.

BL3B

Construction of Vacuum Referred Binding Energy Diagram in $\text{Gd}_3(\text{Al,Ga})_5\text{O}_{12}:\text{Ce}^{3+}$ Phosphors

K. Asami¹, J. Ueda¹, M. Kitaura² and S. Tanabe¹¹ *Graduated School of Human and Environmental Studies, Kyoto University, Kyoto 606-8501, Japan*² *Department of Physics, Faculty of Science, Yamagata University, Yamagata 990-8560, Japan*

Ce^{3+} -doped $\text{Gd}_3\text{Al}_{5-x}\text{Ga}_x\text{O}_{12}$ (GAGG) is a promising optical material for the scintillator [1]. It is known that the quantum efficiency (QE) of GAGG: Ce^{3+} becomes lower with increasing Ga content, x [2]. To understand optical properties of a phosphor, an electronic structure of host material should be investigated. Dorenbos suggested the construction method of the vacuum referred binding energy (VRBE) diagram [3]. This diagram can be constructed from the spectroscopy data of host exciton energy and charge transfer transition (CTS) of Eu^{3+} . To determine those transition energies, we measured photoluminescence excitation (PLE) spectra of both Ce^{3+} - and Eu^{3+} -doped GAGG at UVSOR BL3B.

Figure 1 (a) shows the PLE spectra of Ce^{3+} -doped GAGG phosphors with various Ga content. In PLE spectra, the host exciton peaks are observed at around 200 nm and three bands derived from Ce^{3+} are observed at 220 nm ($4f-5d_{3,4,5}$), 350 nm ($4f-5d_2$) and 450 nm ($4f-5d_1$). Several peaks at 270 nm and 310 nm are due to the intra- $4f$ transitions of Gd^{3+} in the host [1]. From the host exciton peaks, the bandgap energies of GAGG ($x = 1, 2, 3$ and 4) are estimated to be 6.84, 6.81, 6.63 and 6.55 eV, respectively. With increasing Ga content, the bandgap becomes narrower. Figure 1 (b) shows the PLE spectra of Eu^{3+} : GAGG phosphors. The strong broad band is located at around 250 nm, which is attributed to CTS of $\text{O}^{2-}-\text{Eu}^{3+} \rightarrow \text{O}^- - \text{Eu}^{2+}$. With increasing Ga content, the peak wavelength of CTS shifts to longer. The top of valence band is calculated by subtracting the CTS energy from the determined $4f$ state energy of Eu^{2+} .

Based on the method of VRBE diagram construction by Dorenbos [3], the VRBE diagram of Ce^{3+} -doped GAGG are constructed by using measurement data obtained in Fig.2. The energy E_v which is top of valence band shifts higher with increasing Ga content while the energy E_c which is the bottom of conduction band slightly changes. When the energy of $\text{Ce}^{3+}:5d_1$ is close to E_c , the excited electrons located at $\text{Ce}^{3+}:5d_1$ state tend to move to the conduction band by thermal ionization. From this diagram, with increasing Ga content, the energy gap between E_c and $\text{Ce}^{3+}:5d_1$ becomes smaller. Therefore QE of Ce^{3+} in GAGG system becomes decrease by thermal ionization quenching.

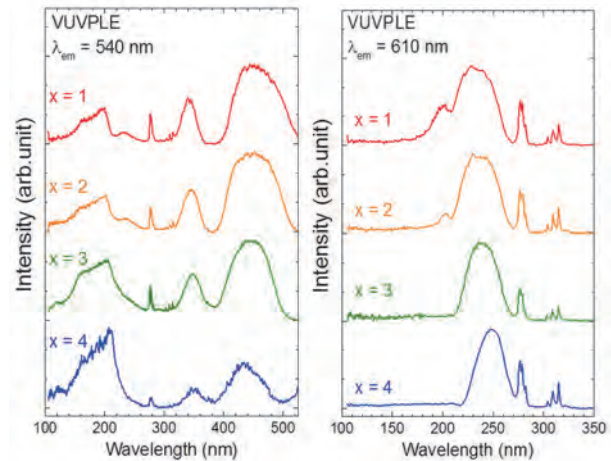


Fig. 1. PLE spectra of (a). Ce^{3+} -doped GAGG (Left) and (b). Eu^{3+} -doped GAGG (Right).

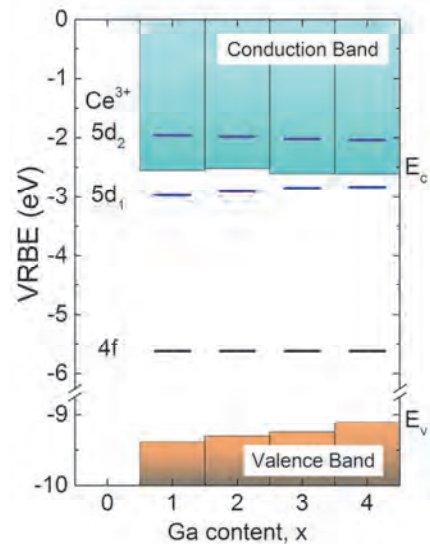


Fig. 2. Constructed VRBE diagram of Ce^{3+} :GAGG.

- [1] M. Kitaura, A. Sato, K. Kamada, A. Ohnishi and M. Sasaki, *J. Appl. Phys.* **115** (2014) 083517.
 [2] J. M. Ogiegłó, A. Katelnikovas, A. Zych, T. Jüstel, A. Meijerink and C. R. Ronda, *J. Phys. Chem. A* **117** (2013) 2479.
 [3] P. Dorenbos, *J. Lumin.* **134** (2013) 310.

BL3B, BL6B

Local Structure of Gd^{3+} and Ce^{3+} Ions in $Gd_3Al_{5(1-x)}Ga_{5x}O_{12}$ Crystals Studied by UV and IR Absorption Spectroscopy

C. Oyama¹, M. Kitaura¹, M. Ishizaki¹, K. Kamada², S. Kurosawa², A. Ohnishi¹ and K. Hara³¹Faculty of Science, Yamagata University, Yamagata 990-8560, Japan²NICHe, Tohoku University, Sendai 980-0845, Japan³RIE, Shizuoka University, Hamamatsu 432-8011, Japan

The Ce:Gd₃Al₂Ga₃O₁₂ (Ce:GAGG) garnet crystals has been known as an inorganic scintillators with high light output, high energy resolution, and no hygroscopic nature [1]. The scintillation properties strongly depend, especially on the composition ratio of Al³⁺ and Ga³⁺ ions. The control of the composition ratio of Ga³⁺ and Al³⁺ ions is of great importance to bring out the high performance of Ce:GAGG. The crystals of garnet type have three cation sites named A, B, and C, in which cations are coordinated by eight, six, and four oxygen ions, respectively. The chemical formula of oxide garnets is expressed as A₃B₂C₃O₁₂. Al³⁺ and Ga³⁺ ions can regularly occupy octahedral (B) and tetrahedral (C) sites. So far, the distribution of Al³⁺ and Ga³⁺ ions has been investigated in garnet solid solutions. Although there are a number of reports on this subject, it still remains obscure which sites Ga³⁺ ions occupy preferentially [2,3]. From the viewpoint of basic science and industrial application, it is worthwhile to investigate the site preference of Ga³⁺ ions in Ce:Gd₃Al_{5(1-x)}}Ga_{5x}O₁₂ crystals. In the present study, Gd³⁺ and Ce³⁺ 4*f*-4*f* absorption spectra of undoped and cerium-doped Gd₃Al_{5(1-x)}}Ga_{5x}O₁₂ (0.4 ≤ *x* ≤ 1) crystals have been measured at low temperatures below 10 K in ultraviolet and infrared ranges [4]. Generally, the 4*f*-4*f* transitions of rare-earth ions give rise to narrow absorption peaks, and they are expected to be sensitive to cation distribution. Thus, Gd³⁺ and Ce³⁺ 4*f*-4*f* absorption peaks can utilize as a probe to clarify the site preference of Ga³⁺ ions.

Figure 1 shows absorption spectra of undoped Gd₃Al_{5(1-x)}}Ga_{5x}O₁₂ (a) and cerium-doped Gd₃Al_{5(1-x)}}Ga_{5x}O₁₂ (b), which are due to 4*f*-4*f* transitions of Gd³⁺ and Ce³⁺ ions, respectively. In Fig. 1(a), the peak positions and spectral widths of absorption peaks for *x* = 0.4 were almost the same as those for *x* = 1.0. This result suggests that, for *x* = 0.4, Ga³⁺ and Al³⁺ ions occupy octahedral and tetrahedral sites, respectively. This opinion is consistent with that by Ogiegro *et al.* [2], but is inconsistent with that by Kanai *et al.* [3]. The peak positions for *x* = 0.6 and 0.8 are shifted to lower energy side. The spectral widths were clearly broader, compared to that for *x* = 0.4 and 1.0. The peak shift and spectral broadening indicate that, for *x* = 0.6 and 0.8, Ga³⁺ and Al³⁺ ions occupy both of octahedral and tetrahedral sites. In Fig. 1(b), the position of the absorption peak shifts to lower wavenumber side with increasing *x*. This is explained by the reduction of crystal field strength at Ce³⁺ ions, which is due to the

replacement of Ga³⁺ ions for Al³⁺ ions [5]. The spectral width for *x* = 0.4 is largest of all *x*, suggesting the variety of crystal field at Ce³⁺ ion sites. In oxide garnets, oxygen vacancies and antisite ions are known as primary imperfections [6]. It is thus likely that various Ce³⁺ ions coupled with such imperfections are formed. The present study reveals that the variety of Ce³⁺ ions coupled with imperfections is the largest for *x* = 0.4. The reason for this is unclear, so that it is an open subject to be solved in near future.

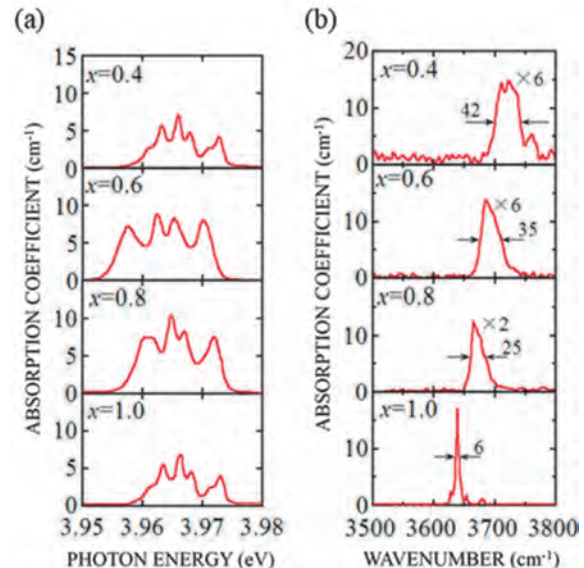


Fig. 1. Absorption spectra due to 4*f*-4*f* transitions of Gd³⁺ ions in undoped Gd₃Al_{5(1-x)}}Ga_{5x}O₁₂ (a) and Ce³⁺ ions in cerium-doped Gd₃Al_{5(1-x)}}Ga_{5x}O₁₂ (b). These data were observed below 10 K.

- [1] K. Kamada *et al.*, *J. Cryst. Growth* **352** (2012) 88.
- [2] J. M. Ogiegro *et al.*, *J. Phys. Chem. C* **35** (2013) 322.
- [3] T. Kanai *et al.*, *J. Am. Ceram. Soc.* **462** (2008) 456.
- [4] For *x* = 0 and 0.2, it is not possible to obtain single crystals of garnet phase.
- [5] P. Dorenbos, *J. Lumi.* **151** (2014) 224.
- [6] M. Kitaura *et al.*, *J. Appl. Phys.* **115** (2014) 083517.

BL4U

Observation of Morphology of a Fuel Cell by Using a Humidity Control Sample Cell for STXM

T. Ohigashi^{1,2}, Y. Inagaki¹, T. Horigome¹ and N. Kosugi^{1,2}

¹ UVSOR Synchrotron, Institute for Molecular Science, Okazaki 444-8585, Japan

² School of Physical Sciences, The Graduate University for Advanced Studies (SOKENDAI), Okazaki 444-8585, Japan

One of the advantages of a scanning transmission X-ray microscopy (STXM) is tolerance for ambient conditions of samples. Due to high transmittance of the X-ray, the STXM does not require a vacuum condition but enables to observe electronic states of various samples in atmospheric pressure or in water. Moreover, a focusing optical element of the STXM, namely, a Fresnel zone plate, has characteristics such as long working distance and long focal depth. These features enable to perform *in-situ* observation, which is impossible for an electron microscopy; therefore, various sample cells have been developed widely [1]. Control of humid atmosphere around the sample is sometimes needed as a promising *in-situ* observation method [2]; for example, a fuel cell working under high humid atmosphere and high temperature. In this study, we have developed a humidity control sample cell and performed a test measurement.

The present humid control sample cell (shown in Fig. 1) is a small chamber consisted of two silicon nitride membranes (thickness of 100 nm) as windows [3]. A small sensor to measure humidity and temperature (SHT7x, Sensirion AG) is set inside of the chamber. The cell has three ports for inlet/outlet of gas flowing and two of them were used in this study. The inlet and outlet were connected to a feedthrough of the STXM chamber with stainless tubes and dry/humid helium gas is flowed into the cell to control the humidity. Humidity in the gas is added by bubbling pure water in a bottle and its flow rate is controlled by using a needle valve manually. The inside of the STXM chamber was transferred by helium gas until air pressure. As a performance test, we could change the humidity from 16.1 to 80.4% at 29°C (temperature inside of the STXM chamber was higher than RT).

By using the cell, morphological change of thin sections of a fuel cell fixed on Formvar membrane was used as a test sample. 2-dimensional distributions of fluorine in the polymer were obtained by using the K-absorption edge of fluorine (687 eV). X-ray transmission images below and above of the edge (682 and 692 eV) were obtained. After conversion to optical density images, the distribution of fluorine was obtained by subtracting these images. The distribution of fluorine of the humidity at 16% and 8% are shown in Fig. 2. In these images, bright areas show high concentration of fluorine and dark areas like cracks are seen on the center. By changing the humidity from 16% to 80%, 11% of the dark area decreased. This

change of the area was caused by swelling of water vapor of the polymer.

As a future plan, temperature control and auto-control (i.e. feedback of the humidity and temperature) system are under consideration. As further application of this humid cell, observation of living biological samples, such as cells and bacteria, will be performed.

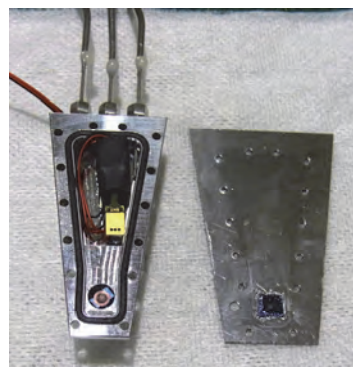


Fig. 1. The inside and the base plate of the humidity control sample cell.

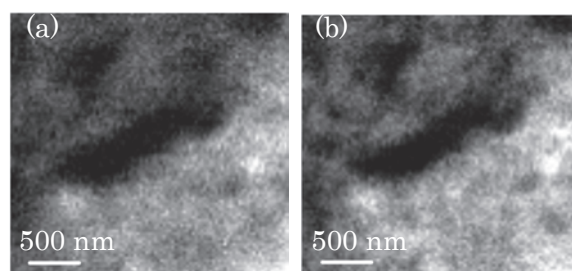


Fig. 2. Distribution of fluorine in the fuel cell (bright pixels show high concentration). The humidity of the cell were at (a) 16% and (b) 80%.

[1] X. H. Zhu *et al.*, UVSOR Activity Report **41** (2014) 72.

[2] V. Berejnov *et al.*, ECS Transactions **41** (2011) 395-402.

[3] T. Ohigashi *et al.*, accepted.

BL4U

Influence of the Oxygen Vacancy at Ta/TaO_x Interface on Resistive Switching Memories

Y. F. Wang¹, W. F. Pong¹, J. S. Chen², J. W. Chiou³, T. Ohgashi⁴ and N. Kosugi⁴

¹Department of Physics, Tamkang University, Tamsui 251, Taiwan

²Department of Materials Science and Engineering, National Cheng Kung University, Tainan 701, Taiwan

³Department of Applied Physics, National University of Kaohsiung, Kaohsiung 811, Taiwan

⁴UVSOR Synchrotron, Institute for Molecular Science, Okazaki 444-8585, Japan

In this work, we have studied the electronic structure and the location of oxygen vacancy in the interface of the Ta/TaO_x/Pt thin film and identify the type of conducting path by scanning transmission x-ray microscopy (STXM). The amorphous TaO_x thin film of thickness of ~150 nm was deposited by electron beam evaporation on Pt/SiO₂/Si substrates. Active electrodes of Ta were thermally evaporated respectively on the TaO_x thin film with an equivalent thickness of ~150 nm. As shown in Fig. 1, the STXM stack mapping displays the cross-sectional views of the Ta/TaO_x/Pt thin film. Obviously, due to a uniform diffusion occurs in the vicinity of the Ta/TaO₂ interface, the image of the Ta/TaO_x/Pt thin film revealed that the interfacial TaO_x was ~180 nm in thickness. The experiments were performed at the 4U beamline. Figure 2 presents the corresponding O K-edge x-ray absorption near-edge structure (XANES) spectra of the Ta/TaO_x/Pt thin film. The O K-edge STXM-XANES spectra were recorded at three selected regions, *cyan*, *red* and *yellow*, in the Ta/TaO_x/Pt thin film, respectively. According to the dipole-transition selection rule, the features at ~530-545 eV are attributed to the electron excitations from O 1s-derived states to 2p-derived states, which are approximately proportional to the density of the unoccupied O 2p-derived states.¹ The intensities of the O K-edge STXM-XANES spectra of the *red* region are significantly higher than that of the *cyan* region, which reflects the increase in the number of unoccupied O 2p-derived states. In other words, the STXM-XANES results demonstrate that the population of defects at the O sites in the Ta/TaO_x interface and confirming the enhanced density of states of O 2p-derived states, as the population of defects and dangling bonds at/above E_{CBM} or E_F in the Ta/TaO_x interface. The STXM-XANES results intensely support the phenomena that the occurrence of O 2p vacancy at Ta/TaO_x interface affects the resistive switching effect of the Ta/TaO_x/Pt thin film.

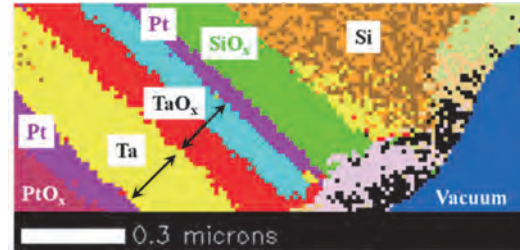


Fig. 1. The STXM stack mapping of the cross-sectional views of the Ta/TaO_x/Pt thin film.

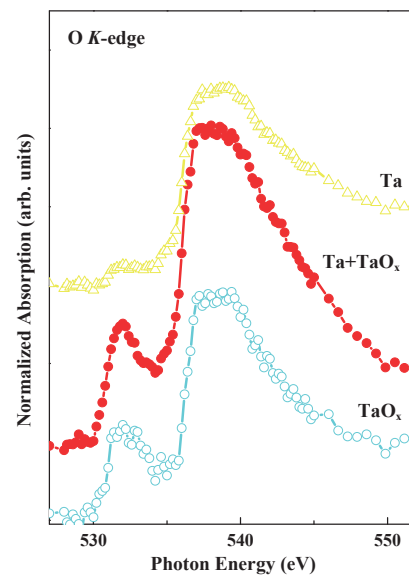


Fig. 2. The corresponding O K-edge STXM-XANES spectra were recorded at three selected regions, *cyan*, *red* and *yellow*, in the Ta/TaO_x/Pt thin film, respectively.

[1] J. W. Chiou *et al.*, Appl. Phys. Lett. **81** (2002) 3389.

BL4U

Resolving the Electronic Structure of TiO₂ Core-Shell Nanostructures Using Scanning Transmission X-Ray Microscope

Y. F. Wang¹, S. H. Hsieh¹, J. W. Chiou², W. F. Pong¹, T. Ohgashi³ and N. Kosugi³

¹Department of Physics, Tamkang University, Tamsui 251, Taiwan

²Department of Applied Physics, National University of Kaohsiung, Kaohsiung 811, Taiwan

³UVSOR Synchrotron, Institute for Molecular Science, Okazaki 444-8585, Japan

In this work, a three-dimensional (3D) hierarchical TiO₂ is successfully constructed using scanning transmission x-ray microscopy (STXM). The core portion of the sample contains rutile TiO₂ nanowire (NW) while the rutile nanoparticles (RNP) and anatase TiO₂ are sequentially located on the shell region. The TiO₂ NW array provides a fast electron transport pathway due to its quasi-single-crystalline structure and the 3D configuration with NPs in the shell portion provides a large surface area for more efficient photo-charge separation without significantly sacrificing the electron collection efficiency [1] which attracted our interest to probe this nano-scale interface phenomenon.

Figure 1 shows the (a) scanning electron microscope (SEM) and (b) STXM images of focused ion beam (FIB) milled ANP/RNP/NW sample (above the red dashed line) on fluorine doped tin oxide (FTO) substrate (below the red dashed line). The STXM image was recorded at 460 eV. Fig. 2(a) shows the magnified STXM image in middle of sample of Fig. 1 (b), where Ti L_{2,3}-edge x-ray absorption near edge spectra (XANES) had been measured and analyzed by principle component analysis (PCA) method. Fig. 2(b) was generated by PCA method analyzed in the same area shown in Fig. 2(a) and indicates similar spectra with the same color which defines the spatial distribution of background (blue), Pt (yellow), carbon film (purple) and surface (red), semi-surface (green), shell (brown), semi-core (orange), core (cyan) regions of ANP/RNP/NW.

Figure 2(c) depicts the Ti L_{2,3}-edge XANES of different regions of ANP/RNP/NW. Line shapes of e_g-states in L₃-edge around 458 eV show the anatase phase TiO₂ in the surface (red) and semi-surface (green) regions [2], the rutile phase TiO₂ in core (cyan) region and mixed spectra of anatase and rutile phases in shell (brown) and semi-core (orange) regions. These results reveal that even the size of ANP is smaller than the spatial resolution of STXM [3], the spatial distribution of different phases of TiO₂ core-shell structures can still be successfully resolved under STXM after FIB milling.

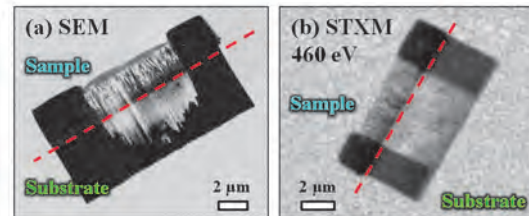


Fig. 1. (a) SEM image of ANP/RNP/NW on FTO. (b) STXM image of ANP/RNP/NW on FTO measured at 460 eV.

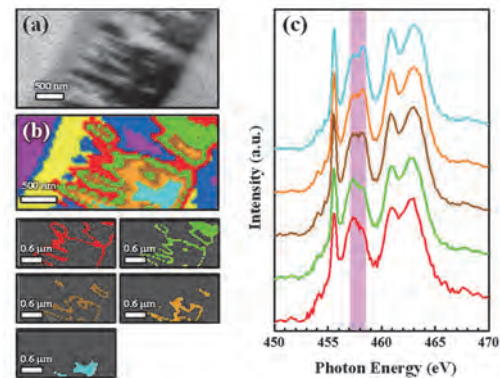


Fig. 2. (a) Magnified STXM image of ANP/RNP/NW. (b) Spatial distribution of background (blue), Pt (yellow), carbon film (purple) and surface (red), semi-surface (green), shell (brown), semi-core (orange), core (cyan) regions of ANP/RNP/NW. (c) Corresponding Ti L_{2,3}-edge XANES of different regions of ANP/RNP/NW.

[1] J. Y. Shin *et al.*, *Adv. Funct. Mater.* **21** (2011) 3464.

[2] J. S. Yang, *Appl. Mater. Interfaces* **5** (2013) 7425.

[3] G. S. Henderson *et al.*, *Phys. Chem. Minerals* **29** (2002) 32.

BL4U

Effect of Fe₂O₃ Coating on ZnO Nanorod Probed by Scanning Transmission X-Ray Microscopy

Y. X. Chen¹, Y. F. Wang¹, J. W. Chiou², C. L. Dong¹, W. F. Pong¹, T. Ohgashi³
and N. Kosugi³

¹Department of Physics, Tamkang University, Tamsui 251, Taiwan

²Department of Applied Physics, National University of Kaohsiung, Kaohsiung 811, Taiwan

³UVSOR Synchrotron, Institute for Molecular Science, Okazaki 444-8585, Japan

A novel Fe₂O₃/ZnO core-shell nanorods for photoelectrochemical (PEC) water splitting is developed recently [1]. The PEC performances, such as photocurrent response and incident photons to electrons (IPCE), vary with the thickness of Fe₂O₃ coating layer. However, the mechanism of the improved PEC activity remains unclear. In this work, pristine and Fe₂O₃ coated-ZnO core-shell nanorods have been investigated by using x-ray spectroscopic coupled with microscopic approaches (i.e., x-ray absorption near-edge structure (XANES) and scanning transmission X-ray microscopy (STXM)).

Figures 1(a)-(d) present the O K-edge STXM images and its stack mappings of selected single nanorod of Fe₂O₃/ZnO and pristine ZnO. The stack mappings display blue, yellow, red and green areas, corresponding to the different regions that are associated with different thickness and chemical properties of the nanorods. Figures 1 (e)-(h) show the XANES spectra, which correspond to Figs. 1 (a)-(d). The different colored spectra reflect the various region of the nanorods. The O K-edge probes the electron transitions from O 1s core level to the O 2p-Zn 3d/4sp hybridized states. The area under the spectrum reflect the amount of density of unoccupied O 2p-derived states. Thus, based on the spectroscopic results, the electronic structures of the layer region and the core area differ in both samples. Besides, strong anisotropic effects are observed for both samples based on polarized-XANES. Notably, the density of states in the surface of the coated- and pristine nanorods are different and the results suggest that the oxygen-related deficiency is formed in the core-shell nanorods which can affect the photocatalytic activity.

The enhanced PEC performance of Fe₂O₃ coated ZnO compared with pristine ZnO is likely to be owing to the presence of interface that causes varied electron density of states in the core-shell structured nanorods.

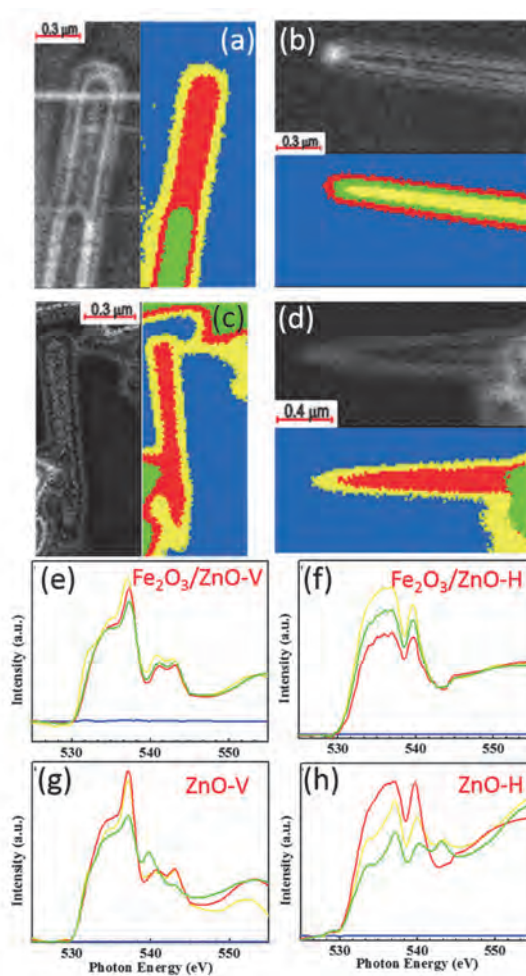


Fig. 1. Upper panel: Polarized O K-edge scanning transmission X-ray microscopy image and its corresponding stack mappings of selected single Fe₂O₃ coated- ((a) and (b)) and pristine ZnO nanorods ((c) and (d)). Lower panel: Polarized O K-edge STXM-XANES spectra of Fe₂O₃ coated- ((e) and (g)) and pristine ZnO nanorods ((f) and (h)). The color corresponds to the different region of the nanorods.

[1] Y. K. Hsu *et al.*, ACS Appl. Interfaces 7 (2015) 14157.

BL4U

Mapping Oxygen Activation on Different Surface Facet of Palladium Nanocrystals for Organic Catalysis

M. W. Lin¹, Y. L. Lai¹, M. H. Cao², T. Ohgashi³, N. Kosugi³, Q. Zhang² and Y. J. Hsu^{1*}

¹National Synchrotron Radiation Research Center, Hsinchu 300, Taiwan

²Institute of Functional Nano- & Soft Materials (FUNSOM) Soochow University, 215123, P. R. China

³Institute for Molecular Science, Okazaki 444-8585, Japan

Electronic mail: yjhsu@nsrc.org.tw

The O₂ activation process where inert ground triplet O₂ is excited to produce highly reactive singlet O₂ involves a key step in many organic oxidation and cancer treatment. However, it puzzles scientist what factor induces the change of electron spin state of O₂ molecules, although it has demonstrated that the presence of noble metal nanoparticles can promote the generation of singlet O₂. In previous works, Q. Zhang *et al.*, first demonstrated that surface facet of metal nanocrystals is a key parameter for tuning the activities of generating singlet oxygen. The experiments and simulations elucidated that a spontaneous spin-flip process may occur during the molecular absorption when appropriate surface facets are selected. On a selected surface facet, the charge state of the Pd surface is a critical parameter to activate O₂ to generate a species that behaves like singlet O₂ both chemically and physically [1]. Based on this finding, we prepared a metal–semiconductor hybrid system in which the nanocrystals of Pd{100} facets are supported on TiO₂ surface. Through illumination of appropriate light, the electrons are anticipated be transferred from TiO₂ to metallic Pd catalysts and thus enhance the oxygen activation.

To confirm the charge transfer at the heterojunction between TiO₂ and Pd heterojunction, chemical maps of oxygen distributions within microaggregates of SiN/TiO₂-Pd were studied by scanning transmission X-ray microscopy (STXM). The TiO₂-Pd hybrid structures were obtained according to following procedures. The Pd nanocubes with 20 mg TiO₂-P25 were synthesized according to a previously described protocol [2]. In a typical synthesis, 8.0 mL of an aqueous solution containing poly(vinyl pyrrolidone) (PVP, MW = 55 000, Sigma–Aldrich, 856568-100g; 105 mg), l-ascorbic acid (AA, Sigma–Aldrich, A0278-25g; 60 mg), and KBr (300 mg) was heated in a 50 mL three-necked flask for 10 min at 80 °C with magnetic stirring. Subsequently, 3.0 mL of an aqueous solution of potassium palladium(II) chloride ([K₂PdCl₄], Aladdin, 1098844-1g ; 63 mg) was added with a pipette, and the reaction mixture was stirred at 80 °C for 3 h. The powders were collected by centrifugation and washed with deionized water to remove excess PVP. The final product was dissolved into the deionized water and then dipped onto the SiN substrate.

Figure 1 displays the STXM images of (a) SiN/TiO₂-Pd (cubes {100} facets) and (b) SiN/TiO₂-Pd (octahedrons {111} facets), which are optical density

(OD) maps obtained at 530.9 eV, the major characteristic absorption peaks of TiO₂. The bright region represents elemental distributions of O in TiO₂. The corresponding micro NEXAFS spectra extracted from different color circles as shown in Figs. 1(a) and (b) are displayed in Figs. 2(a) and 2(b), respectively. The resonance at 530.9 eV for both surface facet is assigned to 1σ_O → 1π_g* transition for TiO₂ contacted with Pd surface. Noticeably, the absorption peak at higher photon energy for TiO₂-Pd{100} (at 533.3 eV) shifts to lower photon energy in comparison with TiO₂-Pd{111} (at 533.6 eV), indicating that significant electrons are transferred from TiO₂ to the Pd{100} surface. The preliminary results indicate that the chemical mapping of oxygen activation on different surface facet of Pd nanocrystals will shed light on designing high efficient noble metal nanocatalysts for organic oxidation and cancer treatments.

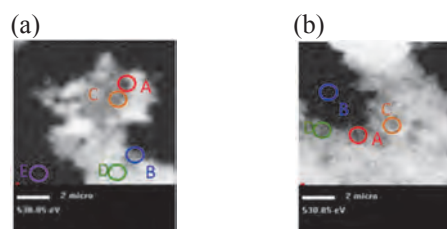


Fig. 1. The OD images of (a) SiN/TiO₂-Pd (cubes {100} facets) and (b) SiN/TiO₂-Pd (octahedrons {111} facets) obtained at 530.9 eV.

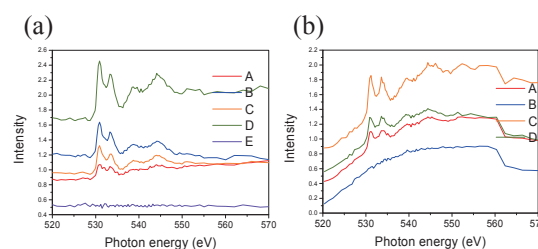


Fig. 2. Micro-NEXAFS spectra of the O K-edge extracted from the Figs. 1(a), and 1(b), respectively.

- [1] L. Ran, M. Keke, Y. Xiaodong, Y. Wensheng, H. Yaobing, W. Jianyong, F. Yao, W. Xisheng, W. Xiaojun, X. Yi and X. Yujie, *J. Am. Chem. Soc.* **135** (2013) 3200.
 [2] B. Li, R. Long, X. Zhong, Y. Bai, Z. Zhu, X. Zhang, M. Zhi, J. He, C. Wang, Z.-Y. Li and Y. Xiong, *Small* **8** (2012) 1710.

BL4B

Valence State Analysis of Mn Ions Doped in CaTiO₃

T. Murai¹, K. Mori¹, D. Yamada¹, H. Murata² and T. Yamamoto^{1,3}

¹Faculty of Science and Engineering, Waseda University, Tokyo 169-8555, Japan

²Association of International Arts and Science Institute of Natural Science, Yokohama City University, Yokohama 236-0027, Japan

³Institute of Condensed-Matter Science, Waseda University, Tokyo 169-8555, Japan

Multiferroic materials, which have both ferroelectric and ferromagnetic properties, have been extensively studied for their potential applications in industry. It was reported that the ABO₃ type oxides, e.g., BiFeO₃ and YMnO₃, show multiferroic properties, and, on the other hand, dilute doping of the magnetic element into the ferroelectric material gives ferromagnetic property, which means such materials also have a multiferroic property. One of the examples of the later ones is Fe doped Bi₄Ti₃O₁₂ [1]. To understand the mechanism of newly appeared ferromagnetism by dilute doping of magnetic element in such ferroelectric materials, it is mandatory to know the local environment of doped ions. However, it is not so easy to determine the local environment of such dilute dopants that one often skips such important analysis. In the case of the valence state analysis of 3d transition metals, analysis with L_{2,3}-edge X-ray absorption spectrum (XAS) is quite powerful. We could successfully determine local environment of Mn and Fe ions doped in Bi₄Ti₃O₁₂ by such XAS analysis [2, 3]. In the current study, valence state of Mn ions in Mn-doped CaTiO₃ is investigated by the Mn-L₃ XAS measurements.

Samples were prepared by the solid state reaction method. High purity powders of CaCO₃, TiO₂ and Mn₂O₃ were used as starting materials. These powders were weighed by changing the concentration of Mn ions, which were mixed and ground in an agate mortar for 30 min. with ethanol. After drying these mixtures, they were calcined in air for 2 hrs at 1423 K. Resultant powders were mixed and ground again, which were pressed into pellet form. These pellets were sintered in air at 1523 K for 6 hrs.

Crystal structures of the sintered samples were examined by the powder X-ray diffraction with Cu-K α X-rays. Resultant XRD patterns show no extra peaks except for those from orthorhombic perovskite structured CaTiO₃. In addition, lattice parameters deduced from the observed XRD pattern decrease due to the doping of Mn ions in CaTiO₃. These results suggest doped Mn ions are substituted at one of the cation sites, i.e., Ca²⁺ or Ti⁴⁺ sites, in CaTiO₃.

Mn-L₃ X-ray absorption spectrum of Mn doped CaTiO₃ were measured at BL4B in UVSOR. Incident beam was monochromatized by varied-spacing plane grating (800 l/mm) and energy resolution was tuned by controlling the heights of the slits settled at upper and lower reaches of grating. Samples were placed on the

carbon adhesive tape, which was attached on the first Cu-Be dinode of the electron multiplier. All the XAS measurements were carried out in a total electron yield (TEY) mode by collecting the sample drain current.

Observed Mn-L₃ XAS spectrum of Mn-doped CaTiO₃ is shown in Fig. 1 together with those of MnO (Mn²⁺) and MnO₂ (Mn⁴⁺), in which that of MnO₂ shows much better agreement with experimental profile of Mn-doped CaTiO₃. From these results, i.e., reduction of cell parameter by XRD and XANES analysis, it can be concluded that Mn ions are substituted as Mn⁴⁺ ions in CaTiO₃.

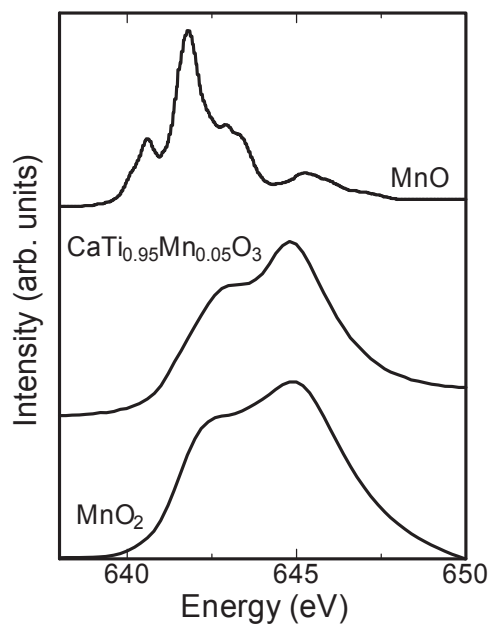


Fig. 1. Observed Mn-L₃ X-ray absorption spectra of Mn-doped CaTiO₃ (middle) and Mn oxides (MnO: top and MnO₂: bottom).

[1] X. Q. Chen *et al.*, Solid State Comm. **150** (2010) 1221.

[2] K. Nishimura *et al.*, IEEE Trans. Mag. **50** (2014) 2502306.

[3] K. Nishimura *et al.*, UVSOR Activity Report 2013.

BL4B

Effect of Carbon Substitution on the Magnetic Properties of Nano-Architectural ZnO

Y. F. Wang¹, W. F. Pong¹, J. W. Chiou², Y. Takagi³, T. Ohgashi³, T. Yokoyama³
and N. Kosugi³

¹Department of Physics, Tamkang University, Tamsui 251, Taiwan

²Department of Applied Physics, National University of Kaohsiung, Kaohsiung 811, Taiwan

³UVSOR Synchrotron, Institute for Molecular Science, Okazaki 444-8585, Japan

Based on our previous publication in *Nanoscale* 6, 9166-9176 (2014) entitled "Observation of the origin of d^0 magnetism in ZnO nanostructure using x-ray-based microscopic and spectroscopic techniques", we observed zinc vacancies (V_{Zn}) induced orbital moments in oxygen sites near the surface of nano-architectural ZnO via combined synchrotron based techniques and first principle calculations [1]. Moreover, since the carbon-doped ZnO have been proposed and observed to be ferromagnetic with Curie temperature well above room temperature, and different carbon-related defects can result entirely different magnetism in carbon-doped ZnO as theoretically predicted. The correlation between carbon-related defects and magnetism has become an important issue experimentally for non-magnetic impurities induced dilute magnetic semiconductors. Due to this novel but controversial issue, nano-architectural ZnO is an ideal system to investigate. The defects-related phenomenon due to the large surface to volume ratio and intrinsic V_{Zn} on the surface of nanostructures provide an opportunity to study how carbon implantation affects the electronic structures and magnetism of ZnO.

Figure 1 shows the C K -edge XANES and XMCD spectrum of (a) carbon-implanted ZnO nano-wires (C:NWs) and (b) carbon-implanted ZnO nano-cactus (C:NCs). The XMCD signals appear around 287-292 eV suggest the origin of enhancement in room temperature ferromagnetism (RTFM) of carbon-implanted nano-architectural ZnO can be correlated to π -like hybridization states between carbon and oxygen [2], or zinc atoms. A weaker XMCD signal shows in C:NCs with respect to NWs suggests V_{Zn} may suppress ferromagnetic ordering between magnetic-impurities since C:NCs contain higher density of V_{Zn} which provides higher possibility for carbon substitution into V_{Zn} sites and hybridize with oxygen to form non-spin-polarized C_{Zn} [3]. Carbon substituted oxygen (C_O) can introduce holes into system which satisfies Stoner criterion easily and results stronger localization spins in carbon with respect to V_{Zn} [4]. Spin-polarized C_{Zn} - C_I (interstitial carbon) complex in V_{Zn} sites should be considered since highly dense C_I can form carbon-related complexes easily, but relatively weak magnetization and XMCD signal in C:NCs with respect to C:NWs suggests dominant spin-polarized carbon impurity is C_O [5].

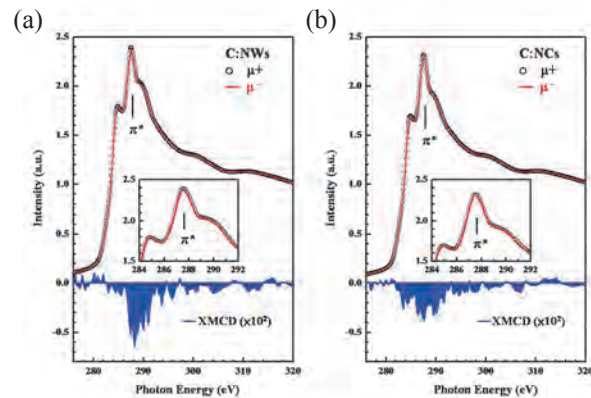


Fig. 1. C K -edge XANES and XMCD spectrum of (a) C:NWs and (b) C:NCs.

- [1] Shashi B. Singh *Nanoscale* **6** (2014) 9166.
- [2] Y. F. Wang *et al.*, *Sci. Rep.* **5** (2015) 15439.
- [3] S. K. Nayak *et al.*, *Phys. Rev. B* **86** (2012) 054441.
- [4] H. Peng *et al.*, *Phys. Rev. Lett.* **102** (2009) 017201.
- [5] S. Sung *et al.*, *Semicond. Sci. Technol.* **26** (2011) 014038.

BL6B

UV-Induced Infrared Absorption Change in SrAl₂O₄:Eu Crystals: Influence of Eu²⁺ Concentration on Trap Filling Process

Y. Tsurumi¹, M. Kitaura¹, A. Ohnishi¹, T. Ishibashi², S. Furukawa², H. Oda² and A. Yamanaka²

¹Faculty of Science, Yamagata University, Yamagata 990-8560, Japan

²Chitose Institute of Science and Technology, Chitose 444-8585, Japan

The control of shallow electron traps is most significant in the development of high luminance long-persistent phosphors. So far, the energies of trap depths have been evaluated from both sides of experimental and theoretical approaches. The so-called “Dorenbos model” [1] provides us fruitful information on the optimization of co-dopants working as photocarrier traps. On the other hand, the trap filling process is also important; however, it has not been discussed so much, and still remains obscure. It is thus necessary to clarify the factors dominating the trap filling process, and to determine the optimal condition which gives rise to high luminance long persistent phosphorescence. For these purposes, we have studied the influence of europium concentration on trap filling process in SrAl₂O₄:Eu²⁺ crystals grown by the Floating zone method.

Figure 1 shows absorption spectra of SrAl₂O₄:Eu crystals with europium concentrations of 0.1 (a), 0.3 (b), and 1 mol% (c). These data were observed at 9 K. Blue and red lines indicate absorption spectra observed before and after UV-irradiation at 375 nm, which can cause long persistent phosphorescence [2,3]. An absorption band appears around 2000 cm⁻¹ under UV-irradiation. The UV-induced band around 2000 cm⁻¹ could not be observed for undoped SrAl₂O₄ crystals. This result suggests that the Eu²⁺ 4*f*-5*d* absorption triggers an appearance of the UV-induced band. According to the Dorenbos model, the lowest-energy 5*d* level in the Eu²⁺ 4*f*⁵ 5*d*¹ configuration locates just below the bottom of the conduction band of host SrAl₂O₄. Excited electrons at the lowest-energy 5*d* level can easily migrate to be trapped by lattice imperfections. Therefore, it is more likely that the UV-induced band is caused by the formation of electron traps.

The UV-induced band was weakened when the europium concentration is increased from 0.1 to 1.0 mol%. Apparently, the efficiency of trap filling is influenced by the concentration of Eu²⁺ ions. As the europium concentration becomes higher, the penetration depth becomes smaller. If excited electrons cannot migrate a long distance, they will be trapped by lattice imperfection in the vicinity of Eu²⁺ ions excited by UV-light. Since the amount of such imperfections becomes low with increasing europium concentration, the UV-induced band is weakened as we observed.

The present study demonstrated that the trap filling occurs most efficiently in the case of low Eu²⁺ concentration. This information gives a guiding principle for the material design of high luminance

long-persistent phosphors. Unfortunately, we could not exhibit UV-induced absorption change for SrAl₂O₄:Eu²⁺ crystals with Eu²⁺ concentrations less than 0.1 mol%, because of difficulties for adjusting such extremely low europium concentration. This subject is now under investigation.

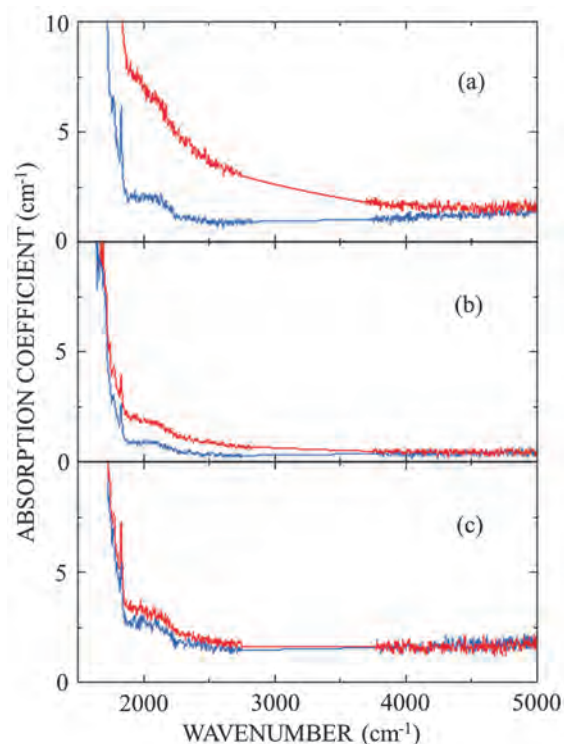


Fig. 1. Absorption spectra of SrAl₂O₄:Eu crystals with europium concentrations of 0.1 (a), 0.3 (b), and 1.0 mol% (c). These data were observed at 9 K. Blue and red lines indicate absorption spectra observed before and after UV-irradiation at 375 nm.

[1] P. Dorenbos and J. J. Bos, *Rad. Meas.* **43** (2008) 139.

[2] Y. Kamiyanagi *et al.*, *J. Lumi.* **122-123** (2007) 509.

[3] M. Kitaura, *J. Ceram. Proc. Res.* **12** (2011) s33.

BL6B

Suppression of Electron Traps in Ce:GAGG Crystals by Mg²⁺ Co-Doping

R. Inaba¹, M. Kitaura², K. Kamada³, S. Kurosawa³, A. Ohnishi² and K. Hara⁴

¹ Graduate School of Science and Engineering, Yamagata University, Yamagata 990-8560, Japan

² Department of Physics, Faculty of Science, Yamagata University, Yamagata 990-8560, Japan

³ New Industry Creation Hatchery Center, Tohoku University, Sendai 980-8579, Japan

⁴ Research Institute of Electronics, Shizuoka University, Hamamatsu 442-8529, Japan

Cerium doped Gd₃Al₂Ga₃O₁₂ (Ce:GAGG) crystals have been developed as an inorganic scintillator with excellent features such as high density, high light yield, and short decay time [1]. The scintillation properties are influenced by the existence of lattice imperfections, because they are responsible for the occurrence of delayed luminescence [2]. In order to improve scintillation properties, it is necessary to find out how to suppress lattice imperfections in the process of crystal growth. Therefore, the information of crystal defects is indispensable. Recently, it was reported that co-doping of alkali-earth ion is effective for the improvement of scintillation properties [3]. However, the mechanism of such alkali-earth ion co-doping has not yet been clarified. So far, we have investigated infrared absorption spectra of Ce:GAGG crystals under UV-irradiation at low temperatures [4]. The data were limited in the energy range of 0.05-1.2 eV. In the present study, we have extended the measurement of absorption spectra to higher energy side. Furthermore, we have investigated UV-induced absorption change for Mg co-doped Ce:GAGG (Ce,Mg:GAGG) crystals.

Ce:GAGG and Ce,Mg:GAGG were grown by the Cz method. The concentration of cerium and magnesium ion was set to 1.0 and 0.1 mol%, respectively. Experiment was performed at the beamline BL6B of UVSOR. The UV-irradiation was carried out at 3.31 eV with a picosecond light pulser. The sample temperature was set to 9K.

Figure 1 shows absorption spectra of Ce:GAGG crystals. A black line represents the absorption spectrum obtained before UV-irradiation. When the UV-irradiation is turned on, the absorption spectrum exhibits a broad band with the peak at 1.5 eV, as indicated by a blue line. The UV-light can excite electrons to a Ce³⁺ 5d level in the conduction band, and triggers the formation of electron traps [4]. In addition, the Ce³⁺ 4f-4f peak around 0.5 eV is weakened by 3 % under UV-irradiation at 9K. As the formation of electron traps is responsible for the weakening of the Ce³⁺ 4f-4f peak, the concentration of electron traps is estimated to be 10¹⁸ cm⁻³. This value is two orders of magnitude higher than the concentration of lattice imperfections in typical intrinsic semiconductors.

Figure 2 shows absorption spectra of Ce,Mg:GAGG crystals before and after UV-irradiation. The UV-induced band around 1.5 eV

disappears by Mg ion co-doping. This fact indicates that the Mg co-doping hinders the formation of electron traps. There are two hypotheses concerning the role of Mg co-doping: One is that Mg²⁺ ions play as charge compensators to suppress lattice imperfections, and the other is that electron traps are destabilized by controlling the energy band of host crystals. Further experimental works are needed to solve the role of Mg co-doping.

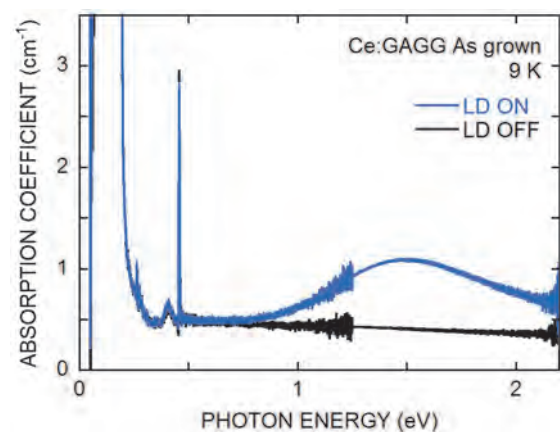


Fig. 1. UV-induced change of absorption spectra in Ce:GAGG crystals measured at 9 K.

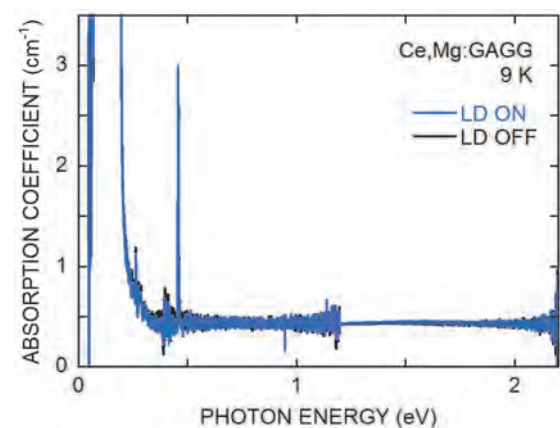


Fig. 2. UV-induced change of absorption spectra in Ce,Mg:GAGG crystals measured at 9 K.

- [1] K. Kamada *et al.*, J.Cryst. Growth **352** (2012) 82.
- [2] M. Kitaura *et al.*, J. Appl. Phys. **115** (2014) 083517.
- [3] K. Kamada *et al.*, Opt. Mater. **41** (2015) 63.
- [4] R. Inaba *et al.*, UVSOR Activity Report **42** (2015) 83.

BL6B

Measurement Temperature Dependency of Ultrashallow Thermal Donors and Observation of Shallow Donors in Carbon- and Hydrogen-Doped Czochralski Silicon Crystals

A. Hara and T. Awano

Department of Electronic Engineering, Tohoku Gakuin University, Tagajo 985-8537, Japan

We previously reported on ultrashallow thermal donors (USTDs) in carbon- and hydrogen-doped Czochralski silicon (CZ Si) crystals [1, 2]. USTDs are hydrogen-like donors with slightly different energy levels, some of which show negative central-cell correction. To the best of our knowledge, these are the shallowest energy levels as compared with those of previously reported donors in Si crystals. However, we identified USTDs as shallow donors by a comparison with effective-mass theory. In this study, we measured the intensity of USTDs as a function of measurement temperature to identify USTDs as shallow donors.

Carbon-doped CZ Si samples were doped with hydrogen by annealing in wet oxygen at 1300°C for 60 min. The samples were then cooled to room temperature by rapidly exposing to air. For carbon doping, the Si melt for preparing the ingot was doped with carbon powder during CZ Si crystal growth. Transmission spectra were obtained with a far-IR spectrometer of the BL6B beamline at different temperatures using a flowing cryostat.

Figure 1 shows the temperature dependency of USTDs and STD(H)s at different measurement temperatures. Both spectra decrease as the measurement temperature increases up to 70 K. Figure 2 shows variations in the peak intensity of USTDs and STD(H)s against the measurement temperature. The intensities of both defects show a similar dependency on the measurement temperature, which indicates that the energy levels of both are very close. Since STD(H)s are identified as shallow donors [3], it is reasonable that the energy levels of USTDs are very close to those of STD(H)s. This is consistent with our previous proposal that USTDs are donors with energy levels close to the conduction band.

In addition, we observed broad peaks at high measurement temperatures of around 50 K. They are indicated as A, B, and C in Fig. 1. The differences in wavenumber between A and B, and B and C, are consistent with the predictions of effective-mass theory. Thus, the peaks A, B, and C are identified as $1s-2p_0$, $1s-2p_{+}$, and $1s-3p_{+}$ transition of new shallow donor, respectively.

In summary, we observed the measurement temperature dependency of the spectra of USTDs. This behavior is consistent with our previous results, which were derived from effective-mass theory. Moreover, we found new broad optical absorption peaks, which is consistent with the predictions of effective-mass theory.

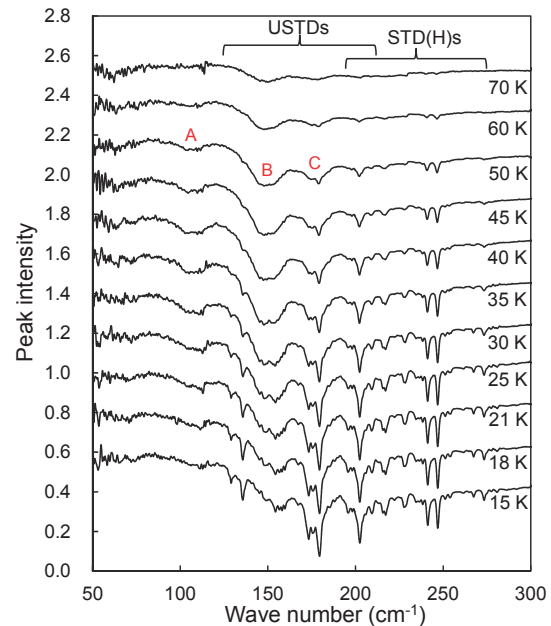


Fig. 1. Temperature dependency of optical absorption peaks of USTDs and STD(H)s.

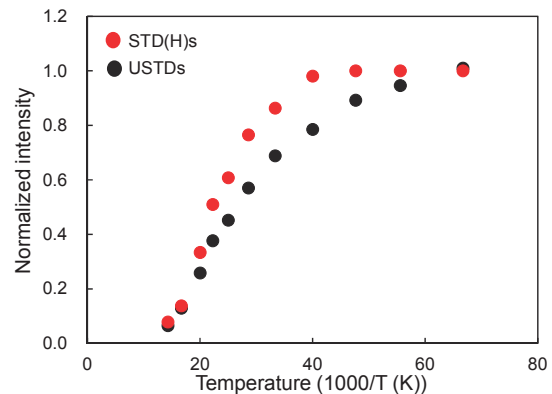


Fig. 2. Temperature dependency of USTDs and STD(H)s.

- [1] A. Hara, T. Awano, Y. Ohno, and I. Yonenaga, *Jpn. J. Appl. Phys.* **49** (2010) 050203.
 [2] A. Hara and T. Awano, *Jpn. J. Appl. Phys.* **54** (2015) 101302.
 [3] R. C. Newman, J. H. Tucker, N. G. Semaltianos, E. C. Lightowers, T. Gregorkiewicz, I. S. Zevenbergen, and C. A. J. Ammerlaan, *Phys. Rev. B* **54** (1996) R6803.

BL6B

Evaluation of Domain Wall in Alkali Niobate Piezoelectrics by Far-Infrared Reflective Method

Y. Taniguchi, N. Matsubara, K. Yoshida, T. Fuchigami and K. Kakimoto
Graduate School of Engineering, Nagoya Institute of Technology, Nagoya 466-8555, Japan

It is generally accepted that domain structure is a major factor for the origin of piezoelectric property, and specifically that domain walls contribute significantly to the properties. We evaluated domain walls both for (Na,K)NbO₃ crystal and ceramics by Raman spectroscopy and suggested that ferroelectric and piezoelectric properties at the walls might be different far from those of adjacent domain regions [1]. In the previous work, we observed various permittivity depending on the focused regions of (Na,K)NbO₃ crystal by using mid-infrared as a light source [2]. However, there were some problems of the short distance in mapping measurement and of the low intensity of Infrared(IR) reflectivity. Therefore, long-distance and high-intensity line mapping measurements were performed in this work using synchrotron radiation source, and we tried to evaluate domain walls especially for the permittivity in a stripe domain structure.

(Na_{0.55}K_{0.45})(Nb_{0.995}Mn_{0.005})O₃(NKN) crystal with stripe domains(20-80 μm width) was measured by a FT-IR spectrometer (Bruker, VERTEX 70v). IR measurements were performed vertically to the domain wall every 10 μm in a total range of 100 μm. The spectra were fitted to obtain permittivity according to the following equation:

$$\varepsilon(\omega) = \varepsilon_{\infty} + \sum_n \frac{\omega_{pn}^2}{\omega_{on}^2 - \omega^2 - n\gamma_n\omega} \quad (1)$$

where, ε_{∞} is the high-frequency dielectric constant, ω_p and ω_o the plasma and longitudinal frequencies, and γ the damping constant. The complex dielectric function is related to the reflectivity spectrum by the equation

$$R = |\sqrt{\varepsilon(\omega)} - 1| / |\sqrt{\varepsilon(\omega)} + 1|^2 \quad (2)$$

Figure 1 shows IR reflectivity spectra of NKN crystal. The reflectivity was 0.6 when using mid-infrared. On the other hand, the reflectivity significantly increased by using synchrotron radiation, and it was 0.8 at a maximum even in 0.25 aperture diameter. The reason is that the synchrotron radiation had a more than 6 times larger reflection intensity in Si bolometer than that of mid-infrared. Hence, IR reflectivity measurement by synchrotron radiation should give reliable data of permittivity.

Considering the width of the stripe domains in the NKN crystal (20-80 μm), permittivity ε' should change periodically in 20-80 μm measurement range owing to the effect of domain wall. Figure 2 shows the permittivity of NKN crystal at each measurement position with an aperture diameter of 0.25 mm. The

permittivity ε' showed values between 65 and 70 except at the measurement positions of 30, 50 and 100 μm. Permittivity ε' increased periodically in 20-50 μm measurement range, and the values at 30, 50 and 100 μm positions were approximately 80, which is approximately 20% higher compared to the other positions. These results suggested that the permittivity increases at the domain walls. Therefore, domain walls could be evaluated on the basis of the increase in permittivity by IR reflectivity measurement. In addition, we think that ferroelectric and piezoelectric properties remarkably improve with increasing the density of domain wall in the materials.

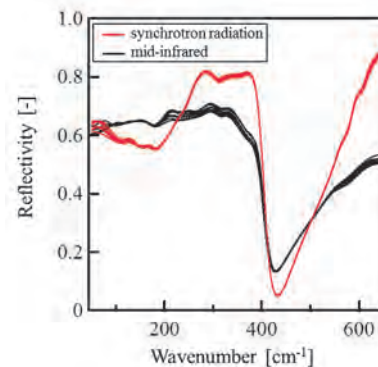


Fig. 1. IR reflectivity spectra of NKN crystal obtained using synchrotron radiation and mid-infrared as light source.

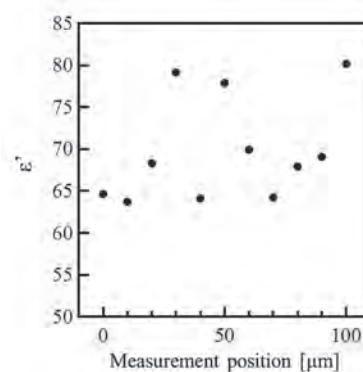


Fig. 2. Permittivity ε' of NKN crystal at measurement positions obtained using synchrotron radiation as light source.

[1] Y. Taniguchi and K. Kakimoto, Japanese Journal of Applied Physics **54** (2015) 10ND09.

[2] Y. Taniguchi, T. Yamazaki, M. Kato and K. Kakimoto, UVSOR Activity Report **42** (2015) 85.

BL7U

High-Resolution ARPES Study of Noncentrosymmetric Weyl Semimetal Candidate NbP

S. Souma¹, Z. Wang², H. Kotaka², T. Sato³, K. Nakayama³, Y. Tanaka³, H. Kimizuka³, K. Yamauchi², T. Oguchi², K. Segawa⁴, Y. Ando^{2,5} and T. Takahashi^{1,3}

¹WPI Research Center, Advanced Institute for Materials Research, Tohoku University, Sendai 980-8577, Japan

²Institute of Scientific and Industrial Research, Osaka University, Ibaraki 567-0047, Japan

³Department of Physics, Tohoku University, Sendai 980-8578, Japan

⁴Department of Physics, Kyoto Sangyo University, Kyoto 603-8555, Japan

⁵Institute of Physics II, University of Cologne, Köln 50937, Germany

Weyl semimetals (WSMs) manifest a novel quantum state of matter where the bulk conduction and valence bands cross at discrete points, defined as Weyl nodes, with linear dispersion in all the momentum (k) directions in three-dimensional Brillouin zone, which can be viewed as a three-dimensional analogue of graphene breaking time-reversal or space-inversion symmetry [1,2]. The WSMs can host many exotic physical phenomena such as anomalous Hall effects, chiral anomalies, and magnetoelectric effects. The most intriguing prediction for WSMs is the emergence of Fermi arcs on their surfaces. Unlike two-dimensional metals showing *closed* Fermi surface (FS), the Fermi arcs in WSMs are disjoint, *open* curves. Recently, density functional theory predicted that noncentrosymmetric transition-metal monpnictide family TaAs, TaP, NbAs, and NbP are WSMs [3,4]. To firmly establish the WSM nature of monpnictides and to build a basis for the proposed exotic phenomena, it is of particular importance to experimentally establish the fermiology of transition-metal monpnictide family.

In this study, we have performed high-resolution angle-resolved photoemission spectroscopy (ARPES) of NbP. By utilizing the low photon energy and variable polarization characteristics of the beamline BL-7U, we have succeeded in observing the fine electronic structure that supports the WSM nature of NbP [5].

Figure 1(a) displays a schematic summary of the experimentally observed FS of NbP around \bar{X} . The energy bands labeled here, S_1 - S_4 , all of which are surface states, obey different selection rules of photoelectron intensity. For example, band S_1 is dominantly seen with vertical polarization [Fig. 1(b)]. On the other hand, the intensity of outer band S_2 , which forms a tadpole FS, is greatly enhanced with circularly polarized photons [Fig. 1(c)]. There exist another dog-bone-shaped FSs, S_3 and S_4 , elongated along \bar{X} \bar{M} , which are better resolved with horizontally polarized photons [Fig. 1(d)]. We found that overall cross-shaped FS in the experiment is reasonably reproduced by our calculation and the FS (S_2) which connects Weyl nodes $W2^\pm$ can be viewed as a combination of two Fermi arcs. Namely, one arc starts and ends at $W2$, and the other is connected to $W1$. It is thus likely that

only S_2 forms a Fermi arc and all the others (S_1 , S_3 , and S_4) form trivial FS.

To examine the WSM nature of NbP, we choose closed k -loop ($\bar{\Gamma}$ - \bar{X} - \bar{M} - $\bar{\Gamma}$) surrounding the odd number of (three) Weyl nodes and counted the total number of FS crossings. Since only an open Fermi arc can cross this loop an odd number of times, the total odd number of FS crossings would be a hallmark of the existence of Fermi arcs in WSM. As seen from Fig. 1(a), the Fermi arc (S_2) crosses this loop only once, and the trivial FSs (S_1 , S_3 , and S_4) cross six times. Therefore the observed FSs cross the k -loop seven times in total, supporting the WSM nature of NbP. The present result opens a pathway for the Fermi-arc engineering of Weyl semimetals.

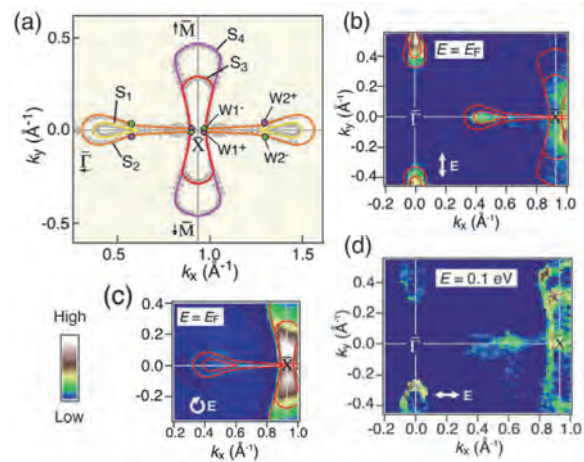


Fig. 1. (a) Experimental FS around \bar{X} of NbP. (b)-(d) Second-derivative intensity of the ARPES spectra measured with vertically-, circularly-, and horizontally-polarized photons, respectively. Polarization vector of lights is indicated by arrow.

- [1] X. Wan *et al.*, Phys. Rev. B **83** (2011) 205101.
- [2] L. Balents, Physics **4** (2011) 36.
- [3] H. Weng *et al.*, Phys. Rev. X **5** (2015) 011029.
- [4] S.-M. Huang *et al.*, Nature Commun. **6** (2015) 7373.
- [5] S. Souma *et al.*, arXiv:1510.01503. (Phys. Rev. B Rapid Commun., *in press*)

BL7U

Angle-Resolved Photoemission Study of the Quasi-One-Dimensional Organic Conductors (TMTTF)₂X (X = AsF₆, SbF₆)

T. Ito^{1,2}, A. Kawakita¹, T. Hajiri¹, K. Tanaka^{3,4}, S. Kimura^{5,6} and T. Nakamura^{3,4}

¹Graduate School of Engineering, Nagoya University, Nagoya 464-8603, Japan

²Nagoya University Synchrotron Radiation Research Center, Nagoya University, Nagoya 464-8603, Japan

³Institute for Molecular Science, Okazaki 444-8585, Japan

⁴School of Physical Sciences, SOKENDAI (The Graduate School of Advanced Studies), Okazaki 444-8585, Japan

⁵Graduate School of Frontier Biosciences, Osaka University, Osaka 565-0871, Japan

⁶Department of Physics, Osaka University, Osaka 565-0871, Japan

The Fabre salts (TMTTF)₂X and Bechgaard salts (TMTSF)₂X (X = PF₆, AsF₆, etc.) belong to a family of quasi-one-dimensional organic conductors. As the chemical pressure of the system tuned with the combination of TMTTF/TMTSF and anion X, these materials allow for a variety of ground states, such as antiferro magnetic insulator, spin-Peierl state, spin-density wave state and superconductor; furthermore one observes a crossover from a Luttinger liquid toward a Fermi-liquid metal, charge-ordered (CO) and charge-localized (loc.) insulator [1, 2].

In this study, we have performed temperature dependent angle-resolved photoemission spectroscopy (ARPES) on single-crystalline (TMTTF)₂X (X = AsF₆, SbF₆) to clarify the relation between the electric structure and the thermodynamic properties. ARPES measurement were performed at UVSOR-III BL7U by utilizing the bulk-sensitive low photon energy ($h\nu = 8$ eV) as well as the micro focus beam ($15 \times 100 \mu\text{m}^2$).

Figures 1 (A1-A8) and (S1-S6) show the temperature dependence of ARPES image along the Γ X direction of (TMTTF)₂AsF₆ and (TMTTF)₂SbF₆, respectively. The schematic illustrations of the corresponding electronic structure have been shown in Fig. 1 (M1) and (M2) for comparison. At low temperature CO states ($T = 30$ K $< T_{CO} = 102$ and 157 K for X = AsF₆ and SbF₆, respectively [3]), we found highly dispersive band away from the Fermi level (E_F) which is accompanied with the lower energy shoulder around X point, and that the band folded around the top of the dispersive features ($k_F \sim 0.25$ and 0.2 \AA^{-1} for X = AsF₆ and SbF₆, respectively). From the comparison with the previous ARPES results of metallic (TMTSF)₂X [4, 5], we have expected that the observed dispersive features can be ascribed as the spinon and holon bands, which is characterized by the spin-charge separation in the one-dimensional system (Figs. 1 (M1) and (M2)).

With increasing temperature, the main dispersive feature of X = AsF₆ and SbF₆ gradually becomes weak around $T = 50 - 150$ K and $T = 100 - 200$ K, respectively. On the other hand, at $T = 200 - 300$ K, the broad non-dispersive feature (shaded area in Figs.1 (M1) and (M2)) around 1 eV dominates the electronic structure of both compounds, though the

slight dispersive feature remains in X = AsF₆. The observed temperature dependence seems to roughly scale with the charge-order transition temperature of each compound. Therefore, we expect that the observed spectral weight transfer from the dispersive spinon-holon bands near E_F to the localized bound state is caused by the transition from charge-ordered insulator to charge-localized state. It should be noted that the metallic states of (TMTTF)₂AsF₆ at $T = 300$ K have been found as a sizable spectral weight at E_F originating from the tail of the localized bound states.

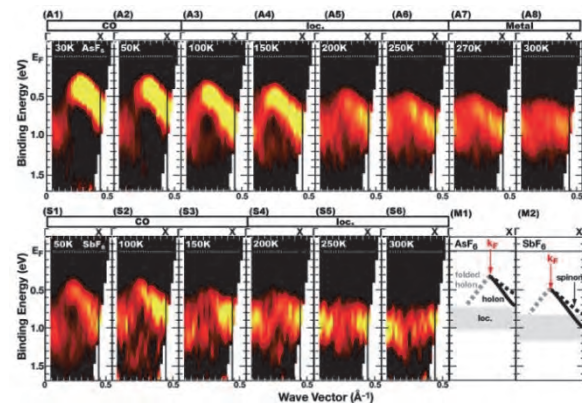


Fig. 1. Temperature dependence of ARPES images of (TMTTF)₂AsF₆ (A1-A8) and (TMTTF)₂SbF₆ (S1-S6) along Γ X direction. (M1, M2) The schematic picture of spinon-holon dispersions (solid and dashed lines) and localized bound state (shaded area) of (TMTTF)₂AsF₆ (M1) and (TMTTF)₂SbF₆ (M2), respectively.

[1] T. Ishiguro *et al.*, *Organic Superconductors* (Springer-Verlag, Berlin, 1998).

[2] E. Rose *et al.*, *J. Phys.: Condens. Mat.* **25** (2013) 014006.

[3] M. Dressel *et al.*, *Adv. Cond. Mat. Phys.* **2012** (2012) 398721.

[4] S. Hirate *et al.*, *UVSOR Activity Report* **39** (2012) 97.

[5] M. Mitamura *et al.*, *UVSOR Activity Report* **40** (2013) 110.

BL7U

Systematic Change of Fermi Surfaces with As Doping in Iron Pnictide Superconductor $\text{NdFeP}_{1-x}\text{As}_x(\text{O},\text{F})$

S. Miyasaka¹, A. Takemori¹, T. Adachi¹, M. Uekubo¹, T. Kobayashi¹, S. Tajima¹, T. Hajiri^{2,3}, M. Matsunami^{3,4} and K. Tanaka^{3,4}

¹Department of Physics, Graduate School of Science, Osaka University, Toyonaka 560-0043, Japan

²Department of Crystalline Materials Science, Graduate School of Engineering, Nagoya University, Nagoya 464-8603, Japan

³UVSOR Facility, Institute for Molecular Science, Okazaki 444-8585, Japan

⁴School of Physical Sciences, The Graduate University for Advanced Studies (SOKENDAI), Okazaki 444-8585, Japan

The iron-based superconductors have various Fermi surface states, which are closely related with the local crystallographic structure around Fe ion. Recently, we studied the physical properties in 1111-type P/As solid solution system, $\text{RFeP}_{1-x}\text{As}_x\text{O}_{0.9}\text{F}_{0.1}$ ($R = \text{La}, \text{Pr}$ and Nd). In these systems, the local structural parameters coupled with Fermi surface conditions are systematically varied by P/As solid solution. Our results have revealed that these systems have two different Fermi surface states and nesting conditions below and above $x = 0.6\sim 0.8$ [1, 2]. To observe the change of Fermi surfaces by P/As solid solution directly, we have investigated the angle resolved photoemission spectroscopy using single crystals of $\text{NdFeP}_{1-x}\text{As}_x(\text{O},\text{F})$ with $x = 0.4, 0.8$ and 1.0 for F concentration $y \sim 0.1$.

The single crystals of $\text{NdFeP}_{1-x}\text{As}_x(\text{O},\text{F})$ were grown by high pressure technique using cubic anvil press and self-flux method [3]. T_c of the single crystals in the present work were 12 K for $x = 0.4$, 23 K for $x = 0.8$ and 44 K for $x = 1.0$, respectively. The angle resolved photoemission spectroscopy were measured at BL7U of UVSOR facility in Institute for Molecular Science using incident photons with $h\nu = 36$ eV linearly polarized.

As shown in Figs. 1(a)-(f), the results of angle resolved photoemission spectroscopy indicate the existence of three hole and two electron Fermi surfaces in $x = 0.4$, and two hole and two electron ones in $x = 0.8$ and 1.0 samples, i.e. the change of FS state around $x = 0.8$. The orbital characters of these Fermi surfaces and electronic bands have been assigned by polarization-dependent angle resolved photoemission spectroscopy, and the d_{xz} hole band around zone center particularly shows the systematic and important x dependence. As shown in Fig. 1(c), the d_{xz} hole Fermi surface exists around zone center at $x = 0.4$. The energy level of d_{xz} band decreases with increasing x , and this band almost sinks below Fermi energy in the $x = 0.8$ sample. With further increasing x , this d_{xz} Fermi surface completely disappears at $x=1.0$ (See Fig. 1(a)).

Other distinct change of Fermi surfaces has been observed around zone boundary. In the $x = 0.4$ and 0.8 samples, we observed two electron Fermi surfaces with circle or elliptic shapes around zone boundary. In

$x = 1.0$, however, the quietly different Fermi surfaces exist. As shown in Figs. 1(a) and (d), this sample has the electron Fermi surface with circle shape and the propeller-like one. These clear changes of Fermi surfaces around zone center and boundary at $x \sim 0.8$ are related with the change of transport and other properties, and supports the scenario of two T_c -rising mechanisms and two Fermi surface states in $\text{RFeP}_{1-x}\text{As}_x(\text{O},\text{F})$.

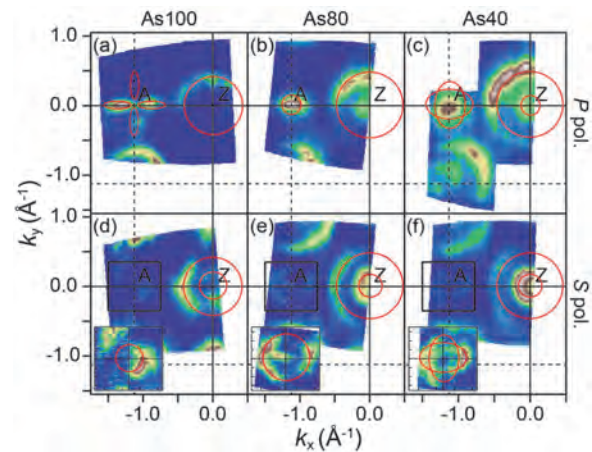


Fig. 1. Fermi surface mapping on k_x - k_y plane of $\text{NdFeP}_{1-x}\text{As}_x(\text{O},\text{F})$ with $x = 1.0$ (As100) ((a) and (d)), $x = 0.8$ (As80) ((b) and (e)) and $x = 0.4$ (As40) ((c) and (f)), respectively. The upper and lower panels show the results by using P - and S -polarization configurations, respectively. The insets of panel (d)-(f) show the detail of Fermi surface mapping around zone boundary in the S -polarization configuration. The red lines indicate the observed Fermi surfaces.

[1] S. Miyasaka *et al.*, J. Phys. Soc. Jpn. **82** (2013) 124706.

[2] K. T. Lai *et al.*, Phys. Rev. B **90** (2014) 064504.

[3] A. Takemori *et al.*, JPS Conf. Proc. **1** (2014) 012111.

BL7U

Electronic Structure of $\text{Sr}_{1-x}\text{Ca}_x\text{Fe}_2(\text{As}_{1-y}\text{P}_y)_2$ ($x = 0.08, y = 0.25$) Revealed by Angle Resolved Photoemission Spectroscopy

 T. Adachi¹, S. Ideta^{2,3}, K. Tanaka^{2,3}, S. Miyasaka¹ and S. Tajima¹
¹Graduate School of Science, Department of Physics, Osaka University, Toyonaka 560-0043, Japan

²UVSOR Facility, Institute for Molecular Science, Okazaki 444-8585, Japan

³School of Physical Sciences, The Graduate University for Advanced Studies (SOKENDAI), Okazaki 444-8585, Japan

It is well known that there is a remarkable correlation between a crystal structure and T_c in iron based superconductor. Thus, it is essential for unraveling the superconducting (SC) mechanism in this system to clarify how the electronic structure changes with the crystal structure. Recent ARPES study has reported that in $\text{SrFe}_2(\text{As}_{1-y}\text{P}_y)_2$ whose c/a (the ratio of a - and c -axes lattice constants), which is index of structural anisotropy, is smaller than that of $\text{BaFe}_2(\text{As}_{1-y}\text{P}_y)_2$, innermost d_{xy} hole Fermi surface shrinks and splits into two pockets, while in $\text{BaFe}_2(\text{As}_{1-y}\text{P}_y)_2$, all the hole Fermi surfaces are connected in the entire k_z region [1, 2]. The reason is considered to be the stronger three-dimensionality (3D) in $\text{SrFe}_2(\text{As}_{1-y}\text{P}_y)_2$ originates from enhanced interlayer hopping matrix elements due to the smaller c -axis lattice constant and thus structural anisotropy (c/a).

In this measurement, we observed the electronic structure of $\text{Sr}_{1-x}\text{Ca}_x\text{Fe}_2(\text{As}_{1-y}\text{P}_y)_2$ ($x = 0.08, y = 0.25$, $T_{\text{cmax}}=32\text{K}$) whose c/a is smaller than that of $\text{SrFe}_2(\text{As}_{1-y}\text{P}_y)_2$ and whose Fermi surfaces are considered to be more three-dimensional. A momentum distribution curve (MDC), a E - k intensity plot and a second derivative plot of hole Fermi surfaces around Γ point measured by using linearized s -polarized light are shown in Fig. 1. As seen in Fig. 1, around Γ point, the hole band whose orbital character is assigned to d_{xy} sinks below E_F , consistent with the ARPES result of $\text{SrFe}_2(\text{As}_{1-y}\text{P}_y)_2$. Figure 2 shows SC gaps around Γ and X points as a function of θ_{FS} in $\text{Sr}_{1-x}\text{Ca}_x\text{Fe}_2(\text{As}_{1-y}\text{P}_y)_2$ ($x = 0.08, y = 0.25$). SC gaps of hole Fermi surface around Γ point are isotropic within the error bar. On the other hand, SC gaps of electron Fermi surface around X point show a different behavior. The SC gap for outer α electron Fermi surface decreases rapidly toward $\theta_{\text{FS}} \sim 40$ deg and at $\theta_{\text{FS}} \sim 40$ deg, node of SC gap is observed. Moreover, the SC gap for inner β electron Fermi surface decreases gently with θ_{FS} increasing. These SC gap anisotropy are different from those of $\text{BaFe}_2(\text{As}_{1-y}\text{P}_y)_2$ ($y=0.30$) [3] and it suggests that there is a relationship between SC gap anisotropy and structural anisotropy (c/a).

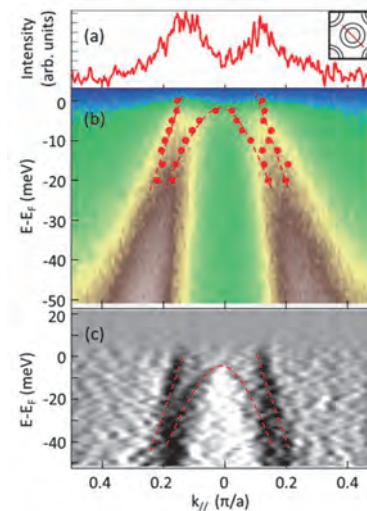


Fig. 1. The electronic structure of $\text{Sr}_{1-x}\text{Ca}_x\text{Fe}_2(\text{As}_{1-y}\text{P}_y)_2$ ($x = 0.08, y = 0.25$) around Γ point. (a) MDC at E_F , (b) E - k intensity plot, and (c) second derivative plot.

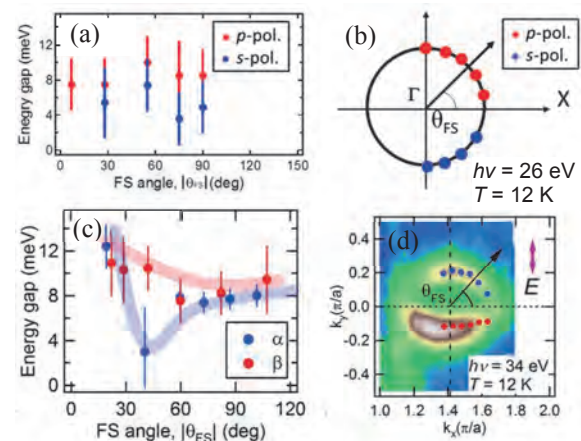


Fig. 2. (a), (c) SC gaps around Γ and X points as a function of θ_{FS} in $\text{Sr}_{1-x}\text{Ca}_x\text{Fe}_2(\text{As}_{1-y}\text{P}_y)_2$ ($x = 0.08, y = 0.25$). (b), (d) k_F around Γ and X point where SC gaps were measured. The Fermi angle is defined so that the Γ -X line is $\theta_{\text{FS}} = 0$ deg.

[1] T. Yoshida *et al.*, Phys. Rev. B **106** (2011) 117001.

[2] H. Suzuki *et al.*, Phys. Rev. B **89** (2014) 184513.

[3] T. Yoshida *et al.*, Sci. Rep. **4** (2014) 7292.

BL7U

Superconducting Gap of the Electron-Doped Cuprate Superconductor $\text{Pr}_{1.3-x}\text{La}_{0.7}\text{Ce}_x\text{CuO}_4$ Studied by Angle-Resolved Photoemission Spectroscopy

M. Horio¹, K. Koshiishi¹, T. Ohgi², S. Ideta³, K. Tanaka³,
T. Adachi⁴, Y. Koike² and A. Fujimori¹

¹Department of Physics, University of Tokyo, Tokyo 113-0033, Japan.

²Department of Applied Physics, Tohoku University, Sendai 980-8579, Japan.

³UVSOR Facility, Institute for Molecular Science, Okazaki 444-8585, Japan

⁴Department of Engineering and Applied Sciences, Sophia University,
Tokyo 102-8554, Japan.

The momentum dependence of the superconducting (SC) gap carries rich information about the mechanism of superconductivity. While it is generally accepted that the SC gap of hole-doped cuprates has d -wave symmetry, the symmetry for electron-doped cuprates is still controversial.

The most direct probe of the symmetry of the SC gap is angle-resolved photoemission spectroscopy (ARPES). Although rapid surface degradation and the small size of the SC gap have prevented thorough investigation of the momentum dependence [1,2], an ARPES study on optimally doped electron-doped cuprates reported that the symmetry was basically d -wave but the gap took a maximum around the hot spot where the Fermi surface and antiferromagnetic (AF) Brillouin zone boundary cross, suggesting large contribution of AF spin fluctuations to the superconductivity [3]. However, some studies have raised the possibility that the gap symmetry changes from d -wave to s -wave by electron doping [4].

Recently, a new annealing method, which is called protect annealing and conducted to remove impurity oxygen that stabilizes AF order and destroys superconductivity, has enabled superconductivity in electron-doped cuprates with less Ce concentration [5]. An ARPES study has revealed that sufficient protect annealing strongly suppresses the quasi-particle scattering at the hot spot while the SC transition temperature (T_c) remains high [6]. In order to reveal the momentum dependence of the SC gap of protect-annealed samples, we have performed ARPES measurements with higher energy resolution.

$\text{Pr}_{1.3-x}\text{La}_{0.7}\text{Ce}_x\text{CuO}_4$ ($x = 0.10$, PLCCO) single crystals were grown by the traveling-solvent floating-zone method. We prepared two PLCCO samples which showed T_c 's of 26.3 K (sample #1) and 26.9 K (sample #2) after annealing at 800 °C for 24 h. ARPES measurements were performed at UVSOR BL7U. Linearly polarized light with $h\nu = 16.5$ eV was used. The total energy resolution was set at 8 meV. Sample #1 was measured once and Sample #2 for three times. Prior to each measurement, the samples were cleaved *in situ* under the pressure $\sim 5 \times 10^{-11}$ Torr.

Figure 1 shows energy distribution curves (EDCs) near $(0, \pi)$ taken below and above T_c . Below T_c , the

leading edge was shifted by 1.2-1.5 meV toward higher binding energy with good reproducibility, suggesting the opening of SC gap, although the amount of shift was a little smaller than 1.9 meV which was reported in previous studies [2,3]. Unfortunately, we could not reveal further detailed momentum dependence during this beam time, and additional measurements are planned in the near future.

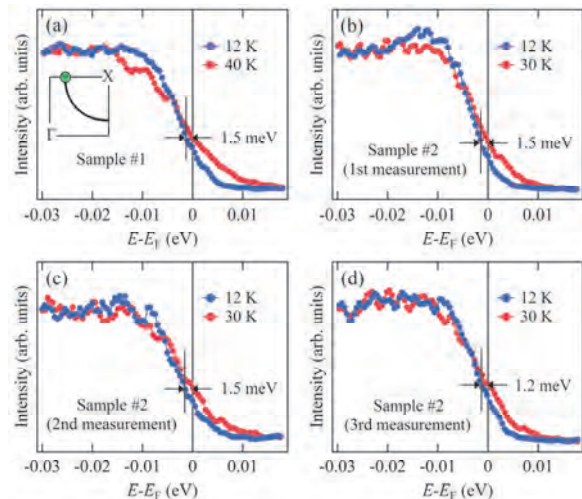


Fig. 1. SC gap of PLCCO. EDCs taken below and above T_c for (a) sample #1 and (b)-(d) sample #2. (b) to (d) are results of the first to third measurements, respectively. All the EDCs were taken at the momentum indicated by a green point in the inset of (a).

- [1] T. Sato *et al.*, Science **291** (2001) 1517.
- [2] N. P. Armitage *et al.*, Phys. Rev. Lett. **86** (2001) 1126.
- [3] H. Matsui *et al.*, Phys. Rev. Lett. **95** (2005) 017003.
- [4] J. A. Skinta *et al.*, Phys. Rev. Lett. **88** (2002) 207005.
- [5] T. Adachi *et al.*, J. Phys. Soc. Jpn. **82** (2013) 063713.
- [6] M. Horio *et al.*, Nat. Commun. **7** (2016) 10567.

BL7U

Electron-Phonon Scattering in Graphene: Probing of the Phonon-Dispersion by the Angle-Resolved Photoelectron Spectroscopy

S. Tanaka

The Institute of Scientific and Industrial Research, Osaka University, Ibaraki 567-0047, Japan

The electron-phonon coupling rules many properties of solids, and have been extensively studied. Recently, we proposed a new experimental method which enables us to probe the electron-phonon scattering, which is the elemental process of the electron-phonon coupling, in HOPG graphite by using the angle-resolved photoelectron spectroscopy (ARPES). Here, we report an investigation using the same method for the epitaxial graphene on SiC.

The sample used was the single-layer graphene on the SiC crystal manufactured by Graphene Platform Inc. (Tokyo, Japan). ARPES measurements were carried out at the BL7U at the UVSOR facility in Institute for Molecular Science. Figure 1(a) shows the photon-energy dependence of the surface normal photoelectron spectra of the graphene. There are steps near 160meV of the binding energy at the photon energy of near 10.8eV. These steps are converted to the peak shapes by differentiating the spectra with the binding energies as shown in Fig. 1(b). The heights of the steps are plotted as a function of the photon energy [Fig. 1(c)]. There are no electronic band near the Γ -point in graphene, and in fact these steps are the Fermi edge which are shifted as much as the energy of the phonon which is scatters the electron from the Dirac cone at the K-point to the Γ -point of the unoccupied band located at 10.3eV above the Fermi level. The energy shift is due to the energy conservation rule during the phonon emission process of the electron. Possible phonon modes are LO- and TO-branches whose calculated dispersions are shown in Fig. 2(b). The ARPES map whose intensities are differentiated with the binding energy are shown in Fig. 2(c) for two directions (Γ -K and Γ -M). Obviously, the energies shift as a function of the electron-momentum. This is due to the momentum conservation rule, and these relate to the phonon dispersion. It should be noted that the electron momentum at the Fermi level of the Dirac cone is somewhat ambiguous since Fermi circle is formed in the case of the graphene/SiC due to the substrate effect. Therefore, a convolution with a phonon momentum should be taken into account. Fig. 2(d) shows simulation for the scattering process including the broadening induced by the experimental resolution. The TO-phonon is assumed in the simulation, and the agreement between the experiments and the calculation are good. The simulation assuming LO-phonon (not shown here) cannot reproduce the experiments at all, indicating that the TO-phonon is responsible for the electron-phonon scattering in this case. Although this suggests a high

efficiency of the TO-mode for the electron-phonon coupling, what observed here is the electron-phonon scattering between specific wave functions of the graphene, and detailed comparison with the theoretical calculation including the matrix elements both of the electron-phonon scattering and the optical transition will be necessary for more detailed discussion.

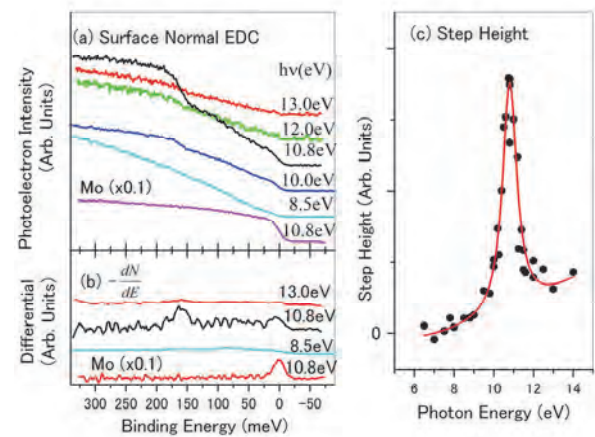


Fig. 1. (a) Surface normal ARPES spectra, (b) their differentiation, and (c) step heights in the spectra as a function of the photon energy.

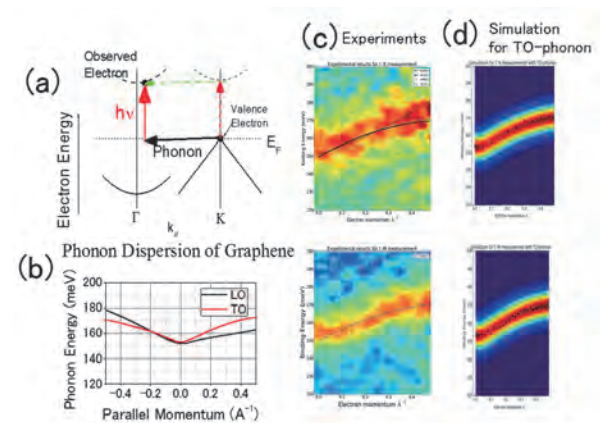


Fig 2. (a) Schematic drawing of the electron emission process, (b) phonon dispersions of graphene, (c) differentiated ARPES maps along the Γ -K (upper) and Γ -M (lower) directions at $h\nu = 10.8\text{eV}$ (d) Simulation of the electron-phonon scattering in graphene.

BL7B

Electronic Structure and Decay Profiles of Auger-Free Luminescence from α - and β -BaLu₂F₈ Crystals

H. Tsuchida¹, S. Tanaka², M. Kitaura¹, A. Ohnishi¹, J. Pejchal³, A. Yamaji⁴ and S. Kurosawa³

¹Faculty of Science, Yamagata University, Yamagata 990-8560, Japan

²Faculty of Science and Engineering, Kinki University, Higashiosaka 577-8502, Japan

³New Industry Creation Hatchery Center, Tohoku University, Sendai 980-8579, Japan

⁴Institute for Materials Research, Tohoku University, Sendai 980-8679, Japan

Auger-Free Luminescence (AFL) is caused by radiative transition of core holes to the valence band [1]. The spectral shape and radiative lifetime of AFLs mainly reflect electronic structure such as density of states (DOS) and wave functions of valence and outermost core bands, which are dependent on local ionic or covalent bonds. AFLs of compounds with different modifications are very much interesting in controlling AFLs. From this viewpoint, we have much attention to the AFL of BaLu₂F₈. This compound has two modifications of α - and β -phases [2]. The former and latter belong to orthorhombic and monoclinic systems, respectively. The α - and β -phases are stable above and below 900 °C, respectively. In the present study, we have studied electronic structures of α - and β -BaLu₂F₈ crystals by measurements of x-ray photoelectron spectroscopy (XPS), and reflectance spectra. Furthermore, we have measured emission spectra and decay profiles of Auger-free luminescence (AFL) from α - and β -BaLu₂F₈ crystals under the single bunch operation of UVSOR.

Figure 1 shows reflectance (red) and absorbance (blue) spectra of α - and β -BaLu₂F₈ crystals, which were measured at room temperature. The absorption edge of α -BaLu₂F₈ is higher than that of β -BaLu₂F₈. Furthermore, the reflectance spectrum of α -BaLu₂F₈ is clearly different from that of β -BaLu₂F₈. On the other hand, it was confirmed that the XPS spectra are in good agreement with each other, indicating that the electronic structures of valence and outermost core bands are almost same between them. Therefore, the difference between reflectance and absorbance spectra is attributed to that in the structure of the conduction band.

From the analysis of XPS spectra, the energy difference between the top of the valence band and that of the outermost core band was determined to be 7.9 eV, the value of which is smaller than the band-gap energy estimated from the higher energy side of the lowest reflectance peak. Therefore, it is evident that α - and β -BaLu₂F₈ crystals accompany radiative core hole transitions between the valence band and the top of the outermost core band, resulting in AFLs. Actually, emission spectra exhibited an AFL band around 5 eV. The spectral shape is same between α - and β -BaLu₂F₈ crystals. Decay profiles of the AFLs were also same, as shown in Fig. 2. The lifetimes of AFLs were determined to be 610 ps (α -BaLu₂F₈) and 560 ps (β -

BaLu₂F₈), respectively. Apparently, similarities in emission spectra and decay curves of AFLs reflect the results of XPS spectra.

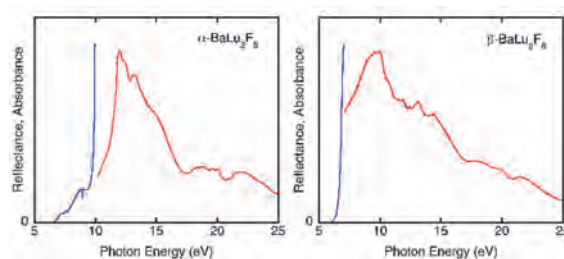


Fig. 1. Reflectance (red) and absorbance (blue) spectra of α - and β -BaLu₂F₈ crystals, measured at room temperature.

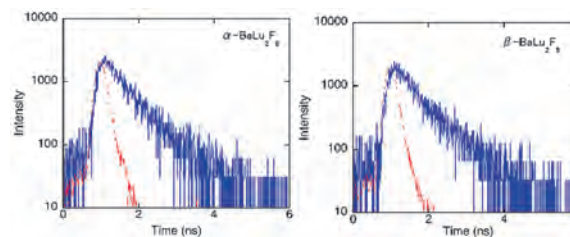


Fig. 2. Decay profiles of AFLs from α - and β -BaLu₂F₈ crystals, measured at room temperature under excitation at 21.4 eV. A red line indicates the pulse profile of an excitation light pulse.

[1] M. Itoh, Recent Res. Devel. Physics **4** (2003) 205.

[2] A. A. Kaminskii *et al.*, J. Alloys Compd. **275-277** (1998) 442.

BL7B

Analysis of the Luminescence Properties of $\text{Gd}_2\text{Si}_2\text{O}_7\text{:Ce}$ and $\text{Gd}_2\text{Si}_2\text{O}_7\text{:La, Ce}$ with Vacuum Ultraviolet Excitation

M. Koshimizu¹, T. Yanagida², Y. Fujimoto¹ and K. Asai¹

¹ Department of Applied Chemistry, Graduate School of Engineering, Tohoku University, Sendai 980-8579, Japan

² Graduate School of Materials Science, Nara Institute of Science and Technology, Ikoma 630-0192, Japan

Ce-doped $\text{Gd}_2\text{Si}_2\text{O}_7$ (GPS) has been attracting considerable attention owing to its excellent scintillation properties [1]. Recently, it is proved that La-doping is an effective method to enhance the performance [2]. In this study, we analyzed the luminescence properties of Ce-doped GPS with and without La with vacuum ultraviolet (VUV) excitation to elucidate the effect of La incorporation on the energy transfer process from the host matrix to Ce^{3+} ions.

The single crystals of Ce-doped GPS with and without La incorporation were grown via floating-zone method. The luminescence properties were characterized at BL7B of UVSOR. Luminescence spectra were obtained using an optical multichannel analyzer equipped with a liquid-nitrogen-cooled CCD at different excitation wavelengths. For the measurements of luminescence time profiles, single bunch operation of UVSOR was used. The luminescence photons were monochromatized and detected with a multichannel-plate-mounted photomultiplier tube.

Figure 1 shows the luminescence spectra of the Ce-doped GPS crystals with and without La incorporation. A prominent band was observed at 370–400 nm for all the crystals, and is attributed to the $5d-4f$ transition of Ce^{3+} .

Figures 2 and 3, respectively, show the luminescence time profiles of the Ce-doped GPS crystals with and without La incorporation with excitation at 60 and 300 nm. The decay behavior was expressed satisfactorily with single exponential functions for all the time profiles. For GPS doped with Ce and La at 1 and 10 mol% respectively, the decay time constants were 52 and 60 ns with excitation at 300 and 60 nm, respectively. On the other hand, the decay time constants were 41 and 52 ns with excitation at 300 and 60 nm, respectively. The excitation at 300 nm corresponds to the direct excitation of Ce^{3+} , whereas the excitation wavelength at 60 nm corresponds to the host excitation. The difference in the luminescence process is that energy transfer is involved in the luminescence process for the excitation wavelength of 60 nm. It is clearly seen that the GPS crystal with La incorporation has a similar decay behavior for excitation wavelengths of 60 and 300 nm, whereas a considerable difference was observed for the GPS crystal without La. This result indicates that the La incorporation has an influence on the energy transfer process.

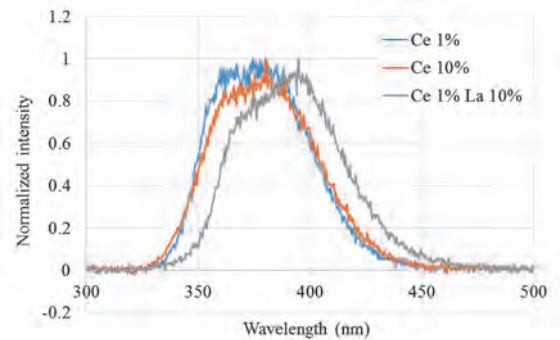


Fig. 1. Luminescence spectra of the Ce-doped GPS crystals with and without La incorporation.

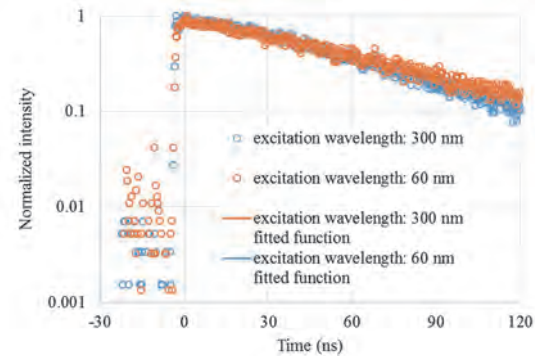


Fig. 2. Luminescence time profiles of GPS doped with Ce and La at 1 and 10 mol%, respectively.

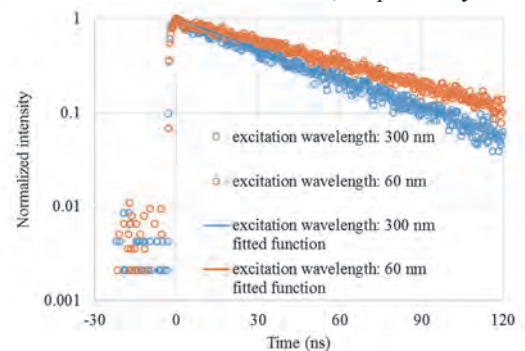


Fig. 3. Luminescence time profiles of GPS doped with Ce at 10 mol%.

[1] S. Kawamura, J. H. Kaneko, M. Higuchi, F. Fujita, A. Homma, J. Haruna, S. Saeki, K. Kurahige, H. Ishibashi and M. Furusaka, Nucl. Instrum. Methods Phys. Res. A **583** (2007) 356.

[2] S. Kurosawa, T. Shishido, A. Suzuki, J. Pejchal, Y. Yokota and A. Yoshikawa, Nucl. Instrum. Methods Phys. Res. A **744** (2014) 30.

BL7B

Influence of Barium Concentration on the Reflection Spectra for Ternary Niobium Bismuth Phosphate Glasses

N. Kitamura¹, K. Fukumi¹, Y. Hisano², A. Uchiyama² and H. Kozuka²

¹National Institute of Advanced Industrial Science and Technology, Osaka 563-8577, Japan

²Kansai University, Osaka 564-8680, Japan

BaO-Nb₂O₅-P₂O₅ glass is one of niobium phosphate glass systems having a wide glass forming region with high Nb₂O₅ contents [1]. In this system, NbO_x polyhedra construct glass network structure with PO₄ tetrahedra. Since the glass shows high refractive index due to high niobium concentration. It is of interest for the application to optical glasses in precision optical devices. However, the glass with high niobium content gives yellowish and blue colours and the relationship between optical properties, such as refractive index, dispersion, absorption edge, etc., and structure around niobium ions or connection of niobium-oxygen polyhedra in the network structure are not clear yet. In the present study, reflectivity of the bismuth phosphate glasses has been measured to investigate compositional dependence of the band structure in the vacuum ultraviolet region.

Ternary xBaO-10Nb₂O₅-(90-x)P₂O₅ (x = 10, 20, 30, 40, 50 and 55 mol%) glasses and xBaO-20Nb₂O₅-(80-x)P₂O₅ glasses (x = 10, 20, 30, 40, 50 and 55 mol%) were prepared by using a conventional liquid-quench method. Reflectivity of optically polished samples was measured in the photon energy region of 4-25 eV with an incident angle of 10° at the BL7B. Figure 1 shows reflection spectra of the xBaO-10Nb₂O₅-(90-x)P₂O₅ glasses. Strong reflection peak was observed at around 9.5 eV and 22 eV for all the glasses. The peak are assigned to the transition from O 2p and P 3p states to Nb 4d and Ba 5d states from a report of DFT calculation for barium niobium phosphate compounds [2]. The origin of the higher band at 22 eV is not clear yet. The unknown peak at 22 eV increased with increasing BaO content. Therefore, the peak could be due to the state of Ba²⁺. Contrary, intensity of the 9.5 eV peak did not show remarkable change with the BaO content. However, the peak position shifted toward lower energy by about 0.3 eV, while the band width (HWHM) decreased by about 0.6 eV from an analysis of multi-Gaussian deconvolution for the K-K transformed absorption spectra. These changes predicted a higher energy shift of absorption edge energy and the prediction was consistent with the experimental result of absorption spectra in visible region [3].

On the other hand, reflection spectra of ternary xBaO-20Nb₂O₅-(80-x)P₂O₅ glasses are shown in Fig. 2. As shown in the figure, the similar peaks were observed. The peak around 22 eV increased with increasing BaO content. The intensity of the 9.5 eV band was almost constant against the BaO content too.

This work was carried out as a study of CSTI, SIP Project (Development of Advanced Glass Processing Technologies).

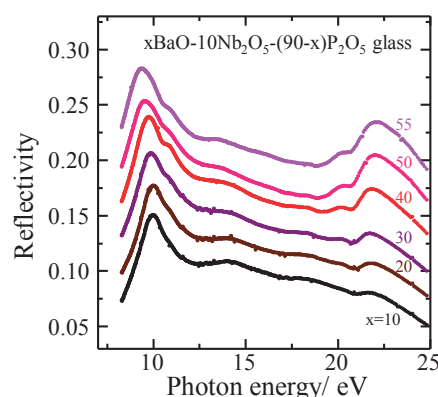


Fig. 1. Reflection spectra of ternary xBaO-10Nb₂O₅-(90-x)P₂O₅ glasses.

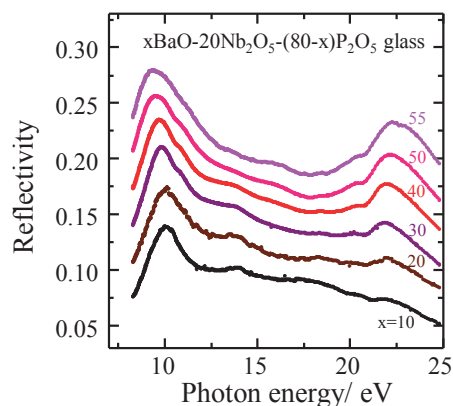


Fig. 2. Reflection spectra of ternary xBaO-20Nb₂O₅-(80-x)P₂O₅ glasses.

[1] N. Shcheglova and T. V. Avlas, *Fiz. Khim. Stekla* **16** (1990) 879.

[2] I. Cho *et al.*, *Eur. J. Inorg. Chem.* **2011**(2011) 2206.

[3] N. Kitamura *et al.*, Extended abstract 1st Int. Nat'l. Conf. Phosphate glasses, Pardvice, 2014.

BL7B

Optical Conductivity Spectra in the Course of Bandwidth-Control Metal-Insulator Transitions in $\text{Nd}_{1-x}\text{Pr}_x\text{Ir}_2\text{O}_7$

J. Fujioka¹, K. Ueda¹ and Y. Tokura^{1,2}¹ Department of Applied Physics, University of Tokyo, Tokyo 113-8656, Japan² RIKEN Center for Emergent Matter Science (CEMS), Wako 351-0198, Japan

Strongly correlated electron system has been one of the central topics in the condensed matter physics where the interplay among charge, spin, orbital degree of freedom frequently induces a variety of intriguing states. Among them, interplay between electron correlation and relativistic spin-orbit coupling in 5d-transition metal oxides has recently attracted much attention for the realization of the correlated topological insulator/semimetals [1]. The Weyl semimetal (WSM) is an example, which is characterized by a Weyl dispersion in bulk and nontrivial surface states with Fermi-arc.

The pyrochlore iridates $\text{R}_2\text{Ir}_2\text{O}_7$ (R = rare-earth, Y, and Bi ions) is one of representative materials to explore these phenomena. The metal-insulator transition (MIT) can be tuned by changing R-ions via the modulation of 5d electron hopping interaction and accordingly of effective electron correlation (U). The R = Pr compound is metallic down to the lowest temperature, while others with smaller R-ionic radius (r) thermally turns into an insulator concomitantly with or separately from the antiferromagnetic (all-in all-out) order at low temperatures. So far, there have been many theoretical studies on the evolution of electronic/magnetic state upon the MIT. For example, it is proposed that the Weyl semimetal can be realized in the vicinity of MIT. Despite extensive research, a systematic study regarding the evolution of electronic structure upon this enigmatic MIT is still lacking.

In this study, we investigate the charge dynamics upon the MIT on series of pyrochlore iridates $(\text{Nd}_{1-x}\text{Pr}_x)_2\text{Ir}_2\text{O}_7$ by means of optical spectroscopy. For the measurements, high-quality (hard, dense, and well-stoichiometric) polycrystalline samples are prepared. We measured reflectivity spectra for polycrystals of $\text{Nd}_2\text{Ir}_2\text{O}_7$ between 12 meV and 5 eV using Fourier-transform spectrometer and grating-type spectrometer in temperature range between 5 K and 290 K. We obtained the reflectivity between 5 and 30 eV at room temperature by using synchrotron radiation at BL7B in UVSOR. We determined complex optical constants through the Kramers-Kronig transformation with proper extrapolations of reflectivity in the low and high energy regions.

In Fig. 1(a), we show the optical conductivity spectra for the mixed compounds of R = $\text{Nd}_{1-x}\text{Pr}_x$ ($x = 0, 0.2, 0.5$, and 1) at 5 K ($< T_N$), which are located in vicinity to the quantum phase transition of the all-in all-out magnetic order [2]. An optical gap is observed for $x = 0.5$ as well as for $x = 0$, while the magnitude of the gap systematically decreases as x increases (0.035

eV for $x = 0.2$ and 0.012 eV for $x = 0.5$). Figure 1 (b) exhibits the T variation of optical conductivity spectra for $x = 0.5$. Upon cooling below T_N , the spectral weight (SW) rapidly piles up around 0.04 eV at the expense of a strong depletion of conductivity in lower energy, resulting in the formation of the charge gap as small as 0.012 eV. It is quite different T evolution of spectra from other compounds indicative of the emergence of unconventional ground states.

We discuss the possible electronic states of $x = 0.5$, which is located near the quantum MIT point. At first glance, the observed T evolution of the spectra is reminiscent of the band reconstruction due to the formation of charge/spin density wave states, in which the SW transfers to right above the optical gap. This is however not likely since the band reconstruction by the folding of Brillouin zone may not occur in the case of all-in all-out type magnetic order. Another possible scenario is emergence of Weyl Mott insulator. It is theoretically proposed that the electronic band can be gapped while maintaining topological aspects by electron-electron correlation. In this state, characteristic absorption peaks due to interband interactions are predicted to show up in optical conductivity, which is not inconsistent with the presently observed results.

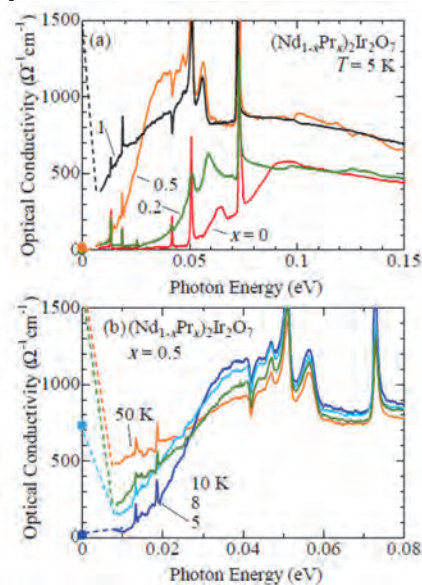


Fig. 1. (a) Optical conductivity spectra for $x = 0, 0.2, 0.5$ and 1 of R = $\text{Nd}_{1-x}\text{Pr}_x$ at 5 K. (b) Optical conductivity spectra at several temperatures for $x = 0.5$.

[1] X. Wan *et al.*, Phys. Rev. B **83** (2011) 205101.[2] K. Ueda *et al.*, Phys. Rev. B **92** (2015) 121110(R).

BL8B

Ultraviolet Photoelectron Spectra of $\text{Sc}_3\text{C}_2@\text{C}_{80}$

T. Miyazaki^{1,*}, H. Yagi¹, T. Zaima¹, R. Sumii²,

H. Okimoto³, N. Izumi³, Y. Nakanishi³, H. Shinohara³ and S. Hino¹

¹Graduate School of Science and Engineering, Ehime University, Matsuyama 790-8577, Japan

²Institutes for Molecular Science, Okazaki 444-858, Japan

³Graduate School of Science, Nagoya University, Nagoya 464-8602, Japan

(*Present address: Faculty of Science, Okayama University, Okayama 700-8530, Japan)

Fullerene cages often encapsulate metal atoms. C_{80} endohedral fullerenes attract attention because of the reasons such as empty $I_h\text{-C}_{80}$ is not stable and cannot be isolated but it becomes stable upon encapsulation of metal atoms. Intramolecular charge transfer from encapsulated species to the carbon cage gives them unique and different characteristics from empty fullerenes. $\text{Sc}_3\text{C}_2@\text{C}_{80}$ is one of such endohedral cluster fullerenes and well studied because its highly symmetric I_h cage structure is expected to result in unique properties. Recently, Sato et al. [1] reported considerably high carrier mobility (the highest among the polycrystalline endohedral fullerene films) and high electrical conductivity of polycrystalline $\text{Sc}_3\text{C}_2@\text{C}_{80}$ film compared to those of $\text{La}_2@\text{C}_{80}$ and $\text{Sc}_3\text{N}@\text{C}_{80}$. Their DFT calculation suggests that high conductivity of $\text{Sc}_3\text{C}_2@\text{C}_{80}$ is attributed not only to the high carrier mobility but also to its small band gap (0.07 eV), and that $\text{Sc}_3\text{C}_2@\text{C}_{80}$ can be considered as a semimetal at room temperature. To examine whether $\text{Sc}_3\text{C}_2@\text{C}_{80}$ really has such a small bandgap, we measured the Ultraviolet Photoelectron Spectra (UPS).

$\text{Sc}_3\text{C}_2@\text{C}_{80}$ was synthesized according to the previous procedures. The UPS were measured by the photoelectron spectrometer at the beamline 8B2 at the Ultraviolet Synchrotron Orbital Radiation Facility (UVSOR), and by our laboratory equipment which consists of He-I, ($h\nu = 21.218$ eV) discharge lamp (combination of MB Scientific L-1 and M-1) and a SCIENTA SES-100 electron energy analyzer. All the spectra are referenced to the Fermi level of the substrate, which was determined by measuring the Fermi edge of the gold. The $\text{Sc}_3\text{C}_2@\text{C}_{80}$ specimen for the UPS measurements were deposited by sublimation from a resistively heated quartz crucible.

Figure 1 shows the UPS of $\text{Sc}_3\text{C}_2@\text{C}_{80}$ obtained with $h\nu = 20 \sim 60$ eV. The spectra exhibit seven peaks denoted as A-G in the figure. The intensity ratios of those peaks oscillate with the incident photon energy, which is due to the spherical shape of the molecule and is the characteristics of the UPS of fullerenes. The onset energy of the UPS (E_{onset}), which is the energy separation between the Fermi level and the valence band maximum, is 0.2 eV for $\text{Sc}_3\text{C}_2@\text{C}_{80}$. This value is much smaller than the E_{onset} of $\text{La}_2@\text{C}_{80}$ (0.77 eV) and $\text{Sc}_3\text{N}@\text{C}_{80}$ (1.1 eV). The Fermi level of the n-type semiconducting fullerene thin film usually does not situate at the mid gap but closer to the conduction band minimum, so the band gap of $\text{Sc}_3\text{C}_2@\text{C}_{80}$, $\text{La}_2@\text{C}_{80}$ and $\text{Sc}_3\text{N}@\text{C}_{80}$ is probably between E_{onset} and twice of

the E_{onset} . The small onset energy of $\text{Sc}_3\text{C}_2@\text{C}_{80}$ is qualitatively consistent with the previous DFT calculation by Sato et al. [1] in which the band gap of $\text{Sc}_3\text{C}_2@\text{C}_{80}$, $\text{La}_2@\text{C}_{80}$ and $\text{Sc}_3\text{N}@\text{C}_{80}$ is estimated to be 0.07, 0.41 and 1.23 eV, respectively.

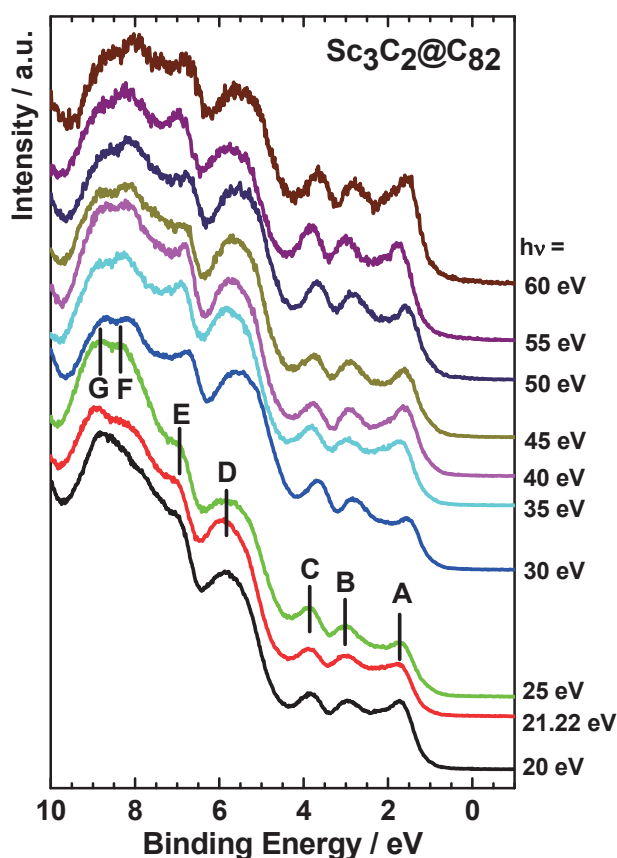


Fig. 1. Ultraviolet photoelectron spectra of $\text{Sc}_3\text{C}_2@\text{C}_{80}$ with incident photon energy at $h\nu = 20 \sim 60$ eV.

[1] S. Sato, S. Seki, G. Luo, M. Suzuki, J. Lu, S. Nagase and T. Akasaka, *J. Am. Chem. Soc.* **134** (2012) 11681.

III-3

Chemistry

BL3U

Surface-Dependent Hydration of Nanodiamonds in Colloidal Dispersions

T. Petit,¹ H. Yuzawa,² M. Nagasaka,² H. Girard,³ J.-C. Arnault,³ O. Shenderova,⁴ N. Kosugi² and E. F. Aziz^{1,2,5}

¹ Institute of Methods for Materials Development, Helmholtz-Zentrum Berlin, Albert-Einstein-Str. 15, 12489 Berlin, Germany

² Institute for Molecular Science, Okazaki 444-8585, Japan

³ CEA, LIST, Diamond Sensors Laboratory, F-91191 Gif-sur-Yvette, France

⁴ Adamas Nanotechnologies Inc., 8100 Brownleigh Dr., Raleigh, North Carolina 27617, USA

⁵ Freie Universität Berlin, FB Physik, Arnimallee 14, 14195 Berlin, Germany

The organization of water molecules close to solid surfaces or around proteins differs significantly from pure water [1]. Reorganization of solvent molecules is likely to occur around colloidal nanoparticles and its understanding is of utmost importance to better estimate their reactivity and interaction with biological moieties in aqueous environment. Nanodiamonds (NDs) are of particular interest for the investigation of interfacial water since the existence of an ordered water shell ranging from 2 to 4 water layers was recently suggested. In 2014, we have observed that X-ray Absorption Spectroscopy (XAS) in pure transmission was particularly efficient to probe water interfacial water around NDs [2].

During this beam time at UVSOR-III, aqueous dispersions of NDs with different surface chemistries prepared from the same initial ND produced by detonation synthesis (diameter ~5nm) by Adamas Nanotechnologies were compared. Carboxylated (NDs-COOH), hydroxylated (NDs-OH) and hydrogenated (NDs-H) were characterized. For comparison, NDs produced by High Pressure High Temperature (NDs-HPHT), with a diameter of 16 nm, were also characterized. By comparing these XAS spectra at oxygen K edge to pure water spectra (Fig. 1), the organization of water molecules in hydration layers of NDs could be investigated.

After normalization to the absorption intensity before and after the oxygen edge, strong intensity variations of the signal were observed, which can be interpreted by surface-dependent variation of the water arrangement around NDs. NDs-OH are positively-charged, like NDs-H and NDs-sp², but its XAS spectrum does not differ from negatively-charged NDs-COOH. This result demonstrates that the water structure is not dependent on the Zeta potential of NDs as previously thought. The strong intensity of the main edge intensity at 538 eV for NDs-H dispersion, although its concentration is half of the other samples, demonstrate that the water organization is extremely different on hydrogenated surface. An enhancement of this feature was previously observed on surface-graphitized NDs (NDs-sp²), also having hydrogenated surface groups.

During this beam time, we could extend the preliminary results obtained in 2014 to NDs with well-defined surface chemistries. This work demonstrates

that hydrogenated surface functional groups are the source of particular water arrangement on NDs. These results will be submitted for publication in the coming months, along with complementary infrared and Raman spectroscopies results.

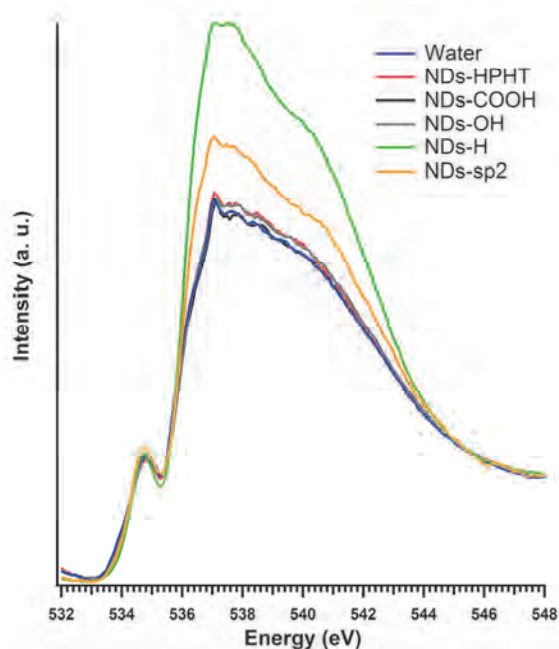


Fig. 1. (a) XAS of oxygen K-edge from water and aqueous dispersion of detonation NDs with different surface chemistries. Concentration is 1 wt % except for NDs-H (0.5 wt %). Surface-graphitized NDs (NDs-sp²) spectrum is extracted from reference 2.

- [1] J.-J. Velasco-Velez *et al.*, *Science* **346** (2014) 831.
 [2] T. Petit *et al.*, *J. Phys. Chem. Lett.* **6** (2015) 2909.

BL1U

Induced Chirality by Circularly Polarized UV Light for Photofunctional Organic/Inorganic Hybrid Materials: Tuning Electrochemical Properties of Artificial Metalloproteins

T. Akitsu¹, M. Sunaga¹, M. Takase¹, T. Konomi² and M. Katoh²¹Department of Chemistry, Faculty of Science, Tokyo University of Science, Tokyo 162-8601, Japan²UVSOR Facility, Institute for Molecular Science, Okazaki 444-8585, Japan

In 2015, we have studied on linearly or circularly polarized UV light induced molecular orientation of chiral metal complexes in polymer matrix (synthetic polymers or proteins) and controlled electronic properties of the metal complexes as organic/inorganic hybrid materials. The advantage of using UVSOR facility (BL1U) is to generate wavelength-selective and polarized UV light with high intensity.

We have prepared supramolecular chiral systems as artificial metalloproteins composed of several chiral salen-type Mn(II) and Co(II) complexes in a human serum albumin (HSA) matrix. After linearly polarized UV light irradiation, that anisotropy of molecular orientation of the complexes increased was confirmed by polarized IR spectra. We have observed that the electrochemical behavior of the aligned complexes incorporating diphenyl groups in HSA can be tuned without UV radiation damage of HSA higher structures.

As shown in Fig. 1, we have simulated several organic/inorganic hybrid materials structurally, in other words, artificial metalloproteins composed of chiral salen-type Mn(II) or Co(II) complexes and HSA proteins. We also measured polarized UV-vis spectra or IR spectra after linearly polarized light UV light or CD spectra after circularly polarized light UV light to confirm induced molecular orientation due to Weigert effect. Weigert effect by linearly polarized UV light causes dichroism due to anisotropic aligned metal complexes in a HSA matrix with photochemical reactions as well as interaction with highly polar molecules.

In addition, even strong synchrotron UV linearly polarized UV light irradiation (at 260, 318, and 380 nm of 10² mm² spot at 10 mW/cm² generated with an undulator at IMS UVSOR BL1U [1]) did not damaged higher structure of HSA for the artificial metalloproteins. Little changes from the initial CD spectra in the range of 200-900 nm could be observed after 1, 3, and 5 min irradiation.

As depicted in Fig. 2, the CV measurements revealed the effects of UV light for not only metal complexes but also the artificial metalloproteins. Relatively UV light-resistant metal complexes exhibited CV changes after UV irradiation for 10 min, which may be in agreement with expectation based on the intra-ligand transitions or stable isolation and O₂ oxidation during preparation from Mn(II) source for the analogous Mn(III) complexes. As for diphenyl incorporating metal complexes-HSA hybrids, little CV

changes could be observed significant CV changes (decreasing current) only after 1 min polarized UV irradiation.

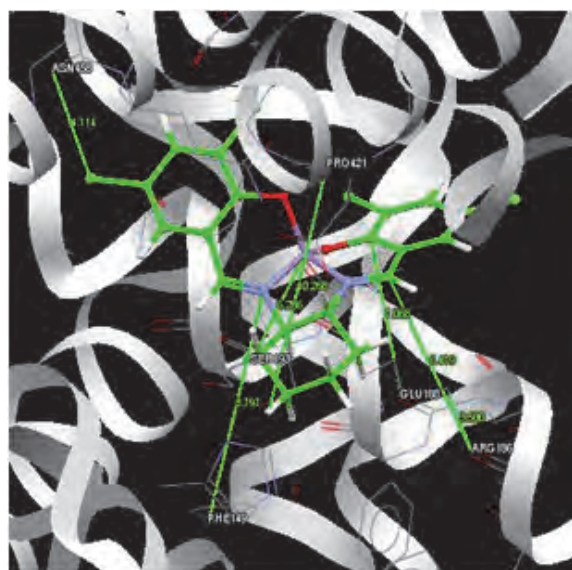


Fig. 1. Docking simulation (GOLD) of a chiral metal complex into HSA protein.

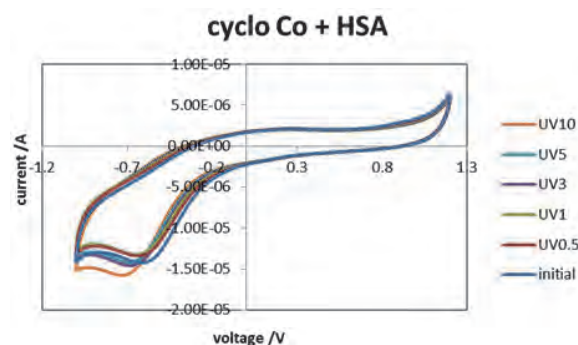


Fig. 2. Changes of CV of an artificial metalloprotein after polarized UV light irradiation.

[1] UVSOR, UVSOR Activity Report 41 (2014).

BL1U

Photoionization of Helium Atoms by Photon Beams Carrying Orbital Angular Momentum

T. Kaneyasu¹, Y. Hikosaka², M. Katoh³, H. Iwayama³ and E. Shigemasa³¹SAGA Light Source, Tosu 841-0005, Japan²Graduate School of Medicine and Pharmaceutical Sciences, University of Toyama, Toyama 930-0194, Japan³UVSOR Facility, Institute for Molecular Science, Okazaki 444-8585, Japan

Light beam characterized by helical wavefront and annular intensity distribution carries orbital angular momentum (OAM). Since the pioneering work by Allen *et al.* [1], the OAM photons have been attracting interests in a variety of research fields such as quantum information, manipulation of micro particles and high-resolution microscope. Until now application of the OAM photons has been limited to the visible and infrared wavelength region because it is generally difficult to produce helical wavefront at short wavelengths using optical elements.

Recently it was found that the n th harmonic radiation from a helical undulator carries OAM of $(n-1)\hbar$ per photon [2,3]. This accelerator-based method directly and efficiently produce circularly polarized OAM photon beams in a wavelength range covering from VUV to hard X-rays. Following the successful generation of the OAM photon beam in the UVSOR storage ring, we started an experimental study [4] on the interaction of the OAM photon with gas-phase atoms in which violation of the dipole selection rule is predicted [5].

The experiments were performed at the beamline BL1U using the OAM photon beam produced as the harmonic radiation from the APPLE-II undulator. The undulator radiation was collimated by $\phi 1$ mm pinhole and transported into the experimental chamber without optical elements. We measured angular distributions of He 1s photoelectron using the imaging method. Although we had experimental problems regarding the photon beam alignment and background subtraction in the image data, some preliminary results are presented in this report.

The left panels in Fig. 1 show the He 1s photoelectron images measured for the circularly polarized fundamental, second and third harmonic radiation, corresponding to the photon beams carrying OAM of $0\hbar$, $1\hbar$ and $2\hbar$ per photon, respectively. The peak photon energy of the undulator radiation was roughly set to 30 eV for each harmonic. The right panels in Fig. 1 show the angular distributions of the photoelectrons converted from the projected images using the peeling-analysis. The measured angular distributions are in reasonable agreement with those calculated for the dipole asymmetry parameter $\beta = 2$ even for the $l = 1$ and 2 cases. This result implies that the dipole transition dominates the OAM photon-atom interaction under the present experimental condition where the He atoms are uniformly distributed among

the photon beam of 1 mm diameter. For confirming the present observation, we plan to perform the photoionization experiment after the beamline construction scheduled in 2016.

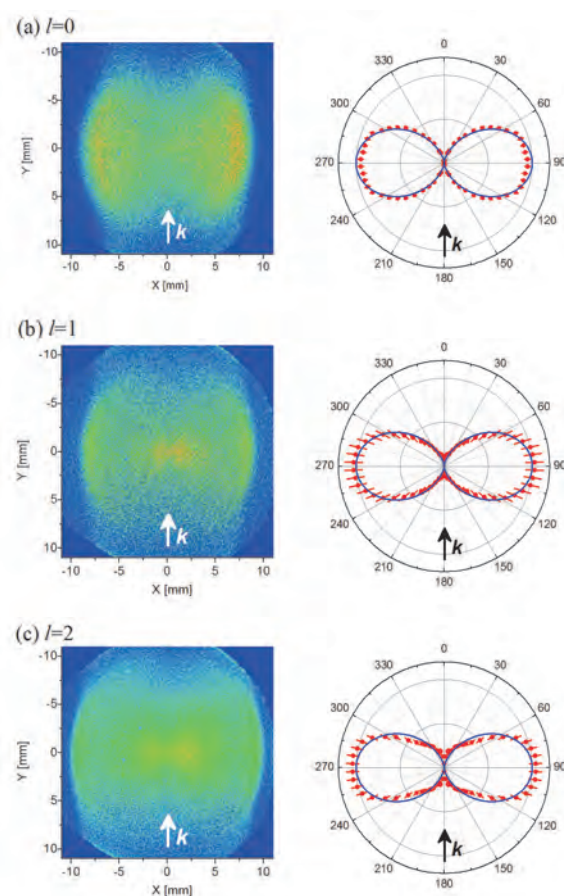


Fig. 1. Left: Images of He 1s photoelectrons. Right: Photoelectron angular distributions converted from the images. Solid curves represent the calculation for $\beta=2$. The photoelectron images were measured for the circularly polarized photon beams carrying OAM of $l\hbar$ ($l=0-2$) per photon.

- [1] L. Allen *et al.*, Phys. Rev. A **45** (1992) 8185.
- [2] S. Sasaki and I. McNulty, Phys. Rev. Lett. **100** (2008) 124801.
- [3] J. Bahrtdt *et al.*, Phys. Rev. Lett. **111** (2013) 034801.
- [4] T. Kaneyasu *et al.*, UVSOR Activity Report **42** (2014) 110.
- [5] A. Picón *et al.*, New J. Phys. **12** (2010) 083053.

BL3U

Local Structure Observation of Aqueous KSCN Solution by Soft X-Ray Absorption Spectroscopy. Part I. O K-Edge XAS for Solvent Water.

H. Yuzawa, M. Nagasaka and N. Kosugi

Institute for Molecular Science, Myodaiji, Okazaki 444-8585, Japan

Aqueous solution of highly concentrated electrolyte has been studied extensively, where cations and anions in water were not completely hydrated and interact with each other to produce complicate aggregated structures [1]. However, since it is difficult to clarify their structures by a few kinds of spectroscopic observation, more accumulation of spectroscopic insights is required.

Our research group has developed a new liquid cell for the soft X-ray XAS in transmission mode and has applied it to O K-edge XAS measurements of some electrolyte solutions. As a result, we have clarified the hydration structure around the cation [2]. In the present study, we have extended the measurement to both water and electrolyte in aqueous KSCN solutions, and have investigated the concentration dependence from dilute to nearly saturated one. In this part, we report the O K-edge XAS of water in the solutions.

The experiments were carried out at BL3U. First, the $(\text{KSCN})_x(\text{H}_2\text{O})_{1-x}$ solution samples (x values are from 0 to 0.3. $x = 0.3$ corresponds to 9.1 M.) were prepared and flowed into the liquid cell which is composed of two Si_3N_4 membranes. Then, the thickness of liquid cell was optimized by controlling the He pressure around the cell and the O K-edge XAS measurement was started. The photon energy was calibrated by the oxygen $1s \rightarrow \pi^*$ excitation peak (530.8 eV) of O_2 gas mixture in He.

Figure 1 shows O K-edge XAS spectra of the $(\text{KSCN})_x(\text{H}_2\text{O})_{1-x}$ samples. In the Fig. 1a, the absorption intensity of the post-edge region around 540 eV decreases with increasing the KSCN concentration. Since this region is assigned to multiple scattering in the hydrogen bond network of water [3], this tendency suggests that the more hydrogen bond is broken by KSCN in higher concentration. In the Fig. 1b, the sharp absorption peak at the main-edge region around 537 eV is clearly observed for high concentration range from $x = 0.2$ to 0.3, whose change of absorption comes close to the spectrum of water vapor [4]. Thus, this peak would be derived from the existence of isolated water molecule (or cluster) surrounded by KSCN.

Figure 2a shows magnified figure of the pre-edge peaks around 534.5 eV in Fig. 1. Figure 2b shows the peak energy shift values of these peak tops. The blue shift of the peak top is larger with increasing the concentration. This indicates that the hydration structure between H_2O and K^+ ($\text{K}^+ - \text{OH}_2$ interaction) increases in number, as reported previously [2].

Therefore, the KSCN concentration dependence of

O K-edge XAS spectra for water can give the information about tendency of the breaking of hydrogen bond network and that of the formation of hydration structure between K^+ and H_2O .

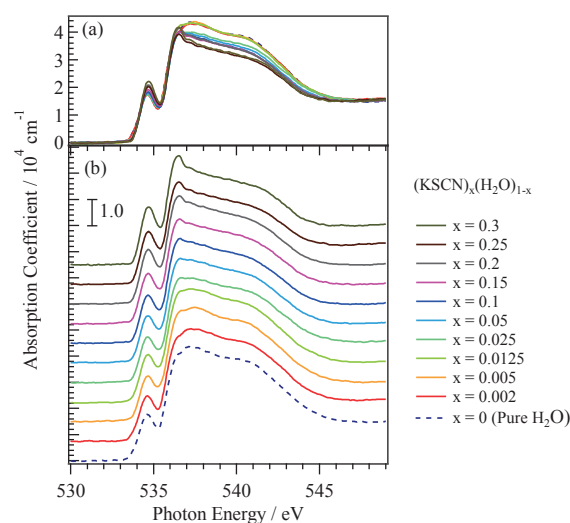


Fig. 1. O K-edge XAS of $(\text{KSCN})_x(\text{H}_2\text{O})_{1-x}$ solutions in various ratios from $x = 0$ to 0.3.

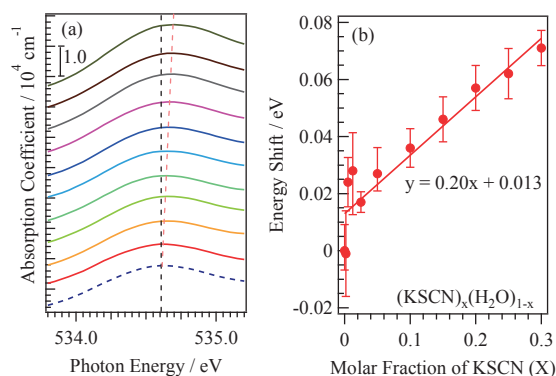


Fig. 2. (a) Magnified figure of the pre-edge region in the O K-edge XAS spectra of the $(\text{KSCN})_x(\text{H}_2\text{O})_{1-x}$ solutions shown in Fig. 1. (b) The energy shifts of the pre-edge peak top.

- [1] Y. Marcus, *Chem. Rev.* **109** (2009) 1346.
- [2] M. Nagasaka, H. Yuzawa and N. Kosugi, *J. Spectrosc. Relat. Phenom.* **200** (2015) 293.
- [3] Ph. Wernet *et al.*, *Science* **304** (2004) 995.
- [4] T. Tokushima *et al.*, *Phys. Chem. Chem. Phys.* **16** (2014) 10753.

BL3U

Local Structure Observation of Aqueous KSCN Solution by Soft X-Ray Absorption Spectroscopy. Part II. C and N K- Edge and K L-Edge XAS for Solute KSCN.

H. Yuzawa, M. Nagasaka and N. Kosugi

Institute for Molecular Science, Myodaiji, Okazaki 444-8585, Japan

Oxygen K-edge XAS spectra of water in $(\text{KSCN})_x(\text{H}_2\text{O})_{1-x}$ ($x = 0 - 0.3$) solutions have revealed that the increase of KSCN induces the breaking of hydrogen bond in water and increases the number of hydration structure ($\text{K}^+ - \text{OH}_2$ interaction) [1]. In this part, we report XAS measurements for the solute KSCN (K L-edge, C K-edge and N K-edge) to investigate the interaction around KSCN.

The experiments were carried out at BL3U. The procedure of the XAS measurements for the solution samples is the same as in Part I [1]. In N K-edge XAS, another liquid cell composed of two SiC membranes was used. The photon energy was calibrated by the CH_4 $1s-3p_{t_2}$ Rydberg peak (297.99 eV) of CH_4 gas mixture in He or N_2 $1s \rightarrow \pi^*$ excitation peak (400.84 eV) of N_2 gas mixture in He. XAS spectra of KSCN solid sample as a reference were also obtained by measuring drain current in a vacuum chamber.

Figure 1a shows K L-edge XAS spectra. Two absorption peaks are assigned to $\text{K } 2p_{3/2} \rightarrow 3d$ excitation around 297 eV and $\text{K } 2p_{1/2} \rightarrow 3d$ excitation around 300 eV, respectively. These peaks show red shift with the increase of KSCN concentration. Since this tendency means that the electronic state around K^+ comes close to that of KSCN solid (Fig. 1d), the number of interaction between K^+ and SCN^- in the solution increase in higher KSCN concentration. Considering the results of O K-edge XAS spectra [1], it is suggested that both interactions of $\text{K}^+ - \text{OH}_2$ (hydration) and $\text{K}^+ - \text{SCN}^-$ (aggregation) increase in number. This conclusion is also supported by a recent report of MD simulation in highly concentrated KSCN solution [2].

Figure 1b shows N K-edge XAS spectra. The obtained peak is assigned to the $\text{N } 1s \rightarrow \pi^*$ excitation. The same tendency (red shift toward the solid state, Fig. 1d) as in the case of K L-edge XAS is obtained. Thus, this can be also explained that the number of interaction between K^+ and N atom in SCN^- increases with higher concentration.

Figure 1c shows C K-edge XAS spectra, which is obtained from the $\text{C } 1s \rightarrow \pi^*$ excitation. The peak top energies of the solution samples in C K-edge XAS are almost constant without any dependence on the KSCN concentration (Fig. 1d). The XAS energy shift induced by intermolecular interaction is mainly derived from two factors. The red shift is occurred by the induced dipole interaction (stabilization) between the excited atom and surroundings, while the blue shift is occurred

by the exchange interaction (repulsion) between the excited electron to an unoccupied orbital and the valence and core electrons of surrounding molecules. These influences are stronger when the intermolecular distance is smaller. Based on this discussion, the result of C K-edge XAS suggests that the distance between C atom in SCN^- and other species is distant, that is, the interaction around the C atom is weaker compared with the interaction around the other atoms.

Therefore, aggregate structure of KSCN in highly concentrated aqueous solution is mainly formed by the $\text{K}^+ - \text{SCN}^-$ interaction and the $\text{K}^+ - \text{NCS}$ interaction, which break the hydrogen bond of water.

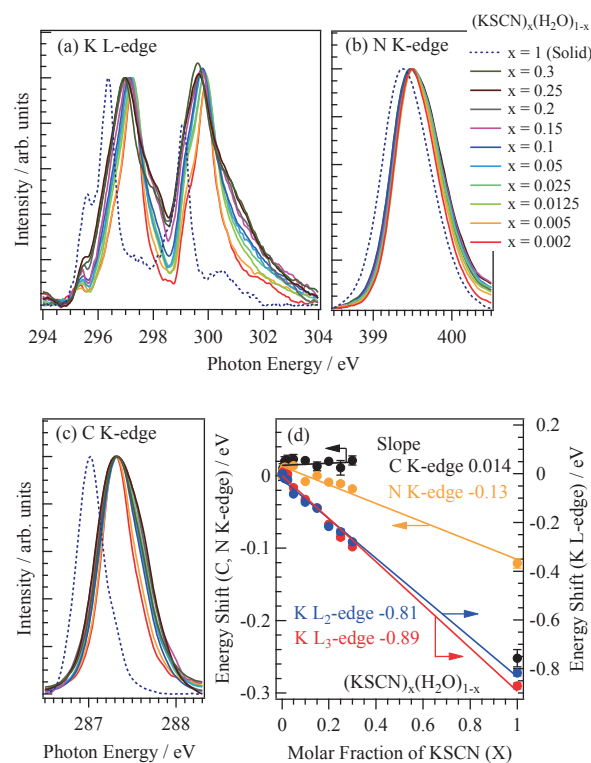


Fig. 1. (a) K L-edge, (b) N K-edge and (c) C K-edge XAS spectra of $(\text{KSCN})_x(\text{H}_2\text{O})_{1-x}$ solutions in various ratios from $x = 0.002$ to 0.3 and KSCN solid sample ($x = 1$). (d) The energy shifts of the obtained absorption peaks from a to c.

[1] H. Yuzawa, M. Nagasaka and N. Kosugi, UVSOR Activity Report in this volume.

[2] S. Kim *et al.*, J. Chem. Phys. **141** (2014) 124510.

BL3U

Development of X-Ray Detecting System Combined with Photomultiplier and Phosphor for Soft X-Ray Absorption Spectroscopy of Dilute Solutions

M. Nagasaka, H. Yuzawa, T. Ohigashi, Y. Okano and N. Kosugi
Institute for Molecular Science, Okazaki 444-8585, Japan

Soft X-ray absorption spectroscopy (XAS) is a powerful method to study local structures of liquid. We have developed a liquid flow cell for XAS in transmission mode, and studied the local structures of several aqueous solutions [1]. In normal aqueous solution, soft X-ray absorption is optimized to several tens of percent by adjusting the thickness of liquid layers. In dilute solutions, on the other hand, thick liquid samples should be prepared for XAS of solute because soft X-ray absorption of solute is low. However, the absorption of solvent is also increased due to the thick liquid samples. It is necessary to detect low flux (10^5 photons/s) of transmitted soft X-rays at the incident X-rays of 10^9 photons/s. Because the detection limit of photodiode is 10^7 photons/s, XAS of 100 mM solution is only measured by the photodiode detector. In this study, we have developed a X-ray detecting system combined with photomultiplier and phosphor for XAS of solute in dilute solutions.

The experiments were performed by using a chamber-type XAS measurement system at BL3U [2]. As shown in Fig. 1, the system consists of two chambers in an ultrahigh vacuum condition and in atmospheric helium condition. These chambers are separated by a 100 nm-thick Si_3N_4 membranes with the window size of $200 \times 200 \mu\text{m}^2$. The vacuum chamber is connected to the beam line. In the helium chamber, a liquid flow cell and a soft X-ray detector are installed. In the liquid cell, the liquid layer is sandwiched between two 100 nm-thick Si_3N_4 membranes, and liquid thickness is controllable from 20 nm to several μm . For XAS of liquid samples, transmitted soft X-rays irradiate to phosphor P43 dipped on the inlet of an optical fiber, soft X-rays are converted to visible lights [3], and visible lights are detected by a photomultiplier connected to the outlet of the optical fiber. We have confirmed that soft X-rays with 10^3 photons/s are detected in this system.

Figure 2 shows Fe L-edge XAS spectrum of 8.7 mM $[\text{Fe}(\text{bpy})_3]$ solution by using the present system. The solvent is DMSO. We have confirmed the presence of Fe peak in XAS regardless of the dilute solutions. The photon flux of incident and transmitted soft X-rays are 10^9 and 4×10^5 photons/s, respectively. The thickness of liquid layer is estimated to be 8 μm . We have succeeded to measure XAS of metal atoms in dilute metal complex solutions below 10 mM. In the future plan, we will investigate the local structures of ligand in dilute metal complex solutions by using C and N K-edge XAS.

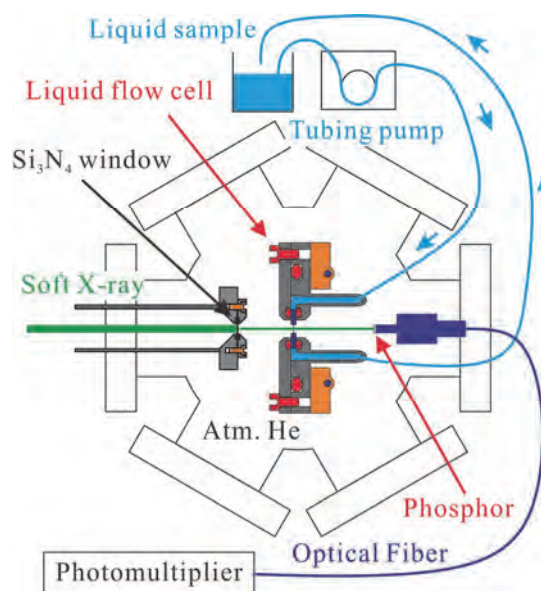


Fig. 1. Schematic of a chamber-type XAS measurement system for liquid samples. Soft X-ray transmission through the liquid sample is detected by a system combined with photomultiplier and phosphor dipped on the inlet of the optical fiber.

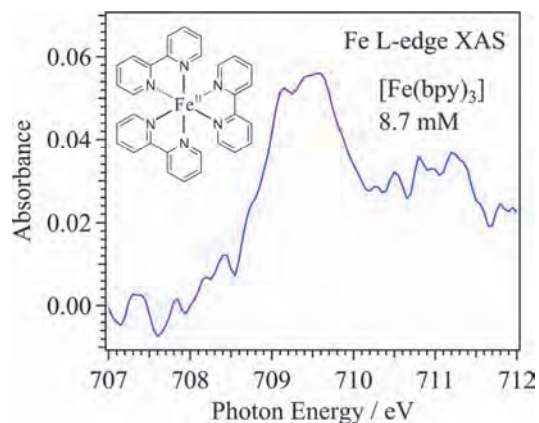


Fig. 2. Fe L-edge XAS spectrum of 8.7 mM $[\text{Fe}(\text{bpy})_3]$ solutions. The inset shows the schematics of the Fe metal complex.

- [1] M. Nagasaka *et al.*, *J. Electron Spectrosc. Relat. Phenom.* **200** (2015) 293.
- [2] M. Nagasaka *et al.*, in preparation.
- [3] A. L. D. Kilcoyne *et al.*, *J. Synchrotron Rad.* **10** (2003) 125.

BL3U

X-Ray Absorption Spectroscopy of Aqueous CO₂: Chemical Shifts of HCO₃⁻ and CO₃²⁻ Ions in Water Matrix

M. Patanen¹, M. Huttula¹, H. Yuzawa², M. Nagasaka² and N. Kosugi²

¹Nano and Molecular Systems Research Unit, Faculty of Science, 90014 University of Oulu, Finland

²Institute for Molecular Science, Okazaki 444-8585, Japan

Increased atmospheric CO₂ emissions after industrial revolution have not only drastic effects for the atmospheric chemistry but lead to acidification of surface water of oceans [1]. The solubility of molecular CO₂ is governed by Henry's law. In water, CO₂ appears in four forms: molecular CO₂, carbonic acid H₂CO₃, bicarbonate ion HCO₃⁻, and carbonate ion CO₃²⁻. A total amount of dissolved aqueous CO₂ species thus varies as a function of pH, since the form which CO₂ takes in water depends strongly on pH. Oceanic CO₂ species play an important role in the global carbon cycle not only at liquid-gas interfaces at the oceans' surfaces, but also at liquid-solid interfaces: e.g., carbonated solutions dissolve silicate minerals releasing metal ions into solution [2]. The electronic structure of the aqueous CO₂ species in pure and saline water is essential in order to model the chemical processes they take part in.

In this work we have studied C 1s and O 1s X-ray absorption spectra (XAS) of CO₂ species as a function of pH at UVSOR BL3U. We have used a liquid flow cell enabling a transmission mode soft X-ray absorption spectroscopy thanks to the thin SiN_x membranes [3]. The solutions were prepared from water solution of Na₂CO₃ (~2 M solution has a pH of 12.5) by adding different amounts of HCl (aq) in order to achieve the desired pH. Figure 1 a) presents the Bjerrum plot indicating with vertical grey bars the mole fractions of different species present in the studied solutions. Since the solubility of CO₂ species decreases with the lower pH, we were able to probe only the neutral/basic solutions consisting mostly of bicarbonate and carbonate species.

Figure 1 b) presents the water background subtracted C 1s XAS as a function of pH. It is clearly observed that the absorption energies get higher and bands broader, which corresponds well to the increase of the mole fraction of HCO₃⁻ and CO₂ species in the solution with decreasing the pH value from 12.5 to 6.4 (Fig. 1 a)). Therefore, the changes in XAS in terms of energy shifts and broadenings evidence clearly different bonding networks for these species.

Figure 1 c) shows the corresponding O 1s XAS of carbonated solutions and pure water. O1s → π* peak from gaseous O₂ is shown for energy calibration. Below the H₂O pre-edge peak we observe a clear shoulder whose magnitude is the greater the more basic the solution is. This tendency is identical with that of solubility for the total amount of CO₂ species, which decreases with the lower pH.

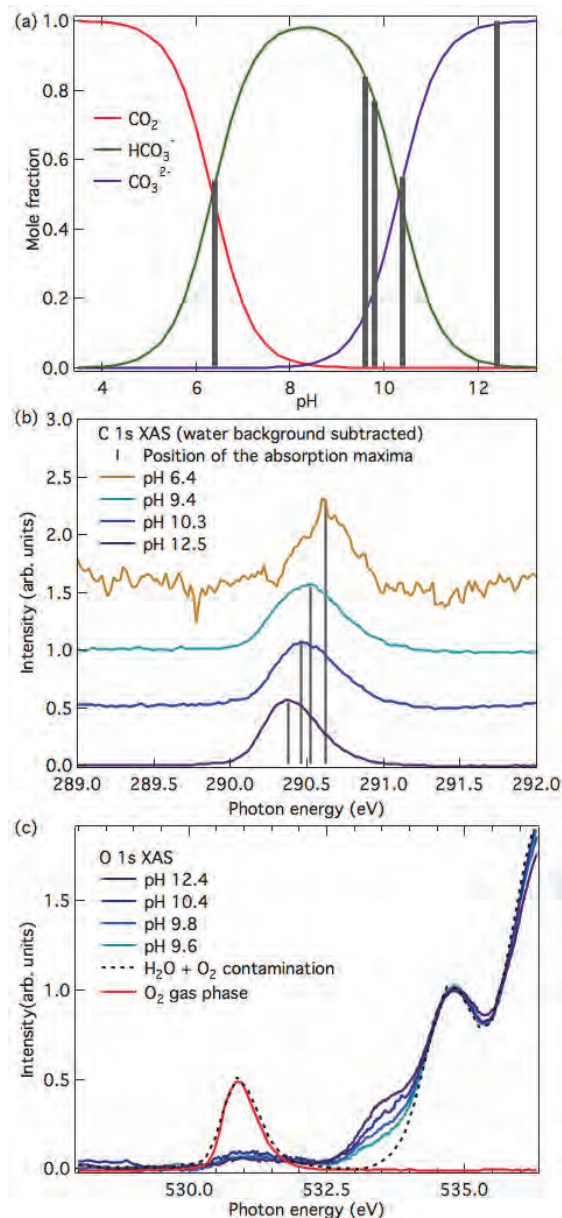


Fig. 1. a) Bjerrum plot showing the mole fractions of CO₂ species as a function of pH. b) C 1s XAS of aqueous Na₂CO₃ solutions. Grey bars indicate the maxima of the XAS. c) O 1s XAS showing a shoulder before the water pre-edge peak at 534.8 eV.

[1] K. Caldeira and M.E. Wickett, *Nature* **425** (2003) 365.

[2] A. Putnis, *Science* **343** (2014) 1441.

[3] M. Nagasaka, T. Hatsui, T. Horigome, Y. Hamamura and N. Kosugi, *J. Electr. Spectrosc. Rel. Phen.* **177** (2010) 130.

BL3U

Impacts of Conformational Geometries in Fluorinated Alkanes

T. Brandenburg^{1,2}, R. Golnak^{1,2}, M. Nagasaka³, K. Atak^{1,2}, S. S. N. Lalithambika^{1,2},
N. Kosugi³ and E. F. Aziz^{1,2,3}

¹ Institute of Methods for Material Development, Helmholtz-Zentrum Berlin für Materialien und Energie, Albert-Einstein-Straße 15, 12489 Berlin, Germany

² Department of Physics, Freie Universität Berlin, Arnimallee 14, 14195 Berlin, Germany

³ Institute for Molecular Science, Okazaki 444-8585, Japan

Research in blood substitute formulations is gaining more attention in the scientific community in recent years as more pharmaceutical companies start clinical trials on different artificial blood approaches. In general, artificial blood consists of emulsions of different liquid or protein compounds to increase oxygen solubility and transport capabilities as well as to decrease toxicity to biological tissue. Two of the more promising approaches center themselves around hemoglobin-based carriers and fluorinated micro-emulsions. Despite setbacks regarding clinical tests and medicinal approval of recent formulations, an emulsion containing perfluorodecalin named Fluosol was successfully approved by the U.S. Food and Drug Administration in 1989 (New Drug Application N860909).

The main oxygen carrier in Fluosol, perfluorodecalin, is part of the family of perfluorocarbons. They have a wide range of applications ranging from tissue oxygenation to post-operative treatment. Their wide range of extraordinary properties - high density, high viscosity, high biological and chemical inertness, high gas solubility - offer opportunities for applications in biomedicine and physical chemistry, as well as subsequently leading to a high interest in scientific development.

An inherent feature to all perfluorocarbons is the so called perfluoro effect, which describes the energy shifts of the spectral features due to the stabilization effect of fluorine in the fluorination process. The magnitude of the energy shift can subsequently be used for a classification of a molecular orbital to either bear σ - or π -character delivering an experimental method for the orbital classification. Some experimental studies based on photoelectron and X-ray absorption spectroscopy have already been performed, but the development of more complex theoretical models and new experimental techniques gives opportunities for further investigation of perfluorocarbons.

In liquid emulsions several effects need to be accounted for. Two of the more prominent are the conformation effect and the van der Waals force. The conformation effect affects peak broadenings and is a result of excited orbital interactions with surrounding molecules of different conformations. In the case of nonpolar systems, the acting van der Waals force is the London dispersion force, that is, an attractive force resulting from induced dipoles.

Through the measurements performed at the beamline BL3U in UVSOR we could obtain X-ray absorption spectra of several liquid fluoroalkanes and their respective hydrocarbons, which are subject to weak van der Waals forces and have a high amount of different conformational geometries.

Insight into the energetic shift induced by fluorination, the so-called perfluoro effect, and a comprehensive picture of the electronic structure of liquid fluoroalkanes and their respective parent hydrocarbon molecules was obtained [1]. In addition DFT calculations for the hydrocarbons, fluoroalkanes and stepwise fluorinated hydrocarbon derivatives were performed. We could reveal a strong involvement of the conformation effect with the local electronic structure and relative inertness of liquid fluoroalkanes. We additionally expose a direct association of different conformational geometries to the solubility rates of the presented perfluorocarbons with other liquid compounds like water and possibly gases like oxygen.

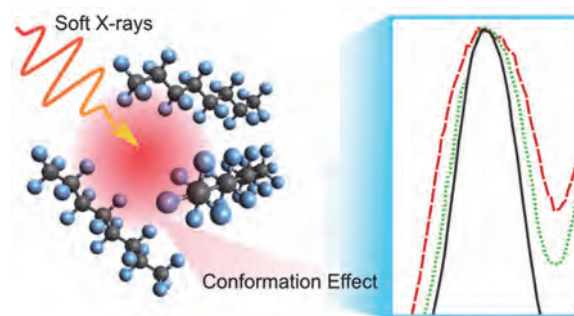


Fig. 1. Sketch of the acquired data for fluoroalkanes with an indication of the discovered peak broadening resulting from the conformational effect [1].

[1] T. Brandenburg *et al.*, under review.

BL4U

In-situ Soft X-Ray Absorption Spectroscopy Measurements of Liquid Samples by Scanning Transmission X-Ray Microscope

M. Nagasaka, T. Ohigashi, H. Yuzawa and N. Kosugi
Institute for Molecular Science, Okazaki 444-8585, Japan

Two different kinds of molecular liquids can be separated as two liquid phases by controlling the temperature due to a phase transition behavior in the mixed liquid. In order to reveal the mechanism of such a phase transition, it is necessary to investigate local structures of liquid-liquid interfaces of two liquids. Soft X-ray absorption spectroscopy (XAS) is an element specific method to study local structures of liquid. Recently, we have developed a liquid flow cell for XAS in transmission mode. In the liquid cell, a liquid layer is sandwiched between two 100 nm-thick Si_3N_4 membranes, and liquid thickness is controllable from 20 nm to several μm . By using this liquid cell, we have revealed local structures of several aqueous solutions [1]. We have also developed a liquid flow cell combined with scanning transmission X-ray microscope (STXM), and measured spatial resolved XAS of liquid samples [2]. However, the window sizes of Si_3N_4 membranes ($0.5 \times 0.5 \text{ mm}^2$) are too small to measure liquid-liquid interfaces, which are widely distributed in the liquid layer. In this study, we have developed a liquid flow cell, whose window size is $2 \times 2 \text{ mm}^2$, to measure spatial resolved XAS of liquid-liquid interfaces by STXM. We have measured O K-edge XAS of liquid water for the test of the liquid flow cell.

The experiments were performed at BL4U by connecting a liquid flow cell to the STXM system. The liquid cell is in the atmospheric helium condition. The liquid layer is sandwiched between two 100 nm-thick Si_3N_4 membranes with the window size of $2 \times 2 \text{ mm}^2$. The membranes are supported by Si frames with the thickness of 0.2 mm. In order to adjust the liquid thickness, 20 μm -thick Teflon spacers are included between two Si frames of the membranes. Liquid samples are exchanged *in situ* by using a tubing pump system. Temperature of a liquid sample is controlled by setting a Cu plate connected with a chiller system.

Figure 1 shows a soft X-ray transmission image of liquid water at the incident photon energy of 550 eV. Because the left part of the image is a Si frame, soft X-ray is not transmitted. On the other hand, soft X-rays are transmitted in the right part due to the existence of liquid water. We have observed line shape structures, in which thick liquid layer exists, with the distance of 250 μm from the edge of the Si frame. Figure 2 shows O K-edge XAS of liquid water. The beam spot of soft X-ray is set to the line shape structures in the liquid layer to obtain appropriate thickness of liquid layers for XAS in transmission mode. The thickness of a liquid layer is 480 nm. The intensity ratio of pre-edge

(535 eV) and main-edge (538 eV) is 0.39, and is consistent with our previous results [3].

In the future plan, we will measure spatial resolved XAS images of liquid-liquid interfaces by using this liquid flow cell, and revealed the mechanism of the phase transition of two liquid structures.

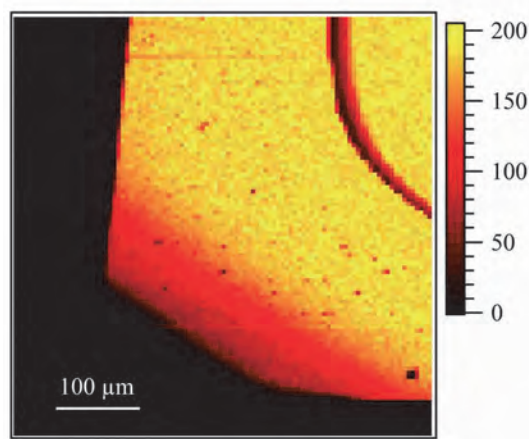


Fig. 1. Soft X-ray transmission image of liquid water at the incident photon energy of 550 eV.

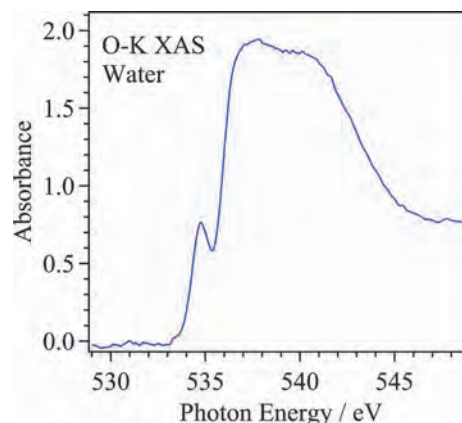


Fig. 2. O K-edge XAS of liquid water, in which the beam spot of soft X-ray is set to the line shape structures in the liquid layer shown in Fig. 1.

[1] M. Nagasaka *et al.*, *J. Electron Spectrosc. Relat. Phenom.* **200** (2015) 293.

[2] T. Ohigashi *et al.*, *AIP Conf. Proc.*, in press.

[3] M. Nagasaka *et al.*, in preparation.

BL4B

Auger Decay of Condensed Water Investigated with a Magnetic Bottle Electron Spectrometer

R. Mashiko¹, K. Soejima¹, E. Shigemasa² and Y. Hikosaka³

¹Department of Environmental Science, Niigata University, Niigata 950-2181, Japan

²UVSOR Facility, Institute for Molecular Science, Okazaki 444-8585, Japan

³ Graduate School of Medicine and Pharmaceutical Science, University of Toyama, Toyama 930-0194, Japan

Slow electron formation relevant to inner-shell photoionization of gas phase H₂O was investigated by multi-electron coincidence spectroscopy [1]. It was found that autoionization from O fragment produced by dissociation of Auger final H₂O²⁺ states is the important source of the slow electron formation. Such slow electron formation from the ionization of water molecules has received particular attention, in connection with DNA strand breaks in living cells exposed to ionizing radiations. The DNA strand breaks are largely caused by the impact of electrons emitted from the ionization of water molecules and biomolecules surrounding the DNA. Here, the majority of the electrons have kinetic energies of less than 20 eV, and the efficiency of the DNA strand breaks is known to be strongly dependent on the incident electron energy of the impacting electrons, due to its resonant character. Thus the knowledge of the energy distribution of the slow electrons is important in modeling the radiation damages of living cells. In this study, we have investigated the slow electron emission process of condensed H₂O irradiated with soft x-ray.

The experiment was performed at the beamline BL4B under the single bunch operation of the storage ring. The synchrotron radiation from a bending magnet of the storage ring was monochromatized by a grazing incidence monochromator using a varied-line-spacing plane grating. The monochromatized light was focused onto a copper wire. Water molecules were adsorbed on the surface of the wire, by continuously cooling the wire down to the liquid nitrogen temperature, under its exposition to the base pressure ($\sim 1.8 \times 10^{-8}$ Torr). Electron coincidence measurements were carried out with the magnetic bottle electron spectrometer [2] whose schematic is shown in Fig. 1.

Coincidence datasets were accumulated for electrons emitted from the copper wire on irradiation of 738.2 eV photons. The two-dimensional map in Fig. 2 displays the energy correlation of the coincident electrons included in the coincidence datasets, where the coincidence counts are plotted as a function of faster (horizontal) and slower electron energies (vertical). A clear structure running horizontally is associated with the coincidences between the O1s photoelectrons and the Auger electrons from condensed water.

We have inspected three-fold coincidences among the O1s photoelectron, Auger electron and slow electron, in order to investigate the energy distribution of the slow electrons emitted after the Auger decay.

The energy distribution (not shown) does not exhibit any tangible structures ascribable to autoionization from O: fragments. This observation implies that dissociations forming O* fragments are suppressed in the condensed phase.

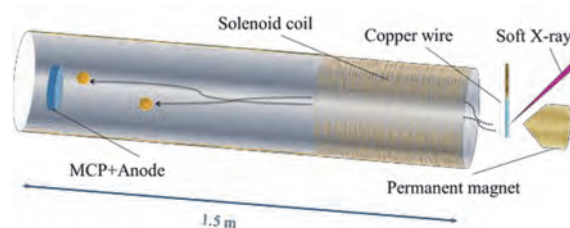


Fig. 1. Schematic of the magnetic bottle electron spectrometer.

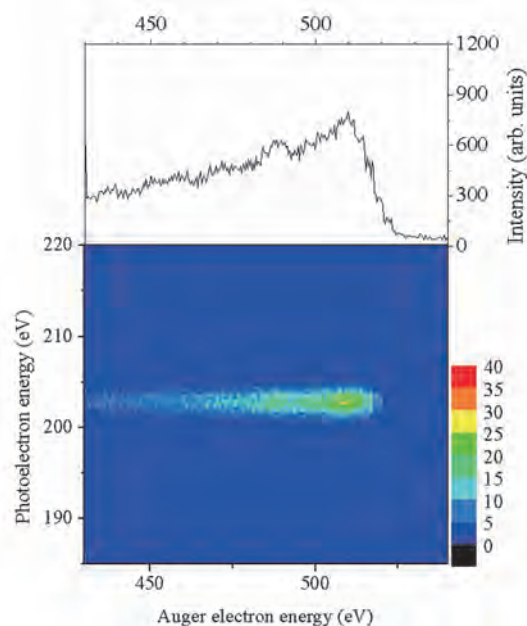


Fig. 2. Two dimensional plot of energy correlation between photoelectron and Auger electron emitted in the inner shell ionization of condensed water molecules.

[1] Y. Hikosaka *et al.*, J. Chem. Phys. **137** (2012) 191101.

[2] Y. Hikosaka *et al.*, J. Ele. Spectrosc. Rel. Phenom. **192** (2014) 69.

BL5B

Improvement of the VMI Spectrometer for Photoelectron Imaging Experiment

T. Kaneyasu¹, Y. Hikosaka², H. Iwayama³ and E. Shigemasa³

¹SAGA Light Source, Tosu 841-0005, Japan

²Graduate School of Medicine and Pharmaceutical Sciences, University of Toyama, Toyama 930-0194, Japan

³UVSOR Facility, Institute for Molecular Science, Okazaki 444-8585, Japan

Velocity map imaging (VMI) [1] is one of the powerful methods for measuring the velocity distribution of charged particles emitted in various atomic and molecular processes. We employed a VMI spectrometer for the experimental investigation on photoionization of gas-phase atoms by circularly polarized undulator radiation which carries orbital angular momentum [2]. Since the VMI spectrometer used in our study was originally developed for the negative ion imaging [3], it was found that slight modification of the spectrometer was necessary for improving the electron image quality.

The details of the VMI spectrometer is described in ref. [3]. Briefly, the spectrometer consists of a repeller plate, electrostatic lenses and a drift tube followed by a two dimensional position sensitive detector. The photoelectrons having same initial velocities are focused to the same detector's position independent of the ionization point by applying the inhomogeneous electrostatic field to the ionization region. When the cylindrical symmetry is assumed, three-dimensional vectors of the photoelectrons can be reconstructed from the projected two-dimensional image.

The improvements of the VMI spectrometer are as follows. Firstly we introduced a magnetic shield around the drift tube for reducing the stray magnetic field in the electron drift space. Next we replaced the repeller electrode with a mesh-type one. This is because secondary electrons are efficiently produced from the electrode surface by photoions colliding with the repeller plate. Finally we constructed a new frame for supporting the experimental chamber, allowing precise positioning of the spectrometer's center with respect to the photon beam axis.

Following the improvements, performance test of the VMI spectrometer has been carried out at BL5B. The images and angular distributions of the He 1s and Ar 3p photoelectrons are shown in Figs. 1 and 2, respectively. The electric vector of the photon beam is parallel to X-axis of the image. The intense ring-shaped structures observed in the images correspond to the photoelectrons, while secondary electrons are weakly distributed inside the ring structures. The secondary electron emission is well suppressed compared to the previous setup consisting of the plate-type repeller electrode. The image distortion observed in the previous measurements is reduced by introducing the magnetic shield. Photoelectron angular distributions are converted from the raw images

without any background subtraction and image corrections. The measured angular distributions are fairly in agreement with the calculation results, confirming that image quality of the VMI spectrometer is sufficiently improved for the photoelectron imaging experiment.

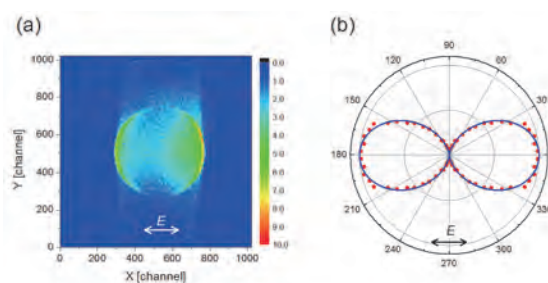


Fig. 1. (a) Projected image and (b) angular distributions of He 1s photoelectrons measured at $h\nu=27.6$ eV. Solid curve represents the calculation for $\beta=2$.

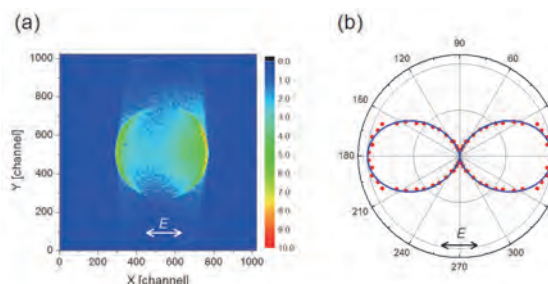


Fig. 2. (a) Projected image and (b) angular distributions of Ar 3p photoelectrons measured at $h\nu=21.0$ eV. Solid curve represents the calculation result for $\beta=0.84$.

[1] A. T. J. B. Eppink and D.H. Parker, Rev. Sci. Instrum. **68** (1997) 3477.

[2] T. Kaneyasu *et al.*, UVSOR Activity Report 2014, **42** (2015) 110.

[3] Y. Hikosaka and E. Shigemasa, J. Electron Spectrosc. Relat. Phenom. **148** (2005) 5.

BL6U

Auger Spectra Measured in Coincidence with the Photofragment Ions Formed after Migration: 3,3,3-Trifluoropropene at the C K-Edge

R. Tateishi¹, T. Kaneda¹, H. Iwayama^{2,3}, M. Kono^{4,5}, K. Okada¹ and E. Shigemasa^{2,3}

¹Department of Chemistry, Hiroshima University, Higashi-Hiroshima 739-8526, Japan

²UVSOR Facility, Institute for Molecular Science, Okazaki 444-8585, Japan

³School of Physical Sciences, The Graduate University for Advanced Studies (SOKENDAI), Okazaki 444-8585, Japan

⁴Senri International School of Kwansai Gakuin, Minoh 562-0032, Japan

⁵RSPE, Australian National University, Canberra, ACT 0200, Australia

Inner-shell excited molecules relax into molecular cations in different states through Auger decays. The cations are in general unstable and dissociate rapidly into fragment ions. In many hydrocarbon molecules a photoexcitation can cause a rapid geometry change in the molecule. Such migration has also been observed for photoexcitation of molecules at the inner-shell level. In the case of the inner-shell excitation and ionization of acetylene, for example, ion yield spectra of H_2^+ and CH_2^+ were observed [1] and the $\text{C}_2^+/\text{H}_2^+$ ion pair was detected [2], indicating a proton migration. We have recently concerned ourselves with the Auger-final states connecting to particular dissociation channels [3]. This report focuses on the rapid migration in the 3,3,3-trifluoropropene (TFP) molecule excited at the C K-edge. We have employed the Auger-electron-photoion coincidence (AEPICO) method to obtain information on the correlation between photofragment ions formed after migration and Auger-final states of the molecular ion.

The experiments were performed on the soft X-ray beamline, BL6U. The experimental setup has been described elsewhere [3,4]. Synchrotron radiation was irradiated at right angles to the effusive beam of the TFP sample. The pressure of the main chamber was kept at 4.0×10^{-4} Pa during the measurements. Auger electrons traveling through a double toroidal analyzer tube were detected with a position sensitive detector. The pass energy was set to 400 eV. Photofragment ions produced in the ionization region were extracted toward a time-of-flight mass spectrometer by a pulsed electric field applied just after the Auger electron detection. AEPICO data were obtained as list-mode files, containing a series of a set of the detected electron positions and the ion arrival times. The photon energies of 284.5 and 310.0 eV were used as typical resonant excitation and photoionization, respectively.

A correlation map of kinetic energy of the emitted Auger electrons versus m/z of photofragment ions can be depicted from the coincidence data. A variety of photofragment ions is found, such as CH_n^+ , F^+ , C_2H_m^+ , CF_m^+ , $\text{C}_2\text{H}_m\text{F}^+$ and so forth, where $n = 0-3$ and $m = 1-3$. They form islands on the map. Auger spectra coincident with particular ions can be obtained by extracting the region of interest on the map. In this study we focus on the $\text{C}_2\text{H}_3\text{F}^+$ ion, which is produced

after a fluorine-atom migration.

Figure 1 gives resonant Auger spectra measured in coincidence with the C_2H_3^+ and $\text{C}_2\text{H}_3\text{F}^+$ detection. The spectra have been obtained after subtraction of the contribution from photoelectrons. Both ions are produced by the C2–C3 bond rupture, with the only difference being with and without the migration before fission. It can be seen that the spectrum coincident with $\text{C}_2\text{H}_3\text{F}^+$ has a specific peak at the electron kinetic energy of 265.7 eV, whereas that coincident with C_2H_3^+ spreads widely with two distinct peaks. The result reveals that the migration occurs from such limited Auger-final states.

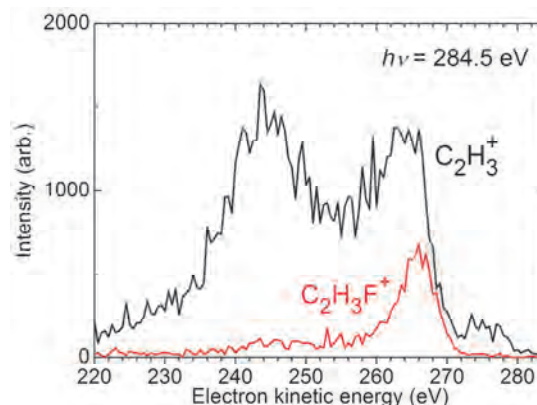


Fig. 1. Resonant Auger spectra measured in coincidence with detection of the C_2H_3^+ and $\text{C}_2\text{H}_3\text{F}^+$ photofragment ions. The contribution from photoelectrons has been subtracted.

[1] M. N. Piancastelli *et al.*, *J. Chem. Phys.* **117** (2002) 8264.

[2] J. Laksman *et al.*, *J. Chem. Phys.* **131** (2009) 244305.

[3] S. Ishikawa, K. Okada, H. Iwayama and E. Shigemasa, *UVSOR Activity Report* **42** (2015) 121.

[4] T. Kaneyasu, Y. Hikosaka and E. Shigemasa, *J. Electron Spectrosc. Relat. Phenom.* **156-158** (2007) 279.

BL6U

Dissociation of CH₃OH Dication Studied by an Electron-Ion Coincidence Method

M. Higuchi¹, H. Iwayama², E. Shigemasa² and Y. Hikosaka³

¹Department of Environmental Science, Niigata University, Niigata 950-2181, Japan

²UVSOR Facility, Institute for Molecular Science, Okazaki 444-8585, Japan

³Graduate School of Medicine and Pharmaceutical Sciences, University of Toyama, Toyama 930-0194, Japan

A molecule absorbing a soft x-ray photon undergoes inner-shell photoionization and subsequently Auger decay. Because two electrons are emitted through this sequential process, the molecule with two positive charges, called dication, is produced. The dication often dissociates into ion pairs, due to the Coulomb repulsion. In this work, we have studied the ion-pair dissociation of CH₃OH dication states by an electron-ion coincidence method.

The experiment was performed at the undulator beamline BL6U of the UVSOR facility. We used an electron-ion coincidence setup consisting of a toroidal electron analyzer and an ion momentum imaging analyzer [1,2].

Figure 1 shows a time-of-flight spectrum of ions produced after the C1s inner-shell ionization of CH₃OH. Peaks for H⁺ and H₂⁺ fragments can be observed in 800-1100 ns. The manifold seen in 1900-2400 ns is allocated to the fragments resulting from the dissociations comparing with the CO bond cleavage. The fragments keeping the C-O framework are observed in 2800-3000 ns. Hereafter, we focused on the dissociation producing H₂⁺ fragments. The two hydrogen atoms can come from C side only, but the hydrogen atom originally at the O-side can contribute. In practice, the time-of-flight spectrum measured for CH₃OD (not shown) exhibits both H₂⁺ and HD⁺ peaks.

Figure 2 shows C1s Auger spectra filtered by detections of H₂⁺ (blue) and HD⁺s (red), compared to the normal Auger spectra (black). While the coincidence Auger spectrum for H₂⁺ shows a peak around 43 eV, the HD⁺ peak lies around 35 eV. This observation implies that formation of HD⁺ fragments is involved by lower dication states which may be longer lifetime and thus allows the exchange of hydrogens of O-side and C-side before dissociation.

Figure 3 shows correlations of ion fragments formed in pair, observed for CH₃OD. The counterparts of HD⁺ fragments are mainly the fragments which keeps CO bond, i.e. COH⁺ and COH₂⁺. On the other hand, half of the H₂⁺ fragments are formed in pair with the fragments resulting from CO-bond breaking, e.g. CH₂⁺ and CH₃⁺.

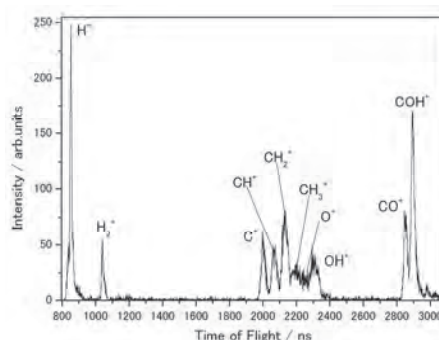


Fig. 1. Time-of-flight spectrum of ions produced after C1s inner-shell ionization of CH₃OH.

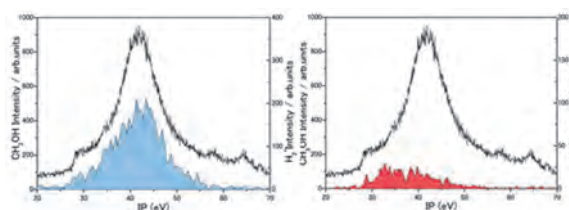


Fig. 2. Coincidence Auger spectra filtered by detections of H₂⁺ (blue) and HD⁺ fragments (red), compared to the normal Auger spectra (black).

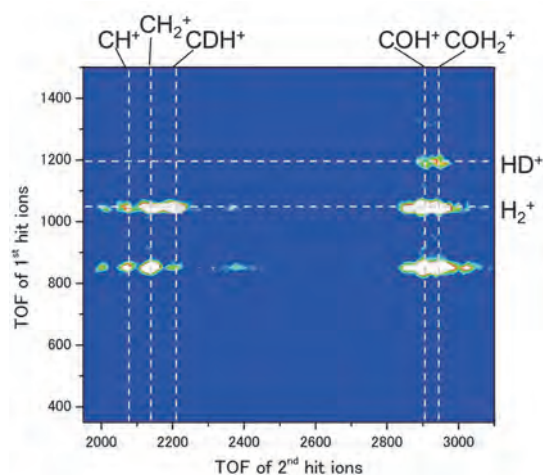


Fig. 3. Correlation map for ion pairs detected in coincidence.

- [1] T. Kaneyasu, Y. Hikosaka and E. Shigemasa, *J. Electron Spectrosc. Rel. Phenom.*, **156-158** (2007) 279.
 [2] Y. Hikosaka, Y. Shibata, K. Soejima, H. Iwayama and E. Shigemasa, *Chem. Phys. Lett.*, **603** (2014) 46.

BL6U

Dissociation Dynamics of Doubly-Ionized Water Molecules

M. Kikuchi¹, M. Higuchi¹, H. Iwayama², E. Shigemasa² and Y. Hikosaka³

¹Department of Environment Science, Niigata University, Niigata 950-2181, Japan

²UVSOR Facility, Institute for Molecular Science, Okazaki 444-8585, Japan

³Graduate School of Medicine and Pharmaceutical Sciences, University of Toyama, Toyama 930-0194, Japan

Interaction of a water molecule with high-energy radiation may lead to inner shell ionization, and an inner shell electron is emitted as a photoelectron. Subsequent Auger decay generates a doubly-ionized water molecule which mainly dissociates to an ion pair by the Coulomb repulsion. In this work, we investigated the dissociation processes of the doubly-ionized water molecule.

The experiment was performed at the beamline BL6U, by using an Auger electron-ion coincidence spectrometer consisting of a double toroidal electron analyzer and an ion time-of-flight (TOF) analyzer. We measured Auger electron-ion coincidences for gas phases D₂O as well as H₂O. Soft X-ray was irradiated to the sample gases introduced to the ionization point. Kinetic energies of the Auger electrons were determined by the arrival positions on the position sensitive detector of the double toroidal electron analyzer. On the detection of the individual Auger electron, an electric field was applied to the ionization point so that fragment ions are measured by the ion TOF analyzer. Auger electron energy determined by the double toroidal electron analyzer indicates the binding energy of the formed doubly-charged ion states, and TOFs of the ions observed in coincidences with the Auger electron reveal the resultant ion-pair.

Figure 1 shows the correlations of TOFs of ion pairs observed in coincidence with all Auger electrons. Clear correlations corresponding to the D⁺+OD⁺ ion pair and the D⁺+O⁺ ion pair are observed. The former ion pair results from the two-body dissociation of D₂O²⁺ → D⁺+OD⁺, and the latter from the three-body dissociation of D₂O²⁺ → D⁺+O⁺+D. It is estimated that, from the coincidence counts of these two structures in Fig. 1, the two-body dissociation is about 4.5 times more probable than the three-body dissociation.

The black curves in Fig. 2 are the Auger spectra of (a) D₂O and (b) H₂O, which show a band structure in 35-50 eV. The coincidence Auger spectra filtered for the two-body dissociation are represented in red, and those filtered for the three-body dissociation is in blue. In both water samples, the two-body dissociation accounts for the majority and yields the peak around 42 eV. In the higher energy side of the band structure, the fraction of the three-body dissociation increases. Comparison between the spectra for D₂O and H₂O implies that the contribution from the three-body dissociation is higher in H₂O than in D₂O. This is probably because elongation of the O-H bond becomes slower by the deuteration.

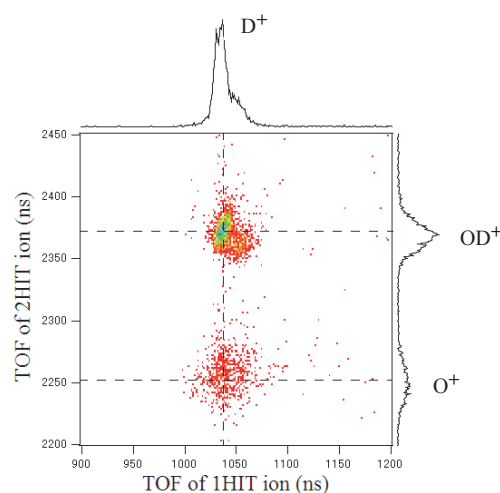


Fig. 1. Correlations of TOFs of ion pairs observed in coincidence with all Auger electrons.

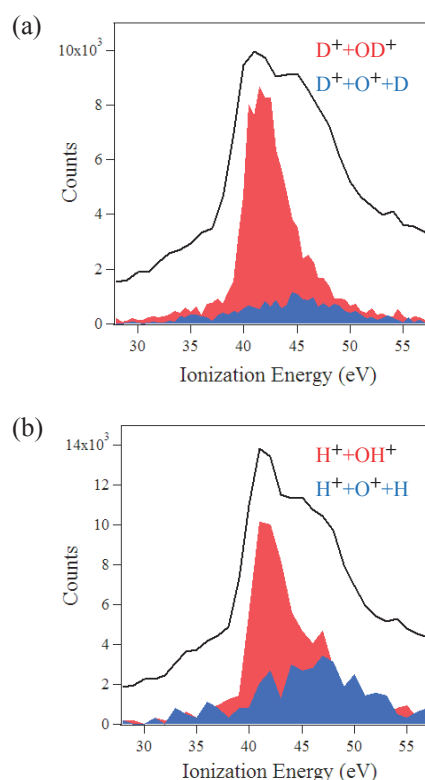


Fig. 2. Total Auger spectra (black) of (a) D₂O and (b) H₂O, (a) D₂O, and coincidence Auger spectra filtered for the two-body dissociation (red) and for the three-body dissociation (blue).

BL6U

Site-Specific Production of H_3^+ Ions Following Core Ionization of CH_3Cl

H. Iwayama^{1,2} and E. Shigemasa^{1,2}¹UVSOR Facility, Institute for Molecular Science, Okazaki 444-8585, Japan²School of Physical Sciences, The Graduate University for Advanced Studies (SOKENDAI), Okazaki 444-8585, Japan

Trihydrogen cation H_3^+ is one of the most interesting molecules in diverse fields from chemistry to astronomy because it is the simplest triatomic molecule and plays an important role in the interstellar. While the H_3^+ ions can be mainly generated from the proton transfer reactant ($H_2 + H_2^+ \rightarrow H_3^+ + H$), it was shown that unimolecular reactions of soft x-ray irradiated CH_3X molecules ($X=Cl, OH, CN, \text{etc.}$) also have small contributions of H_3^+ formation in the interstellar [1].

In this work, we investigate the H_3^+ production mechanism of soft x-ray irradiated CH_3Cl molecules with using an Auger-electron-ion coincidence technique, which allows us to correlate Auger final dicationic states with product ions. From coincidence Auger spectra, we reveal dicationic states which form the H_3^+ ions.

The Auger-electron-ion coincidence measurements were performed on the undulator beamline BL6U at UVSOR. The electron ejected at 54.7° with respect to the electric vector of the incidence radiation were analyzed in the energy by a double toroidal analyzer (DTA), while ions were extracted from the interaction region into a momentum spectrometer by a pulsed electric field according to the electron detection. Arrival position on the detector and time-of-flight (TOF) of ions and electrons were recorder for every event. The pass energy of the DTA was set to 200 eV for observing the Auger electrons. The corresponding electron energy resolution was about 1.9 eV. All signals from the detectors were recorded with an 8ch TDC board. We used the photon energies of 220 and 302 eV for the Cl 2p and C 1s core-ionized states, respectively. To obtain total ion TOF spectra, we also measured ions in coincidence with the Cl 2p and C 1s photoelectrons instead of the Auger electrons.

Figure 1 shows total ion TOF spectra following the Cl 2p and C 1s photoionization. Main fragment ions are H_n^+ ($n=1,2,3$), CH_n^+ ($n=0-3$), Cl^+ and CH_nCl^+ ($n=0,1,2$). CH_3Cl^+ ions were not observed since the parent molecules following the Auger decay are doubly charged. Doubly charged ions such as Cl^{2+} and CH_nCl^{2+} ($n=0-3$) were also observed. The most remarkable difference in fragmentation between the Cl 2p and C 1s photoionization is the relative abundance of H_3^+ ions. The relative intensity of H_3^+ ions for the Cl 2p photoionization is ten times larger than that for the C 1s photoionization.

Figure 2 shows the coincidence Auger spectra with H_n^+ ($n=1,2,3$) ions in the binding energy scale, in comparisons with the total Auger spectra. It is clearly

seen that the formation of the H_3^+ ions is related to only the lowest band around the binding energy of 32 eV for both the Cl 2p and C 1s photoionization, while the total Auger and coincidence Auger spectra with H^+ and H_2^+ ions are quite different in the two cases. In order to understand the mechanism of such a site-specific production of the H_3^+ ions, theoretical calculations for the Auger final states of the CH_3Cl molecule are highly desired.

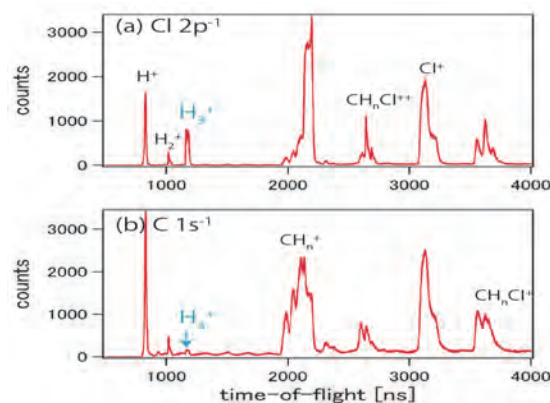


Fig. 1. Time-of-flight spectra of ions taken in coincidence with (a) Cl 2p and (b) C 1s photoelectrons.

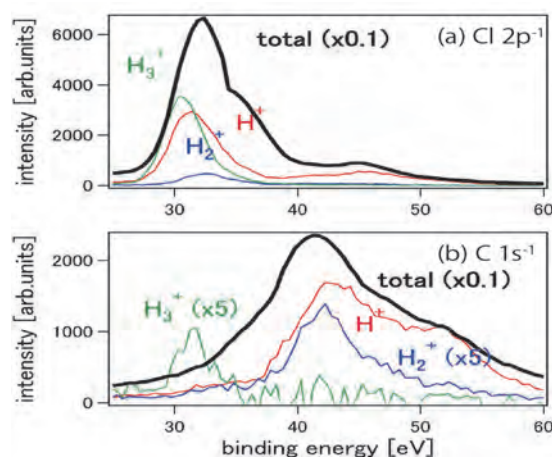


Fig. 2. Total and coincidence Auger spectra with H_n^+ ($n=1,2,3$) for (a) Cl 2p and (b) C 1s photoionization.

[1] S. Pilling *et al.*, Mon. Not. R. Astron. Soc. **375** (2007) 1488.

BL6U

Molecular Dynamics of Core Excited N₂ Molecules Studied by an Auger-Electron-Photoion Coincidence Method

H. Iwayama^{1,2} and E. Shigemasa^{1,2}¹UVSOR Facility, Institute for Molecular Science, Okazaki 444-8585, Japan²School of Physical Sciences, The Graduate University for Advanced Studies (SOKENDAI), Okazaki 444-8585, Japan

A core shell electron in a molecule can be promoted to unoccupied orbitals when a photon energy is tuned to resonances. The core excited molecule thus created is highly unstable and relaxes either by radiative decay or Auger electron emission. For light elements ($Z < 26$), the Auger decay is the dominant process after the core excitation, and various cationic states are formed through the Auger electron emissions. In some cases, core excited molecules become dications by the double Auger decay. The stability and dissociation dynamics of the Auger final states depend on their charge states and electronic states, which can be investigated by using an Auger-electron-photoion coincidence technique. In this work, we investigate the stability and dissociation dynamics of core excited N₂ molecules.

The Auger-electron-ion coincidence measurements were performed on the undulator beamline BL6U at UVSOR. The Auger electrons and product ions were measured in coincidence by a double toroidal electron analyzer (DTA) and an ion momentum spectrometer, respectively. The pass energy of DTA was set to 400 eV. All signals from the ion and electron delay-line detectors were recorded with an 8ch TDC board. The photon energy was tuned to 401.1 eV, which corresponds to the resonance energy of the N 1s $\rightarrow \pi^*$ excitation.

Figures 1(a) and (b) show total and coincidence Auger spectra with N₂⁺ and N⁺ ions, respectively. The energy scale of the bottom axis is obtained by subtracting the kinetic energy (KE) of Auger electrons from the excitation energy of 401.1 eV. Here this is defined as remaining energy. For cations, the remaining energy corresponds to the binding energy, while it is slightly higher than the binding energy for dications, due to the ejection of a second Auger electron. Below the remaining energy of ~ 25 eV, we observe only N₂⁺ ions. This is consistent with the fact that the lowest dissociation limit energy of N⁺ + N is 24.2 eV. On the other hand, we find only N⁺ ions above the binding energy of ~ 25 eV. To identify the contribution of dications resulting from the double Auger decay, we show a coincidence Auger spectrum with N⁺+N⁺ fragment pairs in Fig. 1(c). The spectrum shows the double Auger decay processes can contribute to the Auger final states above the remaining energy of 48 eV.

Figure 2 shows a two-dimensional Auger-electron-photoion coincidence map. The vertical and horizontal axes correspond to the kinetic energy release (KER) of ions

and the remaining energy, respectively. We find several diagonal structures, suggesting several dissociation pathways. Dashed lines in Fig. 2 represent lowest dissociation limit energies for N⁺ + N and N⁺ + N⁺. The horizontal structure at the remaining energy of 48 eV and KER of 0 eV corresponds to metastable N₂⁺⁺ ions. Above the remaining energy of 40 eV, the double Auger decay process is dominant. The detail analysis is in progress

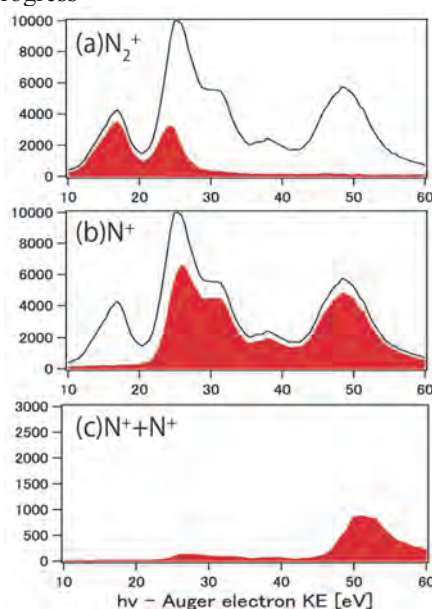


Fig. 1. Total (black line) and coincidence Auger spectra (red filled area) with (a) N₂⁺ ions, (b) N⁺ ions and (c) N⁺+N⁺ fragment pairs.

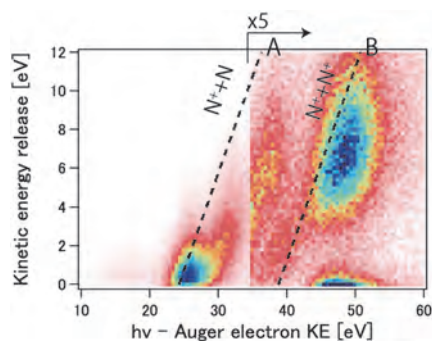


Fig. 2. A two-dimensional Auger-electron-photoion coincidence map. Diagonal dashed lines A and B represent a plot of the KER as a function of the remaining energy for lowest dissociation limits of N⁺+N and N⁺+N⁺, respectively.

BL6B

Infrared Microscopy of T-Shape Microfluidics

M. Nagasaka¹, H. Yuzawa¹, M. Nakano¹, N. Takada¹, M. Aoyama¹, E. Rühl² and N. Kosugi¹

¹Institute for Molecular Science, Okazaki 444-8585, Japan

²Physikalische Chemie, Freie Universität Berlin, Takustr. 3, D-14195 Berlin, Germany

Microfluidics is a chemical technique to realize highly efficient chemical reactions in liquids and solutions. The mechanism of such reactions in microfluidics has been studied by thermal lens microscopy [1] and nuclear magnetic resonance methods [2]. It is difficult to apply spectroscopic techniques to microfluidics, especially in the soft X-ray regime, since this radiation cannot penetrate a microfluidics cell. Recently, we have developed a liquid cell for soft X-ray absorption spectroscopy (XAS) of liquids in the transmission mode [3]. The liquid layer in the cell is sandwiched between two Si₃N₄ membranes with the thickness of 100 nm to transmit soft X-rays.

The purpose of this study is to measure XAS and infrared (IR) spectra of structured liquids by developing a microfluidic cell consisting of Si₃N₄ membranes. In the report, we show results from IR microscopy of a T-shaped microfluidics cell during the mixing process of water and ethanol for a proof-of-concept study of a cell that is currently under development.

The experiments were performed by using the IR microscopy IRT-7000 at BL6B combined with a developed microfluidic cell. A T-shape microfluidics setup with a width of 50 μm is made from PDMS resin which is covered by a 100 nm Si₃N₄ membrane (NTT-AT). The adhesion of PDMS to the Si₃N₄ membrane is realized by pressing a Si frame of the membrane with O-rings. Ethanol and water are mixed in the T-shaped cell with a flow rate of 50 μL/min by using syringe pumps. The spatial resolution of 30 × 30 μm² is reached by using a ×16 Cassegrain mirror. IR spectra are taken by detecting the reflected infrared light with an MCT detector.

Figure 1 shows the 2D plot of the IR absorbance in the T-shape microfluidics at 3507 cm⁻¹, which is due to the OH stretching mode of water. Ethanol is flowed in the left hand part and water is injected into the right hand part. The ethanol-water mixture is flowed to the lower part after the junction of the liquids. Figure 2 shows IR spectra at different positions of the setup, considering that the absorbance at 3507 cm⁻¹ of water is larger than that of ethanol. The IR spectra at the positions A, B, and C after the junction of two liquids are similar to each other. The results indicate, however, that the hydrogen bonds between water decrease rapidly after mixing of both liquids.

In subsequent studies, we intend to investigate IR microscopy of chemical reactions using our T-shaped microfluidics setup.

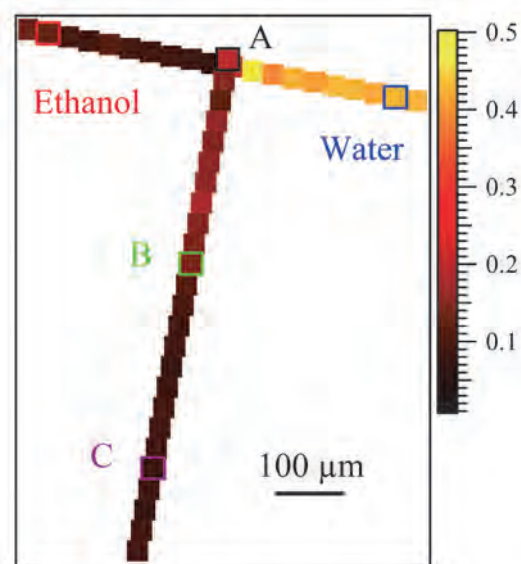


Fig. 1. The 2D plot of the IR absorbance at 3507 cm⁻¹ in the T-shaped microfluidics cell.

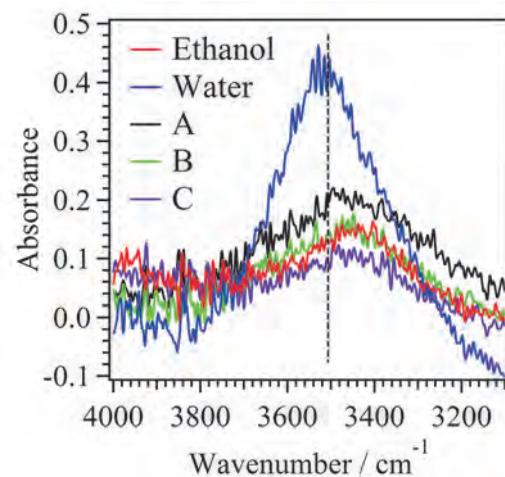


Fig. 2. IR spectra at different positions of the microfluidics cell. The positions of data acquisition are shown in Fig. 1. The dashed line indicates the wavenumber of 3507 cm⁻¹.

[1] T. Kitamori *et al.*, *Anal. Chem.* **76** (2004) 53.

[2] T. Tsukahara *et al.*, *Angew. Chem. Int. Ed.* **46** (2007) 1180.

[3] M. Nagasaka *et al.*, *J. Electron Spectrosc. Relat. Phenom.* **200** (2015) 293.

UVSOR User 3



III-4

Surface,
Interface and
Thin Films

BL4B

Soft X-Ray Absorption Spectroscopy of 1,3,5-Trithia-2,4,6-Triazapentalenyl Thin Film on Ag(111)

K. Eguchi¹, K. Awaga^{1,2}, Y. Takagi^{3,4} and T. Yokoyama^{3,4}

¹Graduate school of Science, Nagoya University, Nagoya 464-8602, Japan

²CREST, JST, Kawaguchi 332-0012, Japan

³Institute for Molecular Science, Okazaki 444-8585, Japan

⁴School of Physical Sciences, The Graduate University for Advanced Studies (SOKENDAI), Okazaki 444-8585, Japan

Organic radicals, which are open-shell molecules, have been attracting significant attention because of their potential applications in organic electronics and spintronics. Because of its magnetic bistability at room temperature,

1,3,5-trithia-2,4,6-triazapentalenyl (TTTA; Fig. 1(a)) is a candidate for such applications [1]. Although its crystal structures as well as the thermally induced and photo-induced magnetic phase transitions in single crystals have been widely studied, few studies have investigated the structures and electronic and magnetic states of TTTA in thin films. In this study, we measure the angular dependence of X-ray absorption spectra (XAS) of a TTTA thin film prepared on Ag(111) using linearly polarized X-rays.

The sample was prepared on Ag(111) by exposure of gaseous TTTA under ultra-high vacuum condition ($\sim 6 \times 10^{-8}$ Pa) at room temperature and subsequent annealing at 500 K. XAS were measured at the end station of the bending magnet beamline 4B using an X-ray magnetic circular dichroism (XMCD) measurement chamber in total electron yield detection mode. Linearly polarized X-rays were irradiated to the sample at incident angles between 0° (normal) and 60° (grazing) in increments of 10° with respect to the substrate normal. Energy resolutions were set to $E/\Delta E = 2000$ and 4000 at N K- and S L-edge, respectively.

Figure 1(b) shows angle-dependent N K-edge XAS of the TTTA thin film on Ag(111). Four peaks labeled A–D were mainly observed in this region, and they increased with the X-ray incidence angle, indicating that molecules adsorbed with a relatively flat-lying orientation because of the π^* bonding characters of the singly occupied molecular orbital (SOMO) and lowest unoccupied molecular orbital (LUMO) of TTTA. Judging from the peak intensities and energy levels, peaks A and B can be assigned to SOMO and LUMO, respectively, indicating that the radical in TTTA can survive in the thin film.

Figure 1(c) shows angle-dependent S L-edge XAS of the TTTA thin film. Five peaks, labeled A–E, were observed. Although the intensity of peaks B–E decreased with increasing X-ray incidence angle, peak A showed an opposite polarization dependence. Therefore, peak A can be attributed to the transition from the $2p_{3/2}$ to the σ^* orbital, as observed in thiophene [2], suggesting less contribution of the S 3d orbitals to the SOMO of TTTA.

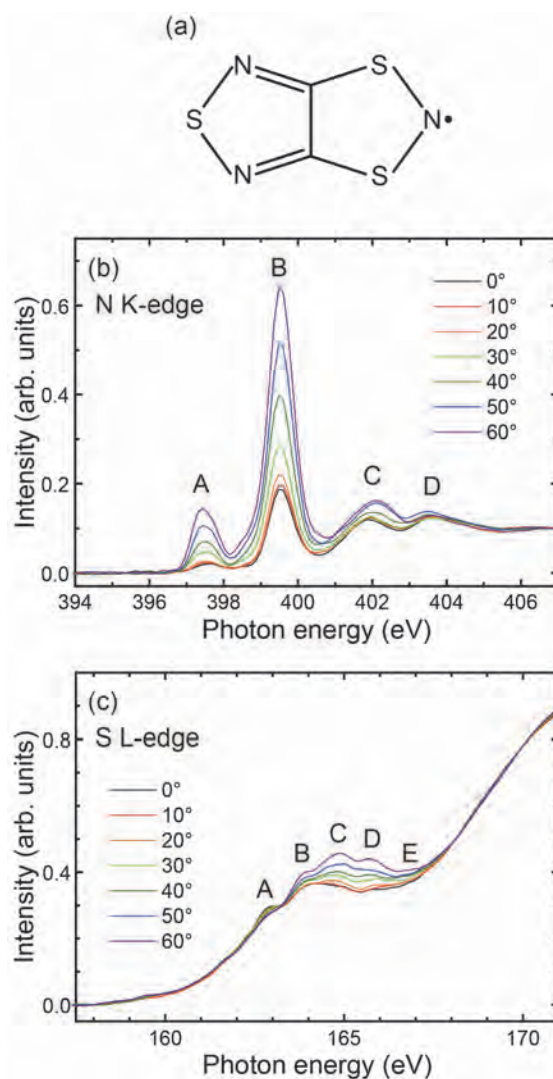


Fig. 1. (a) Chemical structure of TTTA. (b) N K-edge and (c) S L-edge XAS of the TTTA thin film on Ag(111) taken at 220 K.

[1] W. Fujita and K. Awaga, *Science* **286** (1999) 261.

[2] A. P. Hitchcock, J. A. Horsley and J. Stöhr, *J. Chem. Phys.* **85** (1986) 4835.

BL2B

Potassium Doping into Single Crystalline Organic Monolayer

T. Hosokai¹, Y. Hasegawa², M. Yano², K. R. Koswattage³ and Y. Yamada²

¹National Institute of Advanced Industrial Technology and Science, Tsukuba 305-8568, Japan

²Institute of Applied Physics, University of Tsukuba, Tsukuba 305-8573, Japan

³Institute for Molecular Science, Department of Photo-Molecular Science, Okazaki 444-8585, Japan

Metal doping into organic semiconducting thin films (OTFs) is practically relevant technology in *Organic Electronics*. Potassium (K) is known as a very low workfunction (WF) metal showing around 2.3 eV and is often used as the dopant. K-doped OTF systems often show new electronic states within the band gap of the bare OTFs [1]. This is usually interpreted by filling the lowest unoccupied molecular orbital (LUMO) of OTFs by electron-transfer from the doped K atoms. For such experiments bulk OTFs have been often employed. Owing to this, the discussion on the electronic structure of the doped-OTFs with respect to the doped structure in a molecular level was hindered.

To overcome this issue, we will study the single crystalline K-doped organic monolayers fabricated on Au(111) surface by using angle-resolved ultraviolet photoelectron spectroscopy (UPS). Previously, we found a well-ordered monolayer is formed by depositing K atoms onto two kind of organic monolayer of picene (C₂₂H₁₄, Fig. 1(a)) and coronene (C₂₄H₁₂, Fig. 1(b)) [2]. For these doped monolayer systems, here we applied ARUPS to reveal the physics behind the K-doped OTFs.

All the experiments were conducted at BL2B. After preparing a clean Au(111) with conventional Ar sputtering and annealing process, picene, coronene, or K was thermally grown on the substrate. The deposition amount is controlled by a quartz microbalance and is confirmed by a change in WF of the systems. For the well-ordered doped monolayers, K was deposited step-by-step onto the picene or coronene monolayer. ARUPS was measured with a photoelectron emission angle $\theta = -5\sim 15^\circ$, $h\nu = 28$ eV. All the depositions and measurements were performed at room temperature.

Figures 1(a) and 1(b) show the ARUPS spectra of bare Au(111), picene or coronene monolayer, K-doped picene or coronene monolayer, K/Au(111), respectively. The surface state (SS) near the Fermi level in the substrate (top) spectra is vanished by the molecular monolayer formation (second top spectra). The highest occupied MO (HOMO: H) is located at 1.36 eV for picene and 1.57 eV for coronene. The K doping into the films results in the appearance of new states at 0.31 eV for picene and 0.52 eV for coronene. As seen in the K/Au(111) spectra (bottom ones), the new states observed by the K doping are differed to one originating from pure K atoms, which is located at 0.92 eV.

The new states formed in the K/picene and K/coronene systems near the Fermi level can be ascribed to the former LUMO (L') bands. X-ray

photoelectron spectroscopy showed a large chemical shift of C1s in the systems towards higher binding energy side due to electron transfer from K atoms [2]. The resemble features have been observed for other organic/metal systems, such as PTCDA and DIP [3]. The position of L' state is depending on filling amount of the LUMO by electrons. It can be considered that LUMO of picene thin films is partially filled since the L' feature is partly cut at the Fermi level. On the other hand, the L' feature for the K/coronene system is located at higher binding energy side, implying more electrons are transferred to LUMO of coronene. However, the question arises why the doping amount of the electrons are differed between picene and coronene. In previous, a complete filling of LUMO level was reported for the K doped-thick picene and coronene films (thickness is 5 nm) [4]. In this sense, presence of the Au(111) substrate as well as the low dimensional organic monolayer may play the role. To understand this, theoretical investigations based on the ordering model as determined by STM [2] is required.

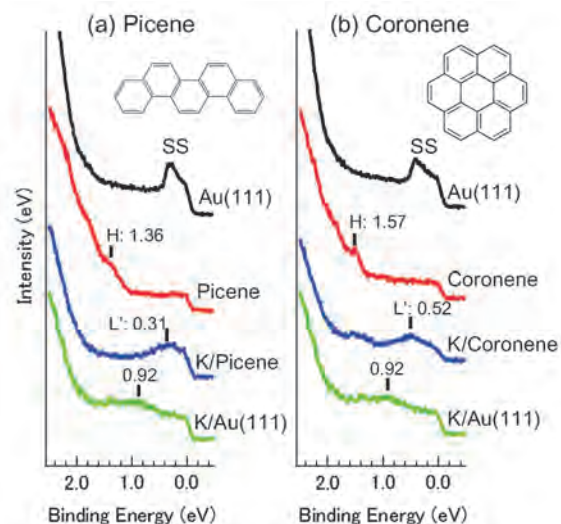


Fig. 1. (a) ARUPS of Au(111), picene monolayer/Au(111), K-doped/picene, and K/Au(111). (b) ARUPS of Au(111), coronene monolayer/Au(111), K-doped/coronene, and K/Au(111).

- [1] C.-P. Cheng *et al.*, *Org. Electron.* **14** (2013) 942.
 [2] M. Yano *et al.*, *J. Chem. Phys.* **141** (2014) 034708.
 [3] T. Hosokai *et al.*, *MRS proceedings* **1647** (2013) mrsf13-1647-gg01-03.
 [4] M. Benjamin *et al.*, *J. Chem. Phys.* **136** (2012) 134503.

BL2B

Electronic Structures of Thienyl-Porphyrin Derivatives

Y. Nakayama¹, A. Nakagawa¹, K. R. Koswattage², T. Aikawa¹, T. Kondo¹ and M. Yuasa¹

¹Department of Pure and Applied Chemistry, Graduate School of Science and Technology,
Tokyo University of Science, Noda 278-8510, Japan

²Center for Frontier Science, Chiba University, Chiba 263-8522, Japan

Porphyrin is a representative bio-functional unit of a large π -conjugated ring and has been attracting much attention of both physico-chemical and bio-medical points of view. Porphyrins functionalized by thiophenes, typical organic semiconductors, are therefore of particular interests for bio-electronics applications [1]. In the present study, we elucidated the electronic structures of two thienyl-porphyrin derivatives, 5,10,15,20-tetra(2-thienyl)porphyrin (2T) and 5,10,15,20-tetra(3-thienyl)porphyrin (3T) (Fig. 1), by means of photoelectron spectroscopy (PES).

Procedures for synthesizing 2T and 3T are found elsewhere [2]. Thin films of 2T and 3T were prepared by vacuum evaporation onto Au-coated Si substrates, where their thicknesses were monitored with a quartz microbalance. PES measurements were conducted at BL2B of UVSOR. The work function of the present electron analyzer (VG-Scienta, R3000) was determined to be 4.40 eV after accurate calibration of the photon energy by using second-order light.

Figure 2 shows wide range PES spectra of *bulk* (16 nm-thick) films of 2T and 3T. The spectral profiles are respectively well reproduced by density-of-states curves which are simulated from each orbital energy distribution. The electronic structures in the highest occupied regions evolve on step-by-step deposition of 2T and 3T as shown in Fig. 3. For both cases, peaks derived from the highest occupied orbitals move toward the Fermi level as the films become thinner. This trend to reduce substantial hole injection barrier (HIB) heights may be attributed to a common screening effect at metal-organic interfaces.

Changes in the work function (WF), HIB, and the ionization potential (IP) values are summarized in Figs. 3(a), (b), and (c), respectively, plotted as a function of the 2T or 3T thickness. These results imply that orientation of the side groups merely gives minor impacts, if any, to the charge carrier conduction characteristics of these thienyl-porphyrin derivatives.

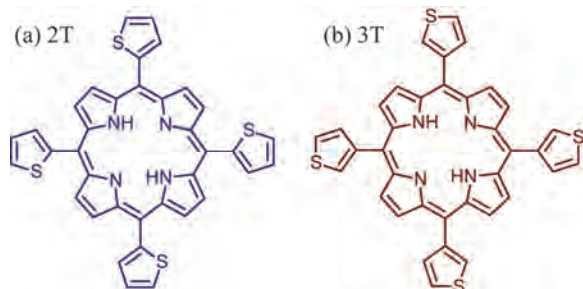


Fig. 1. Molecular structures of (a) 2T and (b) 3T.

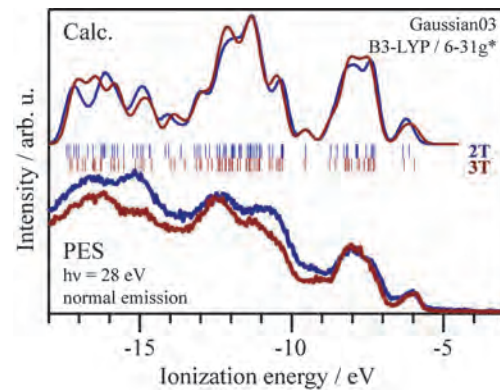


Fig. 2. (Top panel) Quantum chemical calculation results of 2T (blue) and 3T (red) molecules. (Bottom) PES spectra of 16 nm-thick films of 2T and 3T.

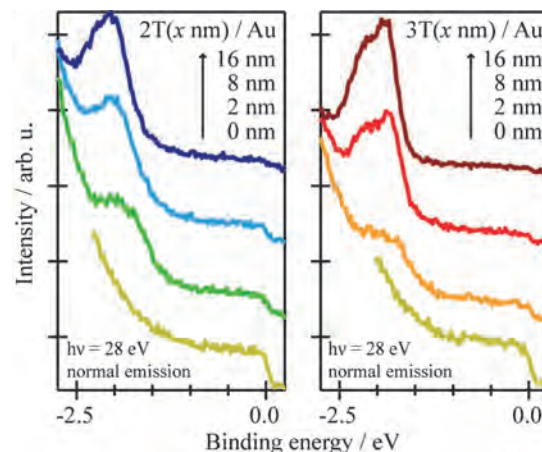


Fig. 3. Evolution of the PES spectra of 2T (left) and 3T (right) thin films grown on Au substrates.

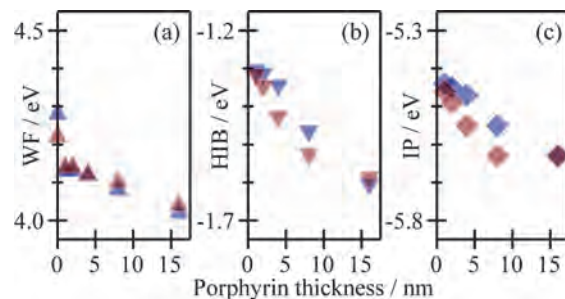


Fig. 4. (a) Work functions (WF), (b) HIB, and (c) ionization potentials (IP) of the 2T (blue) and 3T (red) thin films plotted as a function of the thickness.

[1] K. Oyaizu *et al.*, *J. Polym. Sci. A: Polym. Chem.* **44** (2006) 5403.

[2] M. Yuasa *et al.*, *Polym. Adv. Tech.* **16** (2006) 616.

BL2B

Molecular Orientation of Pentacene Thin Film on Silane-SAM with Different Growth Condition

K. K. Okudaira and Y. Tuboi

Association of Graduate Schools of Science and Technology, Chiba University, Chiba 263-8522, Japan

Recently, organic thin-film transistors (OTFT's) with field-effect mobility and on/off current ratio comparable to hydrogenated amorphous silicon thin-film transistors. OTFT's have been fabricated using pentacene as the active material.

Since the interface between the organic active material and the gate dielectric material is a critical part of the field-effect device, control of this interface is important. The characteristics of pentacene TFT's can be improved by using a self-organizing material like octadecyltrichlorosilane (OTS) between the SiO₂ gate dielectric and the pentacene active layer [1].

To achieve optimum control over SAM growth, a new, efficient, and humidity controlled method of growing highly ordered OTS SAMs has been reported. OTFT field-effect mobility and contact angle of the surface of the SAM show strong dependence of the growth condition such as humidity [2]. The characteristics of OTFT such as mobility are considered to be dependence on not only the electronic structure but also the molecular orientation of organic molecule.

In this work we used OTS SAMs for substrate and examined the molecular orientation of pentacene thin films thermally deposited on these SAM surfaces by angle-resolved ultraviolet photoelectron spectroscopy (ARUPS) measurements. In the ARUPS take-off angle dependence of HOMO peak for π -conjugated organic molecule provides an important information on the molecular orientation [3].

ARUPS measurements were performed at the beam line BL2B of the UVSOR storage ring at the Institute for Molecular Science. The take-off angle (θ) dependencies of photoelectron spectra were measured with the photon energy ($h\nu$) of 28 eV. We use octadecyltrichlorosilane (OTS) as coupling agent for SAM. The SAMs were prepared using a dipping method at room temperatures. To fabricate humidity-controlled SAM growth was performed under ambient conditions in a controlled atmosphere glovebox at varied relative humidity levels with 10%, 60%, and 80%. Pentacene thin film was deposited on these SAMs.

We observed take-off angle (θ) dependence of HOMO peak in UPS of pentacene thin film (thickness of about 1.5 nm) on OTS-SAMs with different growth condition, expressed by humidity (10%) and (60%) (Figs.1(a) and (b)). The HOMO peaks of pentacene on OTS-SAM(with humidity 10%) and 60%) appear at binding energy of about 2 eV. The HOMO peaks of pentacene on both OTS-SAM (10%) and on OTS-

SAM(60%) show intense peaks at normal take-off angle ($\theta = 0^\circ$), and at grazing angle these intensities become small. At grazing angle ($\theta = 60^\circ$) the intensity of HOMO peak of pentacene on OTS-SAM (10%) remains, while the pentacene HOMO peak on OTS-SAM(60%) almost disappears. Take-off angle dependence of HOMO peak on OTS-SAM(10%) is different from that on OTS-SAM (60%). It indicates that the molecular orientation of pentacene on OTS-SAM(10%) is different from that on OTS-SAM(60%). The surface conditions of OTS-SAM due to the growth condition of SAM such as humidity affect the molecular orientation of organic semiconductor layer, which would have an effect on the characteristics of OTFT such as mobility.

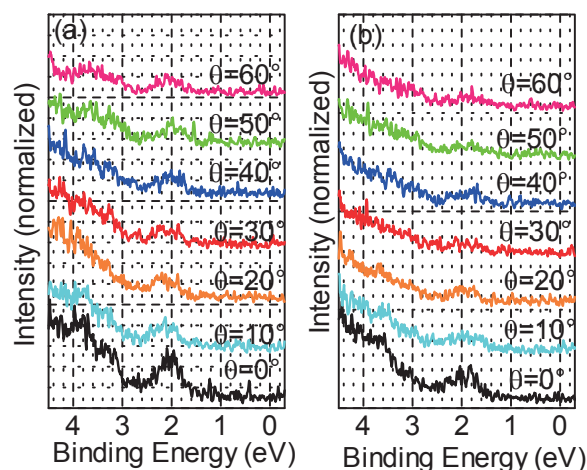


Fig. 1. Take-off angle (θ) dependences of ultraviolet photoelectron spectra with HOMO region of pentacene (1.5nm)/OTS-SAM (with humidity of 10%) (a) and pentacene(1.5nm)/OTS-SAM (with humidity of 60%) (b).

[1] J. -M. Kim *et al.*, Appl. Phys. Lett. **85** (2004) 6368.

[2] S. R. Walter *et al.*, J. Am. Chem. Soc. **134** (2012) 11726.

[3] N. Ueno *et al.*, J. Chem. Phys. **99** (1993) 7169.

BL2B

A Surface Study of CsK2Sb Multi-Alkali Photocathode by UPS

M. Urano¹, M. Kuriki¹, K. Negishi¹, A. Yokota¹, T. Konomi² and Y. Seimiya²

¹Graduate school of Advanced Science of Matter, Hiroshima University, Higashi-hiroshima 739-8530, Japan

²Hight Energy Accelerator Research Organization, Tsukuba 305-0801, Japan

Linear accelerator based facilities such as X-FEL, ERL, Linear colliders break the limitations of the circular accelerators such as 3rd generation light source, ring colliders, etc. In the linear accelerator, high quality and high average current beam has to be provided because of no circulation. Laser photocathode can provide such beam, but conventional cathode material such as metal, GaAs, Cs₂Te are not ideal. CsK₂Sb multi-alkali photocathode is the candidate of the ideal cathode due to the high quantum efficiency (QE), and high robustness, and green laser driver for photo-electron effect. Many experimental efforts has been made to obtain the CsK₂Sb photocathode optimized for the photo-cathode purpose, but it is on the way. In this study, we perform UPS analysis of the CsK₂Sb cathode to reveal the cathode performance and the surface states.

Figure 1 shows QE (405nm) evolution during the cathode activation (Sb, K, and Cs evaporation on Si substrate (Si 100) in this order). Typical pressure was 1.0×10^{-7} Pa.

Amount of Sb, K, and Cs are shown as thickness measured by quartz monitor. The sample is in situ and is transferred to UPS chamber by transfer rod. Amplitude (cross section) ratio of Cs 5s and Cs 5p as a function of QE with laser (405nm) are shown in Fig. 2. Different color shows different samples. QE variation is due to the degradation in time for each sample. According to the results, the small ratio gives a large QE for each sample, but the sample dependence is large. According to a similar measurement for Cs₃Sb [1], the low ratio is interpreted as that Cs is bound to Sb as Cs⁺ ion. From this observation, the bound state of Sb and Cs is a good index to examine the photocathode performance. This is the first observation for the relation between the cathode performance and the Cs-Sb bound state.

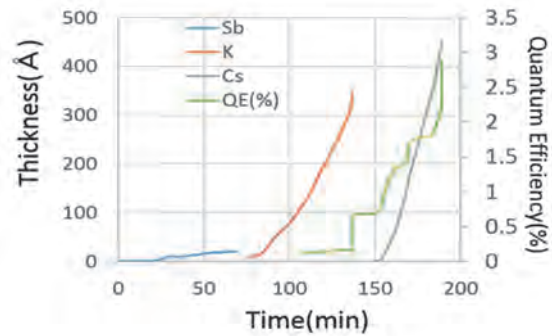


Fig. 1. QE evolution during CsK₂Sb activation.

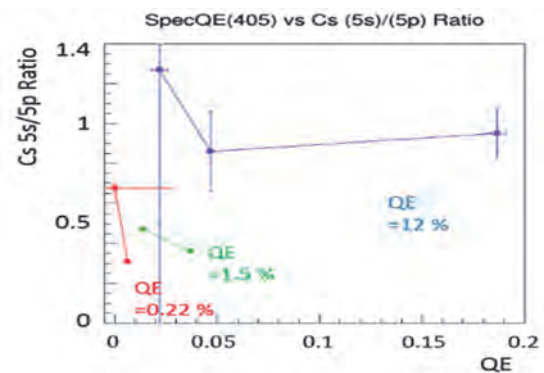


Fig. 2. Cs 5s/5p ratio as a function of QE.

[1] Clayton W. Bates Basic studies of high performance multi-alkali photo-cathodes (1979).

BL3U

Operando Observation of Cobalt Catalyst for Oxygen Evolution Reaction by Soft X-Ray Absorption Spectroscopy

M. Yoshida^{1,2,*}, Y. Mitsutomi¹, S. Onishi¹, F. Yamamoto¹, M. Nagasaka³, H. Yuzawa³, N. Kosugi³ and H. Kondoh¹

¹Department of Chemistry, Keio University, Yokohama 223-8522, Japan

²Cooperative Research Fellow, Institute for Catalysis, Hokkaido University, Japan

³Institute for Molecular Science, Okazaki 444-8585, Japan

Recently, hydrogen production by electrochemical water splitting using renewable energy sources such as solar, wind, and hydroelectric powers attracts attention from the viewpoint of the realization of a sustainable society that does not depend on fossil fuels. For practical applications, the improvement of overall water splitting efficiency has been required by the development of highly active oxygen evolution electrocatalyst. In this situation, Nocera et al. reported that cobalt oxides electrodeposited from a dilute Co^{2+} solution in phosphate or borate buffered electrolyte (Co-P_i or Co-B_i, respectively) are efficient electrocatalysts for oxygen evolution reaction (OER) [1]. The local structures of Co species in the Co-P_i and Co-B_i catalysts were investigated by X-ray absorption fine structure (XAFS) spectroscopy and pair distribution function (PDF) analysis, and it was found that the Co-P_i and Co-B_i thin films form a nano-sized cluster (ca. 2-3 nm and 3-4 nm, respectively) with an edge-sharing CoO_6 octahedral structure [2]. However, the detailed information about oxygen species in these electrocatalysts under working condition is not yet obtained. Thus, we have investigated the reaction mechanism by measuring operando O K-edge XAFS spectra for Co-P_i and Co-B_i under electrochemical potential control.

Electrochemical O K-edge XAFS measurements with transmission mode using soft X-rays were performed at BL3U in the UVSOR Synchrotron, according to the previous work [3]. A home-made electrochemical cell was used with Au/Cr/SiC thin film substrates as working electrodes, a Pt counter electrode, and a Ag/AgCl reference electrode. Co-P_i or Co-B_i electrocatalyst was electrodeposited on the Au/Cr/SiC working electrode at 1.0 V in 0.1 M phosphate or borate buffered electrolyte containing 0.5 mM $\text{Co}(\text{NO}_3)_2$.

The OER activities of Co-P_i and Co-B_i were tested by the linear sweep voltammograms in phosphate and borate buffered electrolytes, respectively. The result exhibited that the OER current for Co-P_i electrode was higher than that for Co-B_i, which means that Co-P_i is a more efficient OER electrocatalyst compared with Co-B_i. Next, the operando O K-edge XAFS spectra for Co-P_i catalyst were taken under electrode potential control in a phosphate buffered electrolyte, as shown in Fig. 1. At 0.0 V, an absorption peak derived from oxygen species of CoOOH was observed around 531 eV. When

the electrode potential was changed from 0.0 to 1.1 V, a new absorption peak attributed to oxygen species of CoO_2 was observed around 529 eV, meaning that the part of CoOOH cluster was oxidized to CoO_2 with the high-valent cobalt species (Co^{4+}) (Fig. 2). Meanwhile, when the similar measurements were tested for Co-B_i, the fraction of generated CoO_2 against CoOOH for Co-B_i was slightly smaller than that for Co-P_i. Therefore, we found that Co-P_i can function as a highly active OER electrocatalyst due to the presence of many CoO_2 species.

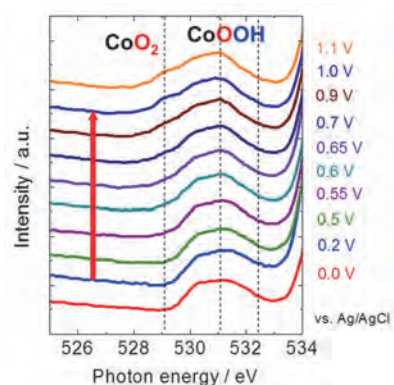


Fig. 1. Operando O K-edge XAFS spectra of Co-P_i electrocatalyst at various electrode potentials in 0.1 M phosphate buffered electrolyte.

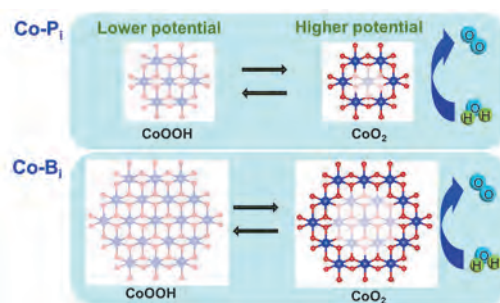


Fig. 2. Proposed reaction mechanism for Co-P_i and Co-B_i OER electrocatalysts.

[1] D. G. Nocera *et al.*, J. Am. Chem. Soc. **131** (2009) 2615.

[2] (a) D. G. Nocera *et al.*, J. Am. Chem. Soc. **132** (2010) 13692. (b) J. Am. Chem. Soc. **135** (2013) 6403.

[3] (a) M. Nagasaka *et al.*, J. Phys. Chem. C **117** (2013) 16343. (b) M. Yoshida *et al.*, J. Phys. Chem. C **119** (2015) 19279.

BL3B

Effects of Ion Implantation and Thermal Annealing on PL due to Cr³⁺ in LaAlO₃

M. Harima, T. Morimoto and Y. Ohki
Waseda University, Tokyo 169-8555, Japan

High permittivity (high-*k*) dielectrics such as LaAlO₃ are expected as a gate insulator in advanced MOS devices. In the manufacturing process of semiconductors, ion implantation and thermal annealing are often used [1]. However, few reports have been published on the influences of such processing procedures on point defects in LaAlO₃.

In the present study, single crystal LaAlO₃ was implanted with B⁺ ions and then annealed in O₂ at 900°C. The effects of such treatments were examined by measuring optical absorption, X-ray diffraction (XRD), and photoluminescence (PL).

Figure 1 shows optical absorption spectra. The sharp increase in the absorption from around 5.0 eV is caused by the bandgap absorption [2]. This absorption becomes weak by the ion implantation, whereas the following thermal annealing increases the absorption in nearly the whole energy range.

Figure 2 shows in-plane XRD spectra. A sharp peak is seen at $2\theta_{\chi} = 23.5^{\circ}$, which corresponds to the diffraction on (012) planes of crystalline LaAlO₃ [3]. The XRD intensity decreases by about 40 percent after the ion implantation. The annealing given following the implantation increases the intensity to almost the same level as the untreated sample. This indicates that the crystallinity of single crystal LaAlO₃ is degraded by the ion implantation and is recovered by the thermal annealing after the ion implantation.

Figure 3 shows PL spectra excited by 6.0-eV photons. A PL, which has three sharp components at 1.62, 1.65, and 1.69 eV, is observable. This PL is due to Cr³⁺ present in LaAlO₃ as an impurity [4]. After the ion implantation, the total intensity of this PL

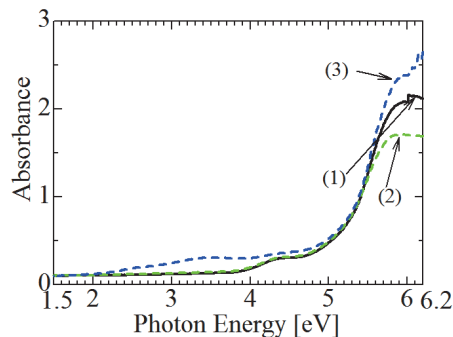


Fig. 1. Optical absorption spectra observed for LaAlO₃ samples with a thickness of about 0.5 mm at room temperature before any treatment (1), after implantation of B⁺ ions at a fluence of 10¹⁵ cm⁻² (2), and after thermal annealing in O₂ at 900 °C given following the B⁺ implantation (3).

decreases by about 79% compared with the untreated sample. When the sample was implanted with B⁺ ions and then annealed at 900°C, the intensity of this PL increases to almost the same level as the untreated sample. Since this PL is sensitive to the crystallinity of LaAlO₃ [5], the decrease of the PL intensity is due to degradation of crystallinity.

These results indicate that the crystallinity of LaAlO₃ is collapsed by the ion implantation and is recovered by the thermal annealing after the ion implantation.

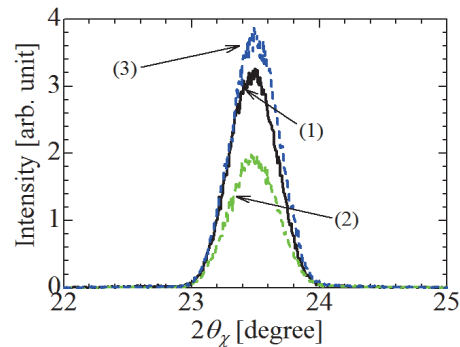


Fig. 2. In-plane XRD pattern. The notations of symbols and curves are the same as those in Fig. 1.

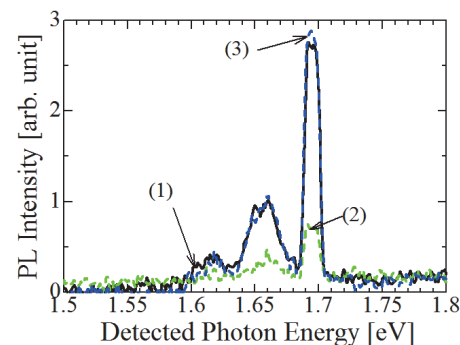


Fig. 3. PL spectra induced by the irradiation of photons with energies of 6.0 eV. The notations of symbols and curves are the same as those in Fig. 1.

- [1] Q. Zhang *et al.*, Proc. Int. Symp. Power Semiconductor Devices and ICs (ISPSD) (2005) 211.
- [2] J. Robertson, Rep. Prog. Phys. **69** (2006) 327.
- [3] C. J. Lu *et al.*, Appl. Phys. A **67** (1998) 253.
- [4] J. Heber *et al.*, Z. Phys. **246** (1971) 261.
- [5] T. Morimoto *et al.*, J. Inst. Eng. Elec. Discharges Japan **57** (2014) 3.

BL4U

STXM Analysis of Adsorbent for Effective Recovery of Radioactive Elements

Y. Sano, S. Watanabe and S. Kibe

Japan Atomic Energy Agency (JAEA), Tokai 319-1194, Japan

Spent nuclear fuels generated from nuclear power plants contain U and Pu which can be reused, and several long-lived radioactive elements. It will be quite important for effective utilization of energy and environmental loading reduction to process the spent fuel adequately. JAEA has been developing the selective recovery process of radioactive elements, which uses adsorbents of SiO₂ supports coated with styrene-divinylbenzene (SDB) copolymer (SiO₂-P) and extractants on its surface. Our recent work shows that the separation and recovery abilities of adsorbent, i.e. adsorption/elution behavior of radioactive elements, in this process are strongly dependent on the condition of its surface in which polymer and extractants are impregnated [1]. In this study, some information about the adsorbent surface, such as thickness of polymer and uniformity of extractants, were investigated by scanning transmission X-ray microscope (STXM).

Some adsorbents with different crosslinking degree of polymer (CDP) were synthesized and octyl (phenyl)-N, N-diisobutylcarboylmethylphosphine oxide (CMPO) was impregnated as an extractant by the flowsheet reported by Wei *et al.* [2]. The average diameter and pore size of the SiO₂ supports were 50 μ m and 600nm, respectively (Fig.1). These adsorbents were sliced to 300nm in thickness by focused ion beam (FIB), and were supplied to STXM analysis.

Figure 2 shows the change of C-NEXAFS spectra (C-K edge) with CDP, which were obtained near the pore surface on the cross section of the sliced adsorbents. The intensity of the peak at 285 eV (which must be attributed to C 1s \rightarrow π^* transition of aromatic C=C) changed with CDP and the impregnation of CMPO. Figure 3 show the colorized composition maps on the cross section of sliced SiO₂-P (CDP=10%) and SiO₂-P (CDP=15%) with 20wt% CMPO, which were calculated by fitting C-NEXAFS spectra with those of SDB polymer and CMPO. The SDB polymer and CMPO were distributed within several hundred nanometers from the pore surface, and their distributions were spread by the increase of CDP and CMPO.

The excess increase of the region with SDB polymer and CMPO in the pore may disturb the fluid flow through the pore, and this will give some interpretation of our previous experiment, in which it was more difficult to elute adsorbed metal ions from the adsorbent with higher CDP [1]. It should be required for effective recovery of radioactive elements to compare the STXM data and adsorption/elution

behavior, and to optimize the distributions of SDB polymer, i.e. polymer thickness, and extractants.

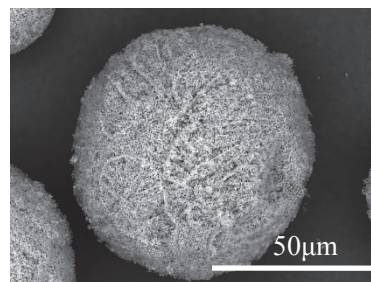
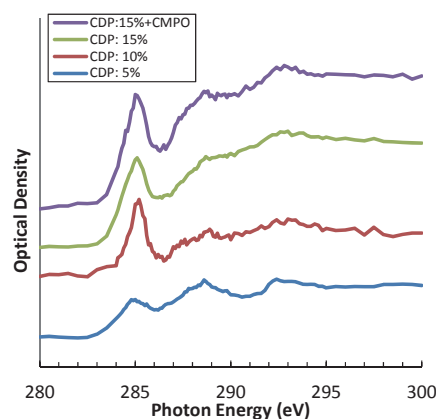
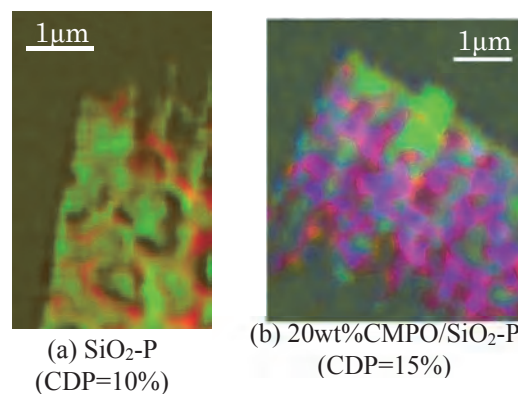
Fig. 1. Photo of the SiO₂ supports.

Fig. 2. Change of C-NEXAFS spectra (C-K edge).

Fig. 3. Colorized composition maps (light green; SiO₂, red; SDB, blue; CMPO (purple; mixture of red and blue)).

[1] S. Watanabe *et al.*, *Procedia Chemistry* 7 (2012) 411.

[2] Y. Wei, M. Kumagai and Y. Takashima, *Nucl. Technol.* **132** (2000) 413.

BL4B

Pd *M*-Edge X-Ray Magnetic Circular Dichroism in Perpendicularly Magnetized Co/Pd Multilayers

J. Okabayashi^{1*} and H. Munekata²

¹Research Center for Spectrochemistry, University of Tokyo, Tokyo 113-0033, Japan

²Imaging Science and Engineering Laboratory, Tokyo Institute of Technology, Yokohama 226-8503

CoPd is a candidate for the spintronics materials possessing perpendicular magnetic anisotropy (PMA) which can be utilized for the low power operation devices [1]. The *4d* transition metal (TM) system of Pd is well recognized as the sustainable elements of *5d* TM system in Pt toward the PMA materials combined with the magnetic *3d* TMs. In order to understand the mechanism of PMA in CoPd, the contributions of orbital magnetic moments of each element have to be clarified explicitly. Bruno theoretically proposed the orbital moment anisotropy in transition-metal multilayers as a second perturbation of spin-orbit interaction [2]. However, even in the strong spin-orbit coupled cases using *4d* or *5d* TMs, the applicability of this formula has been still debated [3].

We reveal the anisotropic orbital magnetic moments in Co/Pd multilayers using angular-dependent x-ray magnetic circular dichroism (XMCD) and their spectral analysis. Core-level X-ray absorption spectra (XAS) of Pd *M*-edge appears at around 530 eV which overlaps with the O *K*-edge absorption. In order to detect the Pd *M*-edge absorption signals, the surface oxide components have to be removed, which enables to measure both Pd *M*-edge and Co *L*-edge absorption at the same experimental condition. Our aim in this study is to discuss both orbital and spin moments of Co and Pd for PMA and in-plane anisotropy samples.

We prepared two kinds of samples of Co/Pd multilayered structures: Co (0.69 nm)/Pd (1.62 nm) for PMA and Co (1.03 nm)/Pd (1.62 nm) for in-plane anisotropy with stacking five periods on the Si substrates [4]. Sample surfaces were sputtered by Ar ions before the XMCD measurements in order to remove the oxygen contamination. We performed XMCD experiments at BL4B, UVSOR, Institute of Molecular Science. Total electron yield mode by directly detecting the sample current was adopted. A magnetic field of ± 5 T was applied along the direction of the incident polarized soft x-ray.

We successfully observed clear XMCD signals in Pd *M*-edges after the removal of surface contamination as shown in Fig. 1. Although the XAS line shapes overlap with those of O *K*-edge absorption, clear XMCD signals induced by the proximity with Co layers are observed. The Pd *M*-edge XMCD line shapes in both PMA and in-plane samples almost remain unchanged. Unfortunately, conventional magneto-optical sum rule analysis, which is defined in the TM *L*-edge absorption, cannot be applicable for *M*-edge XMCD [5]. Precise XAS line shapes in Pd *M*-edges are necessary for the determination of absolute

values of spin and orbital moments. On the other hand, clear Co *L*-edge XAS and XMCD with angular dependence reveal the enhancement of orbital moments in the surface normal direction because of PMA.

Considering these results, we discuss the PMA in Co/Pd multilayers. The Co atoms possess large spin moments and the Pd atoms possess large spin-orbit interaction. The orbital moments in Co is enhanced through the proximity with Pd which induces the spin-orbit coupling. On the other hand, magnetic moments are induced in Pd through the proximity with Co. These collaborate at the interfaces, which enhances the PMA in Co/Pd multilayers. In case of thick Co, the shape anisotropy in Co governs the in-plane anisotropy. Therefore, we propose that the origin of the PMA in Co/Pd interface can be explained by the *orbital moment transfer* at the interface, which opens up new research fields of '*Spin-Orbitronics*'.

We acknowledge to Prof. T. Yokoyama, Dr. Y. Takagi, and Ms. M. Uozumi for the technical supports at BL4B.

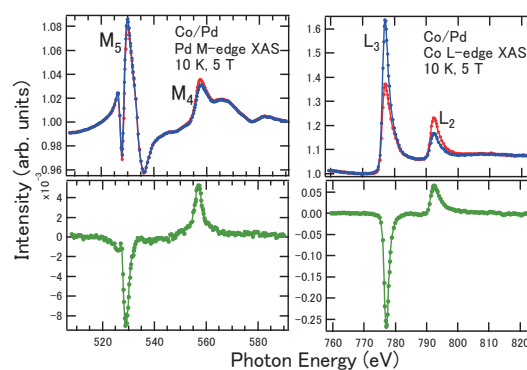


Fig. 1. XAS and XMCD of Pd *M*-edge and Co *L*-edge in perpendicularly magnetized Co (0.69 nm)/Pd (1.62 nm) multilayer.

- [1] M.T. Johnson *et al.*, Rep. Prog. Phys. **59** (1996) 1409.
- [2] P. Bruno, Phys. Rev. B **39** (1989) 865.
- [3] C. Andersson *et al.*, Phys. Rev. Lett. **99** (2007) 177207.
- [4] K. Yamamoto *et al.*, IEEE TRANSACTIONS ON MAGNETICS **49** (2013) 3155.
- [5] T. Ueno *et al.*, Phys. Rev. B **85** (2012) 224406.

*e-mail: jun@chem.s.u-tokyo.ac.jp

BL4B

A Monatomic Layer Iron Nitride Magnetically Coupled with Chromium Nano-Clusters

T. Miyamachi¹, Y. Takahashi¹, S. Nakashima¹, Y. Takagi^{2,3}, M. Uozumi^{2,3},
T. Yokoyama^{2,3} and F. Komori¹

¹*Institute for Solid State Physics, University of Tokyo, Kashiwa 277-8581, Japan*

²*Department of Materials Molecular Science, Institute for Molecular Science, Okazaki 444-8585, Japan*

³*Department of Structural Molecular Science, The Graduate University for Advanced Studies (SOKENDAI),
Okazaki 444-8585, Japan*

An iron nitride compound, Fe₄N, in the ferromagnetic phase is a promising candidate for rare-earth free permanent magnets for their large magnetic anisotropy and high coercivity. The crystal structure of the Fe₄N is composed of so called Fe-plane and Fe₂N plane in the fcc Fe sublattice with a N atom centered in the cubic cell [1].

We have previously investigated atomic scale structural and electronic properties of a monatomic Fe₄N layer grown on a Cu(001) using scanning tunneling microscopy (STM). The surface of the monatomic Fe₄N is composed of the Fe₂N plane with *p4gm*(2×2) surface reconstructed structure, but its appearance alters between *p4gm*(2×2) and *c*(2×2) ones in the STM image due to an orbital selective tunneling process [2].

Magnetic properties of the monatomic Fe₄N layer (Fe₂N layer) have been clarified by x-ray adsorption spectroscopy and x-ray magnetic circular dichroism (XAS/XMCD) conducted at BL4B in UVSOR [3]. We find that the fundamental magnetic properties, such as magnetic moments, magnetic anisotropy and the Curie temperature, rely on the surface quality, being considerably lowered by atomic defects on the surface [4]. In this work, we have further grown Cr nano-clusters on the Fe₂N layer and investigated their influence on the magnetism of the Fe₂N layer.

To grow the Fe₂N layer on Cu(001), N⁺ ions with an energy of 0.5 keV were firstly bombarded to the clean Cu surface and Fe was additionally deposited at room temperature. By subsequent annealing at 570 K, well-ordered Fe₂N layer can be obtained on the surface. The high-quality Fe₂N layer on Cu(001) is achieved by the strict control of the growth condition especially for the amount of deposited Fe and annealing temperature. Thereafter, the Cr deposition is done at room temperature, resulting in the formation of bilayer Cr nano-clusters with an almost identical lateral size of ~ 3 nm, which is confirmed by STM in advance of XAS/XMCD measurements.

The measurements were performed at BL4B in UVSOR by total electron yield mode at B = ± 5 T and T = 7.2 K. In the in-plane (θ = 55°) and the out-of-plane (θ = 0°) geometries, the XMCD spectra are obtained by detecting μ₊ - μ₋, where μ₊ (μ₋) denotes the XAS at Fe and Cr L-adsorption edges with the photon helicity parallel (antiparallel) to the sample magnetization.

Note that θ is the angle between the sample normal and the incident x-ray.

We find no significant difference in the Cr μ₊ and μ₋, and thus the minute XMCD signal from the bilayer Cr nano-cluster. Combined with the structural characterization by STM, the results suggest that the antiferromagnetic coupling between the first and second layers in the Cr nano-cluster. The XMCD spectrum at Fe L-adsorption edges reveals the modification of magnetic properties of the Fe₂N layer. While the magnetic easy axis of the Fe₂N layer with Cr nano-clusters is towards in-plane direction as in the case of the bare Fe₂N layer [3, 4], the reduction of the XMCD signal is observed, indicating the influence of the antiferromagnetic Cr nano-clusters through the magnetic coupling.

Quantitative analyses of the XMCD spectra giving magnetic moments, magnetic anisotropy and the Curie temperature of the system will unravel the details of the magnetic coupling between the Cr nano-clusters and Fe₂N layer.

- [1] Y. Takagi *et al.*, Phys. Rev. B **81** (2010) 035422.
- [2] Y. Takahashi *et al.*, Phys. Rev. Lett. **116** (2016) 056802.
- [3] T. Miyamachi *et al.*, UVSOR Activity Report **42** (2015) 132.
- [4] Y. Takahashi *et al.*, submitted.

BL4B

Magnetism of Single and Double Layer Co Films on W(112)

Y. Takamura¹, S. Mizuno¹, T. Nakagawa¹, Y. Takagi² and T. Yokoyama²

¹Department of Molecular and Material Sciences, Kyushu University, Fukuoka, 816-8580, Japan

²Institute for Molecular Science, Okazaki, 444-8585, Japan

Magnetic thin films on heavy metal surfaces show large anisotropy and coercivity due to their strong spin orbit coupling in the heavy metals [1,2]. Magnetic anisotropy and coercivity can also be enhanced on anisotropic surface structures. bcc(112) surfaces, such as W(112), are good candidates for the highly anisotropic structure since they has ridge and furrow (Fig.1(a)), which would exhibit high magnetic anisotropy. Few investigations of magnetic overlayers on bcc(112) have been examined so far [3]. We have prepared Co nano structures on W(112) surface and investigated their magnetic properties.

X-ray magnetic circular dichroism (XMCD) measurements were done at BL4B using high field and low temperature end station ($T_s \sim 5$ K, $H \sim 6$ T). All the sample preparation and measurements were performed *in situ* under the vacuum of 1×10^{-10} Torr.

Figure 1 shows single and double layer Co on W(112) observed by scanning tunneling microscope (STM). We observed Co atomic wires along [11-1], and found no evidences for W-Co alloy formation. The 1st Co layer as well as the 2nd Co layer keep the same surface structure as W(112), 1×1 structure, irrespective of the large size mismatch between Co and W ($\sim 10\%$).

Figure 2(a) shows Co L edge XAS for 0.6 ML Co/W(112) and its XMCD, which does not show any dichroic signal even at $T_s = 6$ K and the magnetic field of ± 5 T. The absence of the XMCD signal means that the surface is not ferromagnetic. As in Fig. 2(b), increasing the Co thickness above 1 ML exhibits dichroic signal, corresponding to magnetic moment of $0.4 \mu_B$, which is rather small compared with that of bulk Co ($1.6 \mu_B$). The second layer Co is ferromagnetic, which is not ferromagnetically coupled with the 1st layer Co.

Figure 3 shows a magnetization curve (M - H curve) for 1.5 ML Co/W(112), which was measured by monitoring Co L_3 edge XAS intensity as a function of the magnetic field. The M - H curve along the [11-1] direction shows hysteresis with large coercivity of 3 T.

The absence of ferromagnetism in the first Co layer on W(112) is attributed to strong electronic hybridization between Co and W, caused by the reduced bond length. The bond length between Co and W is 0.239 nm, as determined by low energy electron diffraction, which is 8% shorter than that for the hard share model (0.260 nm).

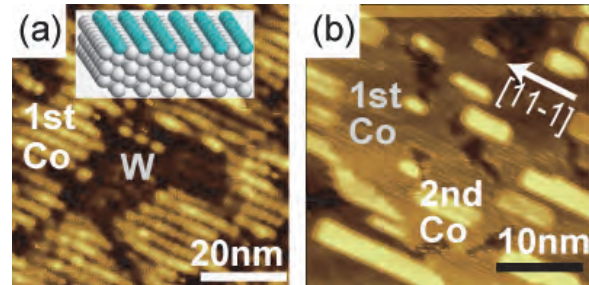


Fig. 1. STM images for (a) Co(0.6 ML)/W(112) and (b) Co/(1.2 ML). The inset in (a) shows a structure model.

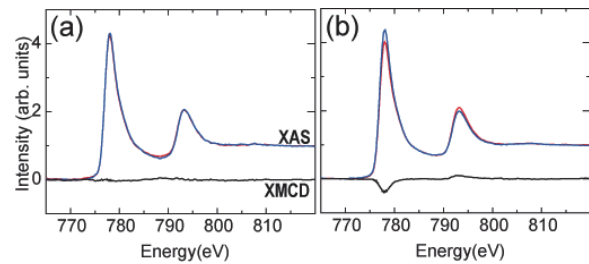


Fig. 2. Co $L_{2,3}$ -edge XAS and XMCD spectra for (a) Co(0.6 ML)/W(112) and (b) Co(1.5 ML). The spectra are taken at $H = \pm 5$ T.

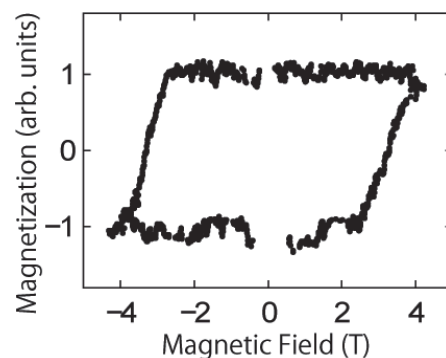


Fig. 3. In-plane magnetization curve for Co(1.5 ML)/W(112) taken along the [11-1] direction.

[1] P. Gambardella *et al.*, Nature, **416** (2002) 301.

[2] T. Nakagawa *et al.*, Phys. Rev. B **86** (2012) 144418.

[3] J. Kołaczekiewicz and E. Bauer, Surf. Sci., **144** (1984) 495.

BL4B

X-Ray Magnetic Circular Dichroism of a Copper-Phthalocyanine Monolayer on Si(111)-($\sqrt{7}\times\sqrt{3}$)-In

S. Yoshizawa and T. Uchihashi

International Center for Materials Nanoarchitectonics (MANA), National Institute for Materials Science (NIMS), Tsukuba 305-0044, Japan

The reconstruction surface Si(111)-($\sqrt{7}\times\sqrt{3}$)-In [hereafter ($\sqrt{7}\times\sqrt{3}$)-In] exhibits superconductivity below about 3 K [1]. The Cooper pairs of this superconductor reside in the surface atomic layer of indium and are sensitive to the surface environment [2]. Our electrical transport measurements have shown that the superconducting characteristics of ($\sqrt{7}\times\sqrt{3}$)-In can be modified by covering the surface with self-assembly layers of various transition-metal phthalocyanines (Pcs). To clarify the mechanism we need to determine the magnetic moments of the Pcs on ($\sqrt{7}\times\sqrt{3}$)-In, because both the electrostatic and magnetic interactions are expected to be involved. We have already performed X-ray magnetic circular dichroism (XMCD) experiments on MnPc and FePc [3, 4], and this time we focus on CuPc to complete the data sets.

The experiments were carried out at the BL4B XMCD system. ($\sqrt{7}\times\sqrt{3}$)-In samples were prepared *in-situ* by depositing indium onto a clean Si(111) surface followed by an annealing at about 400°C. The growth of the $\sqrt{7}\times\sqrt{3}$ phase was confirmed with low-energy electron diffraction. CuPc was thermally deposited from a Knudsen cell onto the ($\sqrt{7}\times\sqrt{3}$)-In surface held at room temperature. The molecular coverage was adjusted to be less than 1 monolayer (ML) for avoiding a second-layer formation. Then, the samples were cooled down to ~ 7 K and X-ray absorption spectra (XAS) were measured by using a circularly polarized light with $\sim 60\%$ polarization. XMCD signals were obtained from the difference of XAS measured in magnetic fields of $B = \pm 5$ T applied in the direction parallel to the incoming light.

Before going to the XMCD measurement, the adsorption geometry of CuPc was checked from XAS at the K edge of nitrogen (Fig. 1). The sharp peaks at around 400 eV in the XAS curve at $\theta = 55^\circ$ are assigned to transitions from the nitrogen 1s orbital to π^* molecular orbitals [5]. Their disappearance at $\theta = 0^\circ$ (normal incidence) demonstrates that the molecular framework of CuPc is nearly parallel to the surface.

Figure 2 shows the XAS and the XMCD at the $L_{2,3}$ edges of copper. By using XMCD sum rules, we estimated the effective spin moments as $\langle S_{\text{eff}} \rangle = 0.7 \pm 0.2 \mu_B$ for $\theta = 0^\circ$ and $\langle S_{\text{eff}} \rangle = 0.5 \pm 0.2 \mu_B$ for $\theta = 55^\circ$. Here, $\langle S_{\text{eff}} \rangle$ is a sum the spin moment and the intra-atomic magnetic dipolar moment. Since the latter contribution goes to zero at $\theta \sim 55^\circ$ for molecular orbitals with C_4 symmetry [6], the non-zero $\langle S_{\text{eff}} \rangle$ at $\theta = 55^\circ$ obtained here clearly indicates the presence of

spins in CuPc molecules adsorbed on the ($\sqrt{7}\times\sqrt{3}$)-In surface. The present results give important clues for understanding the function of a CuPc monolayer on superconducting ($\sqrt{7}\times\sqrt{3}$)-In.

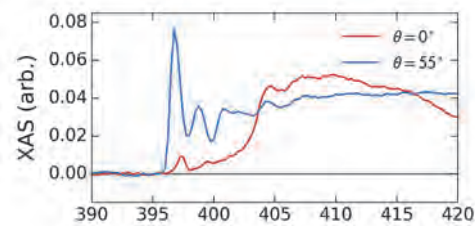


Fig. 1. XAS at the N K edge. The coverage of CuPc is about 0.7 ML.

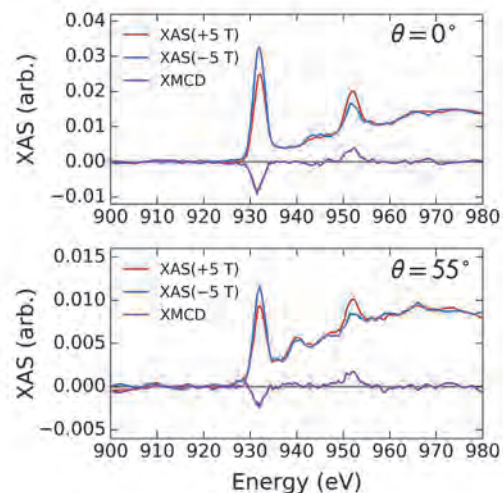


Fig. 2. XAS and XMCD at the Cu $L_{2,3}$ edges. The coverage of CuPc is about 0.7 ML.

- [1] T. Uchihashi *et al.*, Phys. Rev. Lett. **107** (2011) 207001.
- [2] S. Yoshizawa *et al.*, Phys. Rev. Lett. **113** (2014) 247004.
- [3] T. Uchihashi and S. Yoshizawa, UVSOR Activity Report **41** (2014) 133.
- [4] T. Uchihashi and S. Yoshizawa, UVSOR Activity Report **42** (2015) 131.
- [5] K. Eguchi *et al.*, J. Phys. Chem. C **117** (2013) 22843.
- [6] S. Stepanow *et al.*, Phys. Rev. B **82** (2010) 014405.

BL5B

Vacuum Ultraviolet Transmission Spectra of Amorphous Arsenic Chalcogenide Thin Films

K. Hayashi

Department of Electrical, Electronic and Computer Engineering, Gifu University, Gifu 501-1193, Japan

It is well-known that amorphous chalcogenide materials exhibit a variety of photoinduced phenomena by irradiation of light with energy corresponding to the optical band gap [1]. Photoinduced changes observed in amorphous chalcogenide materials are classified into two types, irreversible and reversible changes. Reversible changes can be induced optically in amorphous bulk materials and well-annealed evaporated thin films, in which the changes can be removed by annealing to the glass-transition temperature. The reversible photodarkening arising from the red-shift of the optical absorption edge is a typical reversible photoinduced phenomenon. Irreversible changes are induced in as-deposited evaporated thin films. The irreversible photodarkening in as-deposited amorphous films is an irreversible change, it is believed that it occurred by photopolymerization. The irreversible change observed in EXAFS [2] and IR [3] is interpreted by rearrangement of bonding configurations of molecular species within as-deposited evaporated films.

To our knowledge, little attention has been given to photoinduced changes at the vacuum ultra-violet (VUV) absorption spectrum. In this report, we measure the VUV transmission spectra on as-deposited evaporated amorphous arsenic chalcogenide films.

Samples used for the measurement of the VUV transmission spectra were amorphous arsenic chalcogenide ($a\text{-As}_x\text{Se}_{1-x}$) thin films prepared onto aluminum thin films by conventional evaporation technique. Using different bulk glass of the composition as a source material, different amorphous film of the compositions was prepared. Typical thickness of the amorphous film and the aluminum film were around 200 nm and 100 nm, respectively. The aluminum film of the thickness of 100 nm was also used in order to eliminate the higher order light from the monochromator in the VUV region. The measurements were carried out at room temperature at the BL5B beam line of the UVSOR facility of the Institute for Molecular Science. And the spectrum was measured by using the silicon photodiode as a detector. Two pinholes of 1.5 mm in a diameter were inserted between the monochromator and sample to remove stray light. The intensity of the VUV light was monitored by measuring the TPEY of a gold mesh. The positions of the core levels for the samples were calibrated by referencing to the 2p core level absorption peak of the aluminum film.

Figure 1 shows the VUV transmission spectra of as-

deposited $a\text{-As}_{0.3}\text{Se}_{0.7}$, $a\text{-As}_{0.4}\text{Se}_{0.6}$, and $a\text{-As}_{0.5}\text{Se}_{0.5}$ films. Two main absorption peaks were observed in this wavelength region. One absorption peak around 22 nm corresponds to the 3d core level of selenium atom. Another absorption peak around 28 nm corresponds to the 3d core level of arsenic atom. As shown in the figure, the ratio of the two main absorption peaks changes depending on composition. The spectrum shape also changes depending on composition. We think that those changes are related to the local structures of the amorphous network. We will observe the composition dependence of the change in the spectrum before and after irradiation of light in future. And we are going to investigate the relations between those changes.

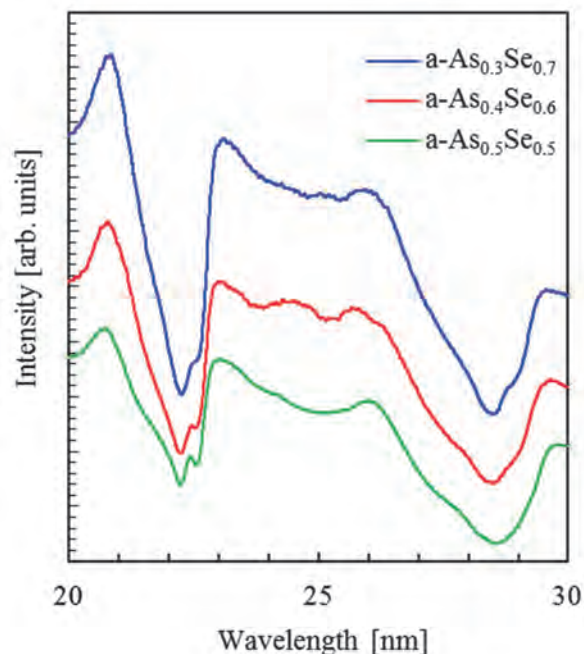


Fig. 1. The VUV transmission spectra of as-deposited $a\text{-As}_{0.3}\text{Se}_{0.7}$, $a\text{-As}_{0.4}\text{Se}_{0.6}$, and $a\text{-As}_{0.5}\text{Se}_{0.5}$ films.

- [1] K. Tanaka, *Rev. Solid State Sci.* **4** (1990) 641.
- [2] A. J. Lowe, S. R. Elliot and G. N. Greaves, *Philos. Mag. B* **54** (1986) 483.
- [3] S. Onari, K. Asai and T. Arai, *J. Non-Cryst. Solids* **77&78** (1985) 1215.

BL5B

Study of M -Edge Resonant Magneto Optical Effect of Fe Ultrathin Films with Large Perpendicular Magnetic Anisotropy Induced by Rashba-Type Spin-Orbit Interaction

Sh. Yamamoto¹, K. Yamamoto¹, K. Takubo¹, K. Fukuta², D. Oshima³, T. Kato², S. Iwata³, H. Wadati¹ and I. Matsuda¹

¹*Institute for Solid State Physics, The University of Tokyo, Kashiwa 277-8581, Japan*

²*Department of Electrical Engineering and Computer Science, Nagoya University, Nagoya 464-8603, Japan*

³*Nagoya University, IMASS, Nagoya 464-8603, Japan*

Magneto-optical Kerr effect (MOKE) in visible region has been widely utilized in condensed matter physics, especially in the field of magnetism. We have been developing a measurement scheme for resonant MOKE (RMOKE), in which an energy for incident light is tuned to particular absorption edge of target element composed of samples [1], and applied to thin ferromagnetic metals, ferrimagnetic alloys, and artificial multilayers, for examples. For exploring the applicability in terms of its sensitivity of this method, we focus on ultrathin ferromagnetic films here. In such systems, interfacial properties contribute to perpendicular magnetic anisotropy (PMA) of ultrathin films. PMA has been one of the important features in spintronics field due to its potential for developing a non-volatile device with higher density. However, its mechanism has not been understood from microscopic point of view. Therefore in order to access such systems, it is essential to probe the ultrathin magnetic systems in methodological point of view. Recently, a novel scheme considering Rashba-type spin-orbit interaction has been shown to explain the existence of PMA and its electric-field dependence as a result of competition with exchange interaction of magnetic systems as an analogy of Dzyaloshinskii-Moriya interaction [2]. The Rashba effect has been known to emerge in the system without inversion symmetry such as surface or interface. In the new scheme, effective Rashba field acts at an interface between a noble metal or an insulator and ultrathin ferromagnetic films.

In this research, at UVSOR BL5B, we conducted Fe M -edge RMOKE measurement of the Fe film that was sandwiched by films of noble metal, Au, and insulator, MgO. We synthesized the sample using molecular beam epitaxy method. The structure of the sample is Au (2 nm)/MgO (2 nm)/Fe (0.29 nm)/Au (25 nm)/Cr (5 nm)/MgO(001, substrate). Fe thickness of 0.29 nm corresponds to ~ 2 monolayer assuming that this layer takes body-centered cubic structure. In measuring RMOKE, rotating-analyzer ellipsometry has been utilized for obtaining Kerr rotation angle at each energy point [1]. The measurement has been conducted at room temperature and external magnetic field (± 0.47 T) that was in perpendicular to sample surface was applied using permanent magnet. The incident light angle was set to 45 degrees.

In Fig. 1, RMOKE spectrum around Fe M -edge is shown with error bars ± 0.5 degrees. There are mainly two structures in the spectrum. One is around the region in 54 – 55 eV that corresponds to Fe M absorption edge, $3p \rightarrow 3d$ transition. The other appears to be broader compared to the former, which can be observed around the region in 60 – 65 eV. This corresponds to Au O_3 edge.

It is shown that this method has sensitivity even for the ultrathin ferromagnetic systems. Furthermore this measurement has been preliminary experiment for time-resolved measurement [3]. It was found that energy around 54 - 55 eV was suitable for tracing dynamics of Fe of this system. Ultrafast spin dynamics of this system has been attracting because this system can be used for investigating effects of spin-orbit interaction at interfaces on its dynamics in sub-picoseconds timescale.

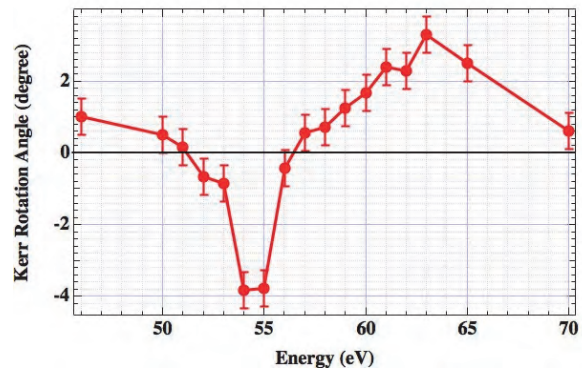


Fig. 1. Fe (0.29 nm) M -edge resonant magneto optical Kerr effect spectrum.

[1] Sh. Yamamoto. *et al.*, Phys. Rev. B **89** (2014) 064423.

[2] S. E. Barnes *et al.*, Sci. Rep. **4** (2014) 4105.

[3] Sh. Yamamoto *et al.*, Rev. Sci. Instrum. **86** (2015) 083901.

BL6U

Various Electronic Structures of SnCl₂Pc Film on Graphite

K. Yonezawa¹, T. Ueba², R. Shiraishi², H. Yamane², N. Kosugi² and S. Kera^{1,2}

¹ Department of Nanomaterial Science, Graduate School of Advanced Integration Science, Chiba University, Chiba 263-8522, Japan

² Department of Photomolecular Science, Institute of Molecular Science, Okazaki 444-8585, Japan,

Organic π -conjugated molecular solid is consisted by a weak intermolecular interaction. Thus, the film structure could be easily modified by a thermal impact, leading a wide variety in the electronic property of the molecular solid. Tin phthalocyanine dichloride (SnCl₂Pc) is a π -conjugated molecule which has been reported as an n-type semiconductor property [Fig. 1(a)]. Since SnCl₂Pc is non-planer molecule, the film structure is considered to be variable depending on the preparation conditions. In this work, we studied impacts of the thermal annealing on the electronic structure of the SnCl₂Pc film prepared on graphite by angle-resolved UPS (ARUPS) and XPS.

The clean surface of graphite was obtained by cleaving a HOPG under the air and subsequent annealing in the UHV chamber. SnCl₂Pc is purified by sublimation method twice. After preparing the monolayer film (0.5 nm) on the graphite at room temperature, valence-band and secondary electron cut-off were measured at 45 eV, and Sn 4d, C 1s, Cl 2p and N 1s core levels were measured at 60 eV, 335 eV, 335 eV and 500 eV, respectively.

In Fig. 1(b), the intense peak at 1.8 eV (label a) and the weak peak at 1.4 eV (label a') are observed for as-deposited film. The peak a is assigned to HOMO. The peak a' must be originated from the electronic structure of SnCl₂Pc, not from that of impurities nor surface contaminations. Upon annealing the film at 343 K for 9h, the spectrum changes drastically from the as-deposited one. New features at 1.6 eV (label b) and 1.2 eV (label b') are observed in addition to the peaks a and a' found for the as-deposited film. Furthermore, weaker features (labels α' and β') at around 0.3 eV are observed after the annealing. From the intensity analysis of ARUPS, the angular dependences of the peaks b, b' and β' are very similar one another, while it is different from those of the peaks a, a' and α' (not shown), indicating two kinds of molecular orientation exist in the film.

It has been reported that dissociation of the Cl atom of SnCl₂Pc has occurred for the monolayer film on Ag(111) after the annealing [1], thus one may consider the peaks b, b' and β' might be ascribed to HOMO of SnPc or SnClPc (radical) etc, which may be formed after the surface chemical reaction upon the annealing. However, the XPS spectra of Cl 2p are nearly identical before/after the annealing (Fig. 1 (c)), indicating almost all the Cl atoms have remained in the film. Therefore, peaks b, b' and β' should be originated from the electronic states of SnCl₂Pc with another molecular orientation or aggregation.

Figure 1 (d) shows Sn 4d states. In contrast to Cl 2p, new features are observed at low-binding energy side of the main peaks of the as-deposited film by 0.33 eV. The spectra of C 1s and N 1s indicate the same trend to Sn 4d, while the energy differences of new features are not equal (not shown). The results indicate the energy shift found in Sn 4d, C 1s, and N 1s could be caused by the charge redistribution at the Pc ring.

The electronic structure of the SnCl₂Pc film on graphite is clearly modified by the annealing, namely rearrangement of the molecular orientation and aggregation. Finally we would assume the origin of various peaks, though further experiments are requested to conclude. The peaks a' and α' (b' and β') are possible to be originated from HOMO and LUMO of anion states of SnCl₂Pc. The wave-function localization in the film would be a key to understand the non-trivial features because adsorption distance of Pc ring could be longer by Cl as a spacer.

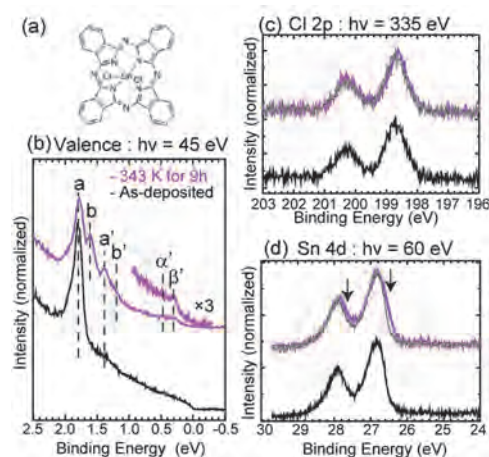


Fig. 1. (a) Chemical structure of SnCl₂Pc. (b) Valence-band spectra for the as-deposited (black) and the annealed at 343 K for 9 h (magenta). (c) Cl 2p XPS spectra. (d) Sn 4d XPS spectra. In (c) and (d), as-deposited spectra (pale gray) are shown with the annealed one for comparison.

[1] S. Kera *et al.*, UVSOR Activity Report **42** (2015) 138.

BL6U

Orbital Energy Rearrangement by the Organic–Metal Interaction: Perfluoropentacene on Ag(111)

T. Ueba¹, K. Yonezawa², H. Yamane¹, N. Kosugi¹ and S. Kera^{1,2}¹ Department of Photomolecular Science, Institute of Molecular Science, Okazaki, 444-8585, Japan,² Department of Nanomaterial Science, Graduate School of Advanced Integration Science, Chiba University, Chiba 263-8522, Japan

Understanding the *weak* interaction at organic-metal interface, including intermolecular interaction and molecule-metal interaction, is of great importance. Even such weak interaction can cause the rearrangement of molecular orbitals both in energy and space, which defines the electronic properties at interfaces.

Perfluoropentacene (PFP), an organic semiconductor, gives us an interesting example. The energy gap between the HOMO and HOMO–1 of PFP monolayer adsorbed on highly oriented pyrolytic graphite (HOPG), observed by ultraviolet photoelectron spectroscopy (UPS), is identical to gaseous PFP (2.42 eV), while it is 70-meV narrower for PFP on Ag(111) [1]. Because PFP adsorbs on both surfaces in a “physisorptive” manner, namely, without chemical bonding nor charge transfer, the orbital energy rearrangement is a consequence of the *weak* interaction at the interface. In this work, we performed photoemission spectroscopy to examine the origin of the orbital energy rearrangement of PFP/Ag(111), by comparing with PFP/HOPG.

The Ag(111) surface was purified by repeated cycles of Ar⁺ sputtering and subsequent annealing. The cleanliness was confirmed by the low-energy electron diffraction (LEED) and the appearance of the Shockley state in angle-resolved UPS. After multilayer deposition on Ag(111), the sample was annealed at 130 K for 5 minutes for obtaining the monolayer [2]. The clean HOPG surface was obtained by cleaving in air and by annealing in the UHV chamber. Valence band and secondary cut-off was measured at a photon energy ($h\nu$) of 45 eV, and the C1s and F1s core levels at $h\nu = 335$ eV and 730 eV, respectively.

Figure 1 shows the valence-band spectra. For PFP/Ag(111), the ordered/disordered phase transition at $T_c \sim 145$ K is reported [2]. However, our results detected no temperature dependence in the HOMO–HOMO–1 gap energy, indicating that the narrower gap arises from the molecule-metal interaction, not the intermolecular interaction.

Figure 2 shows the core-level spectra. The binding energy of the C1s peaks (C–C and C–F) for PFP/Ag(111) are higher than those for PFP/HOPG, as found in the valence band. However, the C–F peak appears at rather similar energy for both films, as compared with the C–C peak. The energy difference of the F1s peak between PFP/Ag(111) and PFP/HOPG is also reasonably less than the C–C peak.

According to the X-ray standing wave analysis [3],

PFP adsorbs on Ag(111) with the flat-lying geometry. Hence, such core-level shift cannot be explained only with the photohole screening by the substrate or with the surface potential. The result can be taking into account the intramolecular charge redistribution, most likely arising from the change in molecular structure upon the weak molecule-substrate interaction. Indeed, our high-resolution electron energy loss spectroscopy (HREELS) for PFP/Ag(111) resolved the change in vibrational energies as compared with PFP/HOPG (not shown). The result clearly indicates the very slight modification in the molecular structure upon adsorption on Ag(111), which probably causes intramolecular charge redistribution and consequently the orbital energy rearrangement.

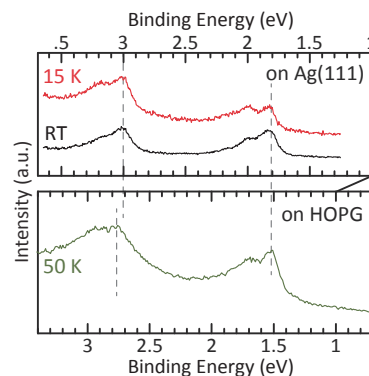


Fig. 1. Valence-band spectra of PFP/Ag(111) (top) and PFP/HOPG (bottom) measured at 45 eV.

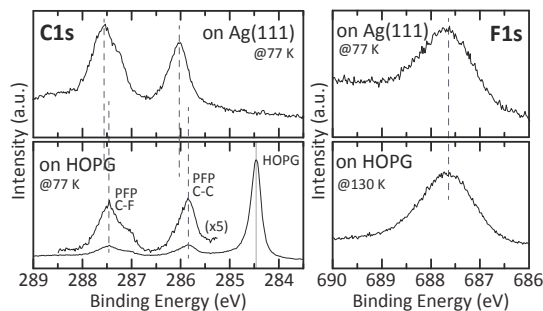


Fig. 2. A comparison of the C1s (left) and F1s (right) core level energies.

[1] S. Kera *et al.*, *J. Electron Spec. Relat. Phenom.* **204** (2015) 2.

[2] M. Marks *et al.*, *J. Phys. Chem. C* **116** (2012) 1904.

[3] S. Duhm *et al.*, *Phys. Rev. B* **81** (2010) 045418.

BL6U

Lateral Intermolecular π -Band Dispersion in the Superstructure of Perylene Monolayer Physisorbed on Au(111)

H. Yamane^{1,2} and N. Kosugi^{1,2}¹Institute for Molecular Science, Okazaki 444-8585, Japan²The Graduate University for Advanced Studies (SOKENDAI), Okazaki 444-8585, Japan

Using angle-resolved photoemission spectroscopy (ARPES), we have recently investigated the lateral intermolecular π -band dispersion in superstructure monolayers of polycyclic aromatic hydrocarbons (PAHs) physisorbed on Au(111), *e.g.*, coronene(4×4)/Au(111), hexa-*peri*-hexabenzocoronene (HBC)(5×5)R0°/Au(111), and HBC(3√3×3√3)R30°/Au(111) [1]. This systematic investigation has revealed that the observed lateral π -band dispersion is dependent on the monolayer's surface Brillouin zone (SBZ) but not on the substrate's SBZ [1]. This finding suggests that the observed π -band dispersion at the PAHs/Au(111) interface is introduced not by a substrate-mediated intermolecular interaction [2,3] but by a genuine lateral intermolecular interaction. In the present work, in order to investigate the impact of the intermolecular space on the lateral intermolecular π -band dispersion, we study the electronic structure of the smaller PAHs of perylene, which also forms the (4×4) superstructure on Au(111) depending on the film growth condition in the monolayer coverage [4].

The experiment was performed at the in-vacuum undulator beamline BL6U. The clean Au(111) surface was obtained by the repeated cycles of the Ar⁺ sputtering and the subsequent annealing at 700 K, as confirmed by the low-energy electron diffraction (LEED) and the Shockley state in ARPES.

Figure 1 shows (a) a LEED image at 20 K and (b) the corresponding SBZ of the perylene monolayer on Au(111). The LEED image shows the (4×4) super-

structure with respect to the Au(111) hexagonal lattice, as reported in Ref. [4]. The ARPES spectra were measured by considering the high symmetric point of Γ' , K' , and M' in the monolayer's SBZ [blue hexagon in Fig. 1(b)].

The E - k map of perylene(4×4)/Au(111) along the Γ' - K' and Γ' - M' ($k_{\Gamma K}$ and $k_{\Gamma M}$) directions, obtained from ARPES, is shown in Fig. 1(c) and 1(d), respectively. The π -type highest occupied molecular orbital (HOMO)-derived peak of perylene is observed at the binding energy of *ca.* 1.15 eV. Although no direct intermolecular π - π overlap exist in the flat-lying monolayer, the HOMO peak shows a very weak lateral π -band dispersion by 20 meV at Γ' - K' and by <10 meV at Γ' - M' . The observed π -band dispersion at perylene(4×4)/Au(111) is narrower than that at the comparable interface of coronene(4×4)/Au(111) [1]. This difference can be explained by the larger intermolecular space in the perylene monolayer than that in the coronene monolayer due to the molecular size. The observed π -band dispersion is ascribed to the long-range lateral intermolecular interaction through the intermolecular space.

- [1] H. Yamane *et al.*, UVSOR Activity Report 2014.
 [2] H. Yamane *et al.*, Phys. Rev. B **76** (2007) 165436; J. Electron Spectrosc. Rel. Phenom. **174** (2009) 28.
 [3] M. Wießner *et al.*, Nat. Commun. **4** (2013) 1514; Phys. Rev. B **88** (2013) 075437.
 [4] C. Seidel *et al.*, Phys. Rev. B **64** (2001) 195418.

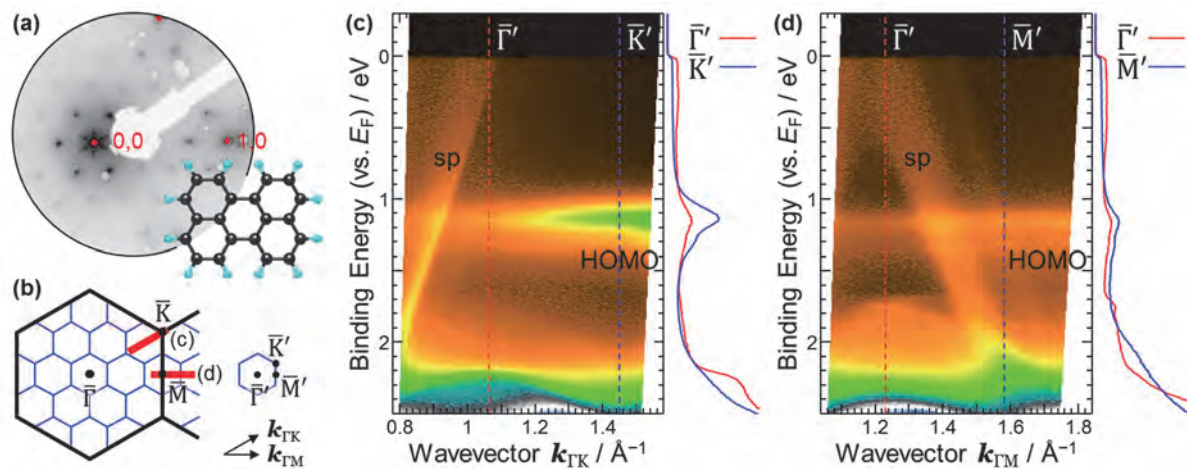


Fig. 1. (a) LEED of the perylene(4×4)/Au(111) at 20 K, wherein the red dot indicates the substrate's spot. The molecular structure of perylene is also shown. (b) SBZ of the Au(111) (black) and the perylene(4×4)/Au(111) (blue). The red line indicates the scanned region in ARPES. (c,d) The E - k maps of the perylene(4×4)/Au(111) at 20 K along the $k_{\Gamma K}$ and $k_{\Gamma M}$ directions and the energy distribution curves.

BL6U

A High Hole-Mobility Molecular Layer Formed by Strong Electron Acceptor F₄TCNQ on Gold Electrode

H. Yamane^{1,2} and N. Kosugi^{1,2}¹ Institute for Molecular Science, Okazaki 444-8585, Japan² The Graduate University for Advanced Studies (SOKENDAI), Okazaki 444-8585, Japan

Because of the large electron affinity, 2,3,5,6-tetra fluoro-7,7,8,8-tetracyanoquinodimethane (F₄TCNQ) is well known as a strong electron-accepting molecule, and has been applied for the *p*-type doping of organic semiconductors [1] and for the work-function control of metal electrodes [2]. It is understood that the cyano group in the molecule plays a crucial role in the charge-transfer (CT) interaction. In particular, at the F₄TCNQ/Au(111) interface, the F₄TCNQ molecule forms a two-dimensional network via the cyano group and the segregated Au atom from the substrate [3]. In the present work, in order to investigate the electronic structure of the F₄TCNQ-Au network, we studied the TCNQ/Au(111) and F₄TCNQ/Au(111) interfaces by angle-resolved photoemission spectroscopy (ARPES) and low-energy electron diffraction (LEED).

The experiment was performed at the in-vacuum undulator beamline BL6U. The clean Au(111) surface was obtained by the repeated cycles of the Ar⁺ sputtering and the subsequent annealing at 700 K, as confirmed by LEED and the Shockley state in ARPES. In order to obtain the ordered monolayer film, the sample was heated at the multilayer desorption temperature of *ca.* 380–390 K, which is slightly lower than the desorption temperature of the TCNQ and F₄TCNQ monolayers on Au(111), as confirmed by the temperature-dependent ARPES.

Figure 1 shows the normal-emission ARPES and LEED data of TCNQ/Au(111) and F₄TCNQ/Au(111). Upon the TCNQ monolayer formation, the Shockley state of Au(111) just below E_F (labeled S) is survived with the lower-energy shift. The LEED image of TCNQ/Au(111) shows the $22 \times \sqrt{3}$ herringbone pattern of Au(111) just around the 0,0 spot. These ARPES and LEED characteristics of TCNQ/Au(111) indicate the weak physisorption at the interface. On the other hand, both the Shockley state in ARPES and the $22 \times \sqrt{3}$ herringbone pattern in LEED are quenched at F₄TCNQ/Au(111). These evidences in ARPES and LEED of F₄TCNQ/Au(111) can be explained by the Au-atom segregation from the Au(111) surface by the strong chemisorption at the interface, which induces the formation of the F₄TCNQ-Au network and the resultant CT-derived peak in ARPES (CT₁ and CT₂). The different interfacial interaction between TCNQ/Au(111) and F₄TCNQ/Au(111) is supported by the N 1s photoemission spectra (not shown here).

Figure 2 shows the E - k map of the F₄TCNQ-Au network on Au(111) at 20 K. Peaks CT₁ and CT₂, originating from the lowest-unoccupied molecular orbital (LUMO) and highest-occupied molecular

orbital (HOMO) as considered in the neutral F₄TCNQ molecule, respectively, show the large dispersion by the 0.3-eV bandwidth for LUMO and by the 0.4-eV bandwidth for HOMO with the same k periodicity. These band dispersions are observable even at 300 K, and can be ascribed to the adatom(Au)-mediated intermolecular interaction, which is not observable at the physisorbed TCNQ/Au(111) interface.

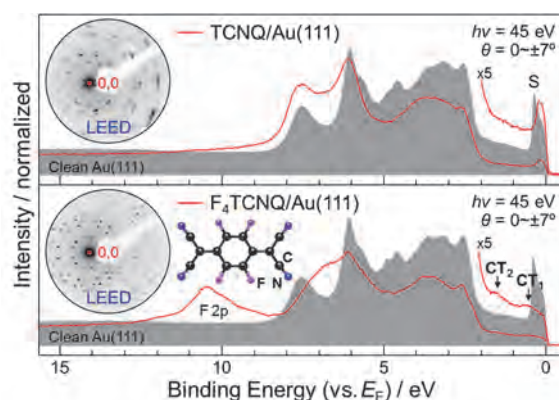


Fig. 1. Normal-emission ARPES and LEED data of TCNQ/Au(111) and F₄TCNQ/Au(111).

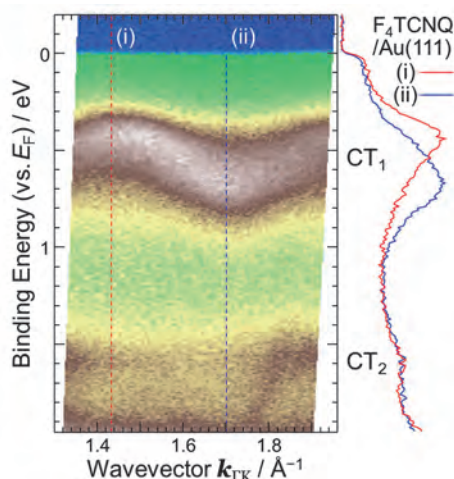


Fig. 2. The E - k map and the selected energy distribution curves of the F₄TCNQ-Au network on Au(111) at 20 K along the Γ - K direction.

[1] W. Y. Gao and A. Kahn, *J. Appl. Phys.* **94** (2003) 359, and references therein.

[2] N. Koch *et al.*, *Phys. Rev. Lett.* **95** (2005) 237601.

[3] M. N. Faraggi *et al.*, *J. Phys. Chem. C* **116** (2012) 24558.

BL6U

Site-Specific Organic/Metal Interactions Revealed from the Analysis of Shockley-Type Interface State

H. Yamane^{1,2} and N. Kosugi^{1,2}¹ Institute for Molecular Science, Okazaki 444-8585, Japan² The Graduate University for Advanced Studies (SOKENDAI), Okazaki 444-8585, Japan

The Shockley state is a well-known surface state associated with the breakdown of the periodic crystal potential at the surface, and can be observed as a parabolic dispersion for normal metals and semiconductors by using angle-resolved photoemission spectroscopy (ARPES). The origin of the Shockley state is also valid for adsorbed-surface systems. Indeed, the Shockley state has been reported for metal surfaces adsorbed with metals, rare gases, and molecules with modified band dispersions, and has recently been applied to the determination of the interfacial bonding strength [1]. In the present work, we have applied the Shockley-state measurement to the well-ordered monolayer of cobalt phthalocyanine (CoPc) on Au(111), for the quantitative study of the site-specific interfacial interaction.

The experiment was performed at the in-vacuum undulator beamline BL6U. The clean Au(111) surface was obtained by the repeated cycles of the Ar⁺ sputtering and the subsequent annealing at 700 K, as confirmed by the low-energy electron diffraction (LEED) and the Shockley state in ARPES.

In Fig. 1, the Shockley state of CoPc/Au(111) is compared with that of H₂Pc/Au(111) and that of the clean Au(111) at 23 K. The Shockley state of both CoPc/Au(111) and H₂Pc/Au(111), labeled S', shows the lower-energy shift from that of the clean Au(111). The upshift of the Shockley state originates from the Pauli repulsion (exchange interaction) of surface electrons by adsorbates. Furthermore, one more dispersive band just below the Fermi level (E_F) is observed for CoPc/Au(111), labeled X, which cannot be observed for H₂Pc/Au(111).

As shown in the inset of Fig. 2, the CoPc/Au(111) interface forms an interface state of the Co 3d character (labeled H'), just above the original highest-occupied molecular orbital of the C 2p character (HOMO, labeled H), due to the strong interaction between the Co atom in the molecule and the Au surface, and is not observed for H₂Pc/Au(111). The observed dispersive band X in Fig. 1 might thus originate from the site-specific Co-Au interaction at the CoPc/Au(111) interface. On the other hand, band S' mainly originates from the interfacial interaction between the Pc-ring site and the Au surface.

In order to examine the site-specific interfacial interaction, we measured the temperature dependence of the Shockley state of CoPc/Au(111) at the Γ point ($k_{TM} = 0 \text{ \AA}^{-1}$). The Shockley state of the clean Au(111), labeled S, shows the higher-energy shift with

decreasing the temperature due to the contraction of the bulk-crystal lattice constant. A similar behavior is observed for peak S' of CoPc/Au(111). However, the amounts of the energy shift is different; $\Delta E(S) = 60 \text{ meV}$ for the clean Au(111) and $\Delta E(S') = 42 \text{ meV}$ for CoPc/Au(111) at 299 \rightarrow 23 K. The energy difference by $\Delta E(S') - \Delta E(S) = -18 \text{ meV}$ is ascribed to the difference in the Pauli repulsion at the interface due to the narrowing of the bonding distance between the Pc ring and the Au surface with decreasing the temperature. Peak X shows the lower-energy shift with decreasing the temperature by $\Delta E(X) = -25 \text{ meV}$, indicating the stronger interaction at the Co site than the Pc-ring site with the Au surface. From the present observation and Ref. [1], the interfacial bonding strength of CoPc/Au(111) at 23 K is determined as 13.0 meV/\AA^2 at the Pc-ring site and 45.9 meV/\AA^2 at the Co site.

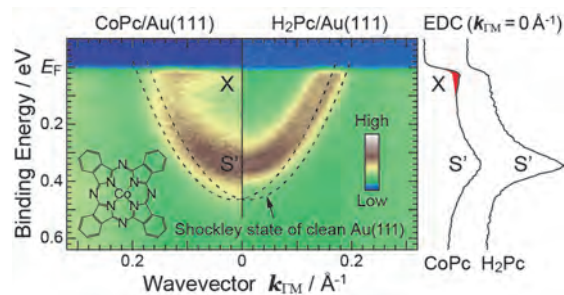


Fig. 1. The E - k map around the Shockley state for CoPc/Au(111) and H₂Pc/Au(111) at 23 K, together with the best-fit curve of the Shockley state for the clean Au(111) at 23 K (black dashed curve).

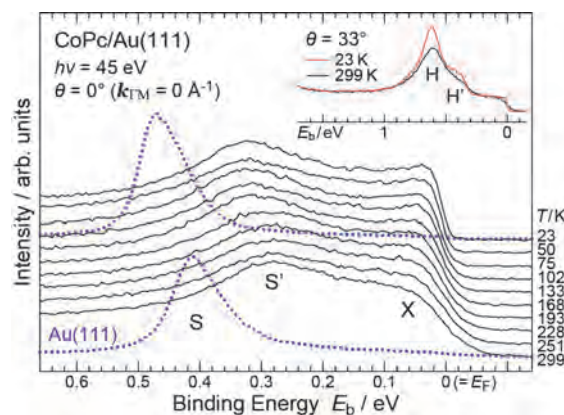


Fig. 2. Temperature dependence of the Shockley state of CoPc/Au(111) and Au(111) at the Γ point. The ARPES near the HOMO are shown in the inset.

[1] J. Ziroff *et al.*, Surf. Sci. **603** (2009) 354.

BL6U

Band Structure Modification of Graphene by Bi Intercalation

Y. Sohn^{1,2}, S. W. Jung^{1,2}, M. Huh^{1,2}, K. Kwon¹, H. Yamane³, N. Kosugi³ and K. S. Kim^{1,2}

¹Department of Physics, Pohang University of Science and Technology (POSTECH), Pohang 37673, Republic of Korea

²Center for Artificial Low Dimensional Electronic Systems, Institute for Basic Science (IBS), Pohang 37673, Republic of Korea

³Department of Photo-Molecular Science, Institute for Molecular Science, Okazaki 444-8585, Japan

Graphene, a two-dimensional atomic crystal with the Dirac band structure, can be grown on the surface of SiC(0001) [1]. It has been well known that intercalating atoms between the epitaxial graphene layer and SiC(0001) can not only decouple graphene from the substrate, but also modify the low-energy band structure such as doping level, band gap, and spin splitting [2-4]. In this report, we have investigated the band structure of graphene modified by the intercalation of heavy-Z atoms with angle-resolved photoemission spectroscopy (ARPES).

We first prepared zero-layer graphene samples, where a single graphitic layer is strongly bonded to the surface atoms of SiC(0001) and lacks the well-known linear π bands. The zero-layer sample was fabricated by thermal sublimation of surface Si atoms out of the SiC(0001) substrate at high temperature. Bismuth (Bi) was then deposited on the zero-layer sample at room temperature followed by mild annealing at elevated temperatures. ARPES and core-level spectroscopy measurement were performed at the in-vacuum undulator beamline BL6U, UVSOR, equipped with a high-performance hemispherical electron analyzer. The overall energy and momentum resolutions were better than 0.02 eV and 0.002 \AA^{-1} , respectively. Data were collected at 60 K with the photon energy of 100 eV.

We checked the intercalation of Bi by using low-energy electron diffraction (LEED) and core-level spectroscopy. After intercalation we observed that (1×1) spot of SiC(0001) is suppressed, while that of graphene layer remains unchanged. $(6\sqrt{3} \times 6\sqrt{3})R30^\circ$ spot, which originates from the lattice mismatch between SiC(0001) and the graphene layer is also suppressed. Bi $5d_{5/2}$ core-level spectra is observed to be shifted by 0.18 eV after intercalation, and the peak position does not change with the sample annealed up to 1200°C. Figure 1 shows a wide-scale ARPES data of Bi-intercalated graphene, taken near the Fermi energy along the ΓK direction of the hexagonal Brillouin zone. Graphene π bands clearly appear after intercalation, demonstrating that graphene is effectively decoupled from the SiC(0001) substrate. From the above facts, we concluded that Bi is successfully intercalated beneath the graphene layer. Further ARPES studies are underway to observe the systematic evolution of the band structure.

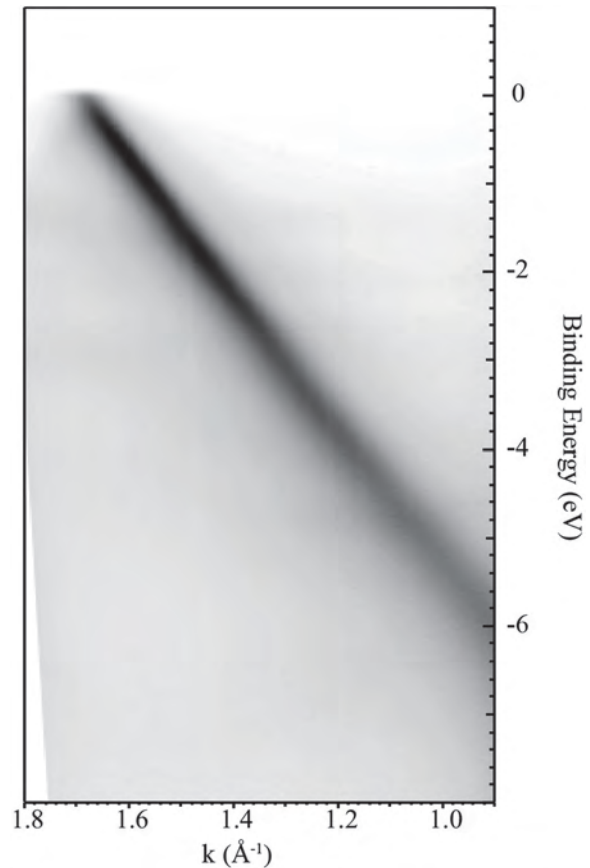


Fig. 1. Band dispersion along the ΓK direction of Bi-intercalated graphene.

- [1] K. V. Emtsev *et al.*, Nat. Mater. **8** (2009) 203.
- [2] I. Gierz *et al.*, Phys. Rev. B **81** (2010) 235408.
- [3] D. Marchenko *et al.*, Nature comm. **3** (2012) 1232.
- [4] A. Varykhalov *et al.*, Nature comm. **6** (2015) 7610.

BL7U

Angle Resolved Photoelectron Spectroscopy on the Clean Surface of the Pentacene Single Crystal

M. Hikasa¹, Y. Mizuno², S. Ideta³, K. Tanaka³, H. Ishii^{2,4} and Y. Nakayama¹

¹Department of Pure and Applied Chemistry, Faculty of Science and Technology, Tokyo University of Science, Noda 278-8510, Japan

²Graduate School of Advanced Integration Science, Chiba University, Chiba 263-8522, Japan

³UVSOR Facility, Institute for Molecular Science, Okazaki 444-8585, Japan

⁴Center for Frontier Science, Chiba University, Chiba 263-8522, Japan

Pentacene (C₂₂H₁₄) single crystal (Pn-SC) is a representative p-type organic field effect transistor material, which indicating a high charge carrier mobility larger than 30 cm²V⁻¹s⁻¹ at room temperature [1]. Therefore, its valence band structures are of particular interest. As reported previously [2], our group succeeded in valence band dispersion measurements of the Pn-SC by angle-resolved photoelectron spectroscopy (ARPES). However, previous ARPES results were obtained on Pn-SC samples which had exposed to ambient air and thus are known to be contaminated by several percent of oxide at their surfaces [3]. On the other hand, in the case of the single crystal of tetracene, a sister molecule of pentacene, existence of the “surface band” was predicted because of surface relaxation [4]. Therefore, ARPES measurements on the clean surface are required in order to clarify the *true* valence band structures of Pn-SC.

In the present study, photoconductivity-assisted ARPES measurements [5] were performed on the Pn-SC clean surface prepared by vacuum cleavage. Extraction of a spectral contribution of the surface bands was attempted through excitation energy dependent measurements.

Plate-shaped (typically several mm² wide and a few μm thick) Pn-SCs were produced by a physical vapor transport technique, which were selected and posted onto conductive carbon tape individually. Ag glue was additionally pasted at the rim of each crystal to ensure good electric conductivity. A strip of adhesive tape was carefully attached onto the top side of the Pn-SC sample prior to introduction into the ultra-high vacuum condition. The Pn-SC clean surface was obtained by cleaving that top side off together with the adhesive tape in vacuum. ARPES measurements were carried out at BL7U of UVSOR. The excitation photon energy ($h\nu$) was set at 8.0 eV and 21.2 eV in this study. In order to cancel sample charging, the sample was shined by continuous wave laser light (405 nm) during the measurements [2-4, 6]. All ARPES measurements were performed at room temperature.

Figures 1(a) and (b) show the ARPES spectra of Pn-SC (measured with the excitation energy of 8.0 eV and 21.2 eV respectively). The former spectra transform by changing emission angle as seen in Fig. 1(a). The probing depth at the valence band region in this

condition is known to be several nanometer [7]. In other words, energy dispersion of the valence bands of the Pn-SC clean surface was observed in a bulk sensitive condition.

In contrast, the ARPES spectra taken at $h\nu = 21.2$ eV do not exhibit apparent dependence on the emission angle. Note that the probing depth in this condition is in the order of sub-nm, namely shallower than one molecular layer of Pn-SC. This implies a shrinkage of the surface valence bands with respect to the bulk ones as predicted in the literature [4]. More precise excitation energy dependence is anticipated in order to clarify the detailed structures of the surface valence bands.

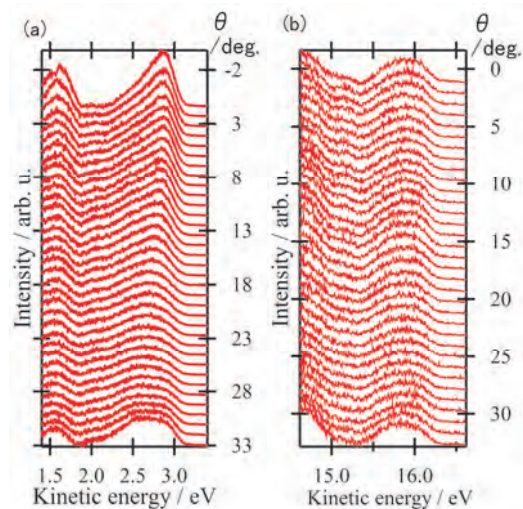


Fig. 1. (a) Bulk-sensitive ($h\nu = 8.0$ eV) and (b) surface-sensitive (21.2 eV) ARPES spectra of Pn-SC.

[1] O. D. Jurchescu *et al.*, Appl. Phys. Lett. **84** (2004) 3061.

[2] Y. Nakayama *et al.*, UVSOR Activity Reports **42** (2015) 88.

[3] Y. Nakayama *et al.*, J. Phys.: Cond. Matter **28** (2016) 094001.

[4] H. Morisaki *et al.*, Nat. Commun. **5** (2014) 5400.

[5] S. Machida *et al.*, Phys. Rev. Lett. **104** (2010) 156401.

[6] Y. Nakayama *et al.*, Jpn. J. Appl. Phys. **53** (2014) 01AD03.

[7] Y. Ozawa, *et al.*, J. Electron Spectrosc. Relat. Phenom. **197** (2014) 17.

BL7U

Electronic Structure of a Monolayer h-BN

Y. Sugiyama¹, Y. Okuyama¹, C. Bernard², S. Ideta³, K. Tanaka³, T. Greber² and T. Hirahara¹

¹Department of Physics, Tokyo Institute of Technology, Tokyo 152-8551, Japan

²Physik-Institut, Universität Zürich, CH 8057 Zürich, Switzerland

³UVSOR Facility, Institute for Molecular Science, Okazaki 444-8585, Japan

Silicene is a monolayer sheet of silicon and believed to host Dirac electrons similar to graphene [1,2]. Experimental studies have been extensively performed recently to reveal the presence of the Dirac-cone-type bands and associated intriguing properties. However, the strong substrate-silicene interaction hinders the exotic properties related to the Dirac physics. For example, we have previously shown that when we try to grow silicene on Ag(111), the Ag atoms from the substrate segregate to the surface of the deposited Si film and the well-known Si(111) $\sqrt{3}\times\sqrt{3}$ -Ag structure is formed [3].

One way to get around this problem is to use a substrate that weakly interacts with Si. Usually an insulating material is the right choice. In this respect, hexagonal boron-nitride (h-BN), which is a large gap insulator, should be an ideal substrate. It has been utilized as a substrate for graphene and this graphene/h-BN system was shown to host fascinating physical properties [4]. Furthermore, silicene formed on h-BN was shown by first-principles calculations to maintain the Dirac-like dispersion [5].

In the present study, we have measured the electronic structure of a monolayer h-BN formed on Rh(111) with high-resolution angle-resolved photoemission spectroscopy (ARPES). The samples were prepared in an ultrahigh vacuum (UHV) system in Switzerland and taken out into air. After they were transported to Japan, they were installed in an UHV chamber and annealed at $\sim 500^\circ\text{C}$ for 30 minutes. Low-energy electron diffraction (LEED) measurements showed sharp spots corresponding to h-BN, Rh(111), as well as the superstructure. Then the h-BN/Rh(111) samples were hydrogenated to flatten the h-BN since the original h-BN/Rh(111) system is buckled due to the interaction among h-BN and Rh(111) [6]. Figure 1 shows the band dispersion of the flattened h-BN measured with ARPES. One can find states near the Fermi level that correspond to the substrate Rh. Below the binding energy of 5 eV, one can find σ and π states that originate from the h-BN. Thus we have succeeded in preparing an atomically flat h-BN, and thus hope to actually grow silicene and other group IV and V monolayer systems.

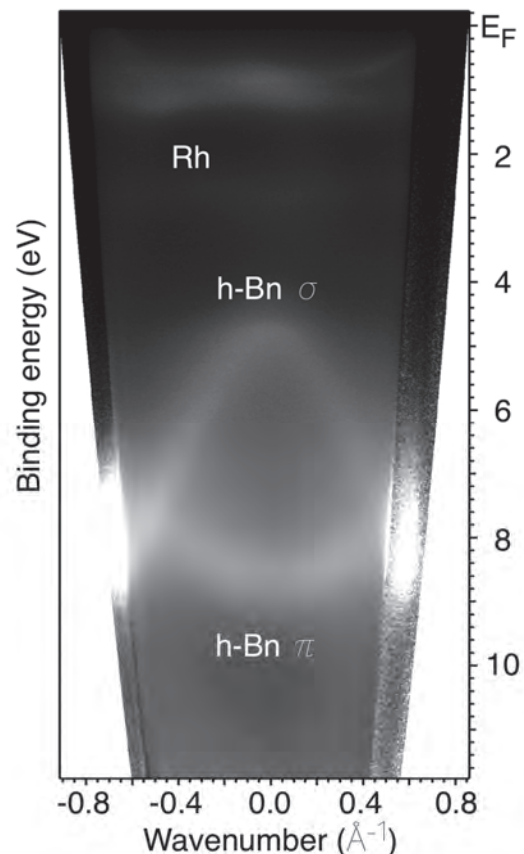


Fig. 1. The band dispersion of h-BN/Rh(111) system measured at $h\nu = 21$ eV with p -polarization.

- [1] K. Takeda and K. Shiraishi, Phys. Rev. B **50** (1994) 14916.
- [2] S. Cahangirov *et al.*, Phys. Rev. Lett. **102** (2009) 236804.
- [3] T. Shirai *et al.*, Phys. Rev. B **89** (2014) 241403.
- [4] C. R. Dean *et al.*, Nature Nanotech. **5** (2010) 722.
- [5] Z.-X. Guo *et al.*, Phys. Rev. B **87** (2013) 235435.
- [6] T. Brugger *et al.*, Angew. Chem. Int. Ed. **49** (2010) 6120.

BL7U

Scattering of Photoelectrons from Graphite via Organic Molecular Monolayer

T. Yamaguchi^{1,2}, F. Bussolotti², K. Kimura³, M. Matsunami^{2,3}, S. Ideta^{2,3}, K. Tanaka^{2,3},
T. Ueba^{2,3} and S. Kera^{1,2,3}

¹Graduate School of Advanced Integration Science, Chiba University, Chiba 263-8522, Japan

²Institute for Molecular Science, Okazaki 444-8585, Japan

³School of Physical Sciences, SOKENDAI, Okazaki 444-8585, Japan

kera@ims.ac.jp

Electron scattering governs fundamental properties in solids, such as thermal and electron conductivity. Recently, photoelectron scattering by phonons of graphite was discovered by low-energy angle resolved ultraviolet photoelectron spectroscopy (LE-ARUPS) [1]. In this work, we observed scattering phenomena of the photoelectron from graphite via organic monolayer interfaces using LE-ARUPS at beam line BL7U.

Figure 1 (a) shows LE-ARUPS intensity maps along Γ -K axis for a clean single crystal graphite (SCG). Fig.1 (b-h) depict pentacene (PEN), zinc phthalocyanine (ZnPc) and tin phthalocyanine dichloride (SnCl₂Pc) monolayers prepared either on SCG or highly oriented pyrolytic graphite (HOPG) substrates. Several linearly dispersive bands with the same slope parameter to the clean SCG band are observed in Fig.1 (b-h), indicating that the origin of

these features is photoelectron scattering of graphite π bands by molecular film. The scattering vector depends on the molecule and the measured temperature. We suggest that the features reflect reciprocal vectors of molecular unit cell of monolayer films. However, there are 6 domains for PEN and general Pc-type molecules on the graphite, which means reciprocal vectors do not match to the graphite ones [2, 3], leading to complicated scattering process. To understand a pure nature of these features, a commensurate superstructure of molecular system should be measured.

[1] S. Tanaka *et al.*, *Sci. Rep.* **3** (2013) 3031.

[2] T. G. Gopakumar *et al.*, *J. Phys. Chem. B* **108** (2004) 7839.

[3] J. Götzen *et al.*, *Phys. Rev. B* **81** (2010) 085440.

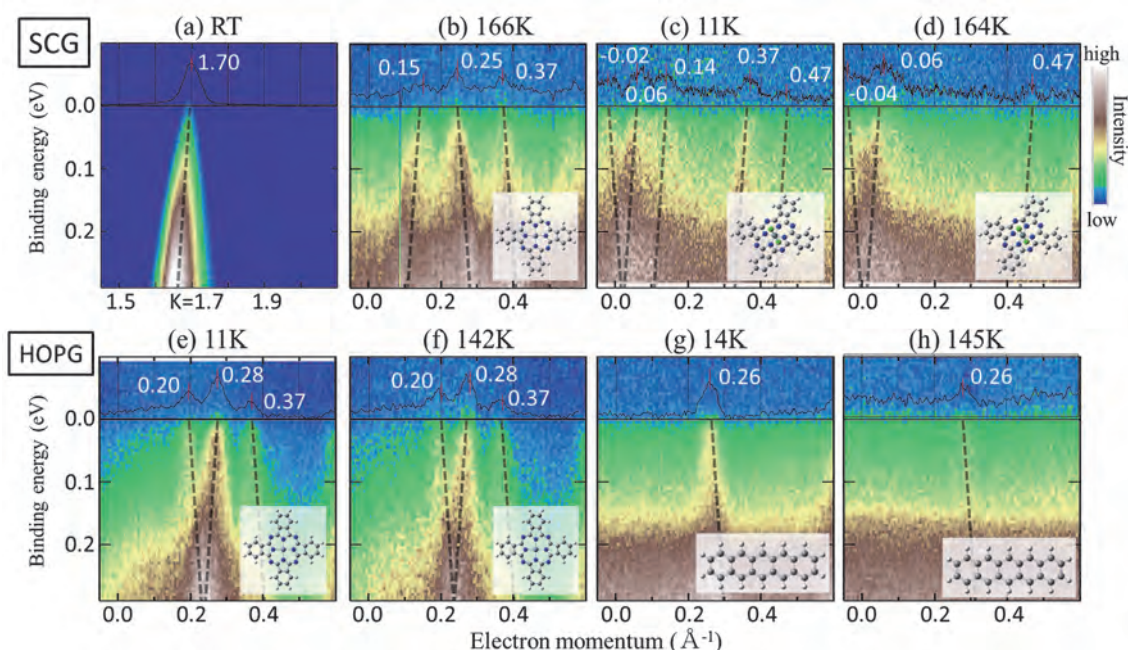


Fig. 1. $E(k)$ intensity maps taken at $h\nu=40\text{eV}$ for (a) bare SCG at room temperature (RT) and at 11eV for the monolayers; (b) ZnPc/SCG at 166K, SnCl₂Pc/SCG at (c) 11K and (d) 164K, ZnPc/HOPG at (e) 11K and (f) 142K, and PEN/HOPG at (g) 14K and (h) 145K. The image was obtained along Γ -K direction for (a-d). Inset spectra show momentum distribution curves at Fermi energy (E_F) integrated $E_F \pm 25\text{meV}$. Dashed lines represent the linearly dispersive band with the same slope to the SCG band. The numbers in the maps indicate the momentum (\AA^{-1}) where the linearly dispersive band crosses the E_F .

BL7U

ARPES of a Kondo Insulator YbB₁₂(001) Surface

K. Hagiwara¹, Y. Ohtsubo^{1,2}, J. Kishi¹, M. Matunami³, S. Ideta³, K. Tanaka³, T. Ito⁴,
H. Miyazaki⁵, F. Iga⁶ and S. Kimura^{1,2}

¹Graduate School of Science, Osaka University, Toyonaka 565-0043, Japan

²Graduate School of Frontier Biosciences, Osaka University, Suita 565-0871, Japan

³UVSOR Facility, Institute for Molecular Science, Okazaki 444-8585, Japan

⁴Department of Materials Engineering, Nagoya University, Nagoya 464-8603, Japan

⁵Department of Frontier Materials, Nagoya Institute of Technology, Nagoya 466-8555, Japan

⁶Department of Physics, Ibaraki University, Mito 310-8512, Japan

Recently, non-trivial topology of the electronic states on Kondo insulator (KI), so-called topological Kondo insulator (TKI) [1], is one of hot topics in solid-state physics as a synergy effect between strong electron correlation and spin-orbit interaction. SmB₆, a well-known KI, is firstly argued as a candidate of TKI. Earlier angle-resolved photoelectron spectroscopy (ARPES) experiments revealed metallic surface states on SmB₆ [2], but its origin and the topological order of SmB₆ is still under debate [3]. Therefore, a survey of another material is desirable to provide further insight into the origin of metallic surface states on KIs.

In this work, we performed high-resolution ARPES experiments of the surface electronic structure of another Kondo insulator, YbB₁₂(001) [4] at BL7U of UVSOR-III. We prepared the well-ordered surfaces of YbB₁₂ (001) by heating the sample up to 1600 K in a preparation chamber at the BL7U end station. The quality of the clean surface was checked by low-energy electron diffraction (LEED) as well as ARPES.

Figure 1 is the band dispersions along [100]. A band with steep dispersion below 100 meV would be a conduction band. This band becomes less dispersive around 35 meV, probably due to the hybridization with localized Yb²⁺ 4f bands. Such hybridization between conduction and 4f bands would be driven by the Kondo effect.

In addition to these states, we observed another state clearly crossing E_F at $k_{\parallel[100]} \sim 0.18 \text{ \AA}^{-1}$, as shown by the momentum distribution curve in Fig. 1. Since the bulk electronic structure of YbB₁₂ has a bandgap at this temperature ($\sim 20 \text{ K}$), this metallic band originates from surface electronic structure. This metallic surface state can be a cause of the remnant conduction path of YbB₁₂ observed at low temperature.

Figure 2 is the constant energy contour at $E_F (\pm 10 \text{ meV})$. It shows closed Fermi contour surrounding the $\bar{\Gamma}$, a time-reversal-invariant momentum. This behavior of the metallic surface state suggests its origin from the topological order.

These results at low temperatures agree with what is expected for a surface state on a theory of the topological Kondo insulator [1].

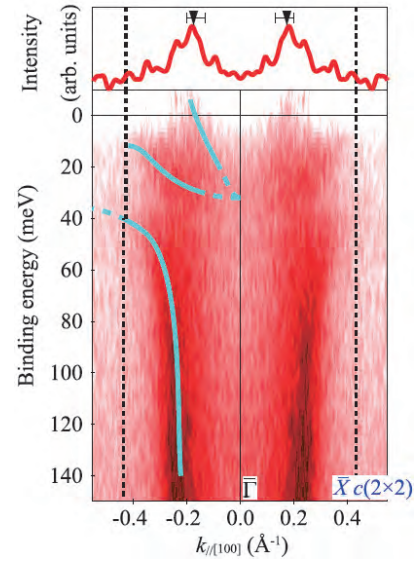


Fig. 1. ARPES intensity plots along [100] near E_F taken with 16.5 eV photons (bottom) and momentum distribution curves at $E_F (\pm 10 \text{ meV})$ (top). Lines in the bottom figure are guides the eyes. Each data are divided by the Fermi distribution function at the sample temperature (20 K) convolved with the instrumental resolution.

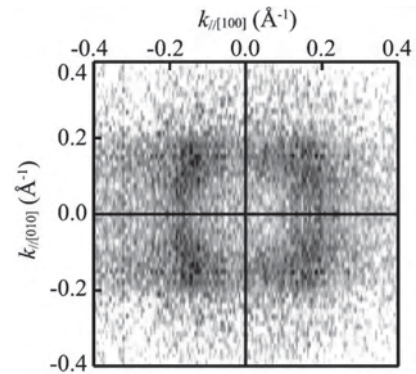


Fig. 2. Constant energy contour at $E_F (\pm 10 \text{ meV})$ taken with 16.5 eV photons at 14 K.

[1] M. Dzero *et al.*, Phys. Rev. Lett. **104** (2010) 106408.

[2] H. Miyazaki *et al.*, Phys. Rev. B **86** (2012) 075105.

[3] P. Hlawenka *et al.*, arXiv:1502.01542.

[4] F. Iga *et al.*, JMMM **177-181** (1998) 377.

BL7U

Surface Electronic Structure Studies of High Quality CrO₂(001) Films

H. Fujiwara¹, M. Sunagawa¹, K. Terashima^{1,2}, T. Nagayama¹, T. Kittaka¹, M. Ogata¹,
S. Ideta³, K. Tanaka³, T. Wakita^{1,2}, Y. Muraoka^{1,2} and T. Yokoya^{1,2}

¹Research Laboratory for Surface Science and Graduate School of Natural Science and Technology, Okayama University, Okayama 700-8530, Japan

²Research Center of New Functional Materials for Energy Production, Storage, and Transport, Okayama University, Okayama 700-8530, Japan

³UVSOR Facility, Institute for Molecular Science, Okazaki 444-8585, Japan

Chromium dioxide, CrO₂, is a half-metallic ferromagnet whose spin polarization at Fermi energy is 100% [1]. Previous studies of spin-resolved photoemission spectroscopy (spin-resolved PES) on CrO₂ films reported insulating-like photoemission spectra [2], while the temperature-dependence of resistivity of CrO₂ is metallic. As the reason of the insulating-like Fermi edge, reconstructions of CrO₂(001) surface has been theoretically suggested. However, it is also known that the surface of CrO₂ easily transforms into antiferromagnetic insulator Cr₂O₃ [3]. Due to the existence of Cr₂O₃, it has been difficult to discuss the intrinsic electronic states of CrO₂(001) surface. Recently, our group has succeeded in preparing high quality CrO₂(100) films by the closed system chemical vapor deposition (CVD) method using Cr₈O₂₁ as a precursor [4]. The photoemission spectrum of our CrO₂(100) film shows a peak at 1 eV with a clear Fermi edge, indicating that there are few contaminants of Cr₂O₃ on the surface of our sample. In this study, we prepared CrO₂(001) epitaxial films on TiO₂ substrates with the closed system CVD method and investigated the electronic structure of the CrO₂(001) surface by PES with synchrotron radiation. In this report, we show photon energy dependence of PES spectra and discuss the surface-metallicity of CrO₂(001) films.

The PES measurements were carried out at BL-7U in UVSOR. The photon energies between 15 eV and 33 eV were used in our measurement. The energy resolution was approximately 15 meV when photon energy of 21 eV.

Figure 1(a) shows the near- E_F valence band PES spectra taken at $h\nu = 15$ eV and 33 eV. Both spectra show clear Fermi edge. In the spectrum taken at $h\nu = 33$ eV, the intensity is higher than one of spectrum taken at $h\nu = 15$ eV because of the difference in cross-section of Cr 3d and O 2p bands, indicating that the Cr 3d and O 2p bands are hybridized at least in the energy region between $E_B = 0.7$ eV and E_F .

Figure 1(b) shows difference spectrum of $h\nu = 33$ eV with $h\nu = 15$ eV in order to emphasize the surface components of the CrO₂(001) film. As seen in Fig. 1(b), two peaks at $E_B = 0.5$ eV and at E_F were observed, indicating that these structures are surface derived bands. It should be noted that the observation of clear Fermi edge indicates existence of metallic (001) surface states, which has not been predicted in band

calculations [5] assuming that oxygen atoms in CrO₂(001) surface is reconstructed into tetrahedral arrangement. On the other hand, the observed surface states are consistent with band calculations [6] assuming that the oxygen atoms remain in octahedral arrangement, which indicates that the surface reconstruction does not occur.

In summary, we investigated the photon energy dependence of photoemission spectra of CrO₂(001) film in order to clarify the surface electronic states. The metallic surface states were observed, consistent with the band calculations not considering surface reconstruction.

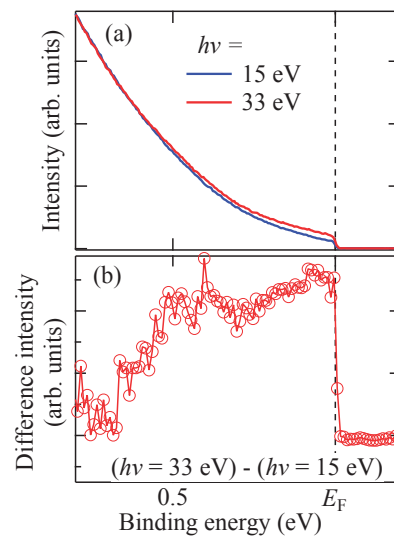


Fig. 1. (a) Near- E_F valence band PES spectra of the CrO₂(001) film at 15 K taken at $h\nu = 15$ eV and 33 eV. These spectra are normalized at $E_B = 0.7$ eV. (b) The surface states of the CrO₂(001) film determined from the difference between spectra taken at 33 eV and 15 eV.

- [1] H. Fujiwara *et al.*, Appl. Phys. Lett. **106** (2015) 202404.
- [2] K. P. Kämper *et al.*, Phys. Rev. Lett. **59** (1987) 2788.
- [3] R. Cheng *et al.*, Appl. Phys. Lett. **79** (2001) 3122.
- [4] K. Iwai *et al.*, J. Appl. Phys. **108** (2010) 043916.
- [5] F. Hong *et al.*, Phys. Rev. Lett. **96** (2006) 167206.
- [6] H. van Leuken *et al.*, Phys. Rev. B **51** (1995) 7176.

BL7B

Development of Photoconductive Detector Based on LaF₃ Thin Film

S. Otani, R. Yamazaki, S. Kokuryu, K. Toyama and S. Ono
Nagoya Institute of Technology, Nagoya 466-8555, Japan

According to increase in application of vacuum ultraviolet (VUV) light source, the detector for monitoring the light source is required. Consequently, the spectral response of the detector is demanded to optimize for each light source. The spectral response of the detector varies according to band gap of the material. Therefore, our group is proceeding to development of the VUV detectors by using fluorides which have extremely wide band gap [1, 2]. In our past study, the detectors based on BaF₂ and YF₃ show response below 147 nm and 170 nm, respectively. Here, we report on the development of filterless VUV photoconductive detector by using LaF₃ thin film.

LaF₃ thin film was deposited by pulsed laser deposition (PLD) on the MgF₂ single crystal substrate. LaF₃ ceramic target was irradiated with the femtosecond laser pulses (wavelength: 790 nm, laser fluence: 16.1 mJ/cm²). The deposition was carried out 4 h under high vacuum condition (2×10^{-4} Pa). The temperature of the substrate was controlled at 670 K. Figure 1 is scanning electron microscope (SEM) images of YbF₃ thin film. A sub-micron-sized particulates make up the majority of the deposition layer.

To evaluate these thin films as photoconductive detectors, a pair of interdigitated aluminum electrodes was fabricated onto the thin film by vacuum deposition. Photoconductivity of the detector was evaluated by measuring variation of the amperage by VUV irradiation. The amperage increased 1-digit by VUV irradiation as shown in Fig. 2. Additionally, transmission spectrum and spectral response of the detector were measured. The transmission edge was around 115 nm in wavelength. The detector showed photoconductivity below 161 nm in wavelength and the response signal increased as the radiation wavelength decreases (Fig. 3). Furthermore, response speed of the detector was evaluated by measuring temporal response of a VUV pulse by a flash lamp (pulse duration: 10.1 μ s). As a result, the temporal waveform by the detector was equivalent to that of a commercially available detector based on diamond.

In summary, we achieved filterless VUV photoconductive detector meeting practical performance by applying LaF₃ thin film grown by PLD.

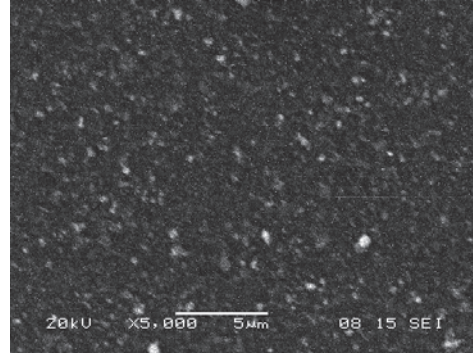


Fig. 1. SEM images of the surface and section of LaF₃ thin films.

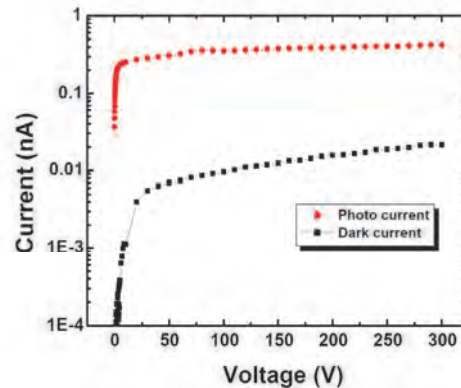


Fig. 2. I-V characteristic of LaF₃ thin film.

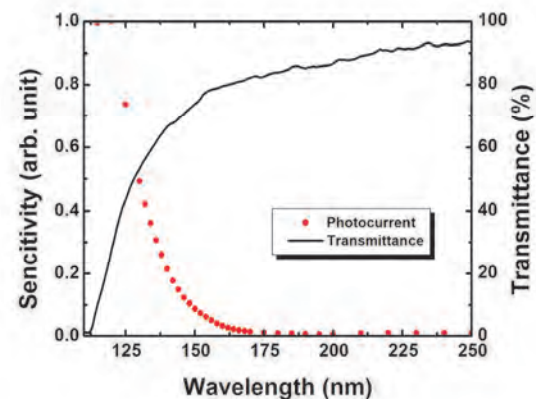


Fig. 3. Transmission spectrum and spectral response of the detector.

[1] M. Ieda, T. Ishimaru, S. Ono, K. Yamanoi, M. Cadatal, T. Shimizu, N. Sarukura, K. Fukuda, T. Suyama, Y. Yokota, T. Yanagida and A. Yoshikawa, *Jpn. J. Appl. Phys.* **51** (2012) 022603.

[2] T. Ishimaru, M. Ieda, S. Ono, Y. Yokota, T. Yanagida and A. Yoshikawa, *Thin Solid Films* **534** (2013) 12.

III-5

Life, Earth and
Planetary Sciences

BL4U

A Key Mechanism of Bacterial Pyrite Leaching Identified by Direct STXM Analysis at Cell-Pyrite Interface

S. Mitsunobu^{1,2}, M. Zhu², Y. Ohashi² and T. Ohgashi³¹Department of Agriculture, Ehime University, Matsuyama 790-8566, Japan²Institute for Environmental Sciences, University of Shizuoka, Shizuoka 422-8526, Japan³UVSOR Facility, Institute for Molecular Science, Okazaki 444-8585, Japan

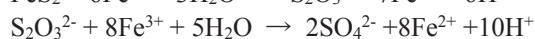
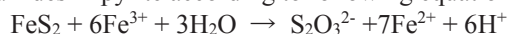
Microbial bioleaching of metal sulfides has been used as a low-cost engineering process for extracting metals from sulfidic ores due to its fast dissolution rate [1]. The microbial bioleaching of metal sulfide also contributes to formation of environmentally detrimental acid mine drainage (AMD), whose acidic nature and heavy-metal constituents cause serious contamination of soil and groundwater in the world. Thus, a better understanding of the mechanisms is of crucial importance for improvement of both industrial bioleaching and AMD formation.

There have been considerable efforts to identify mechanisms of bioleaching. However, little is known on the microbial bioleaching mechanism, because direct chemical speciation of metals and biomolecules at mineral-microbe interface has been difficult due to high spatial resolution in analysis.

Here, we investigated the mechanisms of the bioleaching process in bacterial pyrite leaching by leaching bacteria (*Acidithiobacillus ferrooxidans*) by scanning transmission X-ray microscopy (STXM) based C and Fe near edge X-ray absorption fine structure (NEXAFS) analyses at UVSOR BL4U.

Carbon NEXAFS analysis directly showed that attached *A. ferrooxidans* produces polysaccharide-abundant extracellular polymeric substances (EPS) at the cell-pyrite interface (data not shown, [2-3]). Figure 1 shows the STXM-based merged Fe/C image and Fe 4p NEXAFS of bacteria cells attached to pyrite particles in 2 weeks incubation. The image in Fig. 1a shows that Fe was localized around the surface of the bacteria cells. Considering that C NEXAFS demonstrated the appearance of a polysaccharide-rich EPS layer at the cell-pyrite interface, this suggests that Fe had accumulated in this polysaccharide layer. In the Fe NEXAFS spectra, both the spectra of whole cell and cell-pyrite interface (interface 1 and 2 in Fig. 1b) consist of Fe(II) and Fe(III) peaks. Thus, the Fe species in both cell and cell-pyrite interface were Fe(II) addition to Fe(III) [3].

In previous study, researchers have implied a possible role for the Fe(III) in EPS in whole pyrite bioleaching process, an oxidizing agent for sulfides [1]. That is the Fe(III) in EPS would abiotically oxidize sulfides in pyrite according to following equations.



However, this interfacial process remained speculative because no Fe(II) in the EPS subsequently formed by

this oxidation process had been observed yet. Previous studies determined the Fe species in EPS by indirect methods [1]. The Fe(II) detected by direct STXM based NEXAFS analyses in this study is a first direct evidence supporting the oxidative attack by the Fe(III) in EPS. These findings could be important information for understanding key mechanism of both bacterial mineral leaching and AMD formation.

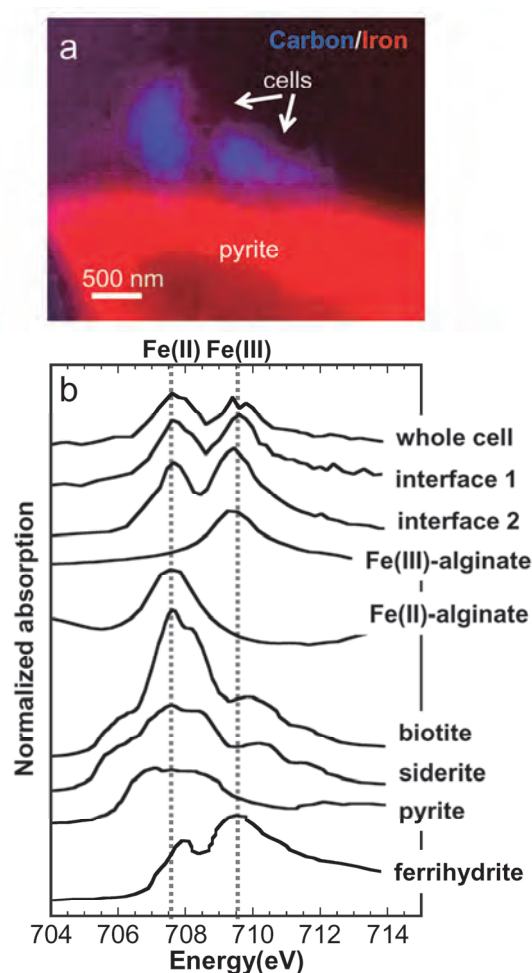


Fig. 1. STXM-based C and Fe images (a) and Fe 4p NEXAFS spectra (b).

[1] W. Sand and T. Gherke, Res. Microbiol. **157** (2006) 49.

[2] S. Mitsunobu *et al.*, Chem. Lett. **44** (2015) 91.

[3] S. Mitsunobu *et al.*, Microbes Environ. (in press).

BL4U

Application of XANES to the Analysis of Carbonaceous Materials in Hayabusa-Returned Samples for Determination of Their Origin

M. Uesugi¹, A. Nakato¹, T. Ohigashi² and Y. Inagaki²¹*Institute of Space and Astronautical Science, Japan aerospace exploration agency, Sagami-hara, 252-5210, Japan*²*UVSOR Synchrotron, Institute for Molecular Science, Okazaki, 444-8585, Japan*

Carbonaceous particles, those have been found in the sample catcher of Hayabusa spacecraft together with silicate particles, were still under the investigations, including precise determination of their origin. Results of isotopic analysis of H, C and N of the carbonaceous materials by NanoSIMS did not show any signatures of their extraterrestrial origin, e.g. isotopic anomalies against the terrestrial composition [1]. Some of the results of analyses by Transmission Electron Microscopy (TEM, [2]) and X-ray absorption near edge structure (XANES, [3]) indicated relation to the terrestrial material. Thus, those particles might indicate the contamination of terrestrial material into the sample catcher before, during and/or after the operation of Hayabusa spacecraft.

In previous study, a particle from the witness plate exposed to the clean room of Hayabusa2 spacecraft construction, where Hayabusa1 spacecraft was constructed, was investigated by XANES/STXM installed in ALS/LBNL, Berkeley. The shape of XANES spectrum of the particle (green, WP1 in Fig. 2) closely relates to that of a Hayabusa-returned sample, RA-QD02-0180-03 (blue line in Fig. 2), and indicate the relation of them.

In this work, we investigated a particle newly picked up from the same witness plate using XANES/STXM installed in UVSOR, in order to confirm the result of previous study.

Figure 2 shows C-XANES spectra of the new particle (red, WP2) and Hayabusa-returned samples (blue, RA-QD02-0180-03). The shape of the spectra was similar, but position of the peaks of WP2 were different from others.

N-XANES spectrum of the WP2 was also largely different from other two samples. Though particles were picked up from the same witness plate and chemical composition of them was similar, those difference of XANES spectrum indicate the different origin of WP1 and WP2. The fact indicate several paths of the contamination to the sample catcher were possible, and should be considered for the precise determination of the origin of the contaminant.

In future work, we will apply the XANES/STXM analysis to further possible contaminants such as particles of biological materials.

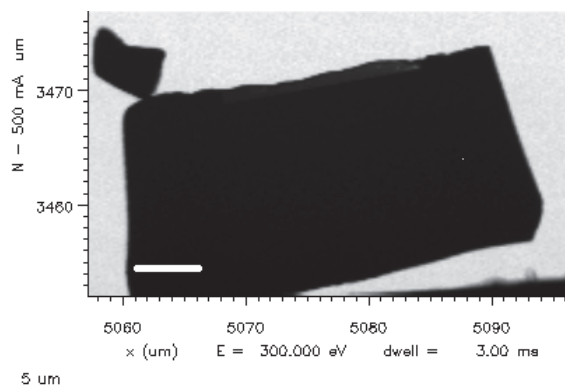


Fig. 1. STXM image of the ultrathin section of WP2 in Fig. 2. The particle was pressed on a gold plate and cut by Focused ion beam to extract ultrathin sections.

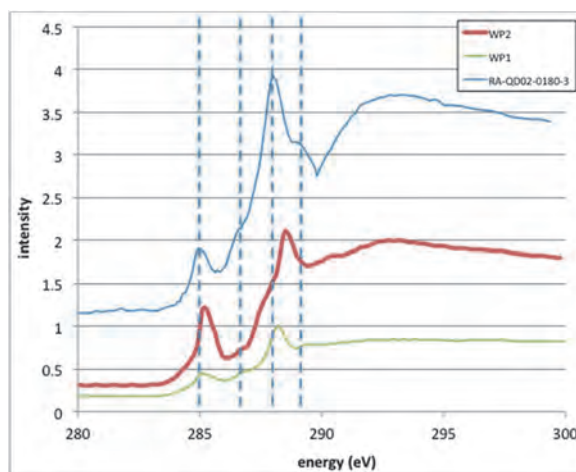


Fig. 2. C-XANES spectra of the particles from the witness plate of clean room of the Hayabusa2 spacecraft construction (green and red), and Hayabusa-returned sample (blue). Peak positions of WP2 were different from those other two samples.

- [1] M. Ito *et al.*, *Earth planet. Space* **66** (2014) 91.
- [2] M. Uesugi *et al.*, *Earth planet. Space* **66** (2014) 102.
- [3] H. Yabuta *et al.*, *Earth planet. Space* **66** (2014) 156.

BL4U

Distribution of DNA and Protein in Mammalian Cell Nuclei Calculated Using NEXAFS Profiles at the N-K and O-K Absorption Edges

A. Ito¹, T. Ohigashi^{2,3}, K. Shinohara¹, S. Tone⁴, M. Kado⁵, Y. Inagaki² and N. Kosugi²

¹School of Engineering, Tokai University, Hiratsuka 259-1292, Japan

²UVSOR Synchrotron, Institute for Molecular Science, Okazaki 444-8585, Japan

³The Graduate University for Advanced Studies (SOKENDAI), Okazaki 444-8585, Japan

⁴Department of Biochemistry, Kawasaki Medical School, Kurashiki 701-0192, Japan

⁵Nat. Inst. Quantum and Radiological Sci. Technol., Kizugawa 619-0215, Japan

Spectromicroscopy using scanning transmission X-ray microscope (STXM) has been applied to DNA and protein distributions in biological specimens such as chromosome and sperm. Our previous study on the DNA mapping in mammalian cell nuclei was successfully carried out for cultured A549 cells with the aid of different NEXAFS (Near Edge X-ray Absorption Fine Structure) profiles between DNA and protein at the N-K absorption edge as shown in the left panel of Fig. 1 [1]. The results gave rather unexpected, different distributions of DNA and histone in nucleoli. In this study, to confirm these results we extended the analysis to the O-K edge, and also to obtain quantitatively consistent results at different absorption edges, we developed the correction of reference NEXAFS spectra used for the “stack fit” method to obtain molecular distribution.

Human HeLa cell was used because of its large nuclear area. Figure 2 shows transmission and optical density (OD) images of a whole cell taken at 400 eV. Four large nucleoli in the nucleus were identified, and for the enlarged area DNA and histone distributions were calculated using aXis2000 software to fit the specimen spectra to the reference spectra. In the center of nucleoli histone content was rather poor compared with DNA, which was consistent with our previous report [1].

For the extension of the analysis to the O-K edge, reference spectra at the O-K edge (Fig. 1) should be correlated to those at the N-K edge, since the fitting results do not necessarily assure the same quantitative distribution due to the independent measurements at each absorption edge. As a trial of the correlation, first we calculated mass thickness, which is defined as a product of the density and thickness of specimen, from OD by considering mass absorption coefficients at 395 eV. Then the OD of reference spectra at the O-K edge was corrected using this mass thickness at 525 eV. Based on these corrected spectra, DNA and histone distributions were obtained as shown in the lower panels of Fig. 3, indicating similar distributions to those at the N-K edge. Table 1 shows OD range of DNA and histone at the N-K and O-K edges. OD differences and the ratio of DNA and histone were also listed. Similar ratios between the N-K and O-K edges were obtained, although the absolute OD values were not totally the same.

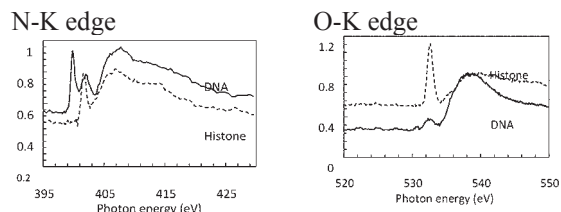


Fig. 1. NEXAFS spectra of DNA and histone at the N-K and O-K edge.

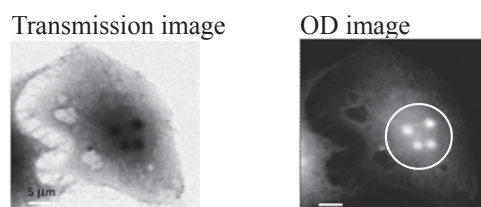


Fig. 2. Transmission and OD images of human HeLa cell at 400 eV. White circle in OD image is enlarged in Fig. 3. Scale bar corresponds to 5 microns.

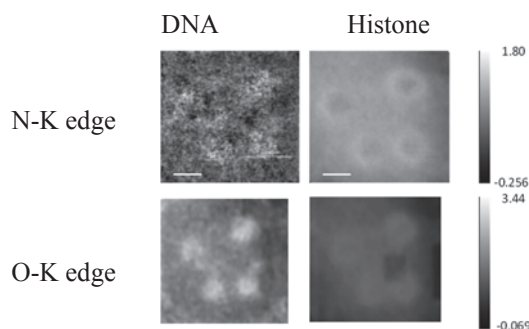


Fig. 3. DNA and histone distributions of nucleus of HeLa cell obtained at the N-K and O-K edges. OD range bar is shown in the right. Scale bar corresponds to 2 microns.

Table 1. Comparison of DNA and histone contents between the N-K and O-K edges.

	OD range	Difference	DNA/Histone
DNA(N-edge)	-0.256~1.80	2.06	2.52
Histone(N-edge)	0.443~1.26	0.817	
DNA(O-edge)	-0.0694~3.44	3.51	2.36
Histone(O-edge)	-0.00413~1.48	1.48	

[1] T. Ohigashi *et al.*, AIP Conference Proceedings **1696** (2016) 020027.

BL4U

Speciation of Sulfur and Calcium in Aerosols by STXM

C. Miyamoto¹, H. Suga², T. Ohigashi³, Y. Inagaki³ and Y. Takahashi¹

¹Graduate School of Science, The University of Tokyo, Tokyo 113-0033, Japan

²Graduate School of Science, Hiroshima University, Higashi-Hiroshima 739-8526, Japan

³UVSOR Synchrotron, Institute for Molecular Science, Okazaki 444-8585, Japan

Aerosols, defined as small particles or droplets in the atmosphere, have important effects on the environment. Sulfate is the main compound in aerosols (in particular anthropogenic ones) and is emitted primarily by human activities. As suggested by the Intergovernmental Panel on Climate Change, sulfate aerosols can cool the earth in two ways: directly by reflecting sunlight, and indirectly by acting as cloud condensation nuclei. The latter cooling role is made possible by the hygroscopic nature of some sulfates. In the atmosphere, sulfate occurs in several forms including ammonium salts (NH_4HSO_4 , $(\text{NH}_4)_2\text{SO}_4$), calcium salt (gypsum; $\text{CaSO}_4 \cdot 2\text{H}_2\text{O}$), and hydrated species (Takahashi *et al.*, 2006). Among these species, ammonium salts are hygroscopic, while calcium salts are not. Thus, sulfate species should be well identified to precisely evaluate the global cooling effect of sulfate aerosols. Thus, this study conducted speciation of sulfur in aerosols by Scanning Transmission X-ray Microscopy installed at BL4U, UVSOR.

In this study, distributions of sulfur and calcium species within aerosol particles were examined for aerosols collected in Higashi-Hiroshima in May, 2014, which can be a basis for understanding chemical processes to form sulfate aerosols. First, distribution of calcium in a particle with a few μm diameter was examined. Although calcium is distributed in the whole particle, calcium oxalate or calcium sulfate was mainly found at the rim of the particle based on the calcium L_{III} - and L_{II} - edge XANES (Figs. 1 and 2). It is known that concentrations of sulfate and oxalate correlate each other [1]. The present results suggested that both sulfuric acid and oxalic acid react with calcium particle, particularly calcite, in the atmosphere.

Distribution of sulfur was also examined by the sulfur L_{III} edge absorption. It was found that calcium sulfate was distributed within the rim where calcium oxalate and/or calcium sulfate were found by calcium L -edge absorption (Fig. 1).

All these results support that secondary calcium species produced by the reactions of calcium carbonate with sulfuric or oxalic acids were formed in the atmosphere. In particular, formation of calcium oxalate at the rim of the particle is found for the first time by any microscopic analyses.

Sulfur speciation was also conducted for the particles collected as a fine particle ranging from 0.69 to 1.3 μm . As a result, sulfur species was almost exclusively ammonium salt within the particles based on the XANES analysis, showing that sulfate aerosols smaller than 1.3 μm is not the products of reactions

with minerals, but sulfate aerosol possibly produced in droplet mode.

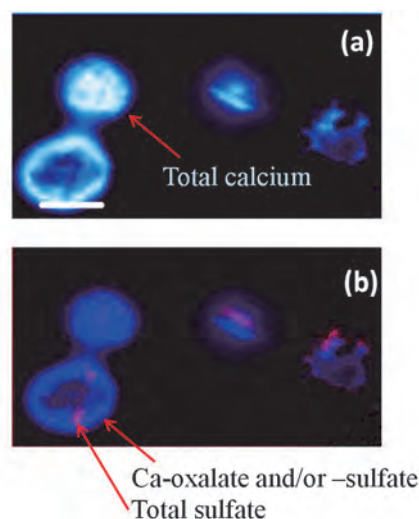


Fig. 1. STXM images of total calcium, Ca-oxalate and/or sulfate, and total sulfate by absorption at Ca and S L -edges.

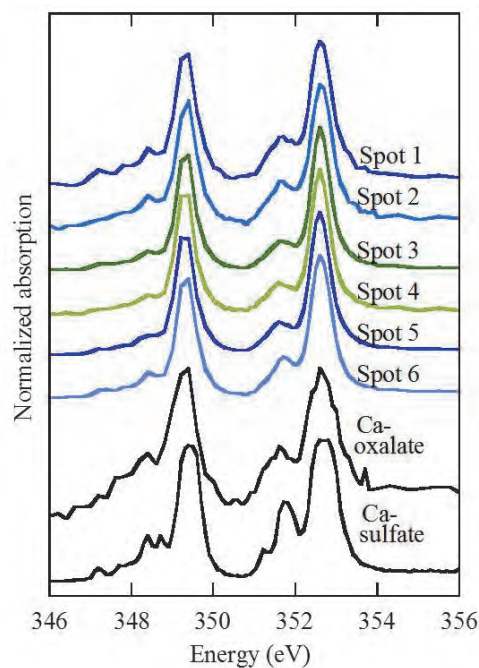


Fig. 2. Calcium L_{III} and L_{II} edges XANES for Ca-oxalate, Ca-sulfate, and Ca in various spots in Fig. 1 (b).

[1] T. Furukawa and Y. Takahashi, *Atmos. Chem. Phys.* **11** (2011) 4289.

BL4U

Chemical Evolution of Meteoritic Organics during Impact Metamorphism

H. Yabuta¹, T. Atou², T. Ohigashi^{3,4}, Y. Inagaki³, P. Beck⁵, L. Bonal⁵ and E. Quirico⁵

¹Department of Earth and Space Science, Osaka University, Osaka 560-0043, Japan

²Laboratory for Materials and Structures, Institute of Innovative Research, Tokyo Institute of Technology, Tokyo 226-8503, Japan

³UVSOR Facility, Institute for Molecular Science, Okazaki 444-8585, Japan

⁴School of Physical Sciences, The Graduate University for Advanced Studies (SOKENDAI), Okazaki 444-8585, Japan

⁵Institut de Planétologie et d'Astrophysique de Grenoble (IPAG), UJF-Grenoble 1 / CNRS-INSU, UMR 5274, Grenoble, F-38041, France

The primitive solar system materials such as meteorites, comets, and these-derived cosmic dusts were formed 4.5 billion years ago by accretion of gas and dusts in interstellar cloud. The interstellar dusts are about ten micron-sized solid particles consisting of silicate mineral core, refractory organics, and amorphous ice mantle. Therefore organic molecules in space can be described as one of the major building blocks of our Solar System and Life. To date, molecular and isotopic compositions of organics from the meteorites ranging various groups and petrologic types have been frequently studied in relation to the chemical history in the early Solar System [1, 2].

Shock metamorphism is one of the important processes in the early Solar System, but its relationship with chemical evolution of meteoritic organic compounds has been less frequently studied than aqueous alteration and long-term heating due to radiogenic elements on a meteorite parent body. Yabuta *et al.* (2010) [3] has revealed that molecular and isotopic characteristics of organic macromolecular solids in the shocked meteorites are distinct from those in the long-term heated meteorites. In this study, for understanding chemical behaviors of organic matter in meteorites, molecular analyses of organic matter the experimentally shocked meteorite were conducted.

As a sample, Murchison meteorite powder was used in this study. The shock experiments of a meteorite powder pellet (~180 mg) in a SUS collecting vessel were conducted at 5 and 10 GPa by a single-stage powder gas gun and at 20 and 40 GPa by a double-stage light gas gun at Tokyo Institute of Technology (Fig. 1). After the experiment, the meteorite sample was recovered and treated with CsF/HF-dioxane [4] to purify the insoluble organic macromolecular solid (IOM). The insoluble organic solids from the experimentally shocked meteorites were analyzed by a scanning x-ray transmission microscope (STXM) - x-ray absorption near edge structure (XANES) at beamline 4U, UVSOR.

Carbon-XANES spectrum of organics the experimentally shocked Murchison IOM at 5 GPa (blue spectrum in Fig. 1) showed a peak of aromatic carbon (285 eV) and a peak of carboxyl carbon (288 eV) with a shoulder of aliphatic carbon (297.6 eV), which was very similar to non-shocked Murchison IOM. The C-XANES spectra of IOM at 10 and 20 GPa

were also similar to that at 5 GPa. On the other hand, in the C-XANES spectrum of organics at 40 GPa, a peak intensity of carboxyl carbon largely decreased and that of aromatic carbon was slightly developed. This result indicates that modification of IOM by shock heating occurs at 40 GPa and is comparable to their Raman spectra [5].

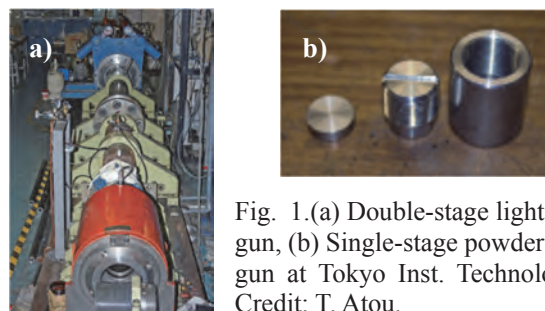


Fig. 1. (a) Double-stage light gas gun, (b) Single-stage powder gas gun at Tokyo Inst. Technology. Credit: T. Atou.

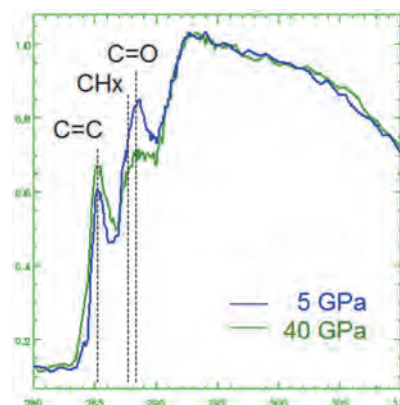


Fig. 2. C-XANES spectra of organic macromolecular solids from the experimentally shocked meteorites. Blue: 5 GPa, Green: 40 GPa.

- [1] C. M. O'D. Alexander *et al.*, *Geochim. Cosmochim. Acta* **71** (2007) 4380.
- [2] G. D. Cody *et al.*, *Earth. Planet. Sci. Lett.* **272** (2008) 446.
- [3] H. Yabuta *et al.*, *Meteor. Planet. Sci.* **45** (2010) 1446.
- [4] G. D. Cody and C. M. O'D. Alexander, *Geochim. Cosmochim. Acta* **69** (2005) 1085.
- [5] P. Beck *et al.*, *Meteor. Planet. Sci.* **45** (2012) 1446.

BL4U

Probing Tacrolimus in Human Skin by Soft X-Ray Spectromicroscopy

K. Yamamoto¹, A. Klossek¹, T. Ohigashi², F. Rancan³, R. Flesch¹, A. Vogt³,
U. Blume-Peytavi³, P. Schrade⁴, S. Bachmann⁴, R. Schulz⁵, R. R. Netz⁵, S. Hedtrich⁶,
M. Schäfer-Korting⁶, N. Kosugi² and E. Rühl¹

¹Institute for Chemistry and Biochemistry, Freie Universität Berlin, Takustr. 3, 14195 Berlin, Germany

²UVSOR Synchrotron, Institute for Molecular Science, Okazaki 444-8585, Japan

³Charité Universitätsmedizin, 10117 Berlin, Germany

⁴Abteilung für Elektronenmikroskopie at CVK, 13353 Berlin, Germany

⁵Fachbereich Physik, Freie Universität Berlin, 14195 Berlin, Germany

⁶Institut für Pharmazie, Freie Universität Berlin, 14195 Berlin, Germany

Lipophilic drugs, such as dexamethasone and tacrolimus, are commonly used to treat by topical application inflammatory skin diseases. We have investigated recently the penetration of dexamethasone ($C_{22}H_{29}FO_5$), a drug that penetrates readily into human skin, as probed by X-ray microscopy [1]. Adequate penetration is due to its moderate lipophilicity and the relatively low molecular weight of 392 Da, which is well below the 500 Da limit [2]. This limit is known to be of relevance for distinguishing low molecular weight drugs that easily penetrate into skin from heavier ones, such as tacrolimus ($C_{44}H_{69}NO_{12}$, $M=804$ Da), requiring advanced formulations for sufficient penetration [3]. We have investigated by label-free X-ray spectromicroscopy tacrolimus in the O 1s-regime. The experiments were performed at the BL4U beamline at UVSOR-III using a scanning transmission X-ray microscope (STXM). Intact skin samples from healthy donors as well as tape-stripped skin for thinning the stratum corneum (SC), the top skin penetration barrier, were investigated. For intact skin the drug was dissolved in aqueous ethanol (50%) with a concentration of 10 mg/mL, where 40 μ L were applied per cm^2 . Tacrolimus was applied to tape-stripped skin by using Protopic ointment 0.1% (Astellas Pharma, Munich, Germany), 30 μ g/ cm^2 . Penetration times ranged between 10 and 1000 min. Chemical selectivity for probing the drug in fixed human skin slices is gained by excitation of the O 1s $\rightarrow \pi^*$ -transition at 531.3 eV, which is suitable to suppress the background absorption of fixed human skin (see Fig. 1). This indicates in addition to recent work [1], that X-ray microscopy is a general approach to probe drugs in fixed human skin slices.

The results indicate that in normal skin tacrolimus can only penetrate into the stratum corneum. The drug was not detected in deeper skin layers, such as in the viable epidermis and dermis. However, if the skin is mechanically removed by repeated tape-stripping (50 times) prior to drug exposure, then penetration of tacrolimus is observed, as indicated in Fig. 2. Clearly, the drug is detected in the viable epidermis. It is anticipated that this finding will also apply to drug penetration in barrier deficient inflamed skin, as known for the improvement of atopic dermatitis

following the use of tacrolimus ointment [3]. The shape of local tacrolimus distribution is similar to earlier work on dexamethasone [1]. This implies that the transport of both drugs is similar, independent of the molecular weight, once the stratum corneum is passed. We also observe that the drug concentration drops to the detection limit at the basal membrane, implying that in the dermis different transport properties occur. Thus, the basal membrane may form another barrier for transdermal drug penetration, as suggested by present X-ray spectromicroscopy studies.

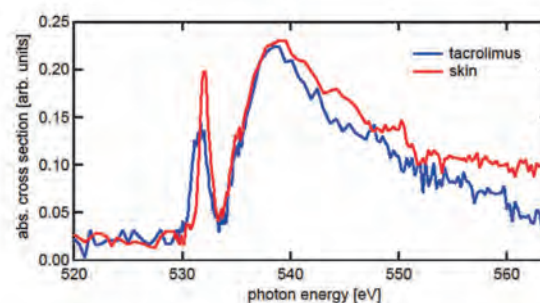


Fig. 1. O 1s-excitation regime of tacrolimus in comparison with fixed human skin. The resonance near 531 eV (O 1s $\rightarrow \pi^*$ -transition) is used for selective probing of the drug.

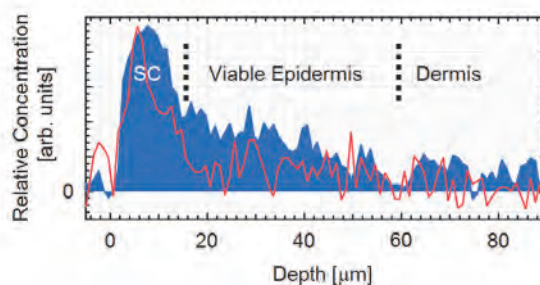


Fig. 2. Penetration of tacrolimus into human skin after tape-stripping. Two different penetration times were studied (10 min: red and 1000 min: blue).

[1] K. Yamamoto *et al.*, *Anal. Chem.* **61** (2015) 6173.

[2] J.D. Bos *et al.*, *Exp. Dermatol.* **9** (2000) 165.

[3] M. Lapteva *et al.*, *Mol. Pharm.* **11** (2014) 2989.

BL4U

Evaluation of FIB Sample Contamination Depends on the Storage Environment Based on XANES Analysis and Application to Organics in Carbonaceous Chondrites

A. Nakato¹ and M. Uesugi²¹Division of Earth and Planetary Sciences, Kyoto University, Kyoto 606-8502, Japan,²JASRI/SPring-8, Sayo-gun 679-5198, Japan

XANES and high resolution STXM installed in UVSOR BL4U are useful tools for the characterization of molecular structure of the unknown carbonaceous material, and understanding of their micro-distribution. We expected to apply these analyses to the hydrous carbonaceous chondrites, since the extraterrestrial organics have some variety and complex structures those could be evidences of the evolution of parent body of the chondrites. In this aspect, samples preparation must avoid the change of their original microstructure.

It is well known that electron beam of the TEM observation could modify the C-XANES spectrum [1]. In contrast, we reported the sample damage induced by C-XANES in the report of the previous study [2]. TEM observations just before and after XANES analysis showed that NaCl and KCl inclusions in the sample were damaged heavily by the XANES analysis. Before further precise description of the carbonaceous materials in carbonaceous chondrite, damage during XANES analyses and contamination during the sample storage must be evaluated. In this study, we evaluated the contamination during the sample storage by changing the storage environment and the period by XANES/STXM.

We fibbed 8 samples from the matrix of Murchison, one of the hydrous carbonaceous chondrites. The size is about 15x10 μm and 100 nm thickness. The samples from #1 to #4 were kept in 4 different conditions for 1 week, and the remaining samples from #5 to #8 were kept for 2 months until the XANES/STXM analysis. #1-4 samples were analyzed again after storage for 3 months. The storage atmospheres were pure Nitrogen and approximately 10^2 Pa vacuumed conditions, and the sample holder made by Si and metal, respectively (Table. 1). C, N-XANES analyses were performed for #1-4 samples after 1 week storage. N, O-XANES spectrum were obtained for #5-8 samples after 2 months storage and for #1-4 samples after 3 months storage.

C-XANES spectrum of #1-4 samples stored for 1 week do not show any changes irrespective of the storage environment. In addition, we can not detect clear N-XANES transition in all samples, even some samples (#1-2, #5-6) were kept in pure N₂ atmosphere (Fig. 2). These results suggest that sample storage does not give any contaminations, under the conditions tested in this study.

In future work, we plan to perform C-XANES

analysis for these samples to confirm the molecular structures of the carbonaceous materials to be unchanged by a few months storage. Besides, we will apply the XANES/STXM analysis to various hydrous carbonaceous chondrites.

Table 1. Samples and storage conditions.

#	Atmosphere	Holder	Storage period and analyzed spectrum		
			1 week	2 months	3 months
1	N ₂	Si	C, N		O, N
2		Metal	C, N		O, N
3	Vacuum	Si	C, N		O, N
4		Metal	C, N		LOST
5	N ₂	Si		O, N	
6		Metal		O, N	
7	Vacuum	Si		O, N	
8		Metal		O, N	

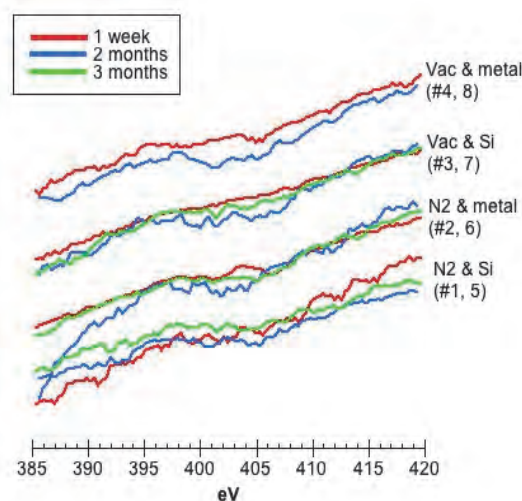


Fig. 1. N-XANES spectrum of samples #1-8.

- [1] H. Yabuta *et al.*, Earth planet. Space **66** (2014) 156.
 [2] M. Uesugi and A. Nakato, UVSOR activity report **42** (2015) 148.

BL6B

Visualization of Spatial Distribution of the Optical Isomers of Amino Acids by Infrared Micro-Spectroscopic Imaging

S. Kamei¹, J. Hibi², H. Yokoyama², Y. Ohtsubo^{1,2}, H. Watanabe^{1,2} and S. Kimura^{1,2}

¹ Graduate School of Frontier Biosciences, Osaka University, Osaka 565-0871, Japan

² Graduate School of Science, Osaka University, Osaka 565-0043, Japan

Protein, which is one of important components of human bodies, consists of essential amino acids. Although amino acids have optical isomers of L- and D-types except for glycine, living bodies mainly consist of L-amino acids. However, in recent years, it has been revealed that the ratio of D-amino acids increases in living body by racemization reaction with aging. It is considered that an increase of D-amino acids causes the change of the higher-order structure of protein, which is the origin of aging sicknesses such as cataract and Alzheimer's disease [1]. For early prevention of those aging diseases, a simple detection method of D-amino acids is required.

Since physical and chemical properties of D-amino acids are the same as those of L-types, special techniques to separate these isomers, for instance a special chromatography with asymmetric catalysts, are used at present.

In the case of the mixing of L- and D-amino acid molecules, so-called racemates, however, the crystal structure is different from those of homochiral L- and D-molecules. This implies that some infrared (IR) absorption peaks owing to molecular vibrations of racemates are different from those corresponding peaks of the homochiral molecules [2]. Therefore, the IR absorption peak as well as the micro-spectroscopic imaging is a good probe to detect the area and density of racemates, that is of D-amino acids, in the background of L-amino acid molecules.

In this paper, we developed the methodology to detect D-amino acid molecules in L-molecules by using different IR absorption peaks of racemates from those of homochiral molecules as a probe.

Thin film samples of L- and D-alanine, which is one of essential amino acids, on potassium bromide (KBr) substrates were fabricated by a vacuum evaporating method, where L- and D-alanine powders were evaporated separately. A part of evaporation area of these materials was overlapped as shown in Fig. 1(c). In the overlapped area, namely L+D area, the interfacial layer between L- and D-alanine becomes racemates. The IR micro-spectroscopic imaging measurement was performed at the infrared beamline 6B. The imaging measurement was carried out at about 5×5 mm² area with 100- μ m step (about 3,000 points in total) on the sample.

Figure 1(a) shows an IR absorption peak of L- and D-alanine and L+D overlapping areas. Although the absorption peak shape of pure L and D areas are similar to each other, but the peak of L+D area is different, that looks to have two components, one is the same as

pure areas and the other is an extra peak. To clarify the speculation, the peak of the L+D area is well fitted by two Lorentz components as shown in Fig. 1(b). The extra peak originates from the racemate because the same peak has been observed in racemic alanine of a pellet yet. Figure 1(d) shows the spatial distribution of racemic ratio (*R*) evaluated from the ratio of the absorption peak area of the racemic alanine by the fitting at each point performed as the same as that in Fig. 1(b). The image suggests that the *R* values in the L+D area are much different from other homochiral area. This result pronounces that it is possible to visualize the spatial distribution and evaluation of the ratio of D-alanine in L-alanine by the IR imaging. In addition, we could evaluate higher spatial resolution up to 10 μ m by using the high-brilliant IR synchrotron radiation (IR-SR). Therefore, the micro-spectroscopic imaging using IR-SR is a suitable tool to detect optical isomers in homochiral amino acids.

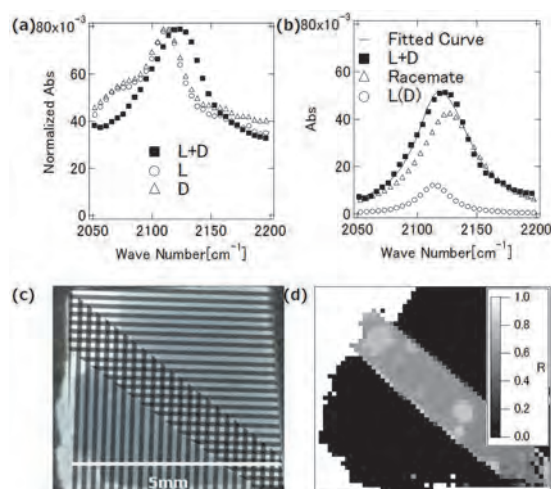


Fig. 1. (a) Infrared absorption spectra of homochiral L-, D-alanine and these overlapping area (L+D). (b) Fitting of the L+D absorption by two Lorentz functions, one is the homochiral spectrum and the other racemic one. (c) Visible image of L-alanine (horizontal line part) and D-alanine (vertical line part) film fabricated on a KBr substrate. (d) Spatial distribution of racemic ratio (*R*) evaluated by the fitting as shown in (b).

[1] Y. Kaji *et al.*, Invest. Ophthalmol. Vis. Sci. **48** (2007) 3923.

[2] V. S. Minkov *et al.*, J. Struct. Chem. **51** (2010) 1052.

The background is a solid red color with several abstract geometric elements. A large, semi-transparent circular graphic is centered on the right side, featuring concentric rings and a dotted border. Diagonal lines and a grid of small dots are also visible, creating a dynamic, modern aesthetic.

IV

List of Publications

List of Publications

- M. Aitani, Y. Sakamoto, T. Hirahara, M. Yamada, H. Miyazaki, M. Matsunami, S. Kimura and S. Hasegawa, **“Fermi-Level Tuning of Topological Insulator Thin Films”**, *Jpn. J. Appl. Phys.*, **52** (2013) 110112.
- T. Brandenburg, T. Petit, A. Neubauer, K. Atak, M. Nagasaka, R. Golnak, N. Kosugi and E. F. Aziz, **“Fluorination-dependent Molecular Orbital Occupancy in Ring-shaped Perfluorocarbons”**, *Phys. Chem. Chem. Phys.*, **17** (2015) 18337.
- K. Eguchi, T. Nakagawa, Y. Takagi and T. Yokoyama, **“Direct Synthesis of Vanadium Phthalocyanine and Its Electronic and Magnetic States in Monolayers and Multilayers on Ag(111)”**, *J. Phys. Chem. C*, **119** (2015) 9805.
- P. K. Gogoi, L. Sponza, D. Schmidt, T. C. Asmara, C. Diao, J. C. W. Lim, S. M. Poh, S. Kimura, P. E. Trevisanutto, V. Olevano and A. Rusydi, **“Anomalous Excitons and Screenings Unveiling Strong Electronic Correlations in $\text{SrTi}_{1-x}\text{Nb}_x\text{O}_3$ ($0 \leq x \leq 0.005$)”**, *Phys. Rev. B*, **92** (2015) 035119.
- T. Hajiri, T. Ito, M. Matsunami, B. H. Min, Y. S. Kwon, K. Kuroki and S. Kimura, **“Orbital-dependent Electron Correlation in LiFeAs Revealed by Angle-resolved Photoemission Spectroscopy”**, *Phys. Rev. B*, **93** (2016) 024503.
- A. Hara and T. Awano, **“Mechanism of Formation of Ultrashallow Thermal Donors in Carbon-doped Oxygen-rich Monocrystalline Silicon Preannealed to Introduce Hydrogen”**, *Jpn. J. Appl. Phys.*, **54** (2015) 101302.
- M. Harima, T. Morimoto and Y. Ohki, **“Structural Change Induced in LaAlO_3 by Ion Implantation”**, *IEEJ Transactions on Electrical and Electronic Engineering*, **11** (2016) 5.
- T. Hirahara, T. Shirai, T. Hajiri, M. Matsunami, K. Tanaka, S. Kimura, S. Hasegawa and K. Kobayashi, **“Role of Quantum and Surface-State Effects in the Bulk Fermi-Level Position of Ultrathin Bi Films”**, *Phys. Rev. Lett.*, **115** (2015) 106803.
- A. Iguchi, T. Kawai and K. Mizoguchi, **“Energy Transfer between TI^+ -type Impurities in NaCl Crystals”**, *Phys. Status Solidi C*, **13** (2016) 85.
- H. J. Im, M. Iwataki, S. Yamazaki, T. Usui, S. Adachi, M. Tsunekawa, T. Watanabe, K. Takegahara, S. Kimura, M. Matsunami, H. Sato, H. Namatame and M. Taniguchi, **“Electronic Structure of Mott-insulator $\text{CaCu}_3\text{Ti}_4\text{O}_{12}$: Photoemission and Inverse Photoemission Study”**, *Solid State Commun.*, **217** (2015) 17.
- H. J. Im, T. Ito, H. Miyazaki, S. Kimura, Y. S. Kwon, Y. Saitoh, S.-I. Fujimori, A. Yasui and H. Yamagami, **“Fermi Surface Variation of Ce 4f-electrons in Hybridization Controlled Heavy-fermion Systems”**, *Solid State Commun.*, **209–210** (2015) 45.
- K. Imura, M. Saito, M. Kaneko, T. Ito, T. Hajiri, M. Matsunami, S. Kimura, K. Deguchi, H. S. Suzuki and N. K. Sato, **“Origin of the Black-golden Transition in $\text{Sm}_{1-x}\text{Y}_x\text{S}$ ”**, *J. Phys.: Conf. Ser.*, **592** (2015) 012028.
- T. Inoue, T. Morimoto and Y. Ohki, **“Experimental Observations on the Crystalline Structures of YAlO_3 Single Crystal at High Temperatures”**, *Appl. Phys. A*, **119** (2015) 1423.
- S. Kaneko, T. Morimoto and Y. Ohki, **“Cause of the Appearance of Oxygen Vacancies in Yttria-stabilized Zirconia and Its Relation to 2.8 eV Photoluminescence”**, *Jpn. J. Appl. Phys.*, **54** (2015) 06GC03.
- T. Kaneyasu, M. Ito, K. Soejima, Y. Hikosaka and E. Shigemasa, **“Site-specific Formation of Metastable OCS^{2+} Studied by Auger-electron-**

- ion Coincidence Method”, J. Phys. B, **48** (2015) 125101.
- S. Kimura, H. Tanida, M. Sera, Y. Muro, T. Takabatake, T. Nishioka, M. Matsumura and R. Kobayashi, “**Relation between *c-f* Hybridization and Magnetic Ordering in CeRu₂Al₁₀: An Optical Conductivity Study of Ce(Ru_{1-x}Rh_x)₂Al₁₀ ($x \leq 0.05$)**”, Phys. Rev. B, **91** (2015) 241120.
- M. Kitaura, S. Tanaka, M. Itoh, A. Ohnishi, H. Kominami and K. Hara, “**Excitation Process of Ce³⁺ and Eu²⁺ Ions Doped in SrGa₂S₄ Crystals under the Condition of Multiplication of Electronic Excitations**”, J. Lumin., **172** (2016) 243.
- T. Kondo, M. Nakayama, R. Chen, J. J. Ishikawa, E.-G. Moon, T. Yamamoto, Y. Ota, W. Malaeb, H. Kanai, Y. Nakashima, Y. Ishida, R. Yoshida, H. Yamamoto, M. Matsunami, S. Kimura, N. Inami, K. Ono, H. Kumigashira, S. Nakatsuji, L. Balents and S. Shin, “**Quadratic Fermi Node in a 3D Strongly Correlated Semimetal**”, Nature Commun., **6** (2015) 10042.
- K. R. Koswattage, H. Kinjo, Y. Nakayama and H. Ishii, “**Interface Electronic Structures of the L-Cysteine on Noble Metal Surfaces Studied by Ultraviolet Photoelectron Spectroscopy**”, e-J. Surf. Sci. Nanotech., **13** (2015) 373.
- A. Masuno, N. Nishiyama, F. Sato, N. Kitamura, T. Taniguchi and H. Inoue, “**Higher Refractive Index and Lower Wavelength Dispersion of SiO₂ Glass by Structural Ordering Evolution *via* Densification at a Higher Temperature**”, RSC Adv., **6** (2016) 19144.
- S. Mitsunobu, M. Zhu, Y. Takeichi, T. Ohgashi, H. Suga, M. Jinno, H. Makita, M. Sakata, K. Ono, K. Mase and Y. Takahashi, “**Direct Detection of Fe(II) in Extracellular Polymeric Substances (EPS) at the Mineral-Microbe Interface in Bacterial Pyrite Leaching**”, Microbes and Environments, **31** (2016) 63.
- T. Morimoto, M. Harima, Y. Horii and Y. Ohki, “**Involvement of Crystallinity in Various Luminescent Bands in Yttrium Aluminate**”, Nucl. Instrum. Meth. B, **366** (2016) 198.
- M. Nagasaka, H. Yuzawa and N. Kosugi, “**Development and Application of *in Situ/operando* Soft X-ray Transmission Cells to Aqueous Solutions and Catalytic and Electrochemical Reactions**”, J. Electron Spectrosc. Relat. Phenom., **200** (2015) 293.
- K. Nakayama, H. Kimizuka, Y. Tanaka, T. Sato, S. Souma, T. Takahashi, S. Sasaki, K. Segawa and Y. Ando, “**Observation of Two-dimensional Bulk Electronic States in the Superconducting Topological Insulator Heterostructure Cu_x(PbSe)₅(Bi₂Se₃)₆: Implications for Unconventional Superconductivity**”, Phys. Rev. B, **92** (2015) 100508(R).
- Y. Ohtsubo, J. Kishi, K. Hagiwara, P. L. Fèvre, F. Bertran, A. Taleb-Ibrahimi, H. Yamane, S. Ideta, M. Matsunami, K. Tanaka and S. Kimura, “**Surface Tomonaga-Luttinger Liquid State on Bi/InSb(001)**”, Phys. Rev. Lett., **115** (2015) 256404.
- J. Okabayashi, S. Miyasaka, K. Hemmi, K. Tanaka, S. Tajima, H. Wadati, A. Tanaka, Y. Takagi and T. Yokoyama “**Investigating Orbital Magnetic Moments in Spinel-Type MnV₂O₄ Using X-ray Magnetic Circular Dichroism**”, J. Phys. Soc. Jpn., **84** (2015) 104703.
- K. Ozaki, S. Aoki, K. Kamada, T. Kosaka, F. Mizutani, E. Shibayama, S. Takahashi, Y. Tateishi, S. Tawa and K. Yamada, “**Development of New-type Nuclear Emulsion for a Balloon-borne Emulsion Gamma-ray Telescope Experiment**”, JINST, **10** (2015) 12018.
- T. Petit, H. Yuzawa, M. Nagasaka, R. Yamanoi, E. Osawa, N. Kosugi and E. F. Aziz, “**Probing Interfacial Water on Nanodiamonds in Colloidal Dispersion**”, J. Phys. Chem. Lett., **6** (2015) 2909.
- P. V. Pikhitsa, C. Kim, S. Chae, S. Shin, S. Jung, M. Kitaura, S. Kimura, K. Fukui and M. Choi, “**Two-band Luminescence from an Intrinsic Defect in Spherical and Terraced MgO Nanoparticles**”, Appl. Phys. Lett., **106** (2015) 183106.
- S. Souma, Z. Wang, H. Kotaka, T. Sato, K. Nakayama, Y. Tanaka, H. Kimizuka, T. Takahashi, K. Yamauchi, T. Oguchi, K. Segawa and Y. Ando, “**Direct Observation of Nonequivalent**

Fermi-arc States of Opposite Surfaces in the Noncentrosymmetric Weyl Semimetal NbP", *Phys. Rev. B*, **93** (2016) 161112.

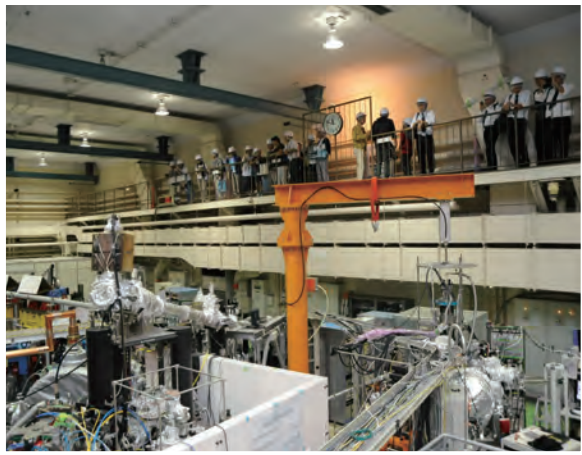
H. Yagi, T. Miyazaki, S. Okita, T. Zaima, H. Okimoto, N. Izumi, Y. Nakanishi, H. Shinohara and S. Hino, **"Ultraviolet Photoelectron Spectra of Sc₃C₂@C₈₀"**, *Chem. Phys. Lett.*, **643** (2015) 98.

M. Yoshida, Y. Mitsutomi, T. Mineo, M. Nagasaka, H. Yuzawa, N. Kosugi and H. Kondoh,

"Direct Observation of Active Nickel Oxide Cluster in Nickel–Borate Electrocatalyst for Water Oxidation by In Situ O K-Edge X-ray Absorption Spectroscopy", *J. Phys. Chem. C*, **119** (2015) 19279.

H. Yuzawa, M. Nagasaka and N. Kosugi, **"In Situ Soft X-ray Absorption Spectroscopy Applied to Solid–Liquid Heterogeneous Cyanopyrazine Hydration Reaction on Titanium Oxide Catalyst"**, *J. Phys. Chem. C*, **119** (2015) 7738.

IMS Open to the public



The background features a large, stylized graphic of concentric circles and radiating lines, resembling a sunburst or a stylized 'V' shape. The circles are composed of dashed lines and small dots, creating a textured effect. The overall color palette is a range of warm, earthy tones from light beige to deep brown.

V

Workshops

UVSOR Symposium 2015

Date: November 6 - 7, 2015

Place: Okazaki Conference Center, Okazaki, Japan

November 6th (Fri.)

13:00 - 13:05 Opening remarks

H. Iwayama (UVSOR)

<Session 1, Chair: **S. Kimura**>

13:05 - 13:25 UVSOR and World Trends of Middle and Low Energy Synchrotron Radiation Facilities

N. Kosugi (UVSOR)

13:25 - 13:45 Valence-Band Dispersion in Organic Thin Films and Interfaces:
Systematic Approach and Discovery of New Dispersion Mechanism

H. Yamane (IMS)

13:45 - 14:05 Development of the Photoelectron Spectroscopy Beamline Suited for Organic Molecular
Solids: BL2B Reconstruction III

S. Kera (IMS)

14:05 - 14:25 Current Status and Future Plans of BL5U and BL7U

K. Tanaka (UVSOR)

14:25 - 14:45 Low-Energy, Polarization-Dependent ARPES Study on the Bulk Fermi Level of Ultrathin Bi
Films

T. Hirahara (Tokyo Tec.)

14:45 - 15:25 Short Presentation

15:25 - 16:00 Coffee Break

<Session 2, Chair: **T. Yokoyama**>

16:00 - 17:00 [Invited] The Mystery of Water, X-Rays Provide Unique Insights

Anders Nilsson (Stockholm Univ.)

<Poster Session & Banquet>

17:30 - 18:30 Poster Session

18:30 - 20:00 Banquet

November 7th (Sat.)

<Session 3, Chair: **E. Shigemasa**>

9:00 - 9:20 Current Status of Light Source Developments at BL1U

M. Katoh (UVSOR)

9:20 - 9:40 Development of Application Technology of Coherent Light Source and Solid-State
Spectroscopy

S. Kimura (Osaka Univ.)

9:40 - 10:00 Comprehensive Study of Photoexcited States of Solids by VUV Emission Spectroscopy

M. Kitaura (Yamagata Univ.)

10:00 - 10:20 Report of the Launch of the Sounding Rocket CLASP (Chromospheric Lyman-Alpha Spectro
Polarimeter)
N. Narukage (NAOJ)

10:20 – 10:50 Coffee Break

<Session 4, Chair: **K. Tanaka**>

10:50 - 11:10 Operando Observation of Efficient Cobalt Oxide Catalysts by Soft X-Ray Absorption
Spectroscopy
M. Yoshida (Keio Univ.)

11:10 - 11:30 Environmental Chemistry based on the Observation of Fine Particles in Environment using
STXM
Y. Takahashi (Tokyo Univ.)

11:30 - 12:00 UUU Meeting

< Poster Presentation >

P01 Generation of 5-MeV Gamma-Ray Beam at BL1U and its Application
H. Zen (Kyoto Univ.)

P02 Modification of Electronic State of DNNT Monolayer on Au(111) Surface by Controlling the Molecular
Arrangement
Y. Hasegawa (Tsukuba Univ.)

P03 Optimization of Liquid Thickness for Soft X-Ray Absorption Spectroscopy in Transmission Mode
M. Nagasaka (IMS)

P04 O K-Edge XAFS Measurement of MnOx Oxygen Evolution Catalyst
F. Yamamoto (Keio Univ.)

P05 Observation of Nickel-Glycine Water Oxidation Catalyst by Soft X-Ray XAFS
S. Onishi (Keio Univ.)

P06 Electrochemical O K-Edge XAFS Spectroscopy for Nickel and Cobalt Borate Catalysts
Y. Mitsutomi (Keio Univ.)

P07 Local Structure Observation of Aqueous KSCN Solution by Soft X-Ray Absorption Spectroscopy
H. Yuzawa (IMS)

P08 Energy Transfer from I⁻ to In³⁺ in NaCl: I⁻, In³⁺ Crystals
A. Iguchi (Osaka Prefecture Univ.)

P09 PL and PLE Spectra of Laser Irradiated α -CN_x Thin Films
K. Ikeda (Fukui Univ.)

P10 Current Status of a Scanning Transmission X-Ray Microscopy Beamline BL4U
T. Ohgashi (UVSOR)

P11 Application of Multi-Electron Coincidence Method to Condensed Molecules
R. Mashiko (Niigata Univ.)

P12 Photoinduced Change of Vacuum Ultra-Violet Absorption Spectra of Amorphous Chalcogenide Thin
Films
K. Hayashi (Gifu Univ.)

P13 Observation of the Optical Isomerization of Amino Acid by Infrared Micro-Spectroscopic Imaging
S. Kamei (Osaka Univ.)

- P14 Stability Evaluation for Improving Accuracy of BL6B, an Infrared-THz Beamline
T. Iizuka (UVSOR)
- P15 Absorption Spectroscopy of Photo-Induced Defects in Ce:GAGG Crystals
R. Inaba (Yamagata Univ.)
- P16 Dissociation Dynamics of Methanol Dication Studied by an Electron-Ion Coincidence Method
M. Higuchi (Niigata Univ.)
- P17 New Findings in Xe Photoelectron Recapture Study of Auger Electron Spectroscopy
S. Kosugi (Sophia Univ.)
- P18 Variation in the Spectator Shifts of Resonant Auger Peaks Measured for Fluorohydrocarbon Molecules
T. Kaneda (Hiroshima Univ.)
- P19 Orbital Energy Rearrangement upon Intermolecular Interaction of Perfluoropentacene Thin Films
T. Ueba (IMS)
- P20 Variation in the Adsorbate Molecular Structure by Surface Chemical Reaction
T. Tago (Chiba Univ.)
- P21 Local Electron-Phonon Coupling in HOMO-Band Dispersion of Rubrene Single Crystals: an Angle-Resolved Ultraviolet Photoelectron Spectroscopy Study
F. Bussolotti (IMS)
- P22 Surface Tomonaga-Luttinger Liquid State on the Bi/InSb(001) surface
Y. Ohtsubo (Osaka Univ.)
- P23 Electronic Structure of Trilayer Cuprate Superconductor Bi2223 Revealed by ARPES Using Low Photon Energy
S. Ideta (UVSOR)
- P24 Angle-Resolved Photoelectron Spectroscopy of a Kondo Insulator YbB₁₂(001)Surface
K. Hagiwara (Osaka Univ.)
- P25 Angle Resolved Photoemission Spectroscopy in NdFeP_{1-x}As_x(O,F) Single Crystals
S. Miyasaka (Osaka Univ.)
- P26 Scattering of Electrons from Graphite Substrate by Organic Molecular Monolayer
T. Yamaguchi (Chiba Univ.)
- P27 Filterless Vacuum Ultraviolet Photoconductive Detector Based on SrF₂ Thin Film Fabricated by Pulsed Laser Deposition
Y. Otani (Nagoya Institute Tech.)
- P28 Statistical Analysis of Photoluminescence Decay in AlGaIn Alloys
Y. Itakura (Fukui Univ.)
- P29 Development and Improvement of Spectroscopic Ellipsometry for VUV Region and Complex Refractive Index of AlN Wafer
M. Miyashita (Fukui Univ.)
- P30 Optical Properties of Infrared Emission Garnet Scintillator Crystals
A. Yamaji (Tohoku Univ.)
- P31 Luminescent Study on Gadolinium Pyrosilicate Crystals Using VUV Photons in UVSOR
S. Kurosawa (Tohoku Univ.)

Future Perspectives of Soft X-Ray Imaging

Date: Sep. 7-8, 2015

Venue: Talk; 201, Main Office Building

Poster; 408 & 409, Main Laboratory Building

Sep 7th, Mon.

<Session #1 Chair: **Mitsunori Toyoda** (Tohoku University)>

- 13:30 - 13:40 Introduction
Takuji Ohigashi (Institute for Molecular Science)
- 13:40 - 14:10 Status of a Scanning Transmission X-Ray Microscopy Beamline, BL4U, and Development of Applied Observation Methods
Takuji Ohigashi (Institute for Molecular Science)
- 14:10 - 14:40 Structural Observation of Rubber Composite using Scanning Transmission X-Ray Microscope
Fusae Kaneko (SUMITOMO RUBBER INDUSTRIES, LTD)
- 14:40 - 15:10 Development of EUV Microscopes for EUV Mask Observation at New SUBARU
Tetsuo Harada (University of Hyogo)
- 15:10 - 15:40 Defect Observation on Mask Blanks Using EUV Illumination
Hiroki Miyai (Lasertec Corporation)
- 15:40 - 16:00 Coffee Brake

<Session #2 Chair: **Takuji Ohigashi** (Institute for Molecular Science)>

- 16:00 - 16:30 Current Status and Future Prospects of the Transmission Soft X-Ray Microscope at The SR Center of Ritsumeikan University
Kuniko Takemoto (Kansai Med. Univ.)
- 16:30 - 17:00 Potential Connectmics Driven by Soft X-Ray Microscopy
Haruo Mizutani (Harvard University)
- 17:00 - 17:50 **Invited talk** “Expectation and Prospects of Soft X-Ray Imaging”
Sadao Aoki (Comprehensive Research Organization for Science and Society)
- 18:00 - 20:00 Poster Session & Banquet

Sep. 8th, Tue.

<Session #3 Chair: **Tetsuo Harada** (University of Hyogo)>

- 9:00 - 9:50 **Invited talk** “Soft X-Ray Spectromicroscopy: Current Status and the Future Perspective”
Tohru Araki (Diamond Light Source)
- 9:50 - 10:20 Wide-Field EUV Microscope Based on Multilayer-Mirror Imaging Objective
Mitsunori Toyoda (Tohoku University)
- 10:20 - 10:40 Coffee Brake
- 10:40 - 11:10 In Situ Soft X-Ray Absorption Spectroscopy of Solid-Liquid Heterogeneous Catalytic Reaction
Hayato Yuzawa (Institute for Molecular Science)
- 11:10 - 11:40 Development and Application of Compact STXM
Yasuo Takeichi (KEK-PF)

- 11:40 - 12:10 Analysis of Organic Materials in Primitive Bodies of Solar System by Soft X-Ray Microscopy
Masayuki Uesugi (JAXA)
- 12:10 - 13:40 Lunch
- (13:00 - 13:40) UVSOR Visiting Tour

<Session #4 Chair: **Takeshi Higashiguchi** (Utsunomiya University)>

- 13:40 - 14:10 Soft X-Ray Nanospectroscopy and Magnetic Dynamics Analysis by Means of Photoemission Electron Microscopy
Takuo Ohkochi (Japan Synchrotron Radiation Research Institute /SPring-8)
- 14:10 - 14:40 Current Status and Prospects of Neutron Imaging
Takenao Shinohara (J-PARC Center, Japan Atomic Energy Agency)
- 14:40 - 15:10 Scanning Transmission X-Ray Microscope Study on Degradation of Positive Electrode Materials
Hisao Yamashige (Toyota Motor Corp)
- 15:10 - 15:30 Coffee Brake

<Session #5 Chair: **Takuo Ohkochi** (Japan Synchrotron Radiation Research Institute /SPring-8)>

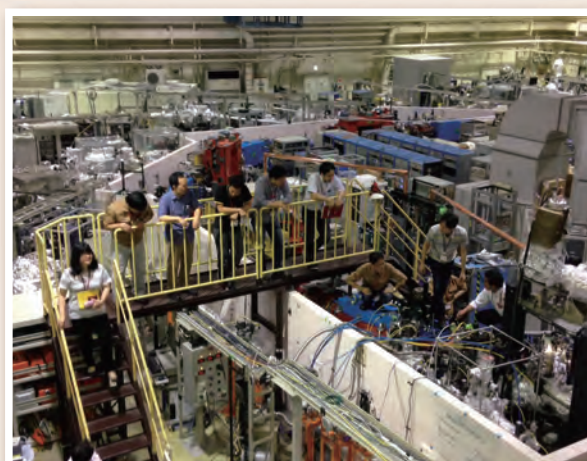
- 15:30 - 16:00 Recent Developments in the Fabrication of X-Ray Imaging Optics
Anthony Baucamp (Kyoto University)
- 16:00 - 16:30 High Spatial Resolution Imaging of Laser Microscopy by Vector Beams
Yuichi Kozawa (Tohoku University)
- 16:30 - 17:00 Laser-Produced Highly Ion Charge Plasma Water Window Soft X-Ray Sources
Takeshi Higashiguchi (Utsunomiya University)
- 17:00 Closing Remark

<Poster Session>

- P01 The Study of Organic Component Mapping by Carbon 1s NEXAFS of STXM
Noriyuki Iwata¹, Mikiko Abe¹, Yuichi Inagaki² and Takuji Ohigashi²
(¹Ricoh Co Ltd., ²UVSOR Facility, Institute for Molecular Science)
- P02 Large-Scale CCD Camera for Wide-Field EUV Microscopy
Toshiyuki Kakudate, Ryoichi Hirose and Mitsunori Toyoda
(Institute of Multidisciplinary Research for Advanced Materials, Tohoku University)
- P03 Development of New Liquid Flow Cell for Scanning Transmission X-Ray Microscope
Masanari Nagasaka, Takuji Ohigashi, Hayato Yuzawa and Nobuhiro Kosugi
(Institute for Molecular Science)
- P04 EUV Mask Observations Using a Coherent EUV Scatterometry Microscope with a High-Harmonic-Generation Source
Takahiro Fujino¹, Yusuke Tanaka¹, Tetsuo Harada¹, Yutaka Nagata², Takeo Watanabe¹ and Hiroo Kinoshita¹
(¹Univ. of Hyogo, ²RIKEN)
- P05 Development of Fabrication Process of Precise Wotler Mirror for Soft X-Ray Imaging
Satoru Egawa, Takehiro Kume, Yoko Takeo, Takahiro Saito, Yoshinori Takei and Hidekazu Mimura

- (Graduate School of Engineering, The University of Tokyo)
- P06 Development of Focusing System for High-order Harmonic Generation with Ellipsoidal Mirror
Hiroto Motoyama¹, Takahiro Sato², Atushi Iwasaki², Satoru Egawa¹, Kaoru Yamanouchi² and
Hidekazu Mimura¹
 (¹School of Engineering, The University of Tokyo, ²School of Science, The University of Tokyo)
- P07 EUV Multilayer Mirrors for Diffraction-Limited Focusing of Isolated Attosecond Pulse
Yuki Tamaru^{1,2}, Satoshi Mori², Kazuhiro Sawada^{1,4}, Yuxi Fu¹, Eiji. J. Takahashi¹, Akira Suda²,
Fumihiko Kannari⁴, Katsumi Midorikawa¹ and Mitsunori Toyoda³
 (¹RIKEN, ²Tokyo Univ. of Sci., ³Tohoku Univ., ⁴Keio Univ)
- P08 Investigation of Bacteria in the Bacteriogenic Iron Oxides Using Scanning Transmission X-Ray
 Microscopy
Hiroki Suga¹, Sakiko Kikuchi², Yasuo Takeichi^{3,4}, Chihiro Miyamoto⁵, Nobuhito Inami³, Kazuhiko
Mase^{3,4}, Kanta Ono^{3,4}, Masaaki Miyahara¹ and Yoshio Takahashi^{3,5}
 (¹Hiroshima Univ., ²JAMSTEC, ³KEK-PF, ⁴SOKENDAI, ⁵The Univ. of Tokyo)
- P09 Development of Micro Coherent EUV Scatterometry Microscope for Phase Defect Characterization
Hiraku Hashimoto¹, Tetsuo Harada¹, Tsuyoshi Amano², Takeo Watanabe¹ and Hiroo Kinoshita¹
 (¹Univ. of Hyogo, ²EIDEC)
- P10 Soft X-Ray Emission Spectroscopy of Electrochemically Li Inserted Si Substrate
Tshihiro Kondo¹, Nana Aoki¹ and Kohei Uosaki²
 (¹Ochanomizu Univ., ²NIMS)
- <Posters from Speakers (No abstract)>
- S11 Soft X-Ray Nanospectroscopy and Magnetic Dynamics Analysis by Means of Photoemission Electron
 Microscopy
Takuo Ohkochi (Spring-8)
- S12 The Effects of Irradiation on Growth and Microstructure of *Pseudanabaena Foetida*
- S13 Current Status and Future Prospects of the Transmission Soft X-Ray Microscope at The SR Center of
 Ritsumeikan University
Kuniko Takemoto (Kansai Med. Univ.)
- S14 High Spatial Resolution Imaging of Laser Microscopy by Vector Beams
Yuichi Kozawa (Tohoku Univ.)
- S15 Current Status of Scanning Transmission X-Ray Microscopy Beamline at UVSOR-III
Takuji Ohigashi (Institute for Molecular Science)
- S16 Development of EUV Microscopes for EUV Mask Observation at New SUBARU
Tetsuo Harada (University of Hyogo)
- S17 Wide-Field EUV Microscope Based on Multilayer-Mirror Imaging Objective
Mitsunori Toyoda (Tohoku University)
- S18 Spectral Analysis of EUV Emission from Highly Charged Zr Ions
- S19 Laser-Produced Highly Ion Charge Plasma Water Window Soft X-Ray Sources
- S20 Development of High Power, Short Pulse CO₂ Laser System for Efficient EUV Sources
Takeshi Higashiguchi (Utsunomiya University)
- S21 Development and Application of Compact STXM
Yasuo Takeichi (KEK-PF)

One year at UVSOR







Editorial Board : H. Iwayama S. Ideta M. Sakai H. Hagiwara H. Fujise

**Institute for Molecular Science
National Institutes of Natural Sciences
Okazaki 444-8585, Japan**

Tel: +81-564-55-7402

Fax: +81-564-54-7079

<http://www.uvsor.ims.ac.jp>

ISSN 0911-5730